Imperial College
London

Reconstruction and Control Laws for Multi-conjugate Adaptive Optics in Astronomy

Fernando Quirós-Pacheco

Submitted in partial fulfilment of the requirements
for the degree of Doctor of Philosophy

Abstract

The optical resolution of ground-based astronomical telescopes is in principle limited by the atmospheric turbulence. Adaptive optics is a technique that enables high-resolution imaging from the ground by compensating in real-time for the phase perturbations introduced by atmospheric turbulence. One of the major limitations of single-conjugate adaptive optics (SCAO) is the fact that compensation is only attainable in a small field of view due to anisoplanatism. Multi-conjugate adaptive optics (MCAO) is a technique that was conceived to overcome this limitation. This is achieved by the use of several wavefront sensors (WFSs) to probe the atmospheric volume in different directions, and several deformable mirrors (DMs) optically conjugated at different altitudes to compensate for the phase perturbations introduced by the atmospheric volume.

Spatial reconstruction in MCAO refers to the problem of estimating from the WFSs measurements the three-dimensional distribution of the atmospheric-turbulence phase perturbations. We present a review of the deterministic and the statistical estimation methods to solve the reconstruction problem in MCAO by describing the problem within the formalism of inverse problems. Then, we have used this formalism to study and fully characterize the propagation of the remaining error —also known as generalized aliasing— in MCAO. We have also studied the application of modal gain optimization in MCAO, and we have shown that the generalized aliasing in MCAO poses a shortcoming to the generalization of this control technique to MCAO.

In the framework of the Multi-conjugate Adaptive optics Demonstrator (MAD) project, we have participated in the experimental validation of the MCAO concept in the laboratory. We present the high-flux optimization of the MAD system and a comparison of simulation and experimental results.

Declaration of conjoint work

Collaboration with ONERA

Fernando Quirós-Pacheco did an internship during the second year of his PhD in the Department of Applied and Theoretical Optics (DOTA) of the *Office National d'Etudes et de Recherches Aerospatiales* (ONERA) in France, under the supervision of Jean-Marc Conan. He collaborated with the ONERA team in the implementation of a simulation tool written in the IDL programming language for the purpose of studying reconstruction and control laws for adaptive optics systems. The simulation results presented in this PhD thesis were carried out with this simulation tool.

Collaboration with ESO

Fernando Quirós-Pacheco did an internship during the third and fourth years of his PhD in the Adaptive Optics Group of the European Southern Observatory (ESO), in Germany, to participate in the *Multi-conjugate Adaptive Optics Demonstrator* (MAD) project, under the supervision of Enrico Marchetti. He developed a simulation tool customized for the MAD system, and collaborated with the MAD team in the system characterization and high-flux optimization of the MAD system.

Acknowledgements

Looking back over the past four years, I realize that I was very lucky to carry out this multi-site PhD collaborating with some of the leading adaptive-optics groups in Europe. But I feel this way not only from the academic point of view. Living in three different countries was most importantly a very enriching experience from the human point of view. I would like to acknowledge below the people and the institutions that contributed to my professional and personal growth during the time of my PhD.

Starting in chronological order, I would like to acknowledge the support of the *Consejo Nacional de Ciencia y Tecnología* (CONACYT) of Mexico who granted me the scholarship (CONACYT grant number 149028) to do this PhD.

I would like to thank my PhD supervisor Chris Dainty for encouraging me to pursue this multi-site PhD, and providing me with all the means to carry out my work, and also for all the freedom and trust he offered me to conduct my research.

I would like to thank my PhD co-supervisor Carl Paterson for all the fruitful discussions regarding adaptive optics and atmospheric turbulence we had particularly during my first PhD year at Imperial College London.

Without any doubt the decisive moment of my first PhD year took place at the meeting of the European Research Training Network (RTN) in adaptive optics for extremely-large telescopes (ELTs), in the Observatory of Haute Provence. Indeed, I would like to thank Norbert Hubin for having invited me during that meeting to participate in the study of control laws for adaptive optics in the framework of the MAD project at ESO. Also, I would like to thank Gérard Rousset who kindly accepted during that meeting too, to let me do an internship at ONERA during my second PhD year in order to participate in the research activities on control taking place at this institution.

During my second PhD year I moved to Paris to do an internship at ONERA. I would like to thank all the members of the *Department of Applied and Theoretical Optics* (DOTA), in particular to Jean-Marc Conan, Cyril Petit, Thierry Fusco, Magalie Nicolle, and Rodolphe Conan, for the great working atmosphere they create, always open for discussions, and always encouraging team working. Special acknowledgements go to my co-supervisor Jean-Marc Conan, for his dedicated compromise and guidance that continued up to the submission of this thesis.

For the last two years of my PhD, I moved to Munich to do an internship at ESO. I would like to thank all the members of the *Adaptive Optics Group*, in particular to the *simulators* Miska Le Louarn, Christophe Verinaud, Visa Korkiakoski, and Carlos Correia for all the fruitful discussions. Also, I would like to thank the project manager of MAD, Enrico Marchetti, for letting me participate in that project, and to all the members of the MAD team, in particular to Sylvain Oberti, Johann Kolb, and Joana Santos, for sharing with me a bit of their know-how and great experience in laboratory work. Also, special acknowledgements to Sylvain Oberti for carefully reading the chapter on MAD and giving me feedback.

I would like to thank all members of the *Applied Optics Group* of the National University of Ireland, in Galway, for the fruitful discussions held during my visits to the group, and to the Science Foundation Ireland under grant SFI/01/PI.2/B039C for travel support.

Finally, I would like to thank to all my friends for all the great moments we spent together during all these years. In London, to Luciana, Caro, Constanza, Marcos, Romina, Sherine, Alessandro, Andrea and Thomas. In Paris, to Valeria, Isis, Ursula, Ambroise, Francois, Irina, Vincent et Diane. In Munich, to Silvia, Joana, Isabelle and Marin, Constanza, Anne, Babak, Raul, and Jerome and Natalia.

At last but not least, I want to thank to all my family in Mexico who supported me and stayed always close despite the ocean in-between.

Contents

List of Figures

List of Tables

Introduction

The optical resolution of ground-based astronomical telescopes is limited by the perturbations introduced by the atmospheric turbulence. Adaptive optics (AO) is a technology that was developed to enable high-resolution imaging from the ground. Although the concept of adaptive optics compensation dates back to the 1950's [9], it was not demonstrated on the sky for astronomical applications until 1989 [129]. The first generation of AO systems were of the *single-conjugate* kind. A single-conjugate adaptive optics (SCAO) system comprises a single deformable mirror (DM) to compensate in real-time for the phase perturbations introduced by the atmospheric turbulence, and a single wavefront sensor (WFS) to measure the phase perturbation residuals after correction by the DM that result in a given direction in the sky where a reference source –or guide star (GS)– is located. Then, from the perspective of control system theory, an AO system is nothing but a multi-variable feedback control system.

At present, most major astronomical telescopes have been equipped with SCAO systems that have effectively allowed to reach a near-diffraction-limited resolution at infrared wavelengths [114]. However, one of the major limitations of SCAO systems is that the atmospheric turbulence compensation is only attainable in a very small field of view (a few tens of arcseconds in the near-infrared) due to the anisoplanatism effect [39]. This effect is related to the fact that the atmospheric turbulence is distributed in altitude. The concept of multi-conjugate adaptive optics (MCAO) was then proposed to overcome this limitation [26, 11]. An MCAO system comprises several deformable mirrors (DMs) conjugated at different altitudes to compensate for the phase perturbations introduced by the atmospheric volume, and several wavefront sensors (WFSs) to probe the atmospheric volume in different directions using several guide stars (GSs). Theoretical studies based on analytical formulations and numerical simulations have shown that MCAO systems comprising 2 to 3 DMs and 3 to 5 WFSs would be capable of providing a near-diffraction-limited resolution in a large field of view (1 to 2 arcminutes in the near-infrared) on an 8/10 m-class telescope [46, 146, 80].

In this work, we will study the topics of spatial reconstruction and temporal control in MCAO systems. Spatial reconstruction in MCAO refers to the problem of estimating from the WFSs measurements the three-dimensional distribution of the atmospheric-turbulence phase perturbations. On the other hand, temporal control in MCAO refers to the problem of how to determine the command signals that drive the DMs in order to compensate in real-time for the atmospheric volume —perhaps also optimizing the correction in a particular field-of-view (FoV) of interest— and ensuring the temporal stability of the control system.

The problem of spatial reconstruction in MCAO can be rigorously studied within the formalism of (linear) inverse problems [62]. Within this formalism, the reconstruction process can be formulated with a simple vector-matrix multiply $\boldsymbol{\varphi}_{tur} = \mathbf{Rs}$, in which $\boldsymbol{\varphi}_{tur}$ is a vector representing the atmospheric turbulence volume, $\mathbf{s}$ is a vector containing the WFSs measurements, and $\mathbf{R}$ is a matrix known as the *MCAO reconstruction matrix*. The application of both deterministic (i.e. following a least-squares approach) and statistical (i.e. following a minimum mean-square error or a maximum a-posteriori approach) methods to derive the MCAO reconstruction matrix has been already studied by several authors [69, 43, 47]. Thus, it has been shown that the statistical methods lead to a better reconstruction thanks to the statistical priors on the atmospheric turbulence and the WFSs measurement noise that regularize the inversion process.

In chapter 2 we will study the problem of wavefront reconstruction in MCAO. In particular, we will thoroughly study the *generalized aliasing* in MCAO, which has been already identified as one of the limitations in MCAO reconstruction [123], but that has not been fully characterized in the past. Thus, we will propose in chapter 2 a full characterization of the generalized aliasing —also known as the *propagation of the remaining error*— in MCAO based on analytical formulations and numerical simulations. We will study how this source of error is propagated through a *least-squares* and a *minimum mean-square error* MCAO reconstruction matrix.

In chapter 3 we will study the problem of temporal control in MCAO systems. In particular, we will study the generalization to MCAO of one of the control techniques that has been successfully implemented in several SCAO systems, namely, the *modal gain optimization* [55, 31]. We will show that the practical implementation of modal gain optimization in MCAO is seriously limited by the generalized aliasing, which —as opposed to the SCAO case— cannot be neglected in the computation of the optimized modal gains for MCAO. We will support our studies with both analytical formulations and numerical simulations.

The numerical simulation results presented in this work were obtained with a simulation tool implemented in the IDL language developed during my internship at ONERA. The simulation tool was developed in collaboration with Cyril Petit —PhD student at ONERA—, and with the contributions of other colleagues since the simulation tool was built on a rich library of AO routines already existing at ONERA.

As part of my PhD thesis, I had the opportunity to participate in the experimental validation of MCAO in the laboratory with the *Multi-conjugate Adaptive optics Demonstrator* (MAD) system developed by the European Southern Observatory (ESO) [95]. I developed a simulation tool in order to accurately match the characteristics of the MAD system and study the performance optimization under high-flux conditions. In chapter 4 we will present a comparison of simulation and experimental results obtained with the MAD system. The reconstruction and control law implemented in the MAD system were a simple *least-squares* reconstruction matrix and a two-parameter temporal controller. The experimental results obtained in the laboratory are, to our knowledge, the first experimental results to validate under realistic conditions the concept of MCAO.

Chapter 1

Atmospheric turbulence and adaptive optics

In the first part of this chapter we will review the general characteristics of the atmospheric turbulence and its effects on the imaging resolution of ground-based astronomical telescopes. In the second part of this chapter we will review the generalities of adaptive optics (AO) systems and introduce the different configurations of *single-conjugate adaptive optics* (SCAO), *ground-layer adaptive optics* (GLAO), and *multi-conjugate adaptive optics* (MCAO). We will also introduce the mathematical models of the AO system components that we will use throughout this work.

1.1 Atmospheric turbulence

Air masses are always in motion mainly due to the solar heating of the Earth's surface that causes convection currents. The air flow can be either laminar (i.e. uniform and regular) or turbulent (i.e. with random subflows). The *Reynolds number* is a dimensionless parameter that gives the conditions under which a laminar flow becomes turbulent. It is defined as the ratio of the inertial forces to the viscous forces within the fluid, and it can be expressed as:

$$Re \equiv \frac{\text{inertial forces}}{\text{viscous forces}} = \frac{Vl}{k_v} \tag{1.1}$$

where V is a characteristic velocity, l is a characteristic size also known as the *length scale*, and k_v is the kinematic viscosity of the fluid. If Re is larger than a critical value Re_c that depends only on the geometry of the flow (e.g. the geography), then the fluid

will move turbulently. The kinematic viscosity of atmospheric air is $k_v = 15{\cdot}10^{-6}\,\mathrm{m^2 s^{-1}}$. Considering typical characteristic velocities ($V > 1$ m/s) and length scales l of several meters to kilometers results in Reynolds numbers larger than $Re > 10^6$. These numbers are sufficiently large to ensure the prevalence of atmospheric turbulence [104].

Atmospheric turbulence —as any other turbulent flow— is characterized by *random* vortices also known as *turbulent eddies* [142]. The velocity V at each point in space (and at each instant) can be represented by a random variable whose spatial (and temporal) statistics need to be characterized. Random fluctuations of the velocity field V are also accompanied by random fluctuations of other variables of interest such as the temperature T, the humidity %, or —-most importantly for imaging studies— the refractive index N.

1.1.1 Statistical descriptions

The second-order statistics of the fluctuations between two points in space (or two instants in time) of any variable of interest $x(\mathbf{r}, t)$ —e.g. velocity, temperature, or refractive index— are characterized by *correlation functions* or *structure functions*. The spatial correlation function of $x(\mathbf{r})$ between two points in space $\mathbf{r_1}$ and $\mathbf{r_2}$ is defined as:

$$B_x(\mathbf{r_1}, \mathbf{r_2}) = \langle x(\mathbf{r_1}) x(\mathbf{r_2}) \rangle \tag{1.2}$$

where $\langle \cdot \rangle$ denotes an ensemble average. On the other hand, the spatial structure function of $x(\mathbf{r})$ between two points in space $\mathbf{r_1}$ and $\mathbf{r_2}$ is defined as the mean-square value of the difference $x(\mathbf{r_2}) - x(\mathbf{r_1})$. That is:

$$D_x(\mathbf{r_1}, \mathbf{r_2}) = \left\langle [x(\mathbf{r_2}) - x(\mathbf{r_1})]^2 \right\rangle \quad . \tag{1.3}$$

Similar definitions can be applied to temporal statistics. In the most general case, atmospheric random variables $x(\mathbf{r}, t)$ are *non-stationary* and *inhomogeneous*, which implies that the first-order temporal and spatial statistics (i.e. mean and variance) are changing over time and space. However in practice, these changes occur rather smoothly and therefore it can be assumed that $x(\mathbf{r}, t)$ are stationary and homogeneous *by increments* [60, Ch.3]. This implies that the second-order statistics will only depend on the time difference τ or the separation vector between two points $\boldsymbol{\rho} = \mathbf{r_2} - \mathbf{r_1}$, as long as τ and $\boldsymbol{\rho}$ are not too large.

The atmospheric turbulence is also considered to be *isotropic*. This implies that the spatial statistics do not depend on orientation. Therefore, the second-order statistics

between two points in space will only depend on the modulus of the separation vector $\rho = |\boldsymbol{\rho}| = |\mathbf{r_2} - \mathbf{r_1}|$. Under these assumptions the mathematical relationship between the structure function $D_x(\rho)$ and the correlation function $B_x(\rho)$ becomes:

$$D_x(\rho) = 2\left[B_x(0) - B_x(\rho)\right] \quad . \tag{1.4}$$

The spatial statistics of a stationary random variable $x(\mathbf{r})$ can also be stated in the Fourier space in terms of the *power spectrum* of $x(\mathbf{r})$, which can be computed as the three-dimensional Fourier transform of the correlation function $B_x(\boldsymbol{\rho})$:

$$\Phi_x\left(\boldsymbol{\kappa}\right) = \int_{-\infty}^{+\infty} B_x(\boldsymbol{\rho}) \exp(2\pi i \boldsymbol{\kappa} \cdot \boldsymbol{\rho})\, d\boldsymbol{\rho} \tag{1.5}$$

where $\boldsymbol{\kappa}$ is the spatial frequency vector [m^{-1}].

1.1.2 Kolmogorov turbulence model

A. N. Kolmogorov [78] developed a model to describe the spatial statistics of a turbulent flow. Kolmogorov realized that in a fully-developed turbulence there were turbulent eddies of all different length scales l within a certain range $l_0 \leq l \leq L_0$. The length scale of the largest and the smallest eddies are known as the *outer scale* L_0 and the *inner scale* l_0 of the turbulence, respectively.

Turbulent eddies are in constant mixing. Mixing mainly implies a transfer of energy between eddies of different length scales. When the atmospheric airflow becomes turbulent —e.g. due to local convection cells or higher wind speeds— large eddies of length scale L_0 are formed first. Rapid mixing starts to take place and large eddies are broken up into smaller and smaller ones. In this way, kinetic energy is transferred from larger to smaller eddies in a so-called *energy cascade*. This process continues until the eddies are so small ($l \approx l_0$) that viscous forces become important ($Re \approx Re_c$). Kinetic energy is then dissipated in the form of heat and energy cascading stops. In equilibrium, the rate of energy transfer per unit mass (ϵ) must be equal to the rate of energy dissipation per unit mass at the smallest scales [28].

The range of length scales $l_0 \leq l \leq L_0$ at which energy cascading takes place is known as the *inertial range*. For atmospheric turbulence, the innter scale l_0 is of the order of some millimeters [20], and the outer scale L_0 is of the order of tens of meters [19, 162, 1].

In his original paper Kolmogorov derived the structure function $D_v(\rho)$ of the velocity fluctuations $v = V - \langle V \rangle$. His main hypothesis was to consider that within the inertial

range the structure function $D_v(\rho)$ should only depend on the rate of energy transfer per unit mass ϵ. Following a dimensional analysis[1] he found that $D_v(\rho)$ follows a 2/3 power law:

$$D_v(\rho) = C_v^2 \rho^{2/3} \tag{1.6}$$

where C_v^2 is the *velocity structure constant*. C_v^2 is just a constant of proportionality that only depends on ϵ. Following Kolmogorov's hypothesis it is also possible to derive similar statistical descriptions for other variables of interest, such as temperature fluctuations $\Theta = T - \langle T \rangle$ or refractive index fluctuations $n = N - \langle N \rangle$. Obukhov [102] showed that the structure function $D_T(\rho)$ of temperature fluctuations also follows a 2/3 power law:

$$D_T(\rho) = C_T^2 \rho^{2/3} \tag{1.7}$$

where C_T^2 is the temperature structure constant. From equations 1.4, 1.5, and 1.7 Tatarski [140] showed that the Kolmogorov power spectrum $\Phi_T(\kappa)$ of temperature fluctuations is given by:

$$\Phi_T(\kappa) = 0.033(2\pi)^{-2/3} C_T^2 \kappa^{-11/3} \tag{1.8}$$

where κ is the modulus of the spatial frequency vector $\kappa = |\boldsymbol{\kappa}|$. Note that the inertial range can also be stated in the spatial frequency domain as $1/L_0 \leq \kappa \leq 1/l_0$.

1.1.2.1 Refractive index fluctuations

The refractive index of the air N is a function of temperature and humidity, but in optical propagation the effects of humidity fluctuations can be neglected [124]. Then, it can be shown that the structure function $D_n(\rho)$ of the refractive index fluctuations also follows a 2/3 power law:

$$D_n(\rho) = C_n^2 \rho^{2/3} \ . \tag{1.9}$$

The refractive index structure constant C_n^2 and the temperature structure constant C_T^2 are related by [124]:

$$C_n^2 = (80 \cdot 10^{-6}) \frac{P}{T^2} C_T^2 \tag{1.10}$$

where P is the air pressure expressed in millibars and T is the absolute temperature expressed in Kelvins. Similarly to equation 1.8, the Kolmogorov power spectrum $\Phi_n(\kappa)$

[1] The units of ϵ are $\left[\frac{\mathrm{J}}{\mathrm{s \cdot kg}}\right] = \left[\frac{\mathrm{m}^2}{\mathrm{s}^3}\right]$, the units of D_v are $\left[\frac{\mathrm{m}^2}{\mathrm{s}^2}\right]$, and the units of ρ are [m]. If D_v only depends on ρ and ϵ then $D_v \propto [\epsilon]^x [\rho]^y$ and a dimensional analysis leads to $x = 2/3$ and $y = 2/3$.

of the refractive index fluctuations n is given by:

$$\Phi_n(\kappa) = 0.033(2\pi)^{-2/3} C_n^2 \kappa^{-11/3} \quad . \tag{1.11}$$

Refractive index fluctuations in the atmospheric turbulence are the main cause of the limitations in astronomical imaging. For this reason refractive index fluctuations are also known as *optical turbulence*. The refractive index structure constant C_n^2 is a measure of the strength of the optical turbulence. It is usually expressed as a function of altitude h. The precise characterization of the $C_n^2(h)$ profile above an astronomical observatory is very important for the design of adaptive optics systems. Different instruments have been developed to determine experimentally the $C_n^2(h)$ profile. Some of these instruments are:

- *Meteorological Balloons.* The launch of meteorological balloons equipped with temperature sensors can characterize the temperature structure constant $C_T(h)$ profile [8]. The $C_n^2(h)$ profile can then be derived from equation 1.10. The resolution in altitude of the $C_n^2(h)$ profile obtained with this method is very high (5 to 10 m). However, note that the resulting $C_n^2(h)$ profile is not an instantaneous one since the balloons take several hours to ascend.

- *Scintillation Detection and Ranging (SCIDAR).* The $C_n^2(h)$ profile can be derived from the analysis of the scintillation patterns produced by binary stars [156]. The SCIDAR technique requires the use of a relatively large telescope ($D =$ 1 m). When the detector is conjugated to the telescope pupil the SCIDAR cannot measure the $C_n^2(h)$ profile at low altitudes ($h < 1$ km). This limitation is overcome when the detector is conjugated to a negative altitude so that the scintillation patterns produced by low-altitude turbulence can be developed [6, 41]. Note that the SCIDAR produces real-time measurements of the $C_n^2(h)$ profile. The resolution in altitude is ≈ 300 m. More recently, a SCIDAR profiling technique that requires only a single star has also been proposed [63].

- *Multi-Aperture Scintillation Sensor (MASS).* The $C_n^2(h)$ profile is retrieved from the analysis of the scintillation patterns produced by several concentric apertures collecting the flux of a single bright star [145]. MASS has the advantage that it requires a smaller telescope ($D \approx 15$ cm) than the SCIDAR. The resolution in altitude is similar to the one of SCIDAR but practical designs of MASS instruments are insensitive to low-altitude turbulence.

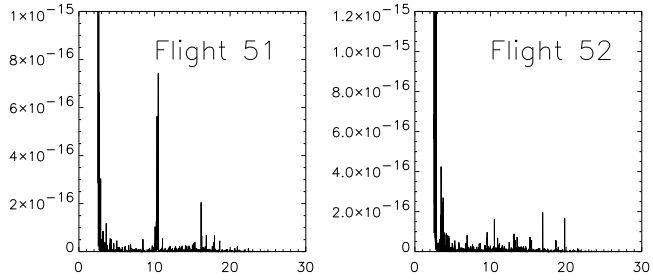

Figure 1.1: $C_n^2(h)$ profiles from Paranal Observatory obtained with meteorological balloons. The altitude (x-axis) is in kilometers above sea level, and the C_n^2 (y-axis) is in $m^{-2/3}$. (Courtesy: M. Le Louarn).

- *Slope Detection and Ranging (SLODAR).* The SLODAR is based on Shack-Hartmann wavefront sensors. The $C_n^2(h)$ profile can be derived from the cross-correlation analysis of the Shack-Hartmann wavefront sensor slopes produced when observing binary stars [159]. The resolution in altitude can be from medium ($\approx$ 150 m) to low ($\approx$ 1500 m) depending on the binary star configuration. The main advantage of SLODAR is that the low-altitude turbulence ($h < 2$ km) can be very well characterized.

Figure 1.1 shows a couple of high-resolution $C_n^2(h)$ profiles obtained with meteorological balloons launched above Paranal Observatory during the 1992 PARSCA campagin [87]. These profiles show that the turbulence strength is concentrated into thin layers at particular altitudes where the value of C_n^2 increases substantially. Furthermore, it can be seen that most of the turbulence strength is concentrated in the first few kilometers of the atmosphere. More recent studies using SLODAR at Paranal have confirmed that the 60% of the turbulence is concentrated within the first two kilometers [66]. Similar $C_n^2(h)$ profiles have been measured for other astronomical observatories [149, 148].

1.1.3 Imaging through the atmosphere

The knowledge of the C_n^2 profile and the statistics of the refractive index fluctuations (eq. 1.9 and 1.11) makes it possible to quantify statistically the perturbations introduced to a plane wave propagating through the atmosphere. Indeed, a plane wave coming from an astronomical object and entering the Earth won't be planar anymore when reaching a ground-based telescope. The resultant complex field at the telescope

pupil $\Psi_0(\mathbf{r})$:

$$\Psi_0(\mathbf{r}) = A(\mathbf{r}) \exp[j\varphi(\mathbf{r})] \tag{1.12}$$

will exhibit random fluctuations in the phase $\varphi(\mathbf{r})$ and the amplitude $A(\mathbf{r})$ after propagation through the atmosphere. In the near-field approximation[2] amplitude fluctuations (i.e. scintillation) may be neglected [124], so $A(\mathbf{r}) = 1$. This is equivalent to adopting a geometrical optics approach. Therefore, phase perturbations in the telescope pupil $\varphi(\mathbf{r})$ are directly linked to the vertical distribution of refractive index fluctuations $n(\mathbf{r}, h)$ by:

$$\varphi(\mathbf{r}) = k \int_0^\infty n(\mathbf{r}, h)\, dh \tag{1.13}$$

where $k = 2\pi/\lambda$ is the wavenumber at the observing wavelength λ. Based on this equation and the statistical descriptions of the refractive index fluctuations, it can be shown [124] that the phase $\varphi(\mathbf{r})$ exhibits Gaussian statistics and the *structure function of the phase fluctuations* $D_\varphi(\rho)$ and the *power spectrum of the phase fluctuations* $\Phi_\varphi(\kappa)$ are given by:

$$\begin{aligned} D_\varphi(\rho) &= \left\langle [\varphi(\mathbf{r}+\boldsymbol{\rho}) - \varphi(\mathbf{r})]^2 \right\rangle \\ &= 6.88 \left(\frac{\rho}{r_0}\right)^{5/3} , \end{aligned} \tag{1.14}$$

$$\Phi_\varphi(\kappa) = 0.023 r_0^{-5/3} \kappa^{-11/3} \tag{1.15}$$

where r_0 is the *Fried parameter* defined as [37]:

$$r_0 = \left[0.42 \left(\frac{2\pi}{\lambda}\right)^2 \sec(\alpha) \int_0^\infty C_n^2(h)\, dh \right]^{-3/5} , \tag{1.16}$$

and α is the zenith angle of observation. Note that r_0 involves the integral of the $C_n^2(h)$ profile, so it is a measure of the whole turbulence strength as seen from the telescope pupil. The significance of this parameter can be fully appreciated by studying the effects of atmospheric turbulence on the images formed by ground-based astronomical telescopes.

[2] In the near-field approximation the diffraction effects are neglected, which is valid when the atmosphere scale height is $\bar{h} \ll \frac{D^2}{\lambda}$. For typical $\bar{h} \approx 8$ km, and large astronomical telescopes ($D > 1$ m) this condition is well satisfied.

1.1.3.1 Point spread function (PSF) characterization

Let us consider the short-exposure and the long-exposure image of a point-like astronomical object produced by a telescope. By definition, the image will be the point-spread function (PSF) of the telescope+atmosphere optical system [127]. According to Fraunhofer diffraction theory, the *short-exposure* PSF can be computed as:

$$\mathrm{PSF}_{se}(\boldsymbol{\xi}) \propto \left\| \mathcal{F}\left\{ \Psi_0(\mathbf{r}) P(\mathbf{r}) \right\} \right\|^2 \tag{1.17}$$

where $\mathcal{F}\{\cdot\}$ denotes the Fourier transform, $\boldsymbol{\xi}$ is the angular position vector in the image plane (radians or arcseconds), $\Psi_0(\mathbf{r})$ is the complex field in the telescope pupil (eq. 1.12), and $P(\mathbf{r})$ is the telescope pupil function defined as:

$$P(\mathbf{r}) = \begin{cases} 1 & : \quad \frac{D_{oc}}{2} \leq |\mathbf{r}| \leq \frac{D}{2} \\ 0 & : \quad \text{elsewhere} \end{cases} \tag{1.18}$$

where D is the telescope diameter and D_{oc} is the central occultation diameter. The *long-exposure* PSF can be computed as the ensemble average of the short-exposure PSFs:

$$\mathrm{PSF}(\boldsymbol{\xi}) \propto \langle \mathrm{PSF}_{se}(\boldsymbol{\xi}) \rangle \tag{1.19}$$

where $\langle \cdot \rangle$ denotes an ensemble average. Note that in the absence of atmospheric turbulence the image would be equal to the *diffraction-limited* PSF of the telescope. For instance, for a perfect telescope (i.e. with no optical aberrations) the image would be equal to the Airy disk. Figure 1.2 shows typical diffraction-limited, short-exposure, and long-exposure PSFs at $\lambda = 2.2\,\mu$m obtained from numerical simulations for a telescope with $D = 8$ m, and $D_{oc} = 0.14D$. The Fried parameter of the simulated Kolmogorov turbulence was $r_0 = 60$ cm at $\lambda = 2.2\,\mu$m.

As can be seen from figure 1.2, the loss in optical resolution due to the atmospheric turbulence is impressive. At the diffraction limit, the full width half maximum (FWHM) of the PSF is given by:

$$\mathrm{FWHM}_{dif} = 1.03 \frac{\lambda}{D} \ , \tag{1.20}$$

whereas for the long-exposure PSF the FWHM is given by [136, 17]:

$$\mathrm{FWHM} = 0.9759 \frac{\lambda}{r_0} \ . \tag{1.21}$$

For an 8-m telescope and for $r_0 = 60$ cm at $\lambda = 2.2\,\mu$m, the corresponding FHWMs are:

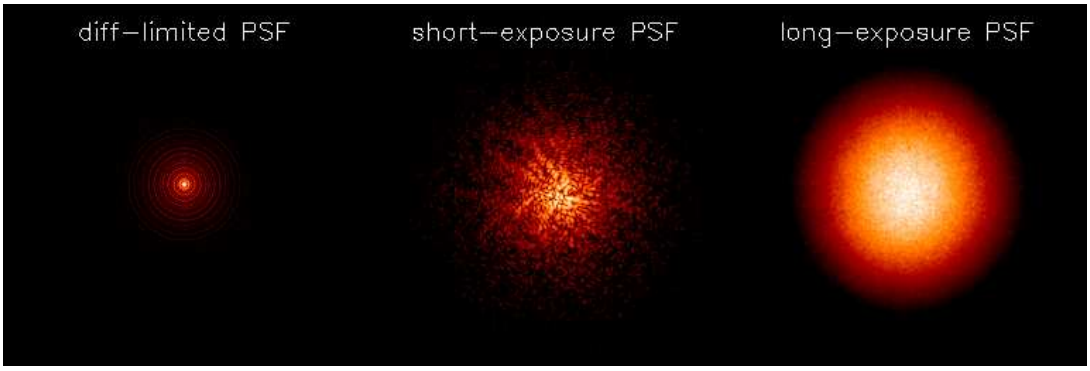

Figure 1.2: Comparison of the diffraction-limited, short-exposure, and long-exposure images at $\lambda = 2.2\,\mu$m of a point-like astronomical object produced by an 8-m telescope.

	FWHM (μrad)	FWHM (arcsec)
diff-limited PSF	0.28	0.06
long-exposure PSF	3.58	0.74

The long-exposure PSF is broadened by a factor of 12 with respect to the diffraction-limited PSF. The size of the long-exposure PSF is better known as the *seeing disk*. It represents the maximum resolution that can be obtained with a ground-based telescope if the atmospheric turbulence is not compensated for. Equivalently, the Fried parameter r_0 can be interpreted as the maximum diameter of a telescope that would operate at its diffraction limit under such atmospheric conditions. In our example above, the real resolution of our 8-m telescope is equivalent to the resolution of a 60-cm telescope. From equation 1.16 it can also be seen that r_0 is proportional to $\lambda^{6/5}$. In our example, the Fried parameter is $r_0 = 60$ cm at $\lambda = 2.2\,\mu$m whereas at visible wavelengths ($\lambda = 0.5\,\mu$m) it becomes $r_0 = 10$ cm. This means that turbulence perturbations are stronger at shorter wavelengths.

Finally, let us discuss briefly the characteristics of the short-exposure PSF. As seen in figure 1.2, at short exposures the intensity pattern in the image plane has a granular or *speckled* appearance. It can be shown that the diameter of each speckle is equal to the diffraction limit of the telescope ($\sim \lambda/D$ radians). However, the speckle pattern exists within a circle of $\sim \lambda/r_0$ radians in diameter.

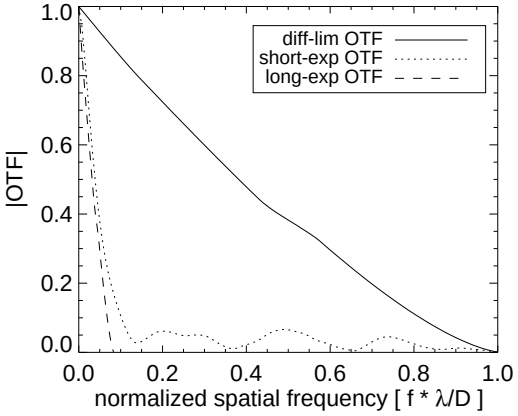

Figure 1.3: Comparison of the diffraction-limited, short-exposure, and long-exposure OTFs at $\lambda = 2.2\,\mu$m of a point-like astronomical object produced by an 8-m telescope. The Fried parameter is $r_0 = 60$ cm. $f = |\mathbf{f}|$ is the modulus of the spatial frequency vector (rad^{-1}).

1.1.3.2 Optical transfer function (OTF) characterization

The optical transfer function (OTF) is defined as the Fourier transform of the PSF. Figure 1.3 shows a cut of the modulus of the normalized OTFs for the diffraction-limited, short-exposure, and long-exposure PSFs shown in figure 1.2. Note that the cut-off frequency of the diffraction-limited OTF is equal to D/λ rad^{-1}.

In the case of short exposures, the spatial frequency content up to the diffraction limit D/λ is present in the OTF, but it is quite distorted and attenuated. Some techniques, such as speckle interferometry, have been developed to partially recover the high-frequency information by post-processing short-exposure images [79].

In the case of long-exposures, since the PSF is the average of the short-exposure PSFs (eq. 1.19), then the speckle pattern is averaged out and the high-frequency information above r_0/λ is completely lost. The cut-off frequency of the long-exposure OTF is effectively equal to r_0/λ rad^{-1}. In our example, it can be seen in figure 1.3 that the cut-off frequency of the long-exposure OTF is 12 times smaller than the diffraction limit, i.e.:

$$\frac{r_0}{\lambda} \sim \frac{D}{12\lambda} = 0.083\frac{D}{\lambda} \ .$$

The long-exposure OTF can be expressed as the product of two optical transfer func-

tions [124]:

$$\mathrm{OTF}(\mathbf{f}) = \mathrm{OTF}_{tur}(\mathbf{f})\ \mathrm{OTF}_{tel}(\mathbf{f}) \tag{1.22}$$

where $\mathrm{OTF}_{tel}(\mathbf{f})$ is the optical transfer function of the telescope and $\mathrm{OTF}_{tur}(\mathbf{f})$ is the optical transfer function of the atmosphere. The OTF of the atmosphere can be computed as the correlation function of the complex field in the telescope pupil $\Psi_0(\mathbf{r})$ (eq. 1.12) evaluated in $\lambda\mathbf{f}$. From equation 1.2, the correlation function of $\Psi_0(\mathbf{r})$ can be expressed as:

$$B_0(\rho) = \langle \Psi_0(\mathbf{r})\Psi_0^*(\mathbf{r}+\boldsymbol{\rho})\rangle \quad . \tag{1.23}$$

Then, the optical transfer function of the atmosphere is given by:

$$\mathrm{OTF}_{tur}(\mathbf{f}) = B_0(\lambda\mathbf{f}) \quad . \tag{1.24}$$

It can also be shown [124] that $B_0(\rho)$ is related to the structure function of the phase fluctuations $D_\varphi(\rho)$ by:

$$B_0(\rho) = \exp\left[-\frac{1}{2}D_\varphi(\rho)\right] \quad . \tag{1.25}$$

Finally, substituting equations 1.24 and 1.25 into 1.22 leads to the full statistical description of the long-exposure OTF:

$$\mathrm{OTF}(\mathbf{f}) = \exp\left[-\frac{1}{2}D_\varphi(\lambda\mathbf{f})\right]\ \mathrm{OTF}_{tel}(\mathbf{f}) \quad . \tag{1.26}$$

The full statistical description of the short-exposure OTF is more elaborate since it is not possible to split the OTF in the product of two optical transfer functions. The details can be found in references [124, 37].

1.1.4 von Kármán turbulence model

In the strict sense, the Kolmogorov turbulence model is only valid within the inertial range $1/L_0 \leq \kappa \leq 1/l_0$. von Kármán proposed a generalization of the Kolmogorov model that takes into account the effects of the inner and outer scales. The von Kármán power spectrum of the refractive index fluctuations is given by [127]:

$$\Phi_n(\kappa) = 0.033(2\pi)^{-2/3}C_n^2(h)\left[\kappa^2 + \left(\frac{1}{L_0}\right)^2\right]^{-11/6}\exp\left\{-\frac{\kappa^2}{\kappa_m^2}\right\} \tag{1.27}$$

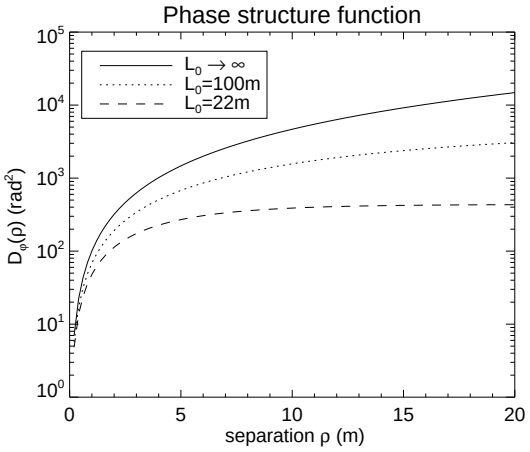

Figure 1.4: Structure function of the phase fluctuations for Kolmogorov turbulence ($L_0 \to \infty$) and for von Kármán turbulence ($L_0 = 100$ m and $L_0 = 22$ m). The Fried parameter is $r_0 = 20$ cm.

where $\kappa_m = 5.92/l_0$. This expression can be considered to be valid for all κ.[3] The Kolmogorov power spectrum becomes a particular case for which $L_0 \to \infty$ and $l_0 \to 0$. In astronomical imaging, the effect of the inner scale l_0 can be in general neglected. On the other hand, the outer scale L_0 has a major impact on most of the statistical descriptions of interest. For instance, the von Kármán structure function of the phase fluctuations $D_\varphi(\rho)$, and the von Kármán power spectrum of the phase fluctuations $\Phi_\varphi(\kappa)$ become [17]:

$$D_\varphi(\rho) = 0.172 \left(\frac{r_0}{L_0}\right)^{-5/3} \left[1 - \left(\frac{2\pi\rho}{L_0}\right)^{5/6} K_{5/6}\left(\frac{2\pi\rho}{L_0}\right)\right] \tag{1.28}$$

$$\Phi_\varphi(\kappa) = 0.023 r_0^{-5/3} \left[\kappa^2 + \left(\frac{1}{L_0}\right)^2\right]^{-11/6} \tag{1.29}$$

where $K_\nu(\cdot)$ denotes the modified Bessel function of the second kind [157]. For example, figure 1.4 shows both the Kolmogorov and the von Kármán phase structure function $D_\varphi(\rho)$ for different values of L_0, and for $r_0 = 20$ cm.

We will discuss the impact of L_0 on the FWHM of the long-exposure PSF in section 4.2.4.1, in the framework of MAD. An in-depth discussion of the effects of L_0 in astronomical imaging can be found in reference [17].

[3] Note that the Kolmogorov power spectrum (equation 1.8) diverges when $\kappa \to 0$.

1.1.5 Modal expansion of the phase perturbation

It is common practice in optical design and analysis to express phase functions $\varphi(\mathbf{r})$ in terms of their expansions in a given modal basis. We have chosen to use the *Zernike basis* for the study of atmospheric turbulence and adaptive optics systems throughout this work. We will briefly review below the properties of modal expansions in Zernike polynomials of the phase perturbations introduced by atmospheric turbulence. If $\varphi(\mathbf{r})$ denotes the turbulent phase, its modal expansion in Zernikes is expressed as:

$$\varphi(\mathbf{r}) \approx \sum_{i=1}^{n_{mod}} z_i Z_i(\mathbf{r}) \tag{1.30}$$

where $Z_i(\mathbf{r})$ is the ith Zernike polynomial and z_i is the corresponding Zernike coefficient. Equation 1.30 can only be an identity if $n_{mod} \to \infty$. The ith Zernike polynomial is expressed as [127, Ch.3]:

$$Z_i(\mathbf{r}) = \begin{cases} \sqrt{n+1}\, R_n^m(r)\sqrt{2}\cos(m\theta) & \text{if} \quad m \neq 0 \quad \text{and} \quad i \text{ is even.} \\ \sqrt{n+1}\, R_n^m(r)\sqrt{2}\sin(m\theta) & \text{if} \quad m \neq 0 \quad \text{and} \quad i \text{ is odd.} \\ \sqrt{n+1}\, R_n^0(r) & \text{if} \quad m = 0 \quad . \end{cases} \tag{1.31}$$

where n is the *radial order*, m is the *azimuthal frequency*, and (r, θ) are the polar coordinates of the position vector $\mathbf{r}$. The function $R_n^m(r)$ is defined by:

$$R_n^m(r) = \sum_{s=0}^{(n-m)/2} \frac{(-1)^s (n-s)!}{s![(n+m)/2-s]![(n-m)/2-s]!} r^{n-2s} \quad . \tag{1.32}$$

We will follow the convention of ordering Zernike polynomials in ascending order of n and m as introduced by Noll [99] and reviewed in [127, Ch.3]. It is important to recall that the maximum spatial frequency κ_{max} contained in a given Zernike is related to its radial order n by [15]:

$$\kappa_{max} \approx 0.37 \frac{n+1}{D} \tag{1.33}$$

where D is the diameter of the circle over which the Zernikes are defined.

Phase perturbations introduced by atmospheric turbulence can now be represented by the set of coefficients $\{z_i\}$. The statistical description of Zernike coefficients for the case of Kolmogorov turbulence was derived by Noll [99]. Since the (piston-removed) phase perturbations exhibit zero-mean Gaussian statistics, the Zernike coefficients $\{z_i\}$ will do so too, and their statistics can be fully described by the *covariance matrix* $\langle z_i z_j \rangle$

given by:

$$\begin{aligned}\langle z_i z_j\rangle &= 0.0072\left(\frac{D}{r_0}\right)^{5/3}(-1)^{\frac{n+n'-2m}{2}}\sqrt{(n+1)(n'+1)}\,\pi^{8/3}\delta_{mm'}\\ &\times\ \Gamma\left[\begin{array}{c}\frac{14}{3},\frac{n+n'-5/3}{2}\\ \frac{n-n'+17/3}{2},\frac{n'-n+17/3}{2},\frac{n+n'+23/3}{2}\end{array}\right]\end{aligned} \tag{1.34}$$

if $i-j$ is even, and $\langle z_i z_j\rangle = 0$ if $i-j$ is odd. In the equation above n and m are associated with z_i and n' and m' are associated with z_j. It is important to recall that $\langle z_1^2\rangle$ — which corresponds to the variance of the piston mode— is infinite as a consequence of the Kolmogorov model of turbulence. For the case of von Kármán turbulence, the covariance matrix of Zernike coefficients depends on L_0 and it is given by [17]:

$$\begin{aligned}\langle z_i z_j\rangle &= 1.16\left(\frac{D}{r_0}\right)^{5/3}(-1)^{\frac{n+n'-2m}{2}}\sqrt{(n+1)(n'+1)}\,\delta_{mm'}\\ &\times\ \sum_{k=0}^{\infty}\left\{\frac{(-1)^k}{k!}\left(\frac{\pi D}{L_0}\right)^{2k+n+n'-5/3}\right.\\ &\times\ \Gamma\left[\begin{array}{c}k+\frac{3+n+n'}{2},k+2+\frac{n+n'}{2},k+1+\frac{n+n'}{2},\frac{5}{6}-k-\frac{n+n'}{2}\\ 3+k+n+n',2+k+n,2+k+n'\end{array}\right]\\ &+\ \left.\left(\frac{\pi D}{L_0}\right)^{2k}\Gamma\left[\begin{array}{c}\frac{n+n'}{2}-\frac{5}{6}-k,k+\frac{7}{3},k+\frac{17}{6},k+\frac{11}{6}\\ \frac{n+n'}{2}+\frac{23}{6}+k,\frac{n-n'}{2}+\frac{17}{6}+k,\frac{n-n'}{2}+\frac{17}{6}+k\end{array}\right]\right\}\end{aligned} \tag{1.35}$$

In practice, the summation in equation 1.35 up to $k = 50$ gives already a good approximation. Figure 1.5 shows a plot of the variance $\langle z_i^2\rangle$ of the first 100 Zernikes for different values of L_0 and for $D/r_0 = 1$. Note that L_0 affects only the variance of the first radial orders.

1.1.6 Temporal characterization

So far we have reviewed the spatial characterization of atmospheric turbulence and their effects on astronomical imaging. We will briefly review in this section the temporal characterization of atmospheric turbulence. As we discussed in section 1.1.1, atmospheric random variables are considered to be *stationary by increments*. Hence, their statistics only depend on the time difference $\tau = t_2 - t_1$, where $t_2 > t_1$, if τ is not too large.

An important hypothesis that allows one to directly link the spatial and the temporal statistics of atmospheric random variables is the *Taylor's frozen flow hypothe-*

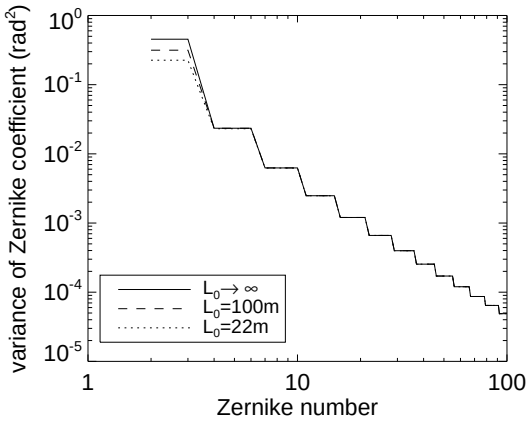

Figure 1.5: Variance of Zernike coefficients $\langle z_i^2 \rangle$ for Kolmogorov turbulence ($L_0 \to \infty$) and for von Kármán turbulence ($L_0 = 100$ m and $L_0 = 22$ m). Plots are shown for $D/r_0 = 1$.

sis [141]. This hypothesis basically states that over short time intervals the phase perturbations $\varphi(\mathbf{r}, h, t)$ introduced by a turbulent layer at height h do not change except for a translation with a constant transverse velocity $\vec{V}$ due to the wind [127]. Therefore, the phase fluctuations at time t_2 are related to the phase fluctuations at time t_1 by:

$$\varphi(\mathbf{r}, h, t_2) = \varphi(\mathbf{r} - \vec{V}\tau, h, t_1) \ . \tag{1.36}$$

Based on this hypothesis it can be shown that the Kolmogorov *spatio-temporal* structure function $D_\varphi(\rho, \tau)$ of the phase fluctuations in the telescope pupil after propagation through the atmospheric turbulence is given by [127]:

$$D_\varphi(\rho, \tau) = 6.88 \int_0^\infty \left(\frac{|\boldsymbol{\rho} + \vec{V}(h)\,\tau|}{r_0} \right)^{5/3} \frac{C_n^2(h)}{I_C}\, dh \tag{1.37}$$

where $I_C = \int_0^\infty C_n^2(h)\, dh$ and $\vec{V}(h)$ is the *wind velocity profile*. Similarly to the $C_n^2(h)$ profile, the $\vec{V}(h)$ profile above an astronomical observatory can also be characterized with the SCIDAR technique [72, 7]. For instance, it has been shown that the peak in wind velocity (about 30 m/s) is reached at an altitude between 9 and 12 km above sea level depending on the geographical site.

A general parameter to evaluate how fast the atmosphere is evolving is the *atmospheric coherence time* —also known as *Greenwood time delay* [40]— which is defined as the time difference τ_0 for which $D_\varphi(0, \tau_0) = 1\,\text{rad}^2$. For Kolmogorov turbulence, the

coherence time τ_0 results in:

$$\tau_0 = 0.314\frac{r_0}{\bar{V}} \tag{1.38}$$

where $\bar{V}$ is a weighted average of the wind speeds of all the turbulent layers computed as:

$$\bar{V} = \left[\frac{\int_0^\infty |\vec{V}(h)|^{5/3} C_n^2(h)\, dh}{\int_0^\infty C_n^2(h)\, dh}\right]^{3/5} . \tag{1.39}$$

1.1.6.1 Temporal power spectra of Zernike coefficients

Based on the Taylor's hypothesis, Conan *et. al.* [16] studied thoroughly the characteristics of the temporal power spectrum of the phase fluctuations. We will be mainly interested in the temporal power spectrum of phase perturbations expanded in Zernike polynomials. Conan *et. al.* [16] showed that the temporal power spectra of the Zernike coefficients $\{z_i\}$ representing the phase in the telescope pupil after propagation through the atmospheric turbulence (i.e. propagation through multiple turbulent layers each one of them with a particular wind velocity $\vec{V}$) have the following asymptotic behavior:

$$W_{z_i}(\nu) \propto \begin{cases} \nu^{-2/3} & \text{if} \quad \nu < \nu_c \quad \text{and} \quad i = \{2,3\} \\ \nu^{0} & \text{if} \quad \nu < \nu_c \quad \text{and} \quad i > 3 \\ \nu^{-17/3} & \text{if} \quad \nu > \nu_c \end{cases} \tag{1.40}$$

where $W_{z_i}(\nu)$ denotes the temporal power spectrum of Zernike coefficient z_i, and ν stands for the temporal frequency in Hertz. The *temporal cut-off frequency* ν_c is given by:

$$\nu_c(n) \approx 0.3(n+1)\frac{\bar{V}}{D} \tag{1.41}$$

where n is the radial order of the ith Zernike, and D is the telescope diameter. It is important to note that the transition around the temporal cut-off frequency ν_c can be broadened if the velocity profile $\vec{V}(h)$ exhibits a wide range of speed values.

1.1.7 Atmospheric turbulence simulation

In this section we will describe the way we have simulated the atmospheric turbulence in our simulation tool. Assuming that the atmospheric turbulence volume is represented by a set of thin turbulent layers, each layer is simulated with a corresponding *phase screen*. The phase screens are generated following the McGlamery method [96], also known as the *Fourier method*. This method consists in generating a two-dimensional array of complex, zero-mean, unit-variance Gaussian random numbers and then *coloring*

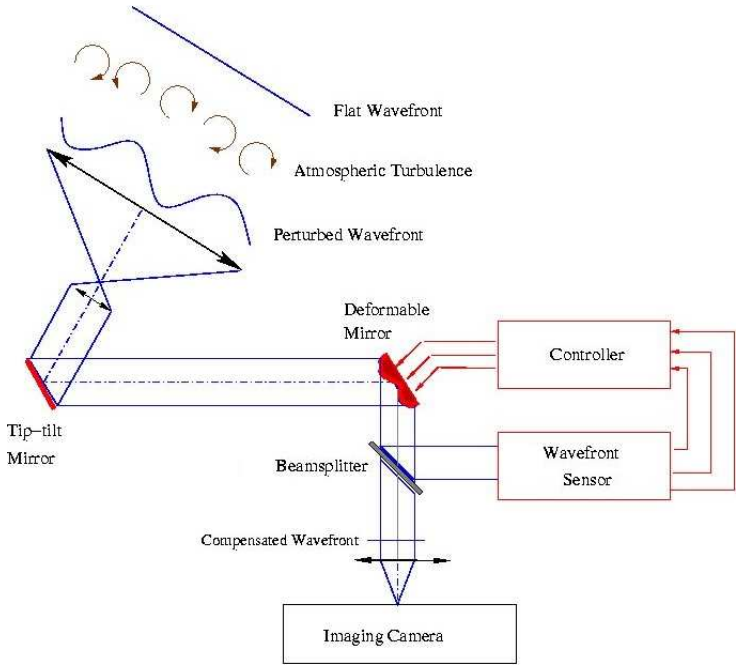

Figure 1.6: Schematic representation of an adaptive optics system (Courtesy: T. Fusco).

this array with the desired spectrum by multiplying it with the square root of the Kolmogorov or von Kármán power spectrum $\Phi_\varphi(\boldsymbol{\kappa})$ (equation 1.15 or 1.29). The two-dimensional, inverse Fourier transform of this array results in the desired phase screen. Finally, the phase screens have to be weighted by a specified $C_n^2(h)$ profile.

The temporal evolution of the turbulence is simulated based on the Taylor's frozen flow hypothesis (section 1.1.6) by displacing the phase screens according to a specified wind speed profile. We will present the characterization of the turbulence generated by our simulation tool in the framework of the MAD system, in chapter 4.

1.2 Adaptive optics systems

Adaptive optics (AO) is a technique that was conceived to compensate in *real time* for the phase perturbations introduced by atmospheric turbulence. Figure 1.6 shows an schematic representation of an AO system. The main components are:

1. one or several deformable mirror (DMs),
2. one or several wavefront sensors (WFSs), and
3. the controller.

Atmospheric turbulence compensation is achieved by adapting the shapes of the DMs in real-time to follow the wavefront perturbations. The control signals that drive the DMs are generated by the controller based on the measurement signals delivered by the WFSs. As seen in figure 1.6, the WFSs are located after the DMs in the optical path. Hence, they measure the wavefront perturbation residuals after correction by the DMs. The goal of the AO control loop is to make these residuals as small as possible. Finally, the compensated wavefront is delivered to the astronomical instrument (e.g. an imaging camera or a spectrograph) located in the focal plane of the telescope. Thanks to adaptive optics the image quality at the focal plane can be close to the diffraction limit in a particular FoV.

In the following sections we will introduce the mathematical models of the AO components that we will use throughout this work. Then, we will briefly describe some of the different configurations of adaptive optics systems that have been conceived for specific applications, namely *single-conjugate adaptive optics* (SCAO), *ground-layer adaptive optics* (GLAO), and *multi-conjugate adaptive optics* (MCAO). The latter configuration is the main topic of this work, but we have also worked with the other two configurations in the framework of the MAD project (chapter 4).

Let us note that other configurations have been recently proposed too, such as *eXtreme adaptive optics* (XAO) —designed to provide very high-order compensation in a tiny FoV, which is the kind of AO compensation required for extra-solar planet imagers [49, 89]; or *multi-object adaptive optics* (MOAO) —designed to provide AO compensation in several tiny patches in a large FoV, which is the kind of AO compensation required for multi-object integral-field spectrographs [54].

1.2.1 Deformable mirrors

The deformable mirrors (DMs) are the opto-mechanical devices that physically perform the wavefront compensation in an AO system. SCAO and GLAO systems have only one DM conjugated to the telescope pupil whereas MCAO systems have two or three DMs each one conjugated to a different altitude.

There are several technologies of deformable mirrors, but the correction principle is basically the same for all of them. That is, the phase shift introduced by the DM —denoted as $\varphi_{cor}(\mathbf{r})$— is produced by a continuous reflective facesheet that is deformed by a set of actuators placed at the back of it. A good review of DM technologies can be found in [126, Ch.4]. Some of the most popular technologies are:

- *Stack actuator mirrors (SAMs).* The reflective facesheet is deformed by a set of stacked piezoelectric[4] actuators driven by voltage signals. These actuators push and pull the facesheet producing localized deformations. SAMs with up to a hundred of actuators were widely used for the first astronomical SCAO systems deployed in medium size ($D \approx 4$ m) telescopes [122, 70]. Recent advances in manufacturing processes have led to the production of SAMs with thousands of actuators.

- *Bimorph deformable mirrors.* The actuators are formed by two continuous wafers of oppositely-polarized piezoelectric materials that are bonded together and placed at the back of the facesheet. A set of electrodes —defining the number of actuators— is deposited between the two wafers. When a voltage signal is applied to one of the electrodes a wafer contracts locally while the other expands inducing a bending of the facesheet. Bimorph deformable mirrors were originally conceived to be used in *curvature SCAO systems* [125].

- *Micro deformable mirrors.* This is a recent technology based on micro-opto-electro-mechanical systems (MOEMS). The reflective facesheet is deformed by an array of micro-machined electrostatic actuators. The number of actuators can range from tens to thousands [106, 161].

- *Voice coil deformable mirrors.* This technology has been developed in particular for the large secondary deformable mirrors currently being manufactured for the Large Binocular Telescope (LBT) and for the Very Large Telescope (VLT) [119, 4]. The deformable surface, more than a meter in diameter, is a concave thin mirror (≈ 1 mm thick) deformed by hundreds of magnetic voice coil actuators placed at the back.

Some of the most important parameters in the design of deformable mirrors are the number of actuators, the spacing between them, the maximum stroke, the drive voltage levels, and the shape of the influence functions.

1.2.1.1 DM linear model

The residual phase after correction by a DM can be mathematically expressed as:

$$\varphi_{res}(\mathbf{r}, h, t) = \varphi_{tur}(\mathbf{r}, h, t) - \varphi_{cor}(\mathbf{r}, h, t) \ . \tag{1.42}$$

[4]The most common material is PZT (Lead zirconate titanate).

where $\varphi_{cor}(\mathbf{r}, h, t)$ denotes the phase shift —or *correction phase*— at time t introduced by a DM conjugated at altitude h. Similarly, $\varphi_{tur}(\mathbf{r}, h, t)$ denotes the *turbulent phase* at the same instant, and for a turbulent layer located at the same altitude h.

Let us consider a deformable mirror with n_{act} actuators. The deformation produced by the DM when an unit control signal is applied to the ith actuator (and setting the control signals of all the other actuators to zero) is called the *influence function* of the ith actuator. We will denote it as $U_i(\mathbf{r})$. If the DM is considered to be a linear device, then the corrective phase can be expressed as a linear combination of the n_{act} influence functions. Denoting the control signal applied to the ith actuator as $u_i(t)$, we can express the corrective phase at time t by:

$$\varphi_{cor}(\mathbf{r}, t) = \sum_{i=1}^{n_{act}} u_i(t) U_i(\mathbf{r}) \ . \tag{1.43}$$

In practice, some non-linearities can take place like *hysteresis* [160, 27] or *saturation* due to the limited stroke of the actuators. The risk of saturation is higher under bad seeing conditions since the DM has to compensate for larger phase fluctuations. In order to reduce the stroke requirements on the actuators of a DM, it is common practice to use a tip-tilt mirror to compensate for low-order modes, as seen in the schema of figure 1.6. As shown in figure 1.5, most of the turbulent power ($\approx 87\%$) is concentrated in the tip and tilt modes (Z_2 and Z_3 Zernike modes). When a tip-tilt mirror is used, the DM is able to dedicate its full stroke to compensate for the high-order ones.

Equation 1.43 can also be expressed as a matrix-vector multiply. For this purpose let us consider that each influence function (IF) is measured and sampled in a grid of $n_{pix} \times n_{pix}$ points. Then, each IF can be expressed as a column-vector $\mathbf{U}_i(k)$ of dimension n_{pix}^2, where $k = \{1, \ldots, n_{pix}^2\}$. We will define the *Influence Function Matrix*, denoted by $\mathbf{N}$, as the matrix whose ith-column contain the vector $\mathbf{U}_i(k)$. In a similar way we can define a column-vector for the (pixelized) correction phase, denoted as $\boldsymbol{\varphi}_{cor}(k)$, and a column-vector, denoted as $\mathbf{u}$, containing the n_{act} control signals. Then, equation 1.43 can be simply written as:

$$\boldsymbol{\varphi}_{cor}(k, t) = \mathbf{N}\mathbf{u}(t) \ . \tag{1.44}$$

1.2.1.2 The mirror space

We will require in chapter 2 to formulate the problem of reconstruction in MCAO using the formalism of linear algebra. Within this formalism, the turbulent phase $\varphi_{tur}(\mathbf{r})$ can be seen as a *vector* of an infinite-dimensional space denoted as $\mathcal{E}$ and known as the

phase space. The Zernike polynomials introduced in section 1.1.5 form a basis of $\mathcal{E}$.

Any deformable mirror comprises a finite number of actuators, and therefore it has a limited number of degrees of freedom. It can only generate a subspace of $\mathcal{E}$, denoted as $\mathcal{M}$, and known as the *mirror space*. The mirror space is spanned by the set of influence functions $\{\mathbf{U}_1(k), \ldots, \mathbf{U}_{n_{act}}(k)\}$. If all influence functions are linearly independent then the dimension of $\mathcal{M}$ will be equal to the number of actuators: $\dim\{\mathcal{M}\} = n_{act}$. Also, the set of influence functions will become a *basis* of $\mathcal{M}$. Throughout this work we will rather work with the *coordinates* of $\mathcal{M}$. These coordinates depend on the chosen basis. For instance, when the basis of $\mathcal{M}$ is given by the set of influence functions, the coordinates are simply given by the corresponding set of control signals $\{u_1, \ldots, u_{n_{act}}\}$. In general, for any chosen basis, we will call *mirror modes* the basis functions, and *modal coordinates* the associated coordinates. The phase space $\mathcal{E}$ can now be expressed as the direct sum:

$$\mathcal{E} = \mathcal{M} \oplus \mathcal{M}^{\perp} \tag{1.45}$$

where $\mathcal{M}^{\perp}$ is the *orthogonal complement* of $\mathcal{M}$. Therefore, the turbulent phase $\boldsymbol{\varphi}_{tur}(k,t)$ can be expressed as the sum of two components:

$$\boldsymbol{\varphi}_{tur}(k,t) = \boldsymbol{\varphi}_{tur\parallel}(k,t) + \boldsymbol{\varphi}_{tur\perp}(k,t) \ , \tag{1.46}$$

where the first component belongs to $\mathcal{M}$ and the second one belongs to $\mathcal{M}^{\perp}$. The DM can only try to compensate for $\boldsymbol{\varphi}_{tur\parallel}(k,t)$. The complement component $\boldsymbol{\varphi}_{tur\perp}(k,t)$ will always remain uncompensated. It is also generally known as the *fitting error* of the DM. The residual phase after DM correction (equation 1.42) can then be expressed as:

$$\varphi_{res}(\mathbf{r},h,t) = \varphi_{tur\parallel}(\mathbf{r},h,t) - \varphi_{cor}(\mathbf{r},h,t) + \varphi_{tur\perp}(\mathbf{r},h,t) \ . \tag{1.47}$$

1.2.1.3 Fitting by a DM

As we mentioned above, the DM can only try to compensate for $\boldsymbol{\varphi}_{tur\parallel}(k,t)$. Let us suppose that we know the shape of the turbulent phase $\boldsymbol{\varphi}_{tur}(k,t)$. Then, the term $\boldsymbol{\varphi}_{tur\parallel}(k,t)$ can be computed as the *orthogonal projection* of the turbulent phase $\boldsymbol{\varphi}_{tur}(k,t)$ onto $\mathcal{M}$. Its modal coordinates $\mathbf{u}_{tur\parallel}(t)$ can be found by minimizing the function [52]:

$$J = \left\| \boldsymbol{\varphi}_{tur}(k,t) - \mathbf{N}\mathbf{u}_{tur\parallel}(t) \right\|^2 \ . \tag{1.48}$$

The solution to this minimization problem is simply given by the generalized inverse of the matrix $\mathbf{N}$. Hence, the modal coordinates of $\boldsymbol{\varphi}_{tur\|}(k,t)$ are computed as:

$$\mathbf{u}_{tur\|}(t) = \left(\mathbf{N}^T\mathbf{N}\right)^{-1}\mathbf{N}^T\boldsymbol{\varphi}_{tur}(k,t) \ , \tag{1.49}$$

and $\boldsymbol{\varphi}_{tur\|}(k,t)$ is simply computed from its modal components as follows:

$$\boldsymbol{\varphi}_{tur\|}(k,t) = \mathbf{N}\mathbf{u}_{tur\|}(t) \ . \tag{1.50}$$

Of course, before attempting to fit a given phase $\boldsymbol{\varphi}_{tur}(k,t)$ with a DM, we need to know first what this phase looks like. This is the problem of *wavefront reconstruction* that we will study in chapter 2 for the case of MCAO.

1.2.2 Wavefront sensors

Wavefront sensors (WFSs) are the devices that are used to measure the wavefront distortions caused by the atmospheric turbulence [128]. Most wavefront sensors do not measure the wavefront directly. Instead, they measure either the wavefront slope (first derivative) or the curvature (second derivative). Some of the WFSs currently used in astronomical adaptive optics are:

- *Shack-Hartmann WFS.* This is probably the most popular slope WFS used in astronomical adaptive optics. We will actually work with this kind of sensors in the framework of MAD (chapter 4), so we will describe it further in section 1.2.2.1.

- *Curvature WFS.* This WFS was invented by F. Roddier [125], and it is normally used with bimorph deformable mirrors in *curvature SCAO systems.*

- *Pyramid WFS.* This WFS was introduced by R. Ragazzoni [115]. The concept of the pyramid WFS is based on the Foucault's *knife-edge test.* A transmissive pyramid located in the focal plane is used to split a beam of light falling on its vertex. A modulation is usually applied to the beam in order to distribute the light among the four facets of the pyramid. It can be shown that —in the geometrical approximation— the sensor's signal is proportional to the wavefront gradient [154].

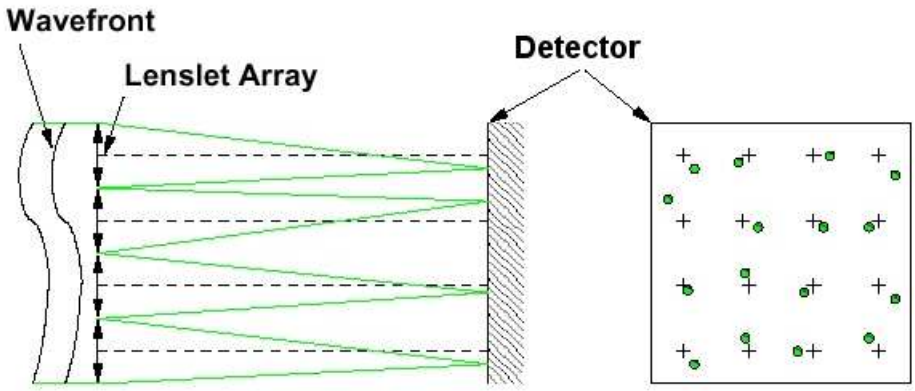

Figure 1.7: Schematic representation of a Shack-Hartmann wavefront sensor (Courtesy: T. Fusco).

1.2.2.1 Shack-Hartmann wavefront sensor

Figure 1.7 shows a diagram of a Shack-Hartmann wavefront sensor (SH-WFS). The *lenslet array* is optically conjugated to the pupil plane of the telescope. It spatially samples the distorted wavefront in the pupil plane by means of a grid of *nxn* tiny lenses, called *subapertures*. Each subaperture forms an image of a small part of the pupil onto a detector located in the focal plane of the lenslet array. When the wavefront in the pupil $\varphi(\mathbf{r})$ is plane, the subapertures images –also known as *spots*– are formed at the reference positions (x_0, y_0) marked with crosses in figure 1.7. On the other hand, when $\varphi(\mathbf{r})$ is distorted by the atmospheric turbulence, the spots are displaced from the reference positions and it can be shown that the centroid (x_c, y_c) of a displaced spot is proportional to the gradient of $\varphi(\mathbf{r})$ averaged on the subaperture area [128]:

$$\begin{aligned} x_c &= f_{wfs} s_x = \frac{f_{wfs}\lambda}{2\pi A} \int\int_A \frac{\partial\varphi(\mathbf{r})}{\partial x} dx\, dy + w_x \\ y_c &= f_{wfs} s_y = \frac{f_{wfs}\lambda}{2\pi A} \int\int_A \frac{\partial\varphi(\mathbf{r})}{\partial y} dy\, dx + w_y \end{aligned} \tag{1.51}$$

where s_x and s_y are the averaged gradients –or slopes– in x and y (in radians), f_{wfs} is the focal length of the lenslet array, λ is the central wavelength of the detector, A is the area of the subaperture, and w_x and w_y denote the additive measurement noise components. The quantities $\frac{\partial\varphi(\mathbf{r})}{\partial x}$ and $\frac{\partial\varphi(\mathbf{r})}{\partial y}$ in equation 1.51 are also known as the *angles of arrival*, α_x and α_y.

In practice, when a Charge-Coupled Device (CCD) is used as the detector, the centroid (x_c, y_c) can be computed as [128]:

$$x_c = \frac{\sum_{i,j} x_{i,j} I_{i,j}}{\sum_{i,j} I_{i,j}} \quad y_c = \frac{\sum_{i,j} y_{i,j} I_{i,j}}{\sum_{i,j} I_{i,j}} \tag{1.52}$$

where $(x_{i,j}, y_{i,j})$ are the coordinates of the pixel (i, j), and $I_{i,j}$ is the signal (i.e. integrated flux) of pixel (i, j). In matrix form, the linear model of the SH-WFS can be expressed as:

$$\mathbf{s}(t) = \mathbf{D}\varphi(\mathbf{r}, t) + \mathbf{w}(t) \tag{1.53}$$

where the vector $\mathbf{s}$ contains the slopes $[s_x; s_y]$ for all subapertures, the vector $\mathbf{w}$ contains the associated measurement noise $[w_x; w_y]$, and the matrix $\mathbf{D}$ stands for the linear operation of equation 1.51.

Measurement noise

The main contributions to the measurement noise $\mathbf{w}$ are the *photon noise* and the *detector noise*. The variance of $\mathbf{w}$ can be expressed as:

$$\sigma_w^2 = \sigma_{ph}^2 + \sigma_{det}^2 \tag{1.54}$$

where σ_{ph}^2 is the photon noise variance and σ_{det}^2 is the detector noise variance. We will consider that the detector is a Charge-Coupled Device (CCD). It can be shown that the variance of the noise contributions (given in terms of the phase difference at the borders of the subaperture in rad^2) are given by [128]:

$$\sigma_{ph}^2 = \frac{\pi^2}{2} \frac{1}{n_{ph}} \left(\frac{X_T}{X_D} \right)^2 \tag{1.55}$$

$$\sigma_{det}^2 = \frac{\pi^2}{3} \frac{\sigma_{e^-}^2}{n_{ph}^2} \left(\frac{X_S^2}{X_D} \right)^2 \tag{1.56}$$

where n_{ph} is the number of photons per subaperture and per frame, X_T is the size of the SH spot, X_D is the size of the diffraction-limited SH spot, X_S is the size of the window used to calculate the centroids of the SH spot, and σ_{e^-} is the rms number of electrons-noise per pixel and per frame.

Aliasing

The larger the number of subapertures in a SH-WFS the better the wavefront is spatially sampled. According to the Shannon theorem, the maximum spatial frequency that the SH-WFS can measure is $|\boldsymbol{\kappa}|_{max} = 1/2d$, where d is the size of the subaperture. Spatial frequencies larger than $|\boldsymbol{\kappa}|_{max}$ will be *aliased* onto the lower frequencies.

1.2.3 Wavefront sensing simulation

In this section we will briefly describe the way we have simulated the wavefront sensing devices. Our simulation tool supports two kinds of wavefront sensors: 1) Shack-Hartmann WFSs, and 2) *Idealized* WFSs. We will describe the computer models of these WFSs below.

1.2.3.1 Shack-Hartmann WFS

The SH-WFS models were developed at ONERA by C. Petit [107] and M. Nicolle [97]. There are two different ways to simulate a SH-WFS, based on either a *geometrical* or a *diffractive* model:

- *Geometrical SH-WFS model.* This model is a generalization of the model originally proposed by Fried [38], in which the slopes s_x and s_y are computed from the phase differences at the border of the subaperture. If we model the input phase as an nxn pixelized phase map $\varphi_{x,y}$, where $x = \{1 \dots n\}$ and $y = \{1 \dots n\}$, then the slopes can be computed as:

$$s_x = \frac{1}{2d} \sum_{y=1}^{n} (\varphi_{n,y} - \varphi_{1,y}) + w_x \tag{1.57}$$

$$s_y = \frac{1}{2d} \sum_{x=1}^{n} (\varphi_{x,n} - \varphi_{x,1}) + w_y \tag{1.58}$$

  where d is the size of the subaperture. The measurement noise components w_x w_y are simulated with zero-mean Gaussian random variables with variance σ_w^2 (equation 1.54).

- *Diffractive SH-WFS model.* This numerical model reproduces the physical process of the formation of subaperture images in the focal plane of the lenslet array, according to equation 1.17. Following equation 1.52, the centroid of each subaperture image provides an estimate of the slopes. Both photon and detector

noise can be added directly onto the pixelized subaperture images prior to the centroid computation.

We have customized the SH-WFS models for the accurate simulation of the star-oriented configuration of the MAD system, as will be described in chapter 4.

1.2.3.2 Idealized WFS

The so-called idealized[5] WFS is a WFS capable of projecting directly the input phase onto the Zernike basis. The output of this module is a set of Zernike coefficients. This kind of WFS has been widely used in previous works to study the problem of reconstruction and control in AO systems [55, 47].

Even if this WFS is not a realistic one, it is possible to introduce a *realistic* measurement noise that matches the characteristics of the propagated measurement noise on Zernike coefficients reconstructed from SH-WFS slopes. In this case, the propagated measurement noise variance on the ith Zernike is computed as:

$$\sigma^2_{Z_i} = p_{m,n}\sigma^2_w \tag{1.59}$$

where $p_{m,n}$ is the propagation coefficient associated with the ith Zernike, and it depends on both the radial order n and the azimuthal frequency m of the ith Zernike. Rigaut & Gendron [121] derived best-fit expressions for these coefficients:

$$\begin{array}{rcll} p_{m,n} & = & 0.295\,(n+1)^{-2.05} & \text{if} \quad n = m \\ p_{m,n} & = & 0.174\,(n+1)^{-2} & \text{if} \quad n \neq m\ . \end{array} \tag{1.60}$$

The measurement noise variance σ^2_w in equation 1.59 can also be computed to emulate the realistic signal-to-noise ratio (SNR) of a SH-WFS. The SNR on each subaperture of a SH-WFS is defined as the ratio between the angle of arrival variance ($\sigma^2_{\alpha_x}$) and the measurement noise variance (σ^2_w):

$$\text{SNR} \triangleq \frac{\sigma^2_{\alpha_x}}{\sigma^2_w}\ . \tag{1.61}$$

It can be shown that the angle of arrival variance $\sigma^2_{\alpha_x}$ due to Kolmogorov turbulence is given by [126]:

$$\sigma^2_{\alpha_x} = \sigma^2_{\alpha_y} = 0.162\,(2\pi)^2\,d^{-5/3}r_0^{-5/3} \quad [\text{rad}^2] \tag{1.62}$$

[5] It was called *idealized* simply to state that this WFS is not a realistic one.

where r_0 is the Fried parameter, and d is the size of a squared subaperture. Substituting equation 1.62 into 1.61 leads to the following expression for the *equivalent* measurement noise variance σ_w^2:

$$\sigma_w^2 = \frac{0.162\,(2\pi)^2}{\mathrm{SNR}} \left(\frac{d}{r_0}\right)^{5/3} \quad . \tag{1.63}$$

We will widely use idealized WFSs in chapters 2 and 3 in our studies of reconstruction and control for MCAO systems.

1.2.4 Calibration of an AO system

In the previous sections we described the characteristics of wavefront sensors and deformable mirrors in an independent way. Once these components are integrated in the AO bench, the response of the AO system as a whole entity needs to be calibrated. The (static) response of an AO system is completely characterized by its *interaction matrix*. Another important calibration issue is related to the non-common path aberrations. We will review these issues below.

1.2.4.1 Interaction matrix

If there is a total of n_{mes} WFSs measurements and a total of n_{act} DMs actuators, the interaction matrix is an n_{mes} x n_{act} matrix whose ith column is the set of WFSs measurements produced when an unit control signal is applied to the ith actuator. Algebraically, the interaction matrix characterizes the mapping between the DMs space and the WFSs space. Assuming linearity, the mapping can be expressed in matrix form as:

$$\mathbf{s} = \mathbf{M}_{int}\mathbf{u} \tag{1.64}$$

where $\mathbf{M}_{int}$ denotes the interaction matrix. In general, the interaction matrix is determined experimentally, but in principle it could also be determined *synthetically* by using the mathematical or numerical models of the AO system components. We will discuss further the differences between experimental and synthetic interaction matrices in section 4.6, in the framework of the MAD system.

1.2.4.2 Non-common path aberrations

The *non-common path aberrations* (NCPA) are the (low-order and static) aberrations introduced by the optical components located between the beamsplitter and the imaging camera (figure 1.6). These aberrations will have an impact on the final image quality

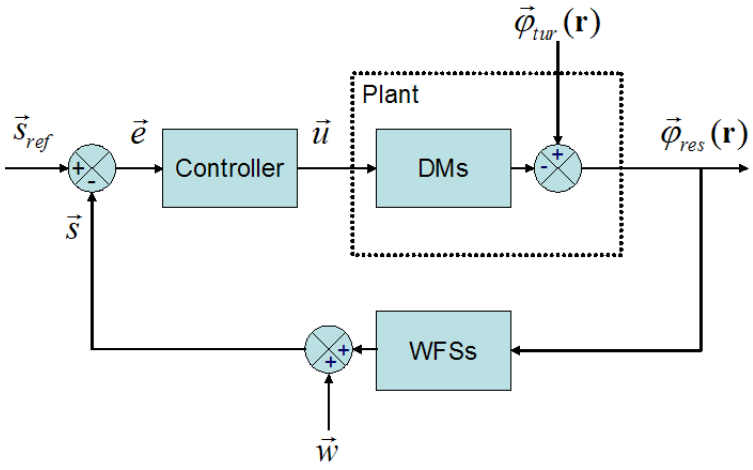

Figure 1.8: Block diagram of a closed-loop AO control system.

produced at the focal plane of the scientific camera. Even if the NCPA cannot be sensed by the WFSs, it is anyway possible to use the AO system itself to compensate for these aberrations, as briefly described below.

The first step is to calibrate the non-common path aberrations. This can be done, for instance, by using the *phase diversity* technique [59]. Once the NCPA are calibrated, the compensation is achieved by introducing *offset voltages* to the DMs to cancel out the effect of the NCPA on the scientific camera. These offset voltages can be translated into *reference slopes* using equation 1.64. As we will discuss in section 1.2.5, the AO control loop can then be closed around the reference slopes, causing the AO system to cancel out the effect of the NCPA at each iteration.

The compensation of NCPA aberrations has been succesfully implemented in several SCAO systems, for instance in the Nasmyth Adaptive Optics System (NAOS) of the VLT [14, 65]. The extension of this technique to MCAO systems has been recently studied [75]. In principle, the several DMs available in an MCAO system can be used to compensate for the NCPA existing in a finite field-of-view.

1.2.5 The controller

Figure 1.8 shows the block diagram of a closed-loop AO control system. The goal of the control system is to make the output of the *plant* —in this case the residual wavefront $\varphi_{res}(\mathbf{r})$— behave in a desired way by manipulating the plant input —in this case the command vector $\mathbf{u}$. For AO systems, the goal is to keep the residual wavefront as flat as

possible in a given FoV. Then, the controller needs to manipulate $\mathbf{u}$ to counteract the effects of the *disturbance* to the plant, i.e. the turbulent phase $\varphi_{tur}(\mathbf{r})$. The feedback signal is provided by the WFSs, and the *error signal* is then given by:

$$\mathbf{e} = \mathbf{s}_{ref} - \mathbf{s} \tag{1.65}$$

where $\mathbf{s}_{ref}$ is the *reference slope vector* (section 1.2.4.2). It is important to note that an AO system is actually a multi-variable spatio-temporal control system. However, the spatial and temporal aspects of control are in general considered separately. In this case, the action of the controller can be expressed in two steps. The first step is related to the spatial reconstruction of the wavefront to be compensated for —expressed in any DM basis (section 1.2.1.2)— computed from the WFS measurements. Considering a linear system, the first step can be expressed as:

$$\mathbf{u} = \mathbf{R}\mathbf{e} \tag{1.66}$$

where $\mathbf{R}$ is known as the *reconstruction matrix*. The simplest reconstruction matrix is the *generalized inverse* of the interaction matrix $\mathbf{M}_{int}$ (eq. 1.64), but other in principle more performing reconstruction matrices incorporating statistical knowledge on the atmospheric turbulence and on the measurement noise have also been studied. We will study in chapter 2 the problem of wavefront reconstruction in MCAO.

The second step is related to the temporal aspects of control, and it can be described as the *temporal filtering* applied to the command vector $\mathbf{u}$ in order to provide a good disturbance rejection and to ensure the stability of the AO system. The simplest temporal controller is an *integrator*, but other more sophisticated controllers have been proposed too. For example, the modal integrator (where the gain of the integrator controller is optimized for each spatial mode [55, 31]), predictive controllers (where the delay introduced by an AO system is compensated for by predicting the evolution of the turbulence [23, 25]), or optimal controllers based on the Kalman filtering technique [103, 132]. In chapter 3, we will study the application of modal integrators for MCAO.

1.2.6 Performance evaluation

There are different metrics to quantify the improvement brought by adaptive optics correction in a particular direction $\boldsymbol{\alpha}$ of the FoV. The most common are the *wavefront error*, the *Strehl ratio*, and the *ensquared energy*:

- The wavefront error (WFE) is defined as the rms value of the residual wavefront $\varphi_{res}(\mathbf{r}, \boldsymbol{\alpha})$ obtained after AO correction in the direction $\boldsymbol{\alpha}$. It can be expressed as:

$$\mathrm{WFE}(\boldsymbol{\alpha}) = \sqrt{\left\langle \frac{1}{S} \iint_S \left[\varphi_{res}(\mathbf{r}, \boldsymbol{\alpha})\right]^2 d\mathbf{r} \right\rangle} \tag{1.67}$$

  where S stands for the telescope pupil area, and $\langle \cdot \rangle$ denotes an ensemble average. The goal of an AO system is to minimize the WFE in a selected FoV $\{\boldsymbol{\alpha}\}$.

- The Strehl ratio (SR) is a performance parameter that characterizes directly a long-exposure AO-corrected image. The Strehl ratio in the direction $\boldsymbol{\alpha}$ is defined as:

$$S_R(\boldsymbol{\alpha}) = \frac{\mathrm{PSF}_{\boldsymbol{\alpha}}(\vec{0})}{\mathrm{PSF}_{Airy}(\vec{0})} \tag{1.68}$$

  where $\mathrm{PSF}_{\boldsymbol{\alpha}}(\vec{0})$ denotes the intensity value at the center of the AO-corrected PSF in the direction $\boldsymbol{\alpha}$ —the vector $\vec{0}$ denotes the center of the PSF—, and $\mathrm{PSF}_{Airy}(\vec{0})$ denotes the intensity value at the center of the diffraction-limited PSF of the telescope. Recalling that the PSF and the long-exposure OTF are Fourier-transform pairs, the Strehl ratio can also be expressed as:

$$S_R(\boldsymbol{\alpha}) = \frac{\int \mathrm{OTF}_{\boldsymbol{\alpha}}(\mathbf{f})\, d\mathbf{f}}{\int T(\mathbf{f})\, d\mathbf{f}} \tag{1.69}$$

  where $\mathrm{OTF}_{\boldsymbol{\alpha}}(\mathbf{f})$ denotes the long-exposure OTF in the direction $\boldsymbol{\alpha}$, $T(\mathbf{f})$ is the transfer function of the (diffraction-limited) telescope, and $\mathbf{f}$ is the spatial frequency vector. The Strehl ratio values lie within 0 and 1 (perfect correction), and they are usually expressed in percent. The goal of an AO system is then to maximize the SR in a selected FoV $\{\boldsymbol{\alpha}\}$. When $S_R > 20\%$, the SR and the WFE can be related by the Maréchal approximation [126]:

$$S_R(\boldsymbol{\alpha}) \simeq \exp\left\{ - \left[\mathrm{WFE}(\boldsymbol{\alpha})\right]^2 \right\} \quad . \tag{1.70}$$

  Note from this expression that minimizing the WFE is equivalent to maximizing the SR in direction $\boldsymbol{\alpha}$.

- The ensquared[6] energy (EE) is defined as the integral of the long-exposure PSF within a square of a given size centered on the PSF (figure 1.9). This metric

[6] The word *ensquared* does not exist in the English language but it has been widely used in this context by the AO community.

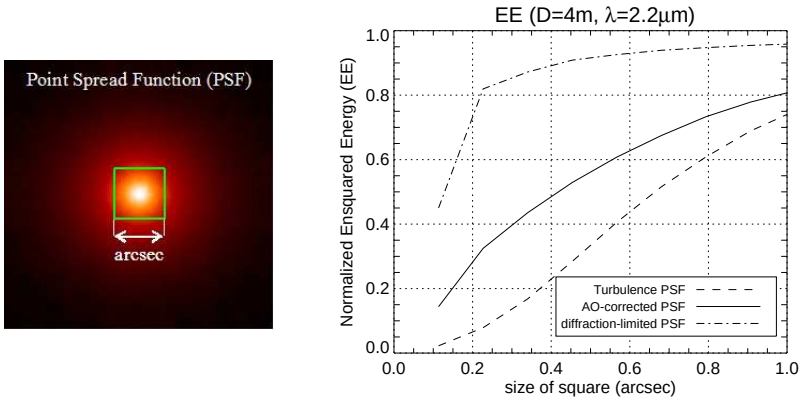

Figure 1.9: (*Left*) Illustration of the ensquared energy (EE) concept. The EE is the integral of the PSF over a square centered on the PSF. (*Right*) EE at 2.2 μm versus the size of the square (in arcsec) for a telescope of $D = 4$ m obtained with numerical simulations. Turbulence strength: $s = 0.73$".

has been adopted to quantify the energy concentrating capabilities of a given AO system. Figure 1.9(right) shows examples of EE curves at 2.2 μm as a function of the size of the square. The EE curve of the AO-corrected PSF lies between the EE curves of the turbulence and the diffraction-limited PSFs. For a given square size x, the performance of an AO system is usually quoted in terms of the *gain in EE*, which is defined as:

$$\mathrm{GEE}_x(\boldsymbol{\alpha}) = \frac{\mathrm{EE}_x(\boldsymbol{\alpha})}{\mathrm{EE}_x^{tur}} \tag{1.71}$$

where EE_x^{tur} denotes the EE in a square of size x of the turbulence PSF and similarly, $\mathrm{EE}_x(\boldsymbol{\alpha})$ denotes the EE in a square of size x of the AO-corrected PSF in direction $\boldsymbol{\alpha}$.

1.2.7 Single-conjugate adaptive optics (SCAO)

Single-conjugate adaptive optics (SCAO) systems consist of a single deformable mirror —in general conjugated to the telescope pupil— and a single wavefront sensor, as depicted in figure 1.10. Although the concept of (single-conjugate) adaptive optics was first proposed in 1953 by H. W. Babcock [9], the first astronomical SCAO prototype system —the COME-ON project [129]— saw its first light in 1989. This prototype system consisted of a 5x5 subapertures SH-WFS and a 19-actuator SAM DM. Since

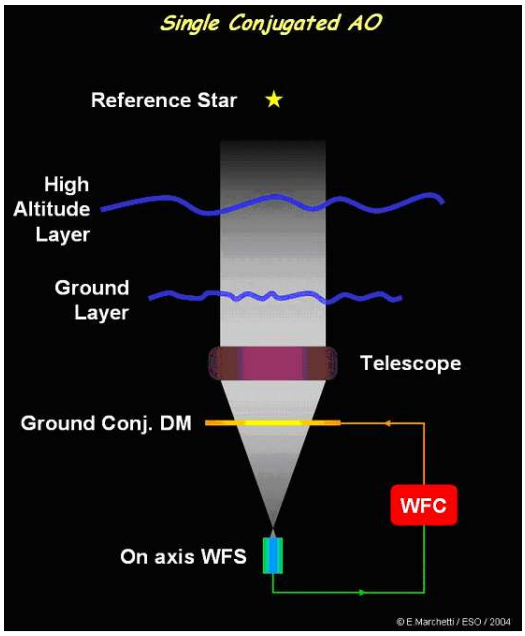

Figure 1.10: Single-conjugate adaptive optics (SCAO) configuration. (Courtesy: E. Marchetti).

then, many 4-m, 8-m, and 10-m class astronomical telescopes have been equipped with SCAO systems, some of them based on a SH-WFS and a SAM DM [13, 130, 151], and others based on a curvature WFS and a bimorph DM [61, 5, 138]. As we will review in the following sections, SCAO correction can provide near-diffraction-limited resolution, but some important limitations do exist, the main one being the *anisoplanatism*.

1.2.7.1 SCAO-corrected PSF and OTF

The optical resolution attained with SCAO correction in the direction of the guide star (GS) is close to the diffraction-limit of the telescope. As an example, figure 1.11 shows the SCAO-corrected PSF obtained from numerical simulations of the MAD system operating in SCAO mode (chapter 4). Note that the SCAO-corrected long-exposure PSF is characterized by a diffraction-limited peak (FWHM $\approx \lambda/D$) that is surrounded by a halo whose size is less than λ/r_0; the actual size depending on the degree of the SCAO correction. The wavefront residuals that contribute to the wavefront error (WFE) are due to the high spatial frequencies not compensated by the DM —known as the *fitting error*—, and the imperfect correction of the low spatial frequencies due to wavefront sensing errors, temporal errors, etc.

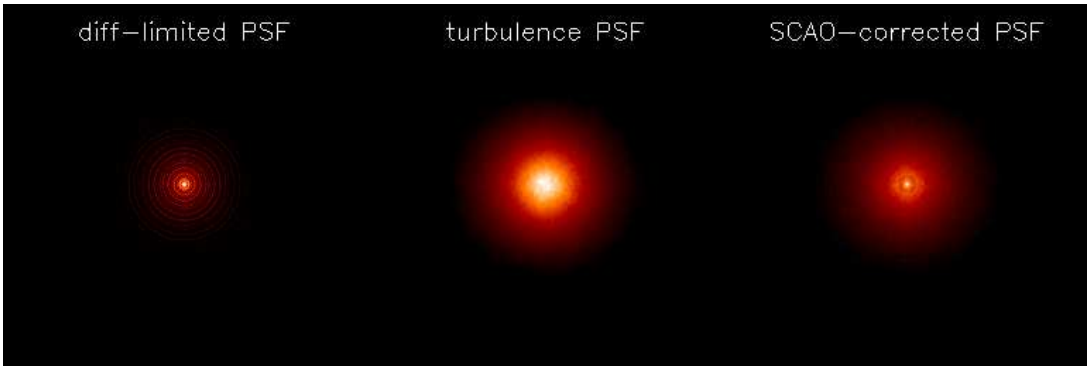

Figure 1.11: Comparison of the diffraction-limited PSF, the long-exposure turbulence PSF ($r_0 = 70$ cm @ $2.2\,\mu$m), and the long-exposure SCAO-corrected PSF at $\lambda = 2.2\,\mu$m for an 8-m telescope. The SCAO system simulated is the MAD system operating in SCAO mode.

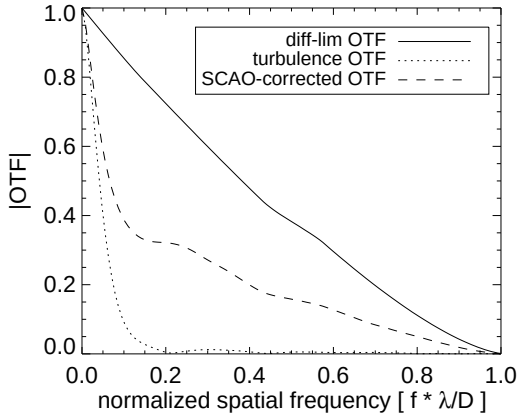

Figure 1.12: Comparison of the diffraction-limited OTF, long-exposure turbulence OTF ($r_0 = 70$ cm @ $2.2\,\mu$m), and SCAO-corrected OTF at $\lambda = 2.2\,\mu$m for an 8-m telescope. $f = |\mathbf{f}|$ is the modulus of the spatial frequency vector (rad^{-1}). The SCAO system simulated is the MAD system operating in SCAO mode.

On the other hand, the SCAO-corrected long-exposure OTF can be approximated by a similar expression to equation 1.26 [15, 152]:

$$\mathrm{OTF}(\mathbf{f}) = \exp\left[-\frac{1}{2}D_{\varphi_{res}}(\lambda\mathbf{f})\right]\ \mathrm{OTF}_{tel}(\mathbf{f})\ , \tag{1.72}$$

where in this case $D_{\varphi_{res}}$ is a structure function characterizing φ_{res}, the residual phase after SCAO correction (equation 1.47). Figure 1.12 shows the long-exposure OTFs associated with the PSFs shown in figure 1.11. Note that at low spatial frequencies the SCAO-corrected OTF is characterized by a less steep drop-off with respect to the turbulence OTF. Also, note that higher spatial frequencies are present up to the diffraction limit D/λ, but they are attenuated with respect to the diffraction-limited OTF. The level of the attenuation of the higher spatial frequencies in the SCAO-corrected OTF is related to the degree of the SCAO correction. It can be shown that the SCAO-corrected OTF at high frequencies saturates to [126]:

$$\mathrm{OTF}(\mathbf{f}_{high}) \approx \exp\left\{-\left[\mathrm{WFE}\right]^2\right\}\ \mathrm{OTF}_{tel}(\mathbf{f}_{high})\ . \tag{1.73}$$

where WFE is the wavefront error (eq. 1.67).

1.2.7.2 Anisoplanatism

The main limitation of SCAO systems is the anisoplanatism. As illustrated in figure 1.13, in most astronomical applications the GS and the astronomical object of interest are not the same. Hence, the wavefront coming from the GS and the wavefront coming from the object of interest will traverse the atmosphere through different paths separated by an angle θ. Because the atmospheric turbulence is distributed in the volume above the telescope, the wavefront perturbations will be different for the two paths. This phenomenon is known as *anisoplanatism*.

The isoplanatic angle θ_0 is defined as the angular separation from the GS for which the mean-square wavefront error between the two paths is equal to 1 rad^2 [64]. The isoplanatic angle θ_0 is given by [39]:

$$\theta_0 = \left[2.91\left(\frac{2\pi}{\lambda}\right)^2\left[\sec(\alpha)\right]^{8/3}\int C_n^2(h)h^{5/3}dh\right]^{-3/5} \tag{1.74}$$

$$= 0.314\cos(\alpha)\frac{r_0}{\bar{h}} \tag{1.75}$$

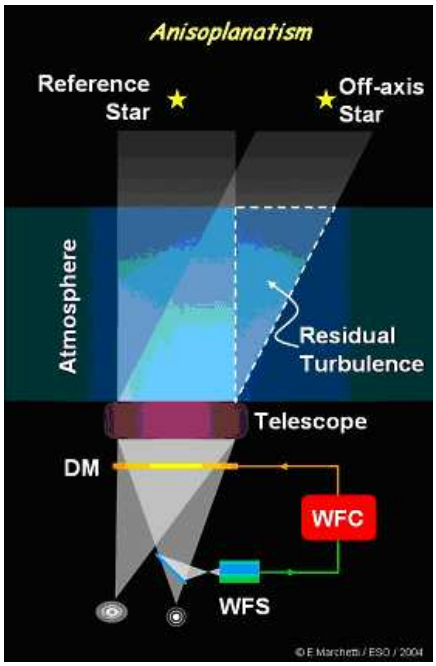

Figure 1.13: Illustration of the anisoplanatism effect in adaptive optics. (Courtesy: E. Marchetti).

where $\bar{h}$ is the *mean turbulence altitude*, defined as [64]:

$$\bar{h} = \left(\frac{\int C_n^2(h) h^{5/3} dh}{\int C_n^2(h)\, dh} \right)^{3/5} . \tag{1.76}$$

The atmospheric turbulence compensation delivered by a SCAO system is only efficient within a FoV equal to $\approx 2\theta_0$ around the GS. This FoV is known as the *isoplanatic patch*. Similarly to the Fried parameter r_0 (eq. 1.16), the isoplanatic angle θ_0 is also wavelength dependent ($\propto \lambda^{6/5}$). The isoplanatic patch varies from a few arcsec in the visible, to a few tens of arcsec in the near infrared.

1.2.7.3 Limiting magnitude, sky coverage and laser guide stars

In order to be able to measure the wavefront perturbations introduced by atmospheric turbulence with the required accuracy ($\ll \lambda$), the signal-to-noise ratio (SNR) on the WFS measurements should be kept as high as possible. This implies that bright stars[7]

[7]The brightness of stars are expressed in terms of *magnitudes*; a logarithmic scale in which an increase of one magnitude corresponds to a decrease in brightness by a factor of $100^{1/5}$.

should be used for wavefront sensing. The magnitude of the faintest GS that could be used for a given SCAO system is known as the *limiting magnitude*. The limiting magnitude is determined by the level of performance sought, and it depends on different system parameters, e.g. the throughput of the optics, the noise introduced by the WFS detector, etc. For example, for the NAOS SCAO system, the limiting magnitude is $M_V \approx 17$ [130].

The probability of finding a NGS brighter than a given limiting magnitude and within a given field of view (FoV) is known as the *sky coverage*. Clearly, those areas in the sky where no suitable GSs are found cannot be observed with adaptive optics. The sky coverage offered by SCAO systems is quite limited because a suitable GS must be found within the isoplanatic patch around the object of interest.

In order to overcome this limitation, the concept of *laser guide star* (LGS) was proposed by Foy & Labeyrie [34]. It consists in creating an artificial star by projecting a laser beam on the sky. Two LGS technologies have been demonstrated: Rayleigh and sodium LGSs [105]. LGSs can boost the sky coverage because a LGS can be conveniently positioned within the isoplanatic patch of the object of interest. Furthermore, in principle the right brightness can be obtained by controlling the power of the laser.

There are nevertheless several limitations associated with LGSs. First, since the LGS spot is produced at a finite altitude (≈ 15 km for Rayleigh LGSs and ≈ 90 km for sodium LGSs), the LGS wavefront propagates down to the telescope pupil in a conical fashion. As a result, the atmospheric turbulence volume probed by the LGS wavefront is not exactly the same as the one traversed by the wavefront coming from the object of interest. This effect is known as the *cone effect* or *focal anisoplanatism* [34]. Another important limitation of LGSs is the *tilt indetermination* [121]. Indeed, since the LGS beam propagates upwards and downwards through the same atmospheric path, the spot appears to be fixed as seen from the launching telescope. This means that wavefront tilt cannot be estimated from the LGS and, in consequence, a natural GS has to be used to sense tip/tilt.

In this work we will only study the case of AO systems based on natural guide stars. Therefore, we will not discuss further the particularities associated with LGSs.

1.2.8 Multi-conjugate adaptive optics (MCAO)

As discussed in section 1.2.7.2, SCAO correction is only efficient in a very tiny FoV —known as the isoplanatic patch— due to the fact that the atmospheric turbulence is distributed in altitude. The concept of multi-conjugate adaptive optics (MCAO) [26, 11] was proposed to overcome this limitation and provide high-resolution correction in a

larger FoV (1′ to 2′ FoV). In order to achieve this, several deformable mirrors conjugated at different altitudes are required to compensate for the phase perturbations introduced by different turbulent layers. MCAO compensation allows to increase the effective isoplanatic patch, and therefore, the corrected FoV. Tokovinin *et. al.* [146] derived a generalization of the isoplanatic angle θ_0 (eq. 1.74) for the case of MCAO, denoted as θ_M, and given by:

$$\theta_M = \left[2.91 \left(\frac{2\pi}{\lambda} \right)^2 [\sec(\alpha)]^{8/3} \int C_n^2(h) F_M(h) dh \right]^{-3/5} . \tag{1.77}$$

where $F_M(h)$ is a function of the number of the DMs and their conjugation altitudes. M. Le Louarn *et. al.* [87] showed that with only 2 to 3 DMs conjugated to the dominant turbulent layers —which can be identified from the $C_n^2(h)$ profile characterization of a given observatory (section 1.1.2.1)— are enough to increase the effective isoplanatic angle θ_M to ≈1' in the visible, and ≈2' in the near-infrared. Furthermore, simulations studies [42, 123] have also shown that the loss in performance due to the misconjugation of the DMs with respect to the dominant turbulent layers is not dramatic (only a few percent in average Strehl ratio). The important conclusion from all these studies is that it is sufficient to design MCAO systems with 2 or 3 DMs in order to obtain near-diffraction-limited correction in a large (1' to 2') FoV for the current 8m/10m-class telescopes.

MCAO systems also require to have several WFSs coupled to GSs in different directions $\{\boldsymbol{\alpha}\}$ within the FoV of interest in order to probe a larger portion of the turbulent volume. Two wavefront sensing strategies have been proposed so far for MCAO, known as *star-oriented* and *layer-oriented* (figure 1.14).

1.2.8.1 Star-oriented wavefront sensing

The star-oriented approach was originally proposed by M. Tallon & R. Foy [139] as a generalization to MCAO of the wavefront sensing strategy followed in SCAO (figure 1.10). Recall that in SCAO there is a single WFS coupled to a GS located in direction $\boldsymbol{\alpha}$ that measures the resultant phase perturbation in the telescope pupil integrated along the line of sight in direction $\boldsymbol{\alpha}$. In star-oriented MCAO, a larger portion of the turbulent volume can be probed by means of several WFSs each one of them coupled to a different GS in the FoV so that each WFS measures the resultant phase in the telescope pupil integrated along a different line of sight. The star-oriented approach can be implemented with any WFSs, e.g. Shack-Hartmann WFSs or pyramid WFSs.

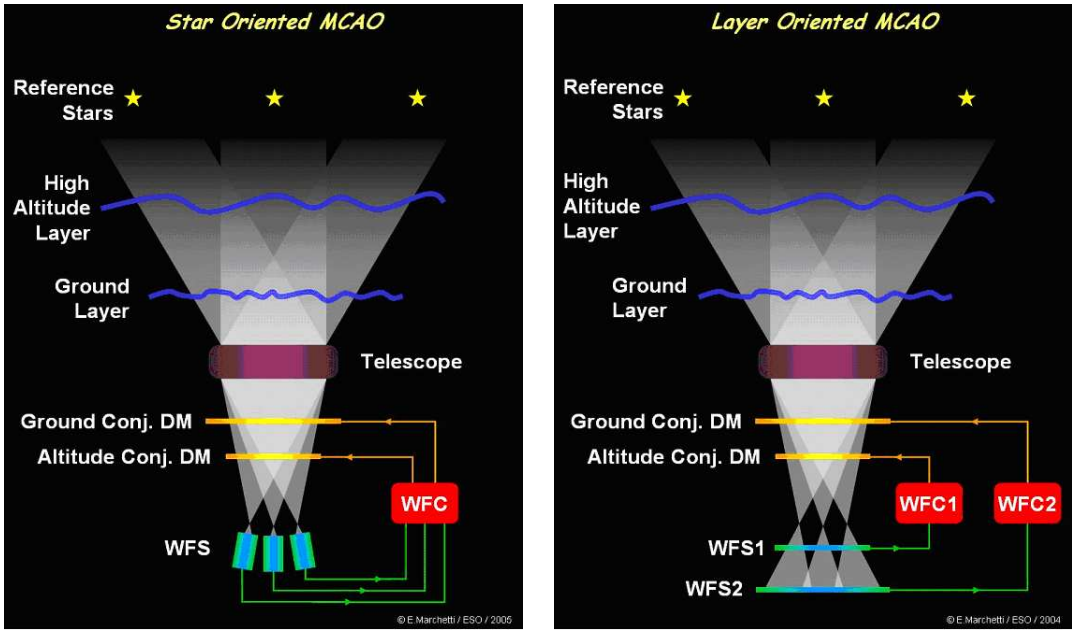

Figure 1.14: Schematic representation of MCAO system configurations. (*Left*) MCAO based on the star-oriented wavefront sensing strategy. (*Right*) MCAO based on the layer-oriented wavefront sensing strategy. (Courtesy: E. Marchetti).

As shown in figure 1.14(left), the WFSs measurements are then delivered to the wavefront controller (WFC) which, in turn, computes the commands that drive the deformable mirrors (DMs).

1.2.8.2 Layer-oriented wavefront sensing

The layer-oriented approach was proposed by R. Ragazzoni *et. al.* [116]. It is referred to as *layer-oriented* because the goal is to try to measure directly the phase perturbations introduced by some particular turbulent layers as opposed to the star-oriented approach, in which the phase perturbation that is measured is the one introduced by the *whole* turbulent volume integrated along different lines of sight.

In the layer-oriented approach there is a WFS detector conjugated to each of the turbulent layers of interest. For instance, in figure 1.14(right) there are two WFS detectors —labelled as WFS1 and WFS2— which are conjugated to the high-altitude turbulent layer and the ground turbulent layer, respectively. The deformable mirrors are also conjugated to the same altitudes as the WFS detectors. In principle, it is possible to establish a control loop for each WFS/DM pair conjugated to the same

altitude, as shown in figure 1.14(right).

Note that the light of the different GSs needs to be combined on the WFS detectors in order to image the turbulent layers of interest. Originally, R. Ragazzoni *et. al.* [116] proposed to use multi-pyramid WFSs to perform the optical co-addition of the light, but in principle it is also possible to combine star-oriented WFS measurements numerically in a computer to render the same kind of information [12]. The optical co-addition has the advantage of increasing the signal-to-noise ratio (SNR) of the WFSs measurements, which is an important aspect in particular when working with noisy WFSs detectors [12]. On the other hand, if there is a large difference in magnitude between the GSs, the optical co-addition of the light will intrinsically give more weight to the information coming from the brightest GSs, leading to a partial loss of information coming from the fainter GSs. T. Fusco *et. al.* [48] have studied different approaches to optimize both star-oriented and layer-oriented wavefront sensing strategies in order to cope with differences in GS magnitudes, WFS measurement noise, etc.

1.2.8.3 Current projects in MCAO

In the last few years, several laboratories in the world have been involved in the experimental validation of the MCAO concept. Both the increase in the effective isoplanatic angle using several DMs, and the possibility of estimating the turbulence volume using several WFSs have been recently validated experimentally using MCAO test-beds [73, 58, 93]. The feasibility of estimating the turbulence volume has also been validated on the sky [118]. As part of my PhD training, I had the opportunity to participate in the experimental characterization and testing of the multi-conjugate adaptive optics demonstrator (MAD) [93]. Chapter 4 is dedicated to the experiments carried out with MAD during my internship at the European Southern Observatory (ESO).

Probably the most ambitious MCAO project are the ones being currently developed for the Gemini-South 8-m telescope [30], and the Large Binocular Telescope (LBT) [51]. The Gemini MCAO system comprises 5 SH-WFSs coupled to sodium LGSs, plus 3 additional SH-WFSs each one coupled to a NGS required to recover tip-tilt information. Wavefront correction will be done with 3 DMs conjugated to 0, 4.5, and 9.0 km height. The LBT MCAO system is a layer-oriented MCAO system using a multi-pyramid WFS. Wavefront correction will be done with 2 DMs, one of them being a large secondary deformable mirror. These MCAO systems will provide a near-diffraction-limited correction in a large (1' to 2') FoV.

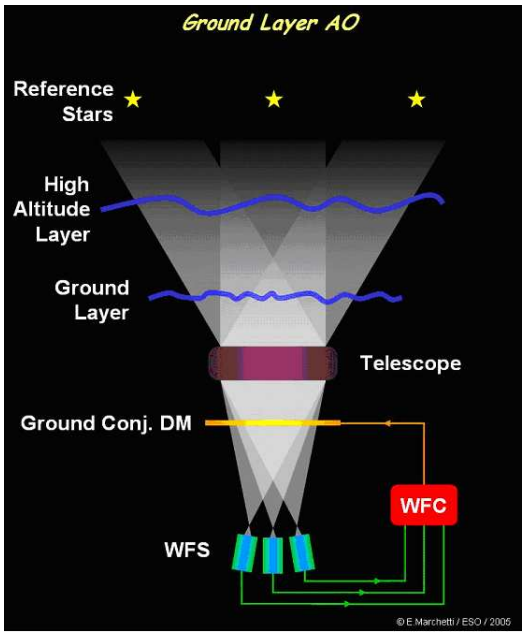

Figure 1.15: Ground layer adaptive optics (GLAO) configuration. (Courtesy: E. Marchetti).

1.2.9 Ground-layer adaptive optics (GLAO)

As discussed in section 1.1.2.1, about 60% of the turbulence strength is concentrated in the first few kilometers above the telescope. This fact inspired the concept of ground-layer adaptive optics (GLAO) [120]. The goal of a GLAO system is to compensate for the ground turbulent layer by using a single DM conjugated to a low altitude. From the system point of view, a GLAO system can be seen as a simplified MCAO system. If only the ground turbulent layer is compensated for, a quite uniform correction in a wide FoV can be achieved [120]. It is important to emphasize that, as opposed to the case of MCAO, the goal of GLAO is not to attain a near-diffraction-limited correction but to simply reduce and stabilize the seeing over a wide FoV [66].

Similarly to the MCAO case, in order to measure the wavefront perturbation introduced by the ground turbulent layer, it is required to have several wavefront sensors coupled to different GSs distributed in the FoV, as illustrated in figure 1.15. Note that all WFSs will measure the contribution of the ground turbulent layer, but also each WFS (coupled to a GS in direction $\boldsymbol{\alpha}$) will measure the contributions of the higher turbulent layers in the corresponding direction $\boldsymbol{\alpha}$. In principle, the contributions of the higher-altitude layers can be averaged out by simply averaging the wavefronts measured

by all WFSs, as long as the number of WFSs is large [98]. A. Tokovinin [144] has shown that the uniformity of the correction in the whole FoV can be maximized if all the GSs are located in the periphery of the FoV. Clearly, this condition can be easily satisfied when using LGSs.

The gain in ensquared energy (GEE) (section 1.2.6) has become the standard metric to evaluate the performance of GLAO systems. At ESO, there are currently a couple of GLAO systems under development for the 8-m Very Large Telescope (VLT) [66]. These GLAO systems are based on a large secondary deformable mirror for wavefront correction, and 4 SH-WFSs coupled to sodium LGSs positioned in the periphery of the FoV for wavefront sensing. Simulation results predict that these GLAO systems will provide a uniform gain of $\text{GEE}_x \approx 2$ at both visible ($x = 0.2''$, corrected FoV$\approx 4'$) and near-infrared ($x = 0.1''$, corrected FoV$\approx 10'$) wavelengths [85, 86].

Chapter 2

Wavefront reconstruction in MCAO

2.1 Introduction

In this chapter we will study the problem of wavefront reconstruction —or phase estimation— in star-oriented MCAO (section 1.2.8.1). The main contribution of this chapter is the characterization of the *propagation of the remaining error* —also known as *generalized aliasing*— in MCAO systems.

We will follow the traditional approach to study the problem of wavefront reconstruction by considering an *open-loop* and *static* MCAO configuration. That is, we will consider that the wavefront sensors (WFSs) measure directly the phase perturbations introduced by the atmospheric turbulence, and no temporal considerations will be taken into account.

The problem of wavefront reconstruction in MCAO can be rigorously described within the formalism of *inverse problems* [62]. Within this formalism, it is first required to formulate what is known as the *direct problem*, which is basically a physical model of the variable of interest and of the process we are using to measure it. Then, the inverse problem consists in finding a method to estimate the variable of interest from the available measurements.

Figure 2.1 shows a representation of the wavefront reconstruction problem in MCAO, showing both the direct problem and the inverse problem associated with it. The direct problem involves the modelling of the phase perturbations introduced by the turbulence volume $\varphi_{tur}(\mathbf{r})$ and also the modelling of how the WFSs are able to measure them. On the other hand, the inverse problem involves the estimation of the phase perturbations

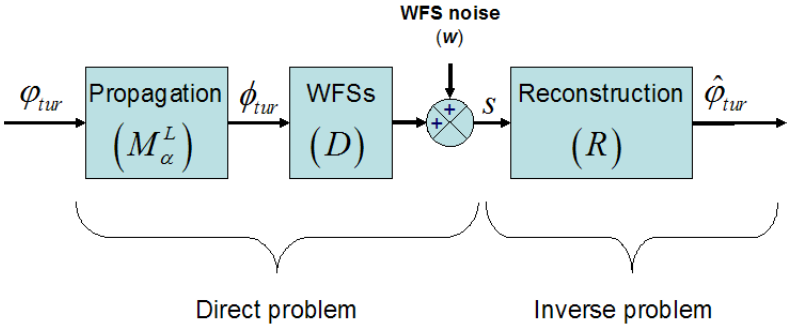

Figure 2.1: Illustration of the direct problem and the inverse problem of wavefront reconstruction in MCAO.

introduced by the turbulence volume from the WFSs measurements.

2.2 The Direct Problem

Figure 2.2 shows a schematic representation of the turbulence volume and a star-oriented MCAO system. We will consider an MCAO system with N_{GS} wavefront sensors each one coupled to a different guide star in the direction denoted by $\boldsymbol{\alpha}_k$ ($k = \{1 \dots N_{GS}\}$).

In star-oriented MCAO, each WFS measures the resultant phase in the telescope pupil. In the near-field approximation, from equation 1.13, the resultant phase perturbation in the telescope pupil for the WFS looking in the direction $\boldsymbol{\alpha}_k$ —denoted as $\phi_{tur}(\mathbf{r}, \boldsymbol{\alpha}_k)$— can be related to the phase perturbations introduced by the turbulence volume φ_{tur} by:

$$\phi_{tur}(\mathbf{r}, \boldsymbol{\alpha}_k) = \int_0^\infty \varphi_{tur}(\mathbf{r} + h\boldsymbol{\alpha}_k)\, dh \ , \tag{2.1}$$

where $\mathbf{r}$ denotes the position vector in the telescope pupil. Furthermore, as discussed in section 1.1.2.1, the continuous turbulence volume can be approximated by a set of thin turbulence layers. As shown in figure 2.2, we will consider that the atmospheric volume is composed of N_L thin turbulent layers ($j = \{1 \dots N_L\}$). Therefore, we can rewrite equation 2.1 as:

$$\phi_{tur}(\mathbf{r}, \boldsymbol{\alpha}_k) \approx \sum_{j=1}^{N_L} \varphi_{tur}^{L_j}(\mathbf{r} + h_j\boldsymbol{\alpha}_k) \tag{2.2}$$

where $\varphi_{tur}^{L_j}$ is the phase perturbation associated with the thin turbulent layer L_j located

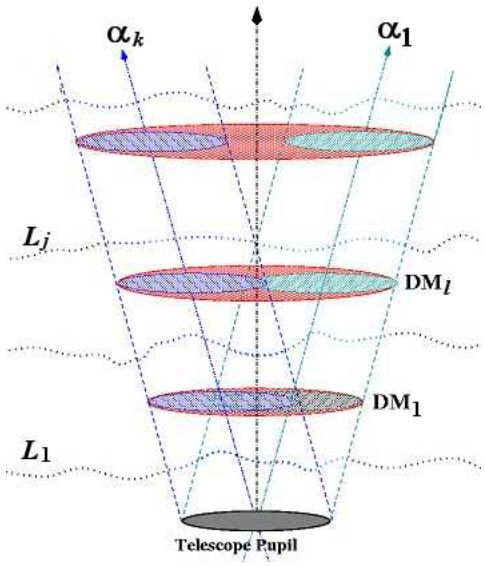

Figure 2.2: Representation of the turbulence volume comprising N_L thin turbulent layers, and a star-oriented MCAO system comprising N_{GS} wavefront sensors each one of them coupled to a different guide star in the direction denoted by $\boldsymbol{\alpha}_k$, and N_{DM} deformable mirrors.

at altitude h_j. Equation 2.2 represents the basic building block in the modelling of the direct problem in MCAO. We will rather continue the formulation of the direct problem using matrix notation, as presented in section 2.2.1.

2.2.1 Matrix formulation

T. Fusco [42] developed a matrix formulation for the problem of wavefront reconstruction in MCAO. In this section we will review this formulation and later we will extend it in order to be able to characterize the generalized aliasing in MCAO.

In this formulation, all phase functions are represented by their associated vectors of Zernike coefficients (section 1.1.5). The telescope pupil diameter is denoted by D and the maximal field-of-view (FoV) angle is denoted by $\alpha_{max} = \|\boldsymbol{\alpha}_{max}\|$.

We will denote as $\boldsymbol{\varphi}_{tur}^{L_j}$ the vector containing the Zernike coefficients of the phase perturbation associated with the turbulent layer L_j located at altitude h_j. The Zernike basis for the L_j layer is defined on the *metapupil* of diameter D_j (figure 2.3):

$$D_j = D + 2h_j\alpha_{max} \ . \tag{2.3}$$

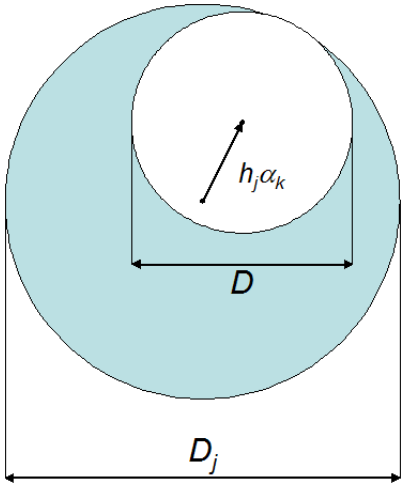

Figure 2.3: Illustration of the metapupil associated with layer L_j at height h_j. The WFS looking at direction $\boldsymbol{\alpha}_k$ sees the footprint of diameter D centered on $h_j\boldsymbol{\alpha}_k$.

Note that $\boldsymbol{\varphi}_{tur}^{L_j}$ is an infinite-dimensional vector. We will denote as $\mathcal{E}_j$ the infinite-dimensional *phase space* defined in the metapupil D_j. We can now define a column vector $\boldsymbol{\varphi}_{tur}$ concatenanting the vectors of Zernike coefficients of *all* the N_L turbulent layers, namely[1]:

$$\boldsymbol{\varphi}_{tur} = \begin{pmatrix} \boldsymbol{\varphi}_{tur}^{L_1} \\ \vdots \\ \boldsymbol{\varphi}_{tur}^{L_j} \\ \vdots \\ \boldsymbol{\varphi}_{tur}^{L_{N_L}} \end{pmatrix} . \tag{2.4}$$

We can also define a *turbulence volume phase space* —denoted as $\mathcal{E}_V$— formed by the N_L infinite-dimensional phase spaces $\{\mathcal{E}_j\}$ each one of them defined in its corresponding metapupil D_j. Note that the vector $\boldsymbol{\varphi}_{tur}$ represents the associated coordinates vector of $\mathcal{E}_V$.

In star-oriented MCAO, each WFS measures the resultant turbulent phase in the telescope pupil in the direction $\boldsymbol{\alpha}_k$. For any turbulent layer in altitude ($h_j \neq 0$) the WFS will only see a portion of size D —known as the *footprint*— as shown in figure 2.3. According to equation 2.2, the resultant turbulent phase in the telescope pupil in the direction $\boldsymbol{\alpha}_k$ is the sum of N_L footprints. In matrix form, equation 2.2 can be

[1]To ease the writing within a paragraph the same column vector will be expressed as $\boldsymbol{\varphi}_{tur} = [\boldsymbol{\varphi}_{tur}^{L_1}; \cdots; \boldsymbol{\varphi}_{tur}^{L_j}; \cdots; \boldsymbol{\varphi}_{tur}^{L_{N_L}}]$.

written as:

$$\boldsymbol{\phi}_{tur}^{\boldsymbol{\alpha}_k} = \mathbf{M}_{\boldsymbol{\alpha}_k}^{L} \boldsymbol{\varphi}_{tur} \tag{2.5}$$

where the vector $\boldsymbol{\phi}_{tur}^{\boldsymbol{\alpha}_k}$ contains the Zernike coefficients of the resultant turbulent phase in the telescope pupil in the direction $\boldsymbol{\alpha}_k$. The matrix $\mathbf{M}_{\boldsymbol{\alpha}_k}^{L}$ represents the sum of the footprints in direction $\boldsymbol{\alpha}_k$. It can be constructed as a meta-matrix containing N_{L} matrices:

$$\mathbf{M}_{\boldsymbol{\alpha}_k}^{L} = \left[\mathbf{M}_{\boldsymbol{\alpha}_k}^{L_1} \cdots \mathbf{M}_{\boldsymbol{\alpha}_k}^{L_j} \cdots \mathbf{M}_{\boldsymbol{\alpha}_k}^{L_{N_L}} \right] \tag{2.6}$$

in which the matrix $\mathbf{M}_{\boldsymbol{\alpha}_k}^{L_j}$ relates the Zernike polynomials defined in the telescope pupil D with the ones defined on the metapupil D_j. The qth-column of $\mathbf{M}_{\boldsymbol{\alpha}_k}^{L_j}$ is associated with the qth Zernike (Z_q) polynomial defined in D_j, and it contains the modal expansion of $Z_q(\mathbf{r} + h_j\boldsymbol{\alpha}_k)$ —i.e. the portion of Z_q delimited by the footprint centered on $h_j\boldsymbol{\alpha}_k$ (figure 2.3)— onto the Zernikes $\{Z_p(\mathbf{r})\}_{2\leq p\leq\infty}$ defined on the telescope pupil D. Note that in principle there is an infinite number ($2 \leq p \leq \infty$) of Zernike coefficients to compute. However, R. Ragazzoni *et. al.* [117] showed that for the qth Zernike defined in D_j, only the coefficients of the Zernikes $\{Z_p(\mathbf{r})\}_{2\leq p\leq q}$ are actually non-zero. This fact will be useful in the formulation of the *approximate direct problem* described in section 2.2.2.

We can now also define a meta-matrix, $\mathbf{M}_{\boldsymbol{\alpha}}^{L}$, that computes the resultant phases in the pupil plane for *all* the N_{GS} directions. This meta-matrix can be constructed as:

$$\mathbf{M}_{\boldsymbol{\alpha}}^{L} = \left[\left(\mathbf{M}_{\boldsymbol{\alpha}_1}^{L}\right)^T \cdots \left(\mathbf{M}_{\boldsymbol{\alpha}_k}^{L}\right)^T \cdots \left(\mathbf{M}_{\boldsymbol{\alpha}_{N_{GS}}}^{L}\right)^T \right]^T \quad . \tag{2.7}$$

The resultant turbulent phase in the telescope pupil for *all* directions can be written as the column vector:

$$\boldsymbol{\phi}_{tur} = \begin{pmatrix} \boldsymbol{\phi}_{tur}^{\boldsymbol{\alpha}_1} \\ \vdots \\ \boldsymbol{\phi}_{tur}^{\boldsymbol{\alpha}_k} \\ \vdots \\ \boldsymbol{\phi}_{tur}^{\boldsymbol{\alpha}_{N_{GS}}} \end{pmatrix} \quad , \tag{2.8}$$

and the linear relationship between the vectors $\boldsymbol{\phi}_{tur}$ and $\boldsymbol{\varphi}_{tur}$ can be stated simply as:

$$\boldsymbol{\phi}_{tur} = \mathbf{M}_{\boldsymbol{\alpha}}^{L} \boldsymbol{\varphi}_{tur} \quad . \tag{2.9}$$

Let us now proceed with the matrix notation for the WFSs response. The measurement

vector produced by the kth WFS is given by (eq. 1.53):

$$\mathbf{s}_k = \mathbf{D}_k \boldsymbol{\phi}_{tur}^{\alpha_k} + \mathbf{w}_k \tag{2.10}$$

where $\mathbf{D}_k$ is the kth-WFS matrix and $\mathbf{w}_k$ is the measurement noise vector. In this context the columns of the matrix $\mathbf{D}_k$ describe the response of the WFS to Zernike polynomials. Note that in principle this matrix has an infinite number of columns, but a finite number of rows equal to the number of WFS measurements. We will define a *block-diagonal* meta-matrix $\mathbf{D}$ containing the N_{GS} WFS matrices. Then, defining also the column vectors $\mathbf{s} = [\mathbf{s}_1; \cdots; \mathbf{s}_k; \cdots; \mathbf{s}_{N_{GS}}]$ and $\mathbf{w} = [\mathbf{w}_1; \cdots; \mathbf{w}_k; \cdots; \mathbf{w}_{N_{GS}}]$, the linear model that takes into account all the N_{GS} WFSs is simply written as:

$$\begin{aligned} \mathbf{s} &= \mathbf{D}\boldsymbol{\phi}_{tur} + \mathbf{w} \\ &= \mathbf{D}\mathbf{M}_{\alpha}^{L}\boldsymbol{\varphi}_{tur} + \mathbf{w} \ . \end{aligned} \tag{2.11}$$

Equation 2.11 summarizes the *direct problem* in MCAO. It states the linear relationship that exists between the available information —i.e. the wavefront sensor measurements $\mathbf{s}$— and the variable of interest —i.e. the turbulence volume represented by $\boldsymbol{\varphi}_{tur}$. The search for the inverse relationship leads to the corresponding inverse problem of *wavefront reconstruction* or *phase estimation* in MCAO. That is, the problem of estimating the vector $\boldsymbol{\varphi}_{tur}$ from the WFSs measurements. However, in practice it is not possible to handle infinite-dimensional vectors and matrices. Therefore, we will have to limit the modal representation of the turbulence volume to a finite number of Zernike modes per layer, leading to the formulation of an *approximate direct problem*. Since most of the turbulence energy is concentrated on the low spatial frequencies (figure 1.5) a reasonable choice is to keep the low order Zernikes in the modelling of the approximate direct problem. We will describe in section 2.2.2 the formulation of the approximate direct problem in MCAO.

2.2.2 Approximate direct problem

We will start the formulation of the approximate direct problem by splitting the infinite-dimensional vector $\boldsymbol{\varphi}_{tur}$ —defined in equation 2.4— in two components, denoted as

$\boldsymbol{\varphi}_{tur_\parallel}$ and $\boldsymbol{\varphi}_{tur_\perp}$:

$$\boldsymbol{\varphi}_{tur_\parallel} = \begin{pmatrix} \boldsymbol{\varphi}_{tur_\parallel}^{L_1} \\ \vdots \\ \boldsymbol{\varphi}_{tur_\parallel}^{L_j} \\ \vdots \\ \boldsymbol{\varphi}_{tur_\parallel}^{L_{N_L}} \end{pmatrix} \quad , \quad \boldsymbol{\varphi}_{tur_\perp} = \begin{pmatrix} \boldsymbol{\varphi}_{tur_\perp}^{L_1} \\ \vdots \\ \boldsymbol{\varphi}_{tur_\perp}^{L_j} \\ \vdots \\ \boldsymbol{\varphi}_{tur_\perp}^{L_{N_L}} \end{pmatrix} \quad . \tag{2.12}$$

For each turbulent layer L_j, the vector $\boldsymbol{\varphi}_{tur_\parallel}^{L_j}$ will contain a finite number of Zernike coefficients, namely the first $n_{mod}^{L_j}$ Zernike modes (excluding piston Z_1), and the vector $\boldsymbol{\varphi}_{tur_\perp}^{L_j}$ will contain the rest of the Zernike coefficients not considered in $\boldsymbol{\varphi}_{tur_\parallel}^{L_j}$, namely the Zernikes from $n_{mod}^{L_j}+1$ to ∞. The finite number of Zernike coefficients contained in $\boldsymbol{\varphi}_{tur_\parallel}$ are the ones that we will seek to estimate when solving the inverse problem.

Within the formalism of linear algebra, we can define two *phase spaces* $\mathcal{M}_V$ and $\mathcal{M}_V^\perp$ as the subspaces of $\mathcal{E}_V$ spanned by the Zernike polynomials whose coefficients are $\{\boldsymbol{\varphi}_{tur_\parallel}\}$ and $\{\boldsymbol{\varphi}_{tur_\perp}\}$ respectively. By construction, $\mathcal{M}_V^\perp$ is the *orthogonal complement* of $\mathcal{M}_V$, so that $\mathcal{E}_V = \mathcal{M}_V \oplus \mathcal{M}_V^\perp$. Note that this formalism is similar to the one introduced in section 1.2.1.2 for the case of a deformable mirror.

- *How many Zernike modes shall we take into account for each layer L_j?* Let us consider that for each layer L_j we seek to estimate the first $n_{mod}^{L_j}$ Zernikes (excluding piston Z_1) up to radial order n^{L_j}. Then, the maximum Zernike number taken into account for layer L_j is:

$$n_{mod}^{L_j} = \frac{\left(n^{L_j}+1\right)\left(n^{L_j}+2\right)}{2} \quad . \tag{2.13}$$

  Recall from equation 1.33 that limiting the estimation to a number of Zernikes up to a maximum radial order is equivalent to limiting the estimation up to a maximum spatial frequency. We will in general choose the values of n^{L_j} so that the maximum spatial frequency estimated in *all* layers is the same. Then, from equation 1.33, and for an arbitrarily chosen n^{L_1}, the values of n^{L_j} for the other layers will be set to:

$$n^{L_j} \approx \frac{D_j}{D_1}\left(n^{L_1}+1\right) - 1 \quad , \tag{2.14}$$

  where D_1 and D_j are the sizes of the metapupils of the first and the jth layer.

We will now require to split accordingly the matrix $\mathbf{M}_\alpha^L$. Let us start with matrix

$\mathbf{M}_{\alpha_k}^{L_j}$ (see equation 2.6). Recall that this matrix relates the Zernike coefficients of the resultant phase in the telescope pupil in direction α_k with the Zernike coefficients associated with layer L_j. This matrix can be simply partitioned as:

$$\mathbf{M}_{\alpha_k}^{L_j} = \left[\mathbf{M}_{\alpha_k\parallel}^{L_j}\mathbf{M}_{\alpha_k\perp}^{L_j}\right] \tag{2.15}$$

where $\mathbf{M}_{\alpha_k\parallel}^{L_j}$ contains only $n_{mod}^{L_j} - 1$ columns associated with the first $n_{mod}^{L_j}$ Zernikes (excluding piston Z_1) of layer L_j, and $\mathbf{M}_{\alpha_k\perp}^{L_j}$ contains an infinite number of columns associated with Zernikes $n_{mod}^{L_j} + 1$ to ∞.

Similarly to equation 2.6, we can now define the meta-matrices that represent the sum of the contributions of the N_L layers in direction $\boldsymbol{\alpha}_k$:

$$\mathbf{M}_{\alpha_k\parallel}^{L} = \left[\mathbf{M}_{\alpha_k\parallel}^{L_1}\cdots\mathbf{M}_{\alpha_k\parallel}^{L_j}\cdots\mathbf{M}_{\alpha_k\parallel}^{L_{N_L}}\right] \tag{2.16}$$

$$\mathbf{M}_{\alpha_k\perp}^{L} = \left[\mathbf{M}_{\alpha_k\perp}^{L_1}\cdots\mathbf{M}_{\alpha_k\perp}^{L_j}\cdots\mathbf{M}_{\alpha_k\perp}^{L_{N_L}}\right] \tag{2.17}$$

and, similarly to equation 2.7, we can also define the meta-matrices that take into account the N_{GS} wavefront sensing directions:

$$\mathbf{M}_{\alpha\parallel}^{L} = \left[\left(\mathbf{M}_{\alpha_1\parallel}^{L}\right)^T\cdots\left(\mathbf{M}_{\alpha_k\parallel}^{L}\right)^T\cdots\left(\mathbf{M}_{\alpha_{N_{GS}}\parallel}^{L}\right)^T\right]^T \tag{2.18}$$

$$\mathbf{M}_{\alpha\perp}^{L} = \left[\left(\mathbf{M}_{\alpha_1\perp}^{L}\right)^T\cdots\left(\mathbf{M}_{\alpha_k\perp}^{L}\right)^T\cdots\left(\mathbf{M}_{\alpha_{N_{GS}}\perp}^{L}\right)^T\right]^T \quad . \tag{2.19}$$

- *What is the size of the matrix $\mathbf{M}_{\alpha\parallel}^{L}$?*. Recalling the discussion in the paragraph below equation 2.6, it is important to realize that since we are considering a limited number of Zernikes representing layer L_j (i.e. up to Zernike number $n_{mod}^{L_j}$), then the number of *non-zero* Zernike coefficients in the telescope pupil (i.e. the coefficients of $\{Z_p(\mathbf{r})\}_{2\leq p\leq p_{max}}$) will be equal to $p_{max} = n_{mod}^{L_j}$.

  Since each layer L_j will be represented with a different number of Zernikes, we will in general choose the total number of Zernike coefficients defined in the telescope pupil to be:

  $$p_{\alpha_k} = \max_j\left\{n_{mod}^{L_j}\right\} \quad . \tag{2.20}$$

  In this case, each matrix $\mathbf{M}_{\alpha_k\parallel}^{L}$ will have a size of $(p_{\alpha_k} - 1)$ x n_{mod}, where:

  $$n_{mod} = \sum_j\left(n_{mod}^{L_j} - 1\right) \quad . \tag{2.21}$$

Then, it follows that the size of the matrix $\mathbf{M}^{L}_{\alpha\parallel}$ will be $N_{GS}(p_{\alpha_k}-1)$ x n_{mod}. In practice, the matrix $\mathbf{M}^{L}_{\alpha\parallel}$ can be computed following numerical or analytical methods [117, 147, 81].

Let us now proceed with our formulation. Taking into account equations 2.12, 2.18, and 2.19, equation 2.11 can be rewritten as:

$$\mathbf{s} = \mathbf{DM}^{L}_{\alpha\parallel}\boldsymbol{\varphi}_{tur_{\parallel}} + \mathbf{DM}^{L}_{\alpha\perp}\boldsymbol{\varphi}_{tur_{\perp}} + \mathbf{w} \ . \tag{2.22}$$

The matrix $\mathbf{DM}^{L}_{\alpha\parallel}$ represents the mathematical model of the *approximate direct problem*. We will call it the *tomographic interaction matrix*, and we will denote as:

$$\mathbf{H} \triangleq \mathbf{DM}^{L}_{\alpha\parallel} \ . \tag{2.23}$$

The matrix $\mathbf{H}$ provides a direct link between the phase space $\mathcal{M}_V$ we want to estimate and the WFSs measurements $\mathbf{s}$. In principle, the solution to the inverse problem in MCAO is attained by inverting the tomographic interaction matrix $\mathbf{H}$. However, the inverse of $\mathbf{H}$ is not straightforward to compute, as we will discuss in detail in section 2.3.

The second term in equation 2.22 quantifies the effect on the WFS measurements of those (higher-order) turbulence modes not taken into account in our approximate model $\mathbf{H}$. The matrix $\mathbf{DM}^{L}_{\alpha\perp}$ will be referred to as the *aliasing interaction matrix* and will be denoted as:

$$\mathbf{H}_{\perp} \triangleq \mathbf{DM}^{L}_{\alpha\perp} \ . \tag{2.24}$$

We will use this matrix to characterize the generalized aliasing in MCAO. Finally, equation 2.22 can be rewritten as:

$$\mathbf{s} = \mathbf{H}\boldsymbol{\varphi}_{tur_{\parallel}} + \mathbf{H}_{\perp}\boldsymbol{\varphi}_{tur_{\perp}} + \mathbf{w} \ . \tag{2.25}$$

2.2.3 Example case

Let us consider an example of the formulation of the approximate direct problem in MCAO. In particular, we will introduce in this section an example of the matrix $\mathbf{H} = \mathbf{DM}^{L}_{\alpha\parallel}$. We will consider that the turbulence volume comprises only two turbulent layers located at $h_1 = 0$ km and $h_2 = 8.5$ km in altitude. The infinite-dimensional column vector representing the turbulence volume is expressed as $\boldsymbol{\varphi}_{tur} = [\boldsymbol{\varphi}^{L_1}_{tur}; \boldsymbol{\varphi}^{L_2}_{tur}]$. Let us consider a telescope whose diameter is $D = 8$ m without central occultation, and a FoV of 1' ($\alpha_{max} = 30\,\text{arcsec}$). Then, from equation 2.3, the diameters of the metapupils are $D_1 = 8$ m and $D_2 = 10.5$ m.

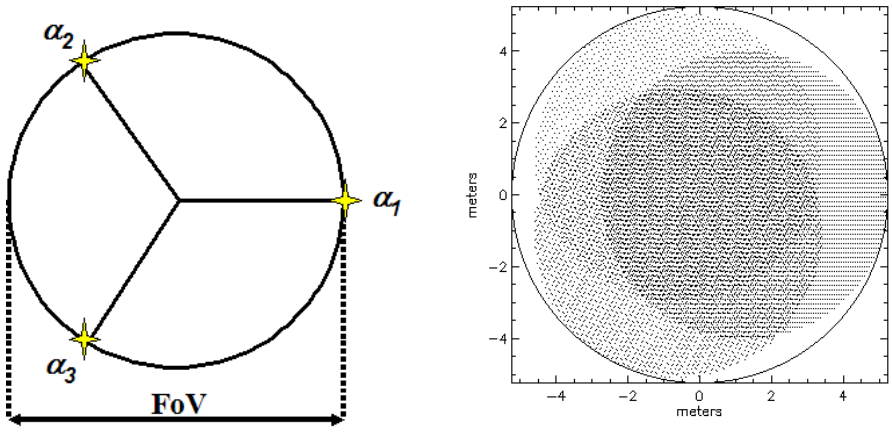

Figure 2.4: (*Left*) Illustration of a guide star asterism. The guide stars are located on the vertices of an equilateral triangle inscribed in a circle whose diameter is equal to the considered FoV. (*Right*) Illustration of the footprints within a metapupil at an altitude of 8.5 km for a FoV of 1 arcmin. The diameter of the footprints is 8 m and the diameter of the metapupil is 10.5 m.

We will now define the size of the finite-dimensional vector that we seek to estimate, namely $\boldsymbol{\varphi}_{tur_{\parallel}} = [\boldsymbol{\varphi}^{L_1}_{tur_{\parallel}}; \boldsymbol{\varphi}^{L_2}_{tur_{\parallel}}]$. Let us arbitrarily choose the first 10 radial orders for layer L_1 ($n^{L_1} = 10$). Then, according to eq. 2.14, $n^{L_2} = 13$. Also, according to eq. 2.13, $n^{L_1}_{mod} = 66$ and $n^{L_2}_{mod} = 106$. Finally, according to eq. 2.21, the total number of Zernike modes sought to be estimated is:

$$n_{mod} = \sum_j \left(n^{L_j}_{mod} - 1 \right) = 65 + 105 = 170 \ . \tag{2.26}$$

We will also consider an MCAO system comprising three WFSs coupled to natural guide stars located on the vertices of an equilateral triangle inscribed in the 1' FoV, as illustrated in figure 2.4(left). Figure 2.4(right) shows the corresponding footprints at $h_2 = 8.5$ km. The column vector $\mathbf{s}$ representing the WFS measurements obtained from the three directions can be expressed as $\mathbf{s} = [\mathbf{s}_1; \mathbf{s}_2; \mathbf{s}_3]$. Let us also consider in our example case that the three WFSs are *idealized* WFSs (section 1.2.3.2) each one of them capable of projecting directly the resultant phase in the telescope pupil onto the Zernike basis. Hence, each WFS delivers a vector $\mathbf{s}_k$ containing Zernike coefficients. Following equation 2.20, we will set each idealized WFS to measure up to Zernike number:

$$p_{\alpha_k} = \max \left\{ n^{L_1}_{mod}, n^{L_2}_{mod} \right\} = 106 \ . \tag{2.27}$$

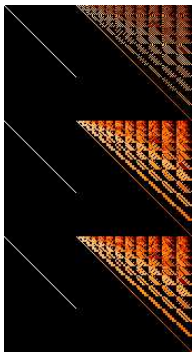

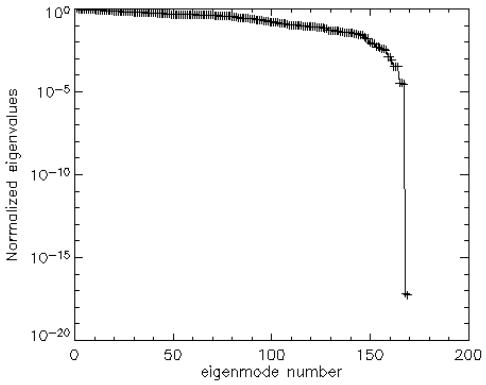

Figure 2.5: (*Left*) Example of a **H** matrix for the geometry shown in figure 2.4 and for a 1' FoV. Two turbulent layers at 0 km and 8.5 km are considered, represented with a total of 65 and 105 Zernikes respectively. Each of the three *idealized* WFSs measures a total of 105 Zernikes. Then, the size of **H** is: number of rows=105x3=315, number of columns=65+105=170. (*Right*) Eigenvalues of $\mathbf{H}^T\mathbf{H}$ in descending order.

Hence, the size of the vector **s** becomes 3x(106-1)=315. We have computed numerically the corresponding matrix **H** (whose size is 315x170), and it is shown in figure 2.5(left). Note the three *meta-rows* corresponding to each of the WFSs, and the two *meta-columns* corresponding to the two turbulent layers.

2.3 The Inverse Problem

The inverse problem in MCAO consists in estimating the turbulence volume from the available WFSs measurements (Figure 2.1). As we will discuss in this section, the solution to this inverse problem is not trivial because the problem of wavefront reconstruction (or phase estimation) in MCAO is an *ill-posed* problem. It does not comply with the properties that a well-posed problem should have, namely [62]:

1. Existence of solution.

2. Uniqueness of solution.

3. Stability of solution.

2.3.1 Existence and uniqueness of solution

We will limit our discussion in this work to the theory of *linear* inverse problems. In this framework, the inverse problem can be stated as:

$$\hat{\boldsymbol{\varphi}}_{tur} = \mathbf{R}\mathbf{s} \tag{2.28}$$

where $\mathbf{R}$ in adaptive optics is known as the *reconstruction matrix*. Then, the solution to the inverse problem is the vector $\hat{\boldsymbol{\varphi}}_{tur}$, which represents the reconstructed (or estimated) turbulence volume. The problem now translates into finding a suitable reconstruction matrix $\mathbf{R}$ that can be used to compute $\hat{\boldsymbol{\varphi}}_{tur}$. In principle, the matrix $\mathbf{R}$ could be computed as the matrix inverse of the tomographic interaction matrix $\mathbf{H}$:

$$\mathbf{R} \stackrel{\triangle}{=} \mathbf{H}^{-1} = (\mathbf{D}\mathbf{M}_{\alpha}^{L})^{-1} \ . \tag{2.29}$$

However, in adaptive optics the number of WFS measurements is usually greater than the number of modes to be estimated. This implies that the system of linear equations represented by equation 2.22 in matrix form is *overdetermined*, so the matrix $\mathbf{H}$ is not square and its direct inverse (eq. 2.29) does not exist.

2.3.1.1 Least-squares solution

The classical approach to solve an overdetermined system of equations is given by the least-squares (LS) estimation method. In our case, the least-squares estimate $\hat{\boldsymbol{\varphi}}_{tur}$ is the one providing the best-fit in the least-squares sense to the actual WFSs measurements $\mathbf{s}$, and it can be found by minimizing the criterion:

$$J_{_{LS}} = \|\mathbf{s} - \mathbf{H}\hat{\boldsymbol{\varphi}}_{tur}\|^2 \ . \tag{2.30}$$

The minimization of $J_{_{LS}}$ with respect to $\hat{\boldsymbol{\varphi}}_{tur}$ leads to the well-known least-squares solution:

$$\mathbf{H}^T\mathbf{H}\hat{\boldsymbol{\varphi}}_{tur} = \mathbf{H}^T\mathbf{s} \tag{2.31}$$

and the least-squares reconstruction matrix $\mathbf{R}_{_{LS}}$ that solves the equation $\hat{\boldsymbol{\varphi}}_{tur} = \mathbf{R}_{_{LS}}\mathbf{s}$ is simply given by the *generalized inverse* of $\mathbf{H}$, denoted as $\mathbf{H}^{\dagger}$:

$$\begin{aligned} \mathbf{R}_{_{LS}} &= \mathbf{H}^{\dagger} \\ &= (\mathbf{H}^T\mathbf{H})^{-1}\mathbf{H}^T \ . \end{aligned} \tag{2.32}$$

Note that the matrix $\mathbf{R}_{LS}$ can only be computed if the inverse of $\mathbf{H}^T\mathbf{H}$ exists; that is, if the matrix $\mathbf{H}^T\mathbf{H}$ is not singular. This condition can be verified by means of the singular value decomposition (SVD) of $\mathbf{H}$.

2.3.1.2 Singular value decomposition

The singular value decomposition (SVD) of $\mathbf{H}$ can be expressed as [137]:

$$\mathbf{H} = \mathbf{U}\Sigma\mathbf{V}^T\,, \tag{2.33}$$

where —if $\mathbf{H}$ is an n by m matrix— then:

- $\mathbf{U}$ is an n by m unitary matrix containing the eigenvectors of $\mathbf{H}\mathbf{H}^T$. Since the matrix $\mathbf{U}$ is unitary then $\mathbf{U}^T = \mathbf{U}^{-1}$.
- $\mathbf{V}$ is an m by m unitary matrix containing the eigenvectors of $\mathbf{H}^T\mathbf{H}$. Since the matrix $\mathbf{V}$ is unitary then $\mathbf{V}^T = \mathbf{V}^{-1}$. We will simply refer to the eigenvectors of $\mathbf{H}^T\mathbf{H}$ as the *eigenmodes* of $\mathbf{H}$. Also, we will refer as *eigenspace* the vector space generated by the eigenmodes of $\mathbf{H}$.
- Σ is an m by m diagonal matrix containing the singular values of $\mathbf{H}$, denoted as $\{\sigma_i\}$.
- The *eigenvalues* of $\mathbf{H}^T\mathbf{H}$, denoted as $\{\lambda_i\}$, are related to the singular values of $\mathbf{H}$, $\{\sigma_i\}$, simply by $\lambda_i = \sigma_i^2$.

The matrix $\mathbf{H}^T\mathbf{H}$ is said to be singular —and hence not invertible— if at least one of its eigenvalues is equal to zero: $\lambda_i = 0$.

2.3.1.3 Minimum-norm least-squares solution

Let us now express the matrix $\mathbf{R}_{LS}$ in terms of the SVD decomposition of $\mathbf{H}$. Substituting equation 2.33 into 2.32, and taking into account that $\mathbf{U}$ and $\mathbf{V}$ are unitary, leads to the following expression for the least-squares reconstruction matrix:

$$\mathbf{R}_{LS} = \mathbf{V}\Sigma^{-1}\mathbf{U}^T\ , \tag{2.34}$$

where the matrix Σ^{-1} is defined as the diagonal matrix whose elements are $\{\sigma_i^{-1}\}$. Note that if $\mathbf{H}^T\mathbf{H}$ is singular, then the matrix Σ is not inversible, and so the matrix $\mathbf{R}_{LS}$ (eq. 2.34) cannot be computed. In other words, the inverse problem does not comply

with the property of *uniqueness of solution*. As we will discuss in section 2.3.1.4, this is in general the case in adaptive optics.

The *general* least-squares solution $\hat{\boldsymbol{\varphi}}_{tur}$ that satisfies equation 2.30 can be expressed as the sum of a *particular* solution $\hat{\boldsymbol{\varphi}}^p_{tur}$ and an *homogeneous* solution $\hat{\boldsymbol{\varphi}}^h_{tur}$ [10, Ch.1]:

$$\hat{\boldsymbol{\varphi}}_{tur} = \hat{\boldsymbol{\varphi}}^p_{tur} + c\,\hat{\boldsymbol{\varphi}}^h_{tur} \ , \tag{2.35}$$

where c is a constant that can take any value, thus leading to an infinite number of solutions for $\hat{\boldsymbol{\varphi}}_{tur}$. Within the formalism of linear algebra, the vector $\hat{\boldsymbol{\varphi}}^p_{tur}$ belongs to the *row-space* of $\mathbf{H}$ and the vector $\hat{\boldsymbol{\varphi}}^h_{tur}$ belongs to the *nullspace* of $\mathbf{H}$, which are orthogonal subspaces of $\mathbb{R}^m$ [137]. The eigenmodes of $\mathbf{H}$ associated with zero eigenvalues ($\lambda_i = 0$) form a basis of the nullspace of $\mathbf{H}$. Note that the uniqueness of solution would be guaranteed if the dimension of the nullspace of $\mathbf{H}$ were equal to zero. In this case, there would be no zero eigenvalues and the only vector in the nullspace of $\mathbf{H}$ would be the zero vector: $\boldsymbol{\varphi}^h_{tur} = \vec{0}$.

When the dimension of the nullspace of $\mathbf{H}$ is not equal to zero, the classical approach to guarantee the uniqueness of solution is to choose from all the possible general solutions (eq. 2.35) the one that has the *minimum norm*. Since $\hat{\boldsymbol{\varphi}}^p_{tur}$ and $\hat{\boldsymbol{\varphi}}^h_{tur}$ are orthonormal vectors, the squared norm of $\hat{\boldsymbol{\varphi}}_{tur}$ can be expressed as [10, Ch.1]:

$$\|\hat{\boldsymbol{\varphi}}_{tur}\|^2 = \|\hat{\boldsymbol{\varphi}}^p_{tur}\|^2 + c^2\|\hat{\boldsymbol{\varphi}}^h_{tur}\|^2 \ . \tag{2.36}$$

From this equation it can be seen that $\|\hat{\boldsymbol{\varphi}}_{tur}\|^2$ will be a minimum if $\|\hat{\boldsymbol{\varphi}}^h_{tur}\|^2 = 0$. That is, if we choose from all the vectors in the nullspace of $\mathbf{H}$ the zero vector: $\hat{\boldsymbol{\varphi}}^h_{tur} = \vec{0}$. This choice corresponds to the *minimum-norm least-squares solution*. In practice, the minimum-norm least-squares reconstructor —denoted as $\mathbf{R}_{MNLS}$— can be computed as:

$$\mathbf{R}_{MNLS} = \mathbf{V}\Sigma_0^{-1}\mathbf{U}^T \ , \tag{2.37}$$

where Σ_0^{-1} is a diagonal matrix defined as:

$$\Sigma_0^{-1} = \mathrm{diag}(x_i) \ \text{ where } \ x_i = \begin{cases} \sigma_i^{-1} & \text{if} \quad \sigma_i \neq 0 \\ 0 & \text{if} \quad \sigma_i = 0 \end{cases} \ , \tag{2.38}$$

where $\mathrm{diag}(x_i)$ simply denotes a diagonal matrix whose elements are given by x_i. With the reconstruction matrix $\mathbf{R}_{MNLS}$ the uniqueness of the least-squares solution is guaranteed.

2.3.1.4 Unseen modes in adaptive optics

Let us now give a physical interpretation to the mathematical concepts introduced in the previous sections. In adaptive optics, the set of eigenvalues $\{\lambda_i\}$ represent the sensitivity of the WFSs to the corresponding eigenmodes [90]. Also, each eigenmode can be represented as a combination of N_L spatial modes $\varphi_{tur}^{L_j}(\mathbf{r})$ (see equation 2.2 and figure 2.2). Then, the eigenmodes associated with zero eigenvalues ($\lambda_i = 0$) can be represented as a combination of spatial modes that produce a null response on the WFSs. That is, they satisfy the equation $\mathbf{H}\boldsymbol{\varphi}_{tur} = \vec{0}$, where the vector $\vec{0}$ represents a null response on the WFSs.

In adaptive optics, the dimension of the nullspace of $\mathbf{H}$ is in general not equal to zero. That is, there are several other combinations of spatial modes that produce a null response on the wavefront sensors. These spatial modes are known in adaptive optics as the *unseen modes*, and the most common examples are:

- *Piston mode.* The piston mode $Z_1(\mathbf{r})$ is just a flat wavefront. It produces no response on the wavefront sensor, and in principle, it does not degrade the image quality in optical systems. However, if it is not filtered out in some way from the reconstruction process, the general solution (eq. 2.35) will be of the form: $\hat{\boldsymbol{\varphi}}_{tur} = \hat{\boldsymbol{\varphi}}_{tur}^{p} + c\vec{1}$, where $\vec{1}$ denotes a vector of ones. If we drove a deformable mirror to fit this solution, the dynamic range would be limited by the piston term $c\vec{1}$ and eventually the DM would saturate (see section 1.2.1.1).

- *Tip-tilt combinations.* This is a particular unseen mode that occurs in MCAO systems. It is illustrated in figure 2.6(left) for the simple case where only two turbulent layers are being reconstructed. Some combinations of tip-tilt modes on the two layers can be totally cancelled out. The resultant phase in the telescope pupil would be equal to a piston term in *any* direction $\boldsymbol{\alpha}$. Once again, if these unseen modes are not filtered out in some way, they will cause the DMs to waste their dynamic range reproducing tip-tilt combinations and eventually saturate.

2.3.2 Stability of solution

The stability of the solution is the last of the three properties that a well-posed problem should comply with. For the MCAO reconstruction problem, the solution would be stable if for small relative variations on the WFSs measurements $\|\delta\mathbf{s}\|/\|\mathbf{s}\|$ —e.g. due to measurement noise $\mathbf{w}$— the resulting relative variations on the estimates $\|\delta\hat{\boldsymbol{\varphi}}_{tur}\|/\|\hat{\boldsymbol{\varphi}}_{tur}\|$ were also small. However, if the problem is ill-posed, the measurement

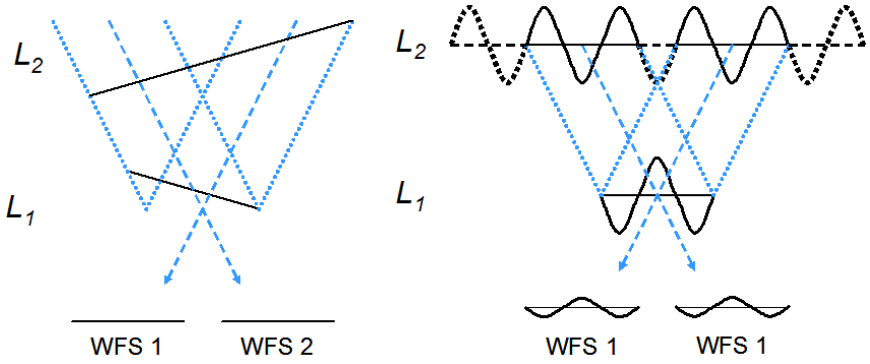

Figure 2.6: *(Left)* Representation of a tip-tilt combination: a typical unseen mode in MCAO. *(Right)* Illustration of the concept of a badly-seen mode in MCAO.

noise will *propagate* strongly through the reconstruction matrix $\mathbf{R}_{MNLS}$ (eq. 2.37), and will cause large fluctuations on the estimates. It can be shown that the maximum relative error $\|\delta\hat{\boldsymbol{\varphi}}_{tur}\|/\|\hat{\boldsymbol{\varphi}}_{tur}\|$ will be bounded by [137]:

$$\frac{\|\delta\hat{\boldsymbol{\varphi}}_{tur}\|}{\|\hat{\boldsymbol{\varphi}}_{tur}\|} \leq \|\mathbf{H}\|\|\mathbf{R}_{MNLS}\|\frac{\|\delta\mathbf{s}\|}{\|\mathbf{s}\|} \tag{2.39}$$

where $\|\mathbf{H}\|$ and $\|\mathbf{R}_{MNLS}\|$ denote the spectral norms[2] of the corresponding matrices, and the constant $\|\mathbf{H}\|\|\mathbf{R}_{MNLS}\|$ is known as the *condition number* of $\mathbf{H}$:

$$\text{cond}\,(\mathbf{H}) \triangleq \|\mathbf{H}\|\|\mathbf{R}_{MNLS}\| \ . \tag{2.40}$$

It is straightforward to show that the norm of $\mathbf{R}_{MNLS}$ is equal to:

$$\|\mathbf{R}_{MNLS}\| = \sigma_{\max}(\mathbf{R}_{MNLS}) = \frac{1}{\sigma_{\min}(\mathbf{H})} \ , \tag{2.41}$$

where $\sigma_{\min}(\mathbf{H})$ denotes the minimum non-zero singular value of $\mathbf{H}$. Hence, equation 2.40 can be also expressed as:

$$\text{cond}\,(\mathbf{H}) = \frac{\sigma_{\max}(\mathbf{H})}{\sigma_{\min}(\mathbf{H})} \ . \tag{2.42}$$

Note from equation 2.39 that large condition numbers indicate that large fluctuations on the estimates will be expected due to the strong propagation of the measurement noise. The matrix $\mathbf{H}$ is said to be *badly conditioned*. In general, the problem of wavefront

[2]The spectral norm of a matrix $\mathbf{A}$ is defined as its maximum singular value: $\|\mathbf{A}\| \triangleq \sigma_{\max}(\mathbf{A})$.

reconstruction in MCAO using the least-squares approach is badly conditioned. This is due to the fact that there are some eigenmodes whose singular values are not zero but very small, $\sigma_{\min}(\mathbf{H}) \rightarrow 0$, so that the condition number becomes quite large. In adaptive optics, the eigenmodes associated with low singular values are better known as the *badly-seen modes*.

2.3.2.1 Badly-seen modes in adaptive optics

As illustrated in figure 2.6(right), a badly-seen mode is a combination of spatial modes that produces a very small signal on the wavefront sensing directions $\{\boldsymbol{\alpha}_k\}$. Note that the resultant phase on the pupil plane for other directions (e.g. in between guide stars) won't be necessarily equal to zero. If these modes are not treated with caution during the reconstruction process, they can really degrade the uniformity of the MCAO correction in the whole field of view.

Badly-seen modes in MCAO depend on the system characteristics (e.g. number and position of guide stars, number of reconstructed layers, etc.). For instance, adaptive optics systems based on SAMs DMs and Shack-Hartmann WFSs are particularly affected by badly-seen modes known as *waffle modes*, which are generated when the control signals of adjacent actuators of the DM are equal in magnitude but with opposite sign [126, 56].

Example. Let us consider once again the matrix $\mathbf{H}$ shown in figure 2.5(left). Figure 2.5(right) shows the eigenvalues of $\mathbf{H}^T\mathbf{H}$. There is a total of 170 eigenmodes and they are all displayed in figure 2.7. Note that each eigenmode can be represented with two phase maps, one for each turbulent layer. Also note that the last two eigenmodes (associated with zero eigenvalues) are tip-tilt combinations. Eigenmodes 154 to 168 are related to the non-seen portions of the metapupil at 8.5 km (figure 2.4), so they have also very low sensitivities ($\lambda_i \approx 10^{-4}$). These are the typical badly-seen modes that arise in MCAO and that are responsible for the large condition numbers.

2.3.2.2 Conditioning of H

In this section we will study the evolution of the condition number of $\mathbf{H}$ as a function of the number of estimated modes per layer, the FoV of interest, and the number of guide stars (GSs). We will consider once again that the telescope diameter is $D = 8$ m without central occultation, and that the turbulence volume comprises only two turbulent layers located at 0 and 8.5 km respectively.

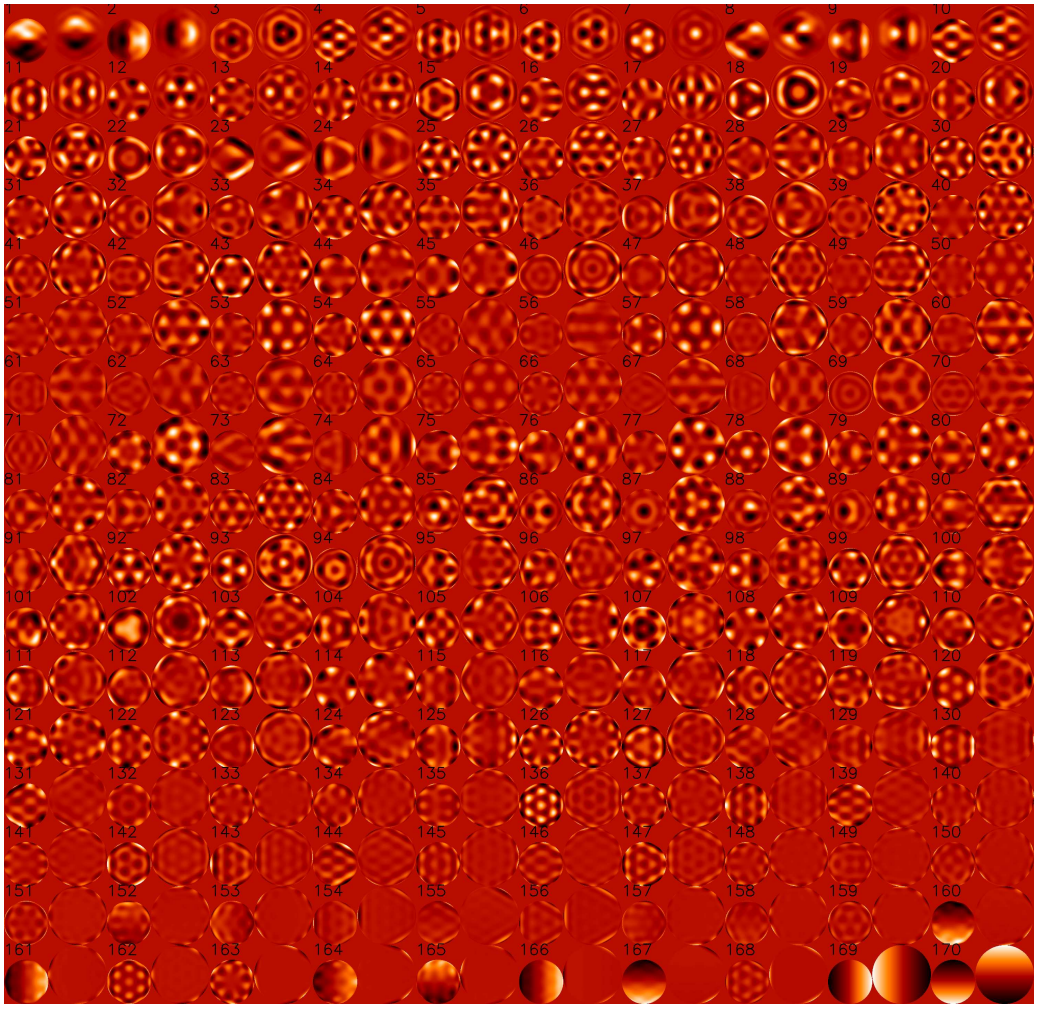

Figure 2.7: Eigenmodes of $\mathbf{H}^T\mathbf{H}$ for the matrix shown in figure 2.5. The associated eigenvalues are also shown in figure 2.5.

Similarly to the example case in section 2.2.3, we will consider that for the first layer L_1 we seek to estimate all Zernikes (piston Z_1 not included) up to radial order n^{L_1}, and for the second layer L_2 up to radial order n^{L_2}. The pair of values for n^{L_1} and n^{L_2} will be chosen so that the maximum spatial frequency estimated in both layers is the same. In our present case, $D_1 = 8$ m and D_2 will depend on the considered FoV (eq. 2.3). Therefore, n^{L_2} will be scaled according to equation 2.14 for each pair $\{n^{L_1}, \text{FoV}\}$ considered.

Let us start our study with the 3-GSs geometry shown in figure 2.4(left), and we will keep on working with *idealized* WFSs (section 1.2.3.2). Following equation 2.20, we will set each idealized WFS to measure up to Zernike number $p_{\alpha_k} = \max\{n^{L_1}_{mod}, n^{L_2}_{mod}\}$. We will study the evolution of the condition number of $\mathbf{H}$ as a function of the considered FoV in which the 3 GSs are inscribed, and as a function of the number of estimated modes. We will study the cases for $n^{L_1} = \{10, 12, 16\}$, which correspond to a maximum Zernike number of $n^{L_1}_{mod} = \{66, 91, 153\}$ respectively. The considered FoVs will vary from 20 arcsec ($\alpha_{max} = 10\,\text{arcsec}$) up to 120 arcsec ($\alpha_{max} = 60\,\text{arcsec}$). We have computed for each pair $\{n^{L_1}, \text{FoV}\}$ the associated n^{L_2} and p_{α_k}, and generated the corresponding matrix $\mathbf{H}$. Figure 2.8 shows the evolution of the condition number of $\mathbf{H}$ as a function of the considered pair $\{n^{L_1}, \text{FoV}\}$. Also, figure 2.9 shows the eigenvalues of $\mathbf{H}^T\mathbf{H}$ for the cases $n^{L_1} = \{10, 16\}$ and for all the considered FoVs. Note that the last two eigenvalues correspond to tip-tilt combinations so they are not considered in the computation of the condition number. We can make from these plots the following remarks:

- For a given FoV, the condition number increases with the number of Zernike modes to be estimated. In principle, the model of the approximate direct problem would be more accurate by considering a larger number of Zernike coefficients for each layer; but this would worsen the conditioning of $\mathbf{H}$ indicating that the inverse problem will be more difficult to solve. From the two plots of figure 2.9, and taking a look at the extreme case of a FoV= 120 arcsec, we can see that increasing the number of Zernikes from $n^{L_1} = 10$ to $n^{L_1} = 16$ will increase the proportion of eigenmodes with low sensitivities, so there will be more modes subject to strong noise propagation. Therefore, in practice, the number of Zernike modes per layer taken into account in the model of the approximate direct problem cannot be arbitrarily large.

- The condition number increases with the considered FoV. Indeed, when the FoV increases the non-seen areas (figure 2.4(right)) increase as well, and the turbu-

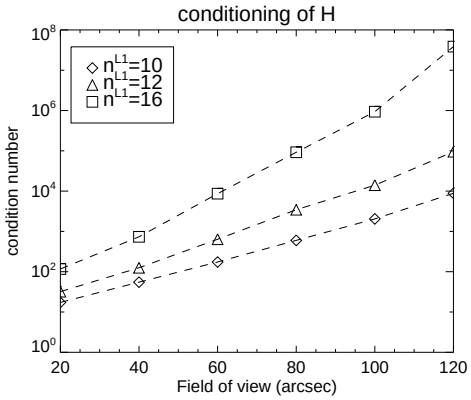

Figure 2.8: Evolution of the condition number of $\mathbf{H}$ as a function of the considered FoV and the selected number of Zernike coefficients (expressed in terms of n^{L_1}). The MCAO reconstruction problem in question is to estimate 2 turbulent layers at 0 and 8.5 km using 3 wavefront sensing directions in an equilateral triangle configuration (figure 2.4).

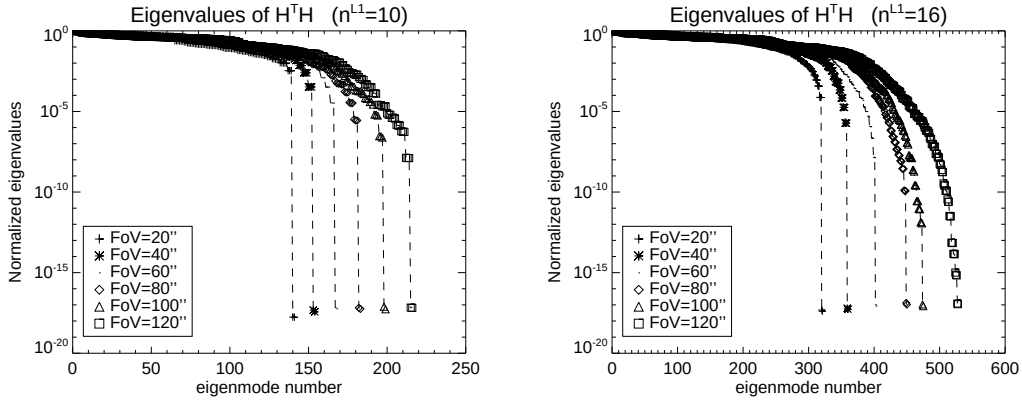

Figure 2.9: Distribution of the eigenvalues of $\mathbf{H}^T\mathbf{H}$ as a function of the considered FoV and the selected number of Zernike coefficients: (*Left*) $n^{L_1} = 10$ (*Right*) $n^{L_1} = 16$. The MCAO reconstruction problem in question is to estimate 2 turbulent layers at 0 and 8.5 km using 3 wavefront sensing directions in an equilateral triangle configuration.

lence volume estimation problem becomes more difficult to solve too. If a larger FoV were required then more WFSs could be added to provide a better sampling of the metapupils. In order to show the improvement brought by an increase in the number of GSs, let us consider the case where 5 wavefront sensing directions are used. The five directions $\{\boldsymbol{\alpha}_k\}$ are located at the vertices of a regular pentagon inscribed in a circle whose diameter is equal to the considered FoV. Figure 2.10(left) shows the evolution of the condition number of the corresponding $\mathbf{H}$ as a function of the considered pair $\{n^{L_1}, \text{FoV}\}$. Also, figure 2.10(right) shows the eigenvalues of $\mathbf{H}^T\mathbf{H}$ for the case where $n^{L_1} = 16$ and for different FoVs. We can clearly appreciate that the reconstruction problem becomes better conditioned with respect to the 3 GSs configuration even for the extreme case of a FoV= 120 arcsec. We can then conclude that if a larger corrected FoV is required, then it should be considered the use of additional WFSs to better sample the turbulence volume.

In conclusion, the number of Zernike modes per layer taken into account in the model of the approximate direct problem (i.e. in the creation of the tomographic interaction matrix $\mathbf{H}$) should be kept low in order to prevent the condition number to reach very large values. This allows to improve the stability of the solution in the least-squares approach. However, there will always remain some eigenmodes with low sensitivity values. In order to effectively ensure the stability of the solution in the least-squares approach it will be required to filter out these eigenmodes as we will discuss in section 2.3.2.3.

We should also note at this point that the limitation of the considered number of Zernike modes per layer in principle is not necessary when using other estimation approaches which take advantage of some statistical prior knowledge to *regularize* the inverse problem and ensure the stability of the solution, as we will discuss in section 2.5.

2.3.2.3 Truncated least-squares solution

For any fixed configuration, the stability of the solution can be substantially improved by *truncating* or filtering out the badly-seen modes. This can be done with the SVD method, just as it was done for the unseen modes in equation 2.37. The truncation is achieved by simply setting $\sigma_i^{-1} = 0$ for all badly-seen modes inside the matrix Σ_0^{-1} in the MNLS reconstructor (eq. 2.37). We will denote this new matrix as Σ_{fil}^{-1}. The resulting reconstructor is known as the *truncated least-squares reconstructor* —denoted

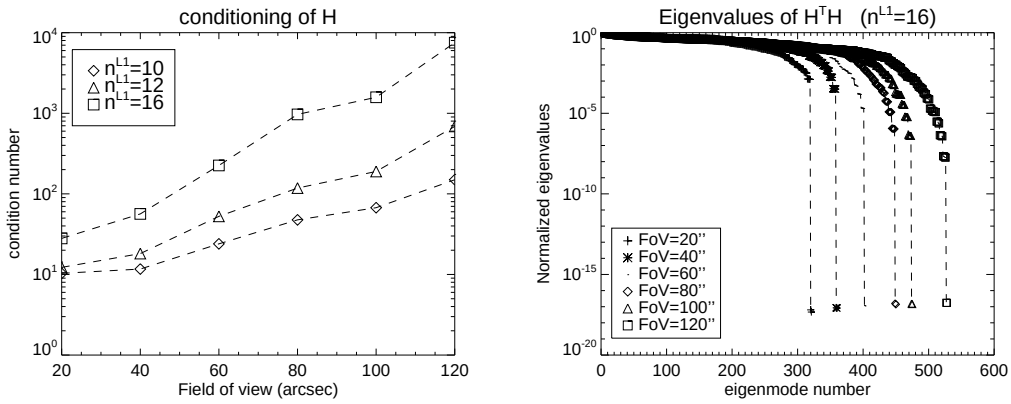

Figure 2.10: (*Left*) Evolution of the condition number of $\mathbf{H}$. (*Right*) Distribution of the eigenvalues of $\mathbf{H}^T\mathbf{H}$ as a function of the considered FoV for the case where $n^{L_1} = 16$. The MCAO reconstruction problem in question is to estimate 2 turbulent layers at 0 and 8.5 km, but this time using 5 wavefront sensing directions in a regular pentagon configuration.

as $\mathbf{R}_{_{TLS}}$— and it can be expressed as:

$$\mathbf{R}_{_{TLS}} = \mathbf{V}\Sigma_{fil}^{-1}\mathbf{U}^T \ . \tag{2.43}$$

The main issue in computing the TLS reconstructor is to decide how many eigenmodes need to be truncated. Let us first study the general characteristics of MCAO eigenmodes. Le Louarn & Tallon [88] remarked that MCAO eigenmodes can be classified in *even* and *odd* modes. Even modes are characterized by deformations of the same sign on all metapupils, so that when the footprints add up they don't cancel each other. Hence, even modes are characterized by high sensitivities. For example, for the eigenmodes shown in figure 2.7, the first eigenmodes have high sensitivities associated with them, so they are properly measured by the MCAO system. Note that they are actually very similar to low-order Zernike polynomials.

On the other hand, odd modes are characterized by deformations of opposite signs on the metapupils. When the footprints add up the deformations subtract each other. Therefore, odd modes run the risk of becoming badly-seen modes. In the extreme case, the deformations cancel out completely and the odd eigenmode becomes an unseen mode. The border between even and odd modes is characterized by a slight change in the slope of the eigenvalues distribution [88]. For example, in the eigenvalues distribution shown in figure 2.5 this change occurs around the eigenmode number 80.

Taking a look at the eigenvalues distribution for the examples shown in figure 2.9, we can see that in general the evolution in sensitivities occurs rather smoothly. Hence, it is not trivial to tag an eigenmode as *badly-seen* or not. The classical approach is to select a *threshold* for the eigenvalues and truncate *all* eigenmodes whose eigenvalues (normalized to the maximum eigenvalue λ_{max}) lie below this threshold. Based on this criterion, the matrix Σ_{fil}^{-1} in equation 2.43 can be expressed as:

$$\Sigma_{fil}^{-1} = \mathrm{diag}(x_i) \quad \text{where} \quad x_i = \begin{cases} \sigma_i^{-1} & \text{if} \quad \frac{\lambda_i}{\lambda_{\max}} > \Lambda \\ 0 & \text{if} \quad \frac{\lambda_i}{\lambda_{\max}} < \Lambda \end{cases} \tag{2.44}$$

where Λ is the threshold value. Note that the condition number $\sigma_{\max}/\sigma_{\min}$ (eq. 2.42) is effectively reduced since now $\sigma_{\min} = \sqrt{\lambda}_{min}$ represents the smallest non-truncated singular value. The threshold becomes then the most important parameter that needs to be adjusted in the least-squares reconstructor. The best or *optimal* threshold — denoted as Λ_{opt}— for a given MCAO configuration will depend on the observation conditions, the signal-to-noise ratio (SNR), etc. In section 2.4.3 we will present a criterion that can be used to compute the optimal threshold. This criterion is based on the minimization of the *global reconstruction error*. In the following section we will describe how to evaluate the reconstruction error in MCAO.

2.4 Evaluation of the reconstruction error

We will be interested in quantifying the reconstruction error –or estimation error– for any reconstruction matrix $\mathbf{R}$. By substituting equation 2.25 in equation 2.28, the estimate $\hat{\boldsymbol{\varphi}}_{tur}$ results in:

$$\hat{\boldsymbol{\varphi}}_{tur} = \mathbf{R}\left(\mathbf{H}\boldsymbol{\varphi}_{tur_{\parallel}} + \mathbf{H}_{\perp}\boldsymbol{\varphi}_{tur_{\perp}} + \mathbf{w}\right) \ . \tag{2.45}$$

The reconstruction error, $\boldsymbol{\epsilon}$, is defined as the vector difference between the *true* turbulence vector $\boldsymbol{\varphi}_{tur_{\parallel}}$ and its estimate $\hat{\boldsymbol{\varphi}}_{tur}$. From equation 2.45, $\boldsymbol{\epsilon}$ can be expressed as:

$$\begin{aligned} \boldsymbol{\epsilon} &= \hat{\boldsymbol{\varphi}}_{tur} - \boldsymbol{\varphi}_{tur_{\parallel}} \\ &= \left[\mathbf{RH} - \mathbf{I}\right]\boldsymbol{\varphi}_{tur_{\parallel}} + \mathbf{RH}_{\perp}\boldsymbol{\varphi}_{tur_{\perp}} + \mathbf{Rw} \end{aligned} \tag{2.46}$$

where $\mathbf{I}$ is the identity matrix. The covariance matrix of the reconstruction error provides a full description of the stochastic properties of $\boldsymbol{\epsilon}$. It can be computed as:

$$\begin{aligned}\mathbf{C}_\epsilon &= \left\langle \boldsymbol{\epsilon}\boldsymbol{\epsilon}^T \right\rangle \\ &= \Big\langle \Big(\left[\mathbf{RH}-\mathbf{I}\right] \boldsymbol{\varphi}_{tur_\parallel} + \mathbf{RH}_\perp \boldsymbol{\varphi}_{tur_\perp} + \mathbf{Rw} \Big) \times \\ &\quad \Big(\left[\mathbf{RH}-\mathbf{I}\right] \boldsymbol{\varphi}_{tur_\parallel} + \mathbf{RH}_\perp \boldsymbol{\varphi}_{tur_\perp} + \mathbf{Rw} \Big)^T \Big\rangle \end{aligned} \tag{2.47}$$

where $\langle\cdot\rangle$ denotes an ensemble average. Assuming that the turbulence and the measurement noise are statistically uncorrelated, we can express equation 2.47 as:

$$\begin{aligned}\mathbf{C}_\epsilon &= \mathbf{R}\left\langle \mathbf{w}\mathbf{w}^T \right\rangle \mathbf{R}^T + \left[\mathbf{RH}-\mathbf{I}\right] \left\langle \boldsymbol{\varphi}_{tur_\parallel} \boldsymbol{\varphi}_{tur_\parallel}^T \right\rangle \left[\mathbf{RH}-\mathbf{I}\right]^T \\ &+ \left[\mathbf{RH}_\perp\right] \left\langle \boldsymbol{\varphi}_{tur_\perp} \boldsymbol{\varphi}_{tur_\perp}^T \right\rangle \left[\mathbf{RH}_\perp\right]^T \\ &+ \left[\mathbf{RH}-\mathbf{I}\right] \left\langle \boldsymbol{\varphi}_{tur_\parallel} \boldsymbol{\varphi}_{tur_\perp}^T \right\rangle \left[\mathbf{RH}_\perp\right]^T \\ &+ \left[\mathbf{RH}_\perp\right] \left\langle \boldsymbol{\varphi}_{tur_\perp} \boldsymbol{\varphi}_{tur_\parallel}^T \right\rangle \left[\mathbf{RH}-\mathbf{I}\right]^T \end{aligned} \tag{2.48}$$

The last two terms are negligible since they involve the correlation between low-order and high-order turbulent modes. The other covariance matrices involved in equation 2.48 are:

$$\mathbf{C}_\mathbf{w} = \left\langle \mathbf{w}\mathbf{w}^T \right\rangle \tag{2.49}$$

$$\mathbf{C}_{\varphi_\parallel} = \left\langle \boldsymbol{\varphi}_{tur_\parallel} \boldsymbol{\varphi}_{tur_\parallel}^T \right\rangle \tag{2.50}$$

$$\mathbf{C}_{\varphi_\perp} = \left\langle \boldsymbol{\varphi}_{tur_\perp} \boldsymbol{\varphi}_{tur_\perp}^T \right\rangle \tag{2.51}$$

$\mathbf{C}_\mathbf{w}$ is the measurement noise covariance matrix. Assuming that the measurement noise of different wavefront sensors is uncorrelated the matrix $\mathbf{C}_\mathbf{w}$ becomes a block-diagonal matrix with N_{GS} blocks. Similarly, assuming that the turbulent layers are uncorrelated the matrices $\mathbf{C}_{\varphi_\parallel}$ and $\mathbf{C}_{\varphi_\perp}$ become block-diagonal matrices with N_L blocks. For modal representation of the turbulence using Zernike polynomials these matrices are computed from equations 1.34 or 1.35. Then, equation 2.48 can be rewritten as:

$$\begin{aligned}\mathbf{C}_\epsilon &= \mathbf{R}\mathbf{C}_\mathbf{w}\mathbf{R}^T \\ &+ \left[\mathbf{RH}-\mathbf{I}\right] \mathbf{C}_{\varphi_\parallel} \left[\mathbf{RH}-\mathbf{I}\right]^T \\ &+ \left[\mathbf{RH}_\perp\right] \mathbf{C}_{\varphi_\perp} \left[\mathbf{RH}_\perp\right]^T \quad . \end{aligned} \tag{2.52}$$

Let us now discuss the significance of each of the three terms in equation 2.52:

- The first term describes the propagation of the measurement noise in the reconstruction process. Noise propagation in SCAO systems has been widely studied [128]. It has also been studied for the case of MCAO [150, 44].

- The second term of equation 2.52 describes the error related to the reconstruction matrix. It could only be equal to zero if $\mathbf{R} \equiv (\mathbf{H})^{-1}$, but as we discussed in section 2.3.1 this is never possible.

- The third term of equation 2.52 describes the contribution to the reconstruction error coming from those (high-order) turbulent modes that belong to $\mathcal{M}_V^{\perp}$. It was originally called the *remaining error* by G. Dai [21] because he realized that this error term was always present even in the case of noiseless WFSs ($\mathbf{w} = \vec{0}$). J. P. Veran [152] called it the under-calibration error, and showed that it is a sort of aliasing error. This error term has not been previously studied in the case of MCAO. In the following sections we will fully characterize it. Following G. Dai, we will refer to it as remaining error.

2.4.1 Variance distribution in eigenspace

We will be interested in expressing the reconstruction error in the *eigenspace* (section 2.3.1.2). In order to do this, it is important to note that the matrix $\mathbf{V}$ of the SVD decomposition of $\mathbf{H}$ (eq. 2.33) can be seen as the transformation matrix that goes from the eigenspace to the phase space $\mathcal{M}_V$. Thus, the covariance matrix of $\varphi_{\parallel}$ in the eigenspace —denoted[3] as $\mathbf{C}_{\varphi_{\parallel}}^{MP}$— can be computed as:

$$\mathbf{C}_{\varphi_{\parallel}}^{MP} \triangleq \mathbf{V}^T \mathbf{C}_{\varphi_{\parallel}} \mathbf{V} \ . \tag{2.53}$$

Similarly, the covariance matrix of the reconstruction error $\boldsymbol{\epsilon}$ in the eigenspace can be computed as:

$$\mathbf{C}_{\epsilon}^{MP} \triangleq \mathbf{V}^T \mathbf{C}_{\epsilon} \mathbf{V} \ . \tag{2.54}$$

Substituting equation 2.52 into 2.54 leads to:

$$\mathbf{C}_{\epsilon}^{MP} = \mathbf{C}_{\mathbf{w}}^{MP} + \mathbf{C}_{R}^{MP} + \mathbf{C}_{\varphi_{\perp}}^{MP} \ , \tag{2.55}$$

[3]We will denote the covariance matrices in the eigenspace with an *MP*, which stands for *modes propres*, or eigenmodes in French.

where:

$$\mathbf{C}_{\mathbf{w}}^{MP} \triangleq \mathbf{V}^T \mathbf{R} \mathbf{C}_{\mathbf{w}} \mathbf{R}^T \mathbf{V} \tag{2.56}$$

$$\mathbf{C}_{R}^{MP} \triangleq \mathbf{V}^T \left[\mathbf{R}\mathbf{H} - \mathbf{I}\right] \mathbf{C}_{\varphi_\parallel} \left[\mathbf{R}\mathbf{H} - \mathbf{I}\right]^T \mathbf{V} \tag{2.57}$$

$$\mathbf{C}_{\varphi_\perp}^{MP} \triangleq \mathbf{V}^T \mathbf{R} \left[\mathbf{H}_\perp\right] \mathbf{C}_{\varphi_\perp} \left[\mathbf{H}_\perp\right]^T \mathbf{R}^T \mathbf{V} \ . \tag{2.58}$$

We will be particularly interested in the *diagonals* of $\mathbf{C}_{\varphi_\parallel}^{MP}$, $\mathbf{C}_{\mathbf{w}}^{MP}$, $\mathbf{C}_{R}^{MP}$, and $\mathbf{C}_{\varphi_\perp}^{MP}$, because they characterize the repartition (or distribution) among the eigenmodes of the variance of the turbulence, the measurement noise, the error related to the reconstruction matrix, and the remaining error respectively. We will refer to all these diagonals simply as the *variance distribution in the eigenspace*.

2.4.2 Global reconstruction error

Let us define also a *global reconstruction error* as:

$$\sigma_{rec}^2 \triangleq \left\langle \|\boldsymbol{\epsilon}\|^2 \right\rangle = \left\langle \left\| \hat{\boldsymbol{\varphi}}_{tur} - \boldsymbol{\varphi}_{tur_\parallel} \right\|^2 \right\rangle \ . \tag{2.59}$$

The global reconstruction error is equivalent to the sum of the reconstruction error variances on each layer. It can be computed from equation 2.55 as:

$$\begin{aligned} \sigma_{rec}^2 &= \operatorname{trace}\left\{\mathbf{C}_{\epsilon}^{MP}\right\} \\ &= \operatorname{trace}\left\{\mathbf{C}_{\mathbf{w}}^{MP}\right\} + \operatorname{trace}\left\{\mathbf{C}_{R}^{MP}\right\} + \operatorname{trace}\left\{\mathbf{C}_{\varphi_\perp}^{MP}\right\} \ , \end{aligned} \tag{2.60}$$

and we will denote the separate contributions to the global reconstruction error as:

$$\sigma_{\mathbf{w}}^2 \triangleq \operatorname{trace}\left\{\mathbf{C}_{\mathbf{w}}^{MP}\right\} \tag{2.61}$$

$$\sigma_{R}^2 \triangleq \operatorname{trace}\left\{\mathbf{C}_{R}^{MP}\right\} \tag{2.62}$$

$$\sigma_{\varphi_\perp}^2 \triangleq \operatorname{trace}\left\{\mathbf{C}_{\varphi_\perp}^{MP}\right\} \ . \tag{2.63}$$

The global reconstruction error σ_{rec}^2 is an useful scalar *performance metric*. As we mentioned in section 2.3.2.3, the optimal threshold for the TLS reconstructor can be defined as the threshold value that minimizes σ_{rec}^2. We will illustrate this with an example in section 2.4.4.

2.4.3 Reconstruction error for the TLS reconstructor

In this section we will derive the reconstruction error for the TLS reconstructor. Let us start by computing the covariance matrices $\mathbf{C}_{\mathbf{w}}^{MP}$, $\mathbf{C}_{R}^{MP}$, and $\mathbf{C}_{\varphi_\perp}^{MP}$ for the TLS reconstructor. Substituting equations 2.33 and 2.43 into equations 2.56, 2.57, and 2.58 leads to:

$$\mathbf{C}_{\mathbf{w}}^{MP} = \left[\Sigma_{fil}^{-1}\mathbf{U}^T\right]\mathbf{C}_{\mathbf{w}}\left[\Sigma_{fil}^{-1}\mathbf{U}^T\right]^T \tag{2.64}$$

$$\mathbf{C}_{R}^{MP} = \left[\Sigma\Sigma_{fil}^{-1}-\mathbf{I}\right]\mathbf{V}^T\mathbf{C}_{\varphi_\parallel}\mathbf{V}\left[\Sigma\Sigma_{fil}^{-1}-\mathbf{I}\right] \tag{2.65}$$

$$\mathbf{C}_{\varphi_\perp}^{MP} = \left[\Sigma_{fil}^{-1}\mathbf{U}^T\right]\left[\mathbf{H}_\perp\right]\mathbf{C}_{\varphi_\perp}\left[\mathbf{H}_\perp\right]^T\left[\Sigma_{fil}^{-1}\mathbf{U}^T\right]^T \quad . \tag{2.66}$$

Note that the diagonal of $\mathbf{C}_{R}^{MP}$ is equal to the diagonal of $\mathbf{C}_{\varphi_\parallel}^{MP}$ (eq. 2.53) for all truncated eigenmodes, and equal to zero for all the non-truncated ones. We can now also compute the different contributions to the global reconstruction error σ_{rec}^2 for the TLS reconstructor. Substituting equations 2.64 to 2.66 into equations 2.61 to 2.63 leads to:

$$\sigma_{\mathbf{w}}^2 = \text{trace}\left\{\left[\Sigma_{fil}^{-1}\mathbf{U}^T\right]\mathbf{C}_{\mathbf{w}}\left[\Sigma_{fil}^{-1}\mathbf{U}^T\right]^T\right\} \tag{2.67}$$

$$\sigma_{R}^2 = \text{trace}\left\{\left[\Sigma\Sigma_{fil}^{-1}-\mathbf{I}\right]\mathbf{V}^T\mathbf{C}_{\varphi_\parallel}\mathbf{V}\left[\Sigma\Sigma_{fil}^{-1}-\mathbf{I}\right]\right\} \tag{2.68}$$

$$\sigma_{\varphi_\perp}^2 = \text{trace}\left\{\left[\Sigma_{fil}^{-1}\mathbf{U}^T\right]\left[\mathbf{H}_\perp\right]\mathbf{C}_{\varphi_\perp}\left[\mathbf{H}_\perp\right]^T\left[\Sigma_{fil}^{-1}\mathbf{U}^T\right]^T\right\} \quad . \tag{2.69}$$

The contributions of $\sigma_{\mathbf{w}}^2$ and σ_{R}^2 to the global reconstruction error for the TLS reconstructor have been already studied by Fusco *et. al.* [45], but the contribution of $\sigma_{\varphi_\perp}^2$ has not been studied before. We will study this in the following section with an example.

2.4.4 Example case

Let us illustrate in this section with an example case the evaluation of the reconstruction error through the TLS reconstructor. We will consider once again that the turbulence volume comprises only two turbulent layers located at $h_1 = 0$ km and $h_2 = 8.5$ km in altitude. Also, we will consider a telescope whose diameter is $D = 8$ m without central occultation. Let us consider for this example a FoV of 2' ($\alpha_{max} = 60$ arcsec). Then, from equation 2.3, the diameters of the metapupils are $D_1 = 8$ m and $D_2 = 12.95$ m.

We will also consider for this example an MCAO system comprising three *idealized* WFSs coupled to natural guide stars located on the vertices of an equilateral triangle (figure 2.4(left)) inscribed in the 2' FoV.

The matrix H For the model of the approximate direct problem in this example, let us consider the first 10 radial orders for layer L_1 ($n^{L_1} = 10$). Then, according to eq. 2.14, $n^{L_2} = 16$. Also, according to eq. 2.13, $n^{L_1}_{mod} = 66$ and $n^{L_2}_{mod} = 153$. Hence, the total number of Zernike modes taken into account in the creation of $\mathbf{H}$ is:

$$n_{mod} = \sum_j \left(n^{L_j}_{mod} - 1 \right) = 65 + 152 = 217 \ , \tag{2.70}$$

which is of course also the size of the vector $\boldsymbol{\varphi}_{tur_\parallel} = [\boldsymbol{\varphi}^{L_1}_{tur_\parallel}; \boldsymbol{\varphi}^{L_2}_{tur_\parallel}]$ that we seek to estimate. Following equation 2.20, we will set each idealized WFS to measure up to Zernike number $p_{\alpha_k} = \max\{n^{L_1}_{mod}, n^{L_2}_{mod}\}$. Then, $p_{\alpha_k} = 153$ and the total number of Zernike coefficients measured by the three WFSs is 3x(153-1)=456. The size of the matrix $\mathbf{H}$ becomes 456x217, and it is shown in figure 2.11(b).

The matrix $\mathbf{H}_\perp$ The aliasing interaction matrix $\mathbf{H}_\perp$ has in principle an infinite number of columns associated with the Zernike modes number $n^{L_j}_{mod}+1$ to ∞. In order to evaluate analytically the quantities $\mathbf{C}^{MP}_{\varphi_\perp}$ (eq. 2.66) or $\sigma^2_{\varphi_\perp}$ (eq. 2.63) we will have to limit the number of Zernike modes representing *in full* each turbulent layer, so that we can compute a finite-dimensional $\mathbf{H}_\perp$ matrix. We will choose nevertheless a relatively large number of Zernike polynomials for each layer (with respect to the number of Zernikes taken into account in the creation of the matrix $\mathbf{H}$) in order to obtain a good representation of the subspace $\mathcal{M}^\perp_V$. Furthermore, as we will describe in section 2.4.6, the analytical results presented in this section will be shown to be in good agreement with the results obtained with numerical simulations in which a much larger range of higher spatial frequencies can be effectively taken into account in the evaluation of the propagated remaining error.

Continuing with our analytical approximation, we will limit in this example the number of Zernike modes to the first 16 radial orders (i.e. a total of 152 Zernikes) for layer L_1 and, still following equation 2.14, we will consider the first 26 radial orders (i.e. a total of 377 Zernikes) for layer L_2. Note that the turbulence volume phase space $\mathcal{E}_V$ —in principle infinite-dimensional— is now represented by only a total of $152 + 377 = 529$ Zernike modes. The matrix $\mathbf{DM}^L_\alpha$ in equation 2.11 for our example becomes a finite (456x529) matrix, and it is shown in figure 2.11(a).

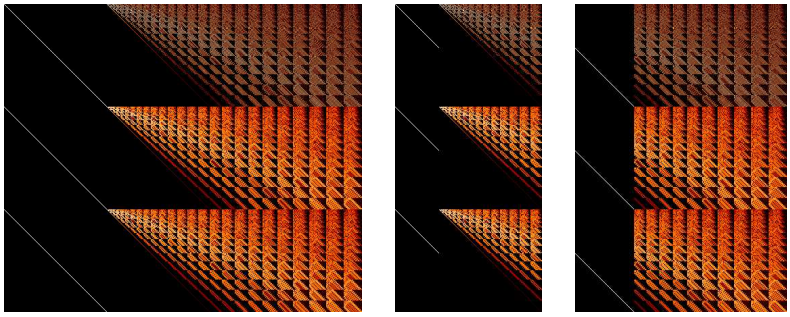

Figure 2.11: The matrices $\mathbf{DM}_{\alpha}^{L}$, $\mathbf{H}$, and $\mathbf{H}_{\perp}$ for the example case described in section 2.4.4. The sizes of these matrices are 456x529, 456x217 and 456x312 respectively.

We can now consider the creation of the matrix $\mathbf{H}_{\perp}$. The number of columns of $\mathbf{H}_{\perp}$ will be equal to $529-217 = 312$. This is the total number of Zernike modes representing the subspace $\mathcal{M}_{V}^{\perp}$. The size of the matrix $\mathbf{H}_{\perp}$ in this example becomes 456x312 and it is shown in figure 2.11(c).

The covariance matrices $\mathbf{C_w}$, $\mathbf{C}_{\varphi_\parallel}$ and $\mathbf{C}_{\varphi_\perp}$ The measurement noise covariance matrix $\mathbf{C_w}$ (eq. 2.49) is a 456x456 diagonal matrix containing the values of the noise variance on each Zernike coefficient. According to section 1.2.3.2, even if we are using the so-called *idealized* WFSs in our example, we can take into account the characteristic noise propagation of a realistic Shack-Hartmann WFS. In order to do this, the measurement noise variance propagated on each Zernike coefficient will be computed using equation 1.59, namely $\sigma_{Z_i}^2 = p_{m,n}\sigma_n^2$, where the value of σ_n^2 will be computed from equation 1.63 for a given *equivalent* SNR:

$$\sigma_n^2 = \frac{0.162\,(2\pi)^2}{\mathrm{SNR}} \left(\frac{D}{r_0}\right)^{5/3} \left(\frac{1}{n_s}\right)^{5/3} \quad . \tag{2.71}$$

It can be shown that an equivalent SH-WFS would require roughly 12x12 subapertures ($n_s = 12$) to be able to sample at Shannon on an 8m-telescope up to Zernike number 153. The noise covariance matrix $\mathbf{C_w}$ is then a diagonal matrix containing the values of $\sigma_{Z_i}^2$, and it depends on the chosen (D/r_0) ratio and the chosen SNR.

The covariance matrices $\mathbf{C}_{\varphi_\parallel}$ (eq. 2.50) and $\mathbf{C}_{\varphi_\perp}$ (eq. 2.51) are 217x217 and 312x312 block-diagonal matrices, respectively, whose elements can be computed from equation 1.34 for Kolomogorov turbulence. These matrices also depend on the chosen (D/r_0) ratio.

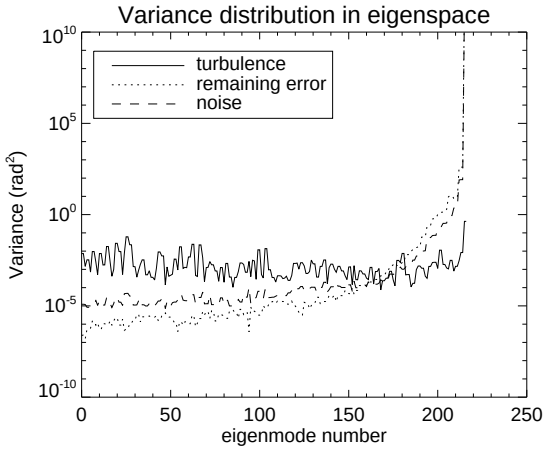

Figure 2.12: Example of variance distribution in the eigenspace after propagation through the TLS reconstructor for the MCAO example described in section 2.4.4. The turbulence (diagonal of $\mathbf{C}_{\varphi_\parallel}^{MP}$), the remaining error (diagonal of $\mathbf{C}_{\varphi_\perp}^{MP}$), and the noise (diagonal of $\mathbf{C}_{\mathbf{w}}^{MP}$) are all shown. The turbulence strength is $D/r_0 = 1$ and SNR $= 10$.

Variance distribution in eigenspace We have now all ingredients to compute the covariance matrices $\mathbf{C}_{\varphi_\parallel}^{MP}$ (eq. 2.53), $\mathbf{C}_{\mathbf{w}}^{MP}$ (eq. 2.64), $\mathbf{C}_{R}^{MP}$ (eq. 2.65), and $\mathbf{C}_{\varphi_\perp}^{MP}$ (eq. 2.66). Recall from section 2.4.1 that the diagonals of these covariance matrices represent the *variance distribution in the eigenspace* of the turbulence, the measurement noise, the error related to the reconstruction matrix, and the remaining error respectively, after propagation through the TLS reconstructor.

Let us consider in our current example a normalized value of $(D/r_0) = 1$ and a SNR $= 10$. Figure 2.12 shows the corresponding variance distribution in the eigenspace. No eigenmodes were filtered out in the matrix Σ_{fil}^{-1} in order to visualize the magnitude of the propagation of the errors onto all the eigenmodes. Note that the diagonal of $\mathbf{C}_{R}^{MP}$ is in this case equal to zero, so it is not displayed in figure 2.12. As was already discussed in reference [45], the turbulence variance is rather equally distributed among the eigenmodes, and the measurement noise propagates strongly on the last eigenmodes –the ones associated with low eigenvalues. What is new from this plot is the fact that the propagated remaining error follows a similar pattern of the measurement noise. As we will discuss in chapter 3, this will have important implications on the implementation of modal gain optimization for MCAO.

Optimal threshold Let us compute the optimal number of truncated modes and the associated optimal threshold Λ_{opt} for this example. Figure 2.13(left) shows the

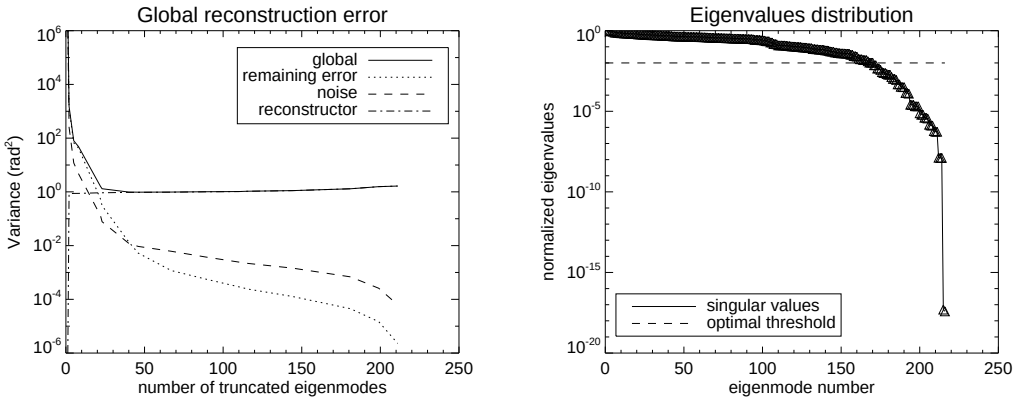

Figure 2.13: (*Left*) Evolution of the global error σ^2_{rec} as a function of the total number of truncated eigenmodes for the MCAO example described in section 2.4.4. The different contributions are also shown: the remaining error $\sigma^2_{\varphi_\perp}$, the measurement noise $\sigma^2_{\mathbf{w}}$, and the reconstructor error σ^2_R. (*Right*) Normalized eigenvalues and optimal threshold for this MCAO configuration. The last 50 eigenmodes need to be truncated.

evolution of the global reconstruction error σ^2_{rec} as a function of the total number of truncated eigenmodes. The three contributions to the global error: $\sigma^2_{\mathbf{w}}$, σ^2_R, and $\sigma^2_{\varphi_\perp}$ are also shown. When no eigenmodes are truncated $\sigma^2_{\varphi_\perp}$ and $\sigma^2_{\mathbf{w}} \to \infty$ and $\sigma^2_R = 0$. Just after a few modes are truncated both $\sigma^2_{\varphi_\perp}$ and $\sigma^2_{\mathbf{w}}$ drop steeply, and σ^2_R increases rather smoothly. The optimal number of truncated modes is 50 and the minimum global reconstruction error is $\sigma^2_{rec} = 0.98\,\text{rad}^2$. The plot on figure 2.13(right) shows the distribution of normalized eigenvalues $\lambda_i/\lambda_{\max}$ for this example. The optimal threshold is $\Lambda_{opt} \approx 10^{-2}$, and it is also indicated in this plot. For this particular case, the last 50 eigenmodes that lie below this threshold are the ones that need to be truncated.

2.4.5 Field-of-view dependence

In section 2.3.2.2 we showed that the proportion of eigenmodes with low eigenvalues increased with the FoV. Let us now study the field-of-view dependence of the contributions to the global reconstruction error σ^2_{rec} (eq. 2.60). Recall that the different contributions are: the measurement noise $\sigma^2_{\mathbf{w}}$ (eq. 2.67), the reconstructor error σ^2_R (eq. 2.68), and the remaining error $\sigma^2_{\varphi_\perp}$ (eq. 2.69). We will consider the same MCAO configuration and turbulence model presented in section 2.4.4.

Regarding the number of modes to be considered in this study, we will consider once again that the turbulence volume phase space $\mathcal{E}_V$ is approximated by a total of 529 Zernike modes (152 for L_1 and 377 for L_2). Hence, the matrix $\mathbf{DM}^L_\alpha$ shown in

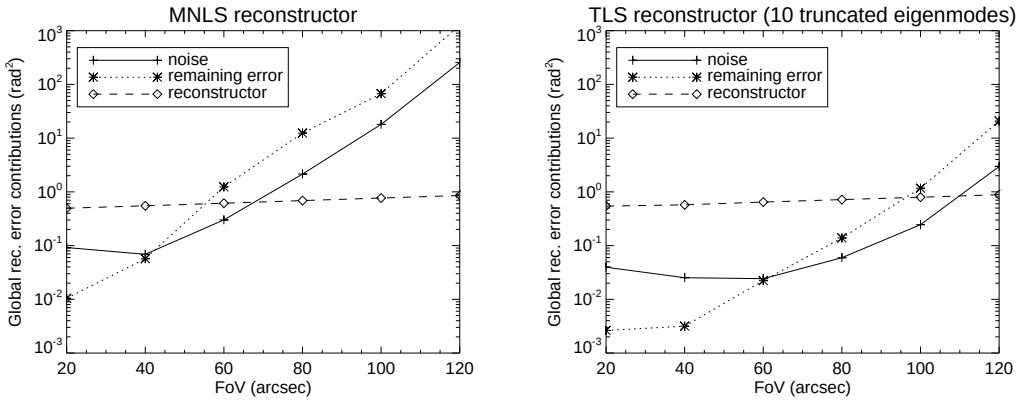

Figure 2.14: Contributions to the global reconstruction error σ^2_{rec} as a function of the FoV. The different contributions are: the remaining error $\sigma^2_{\varphi_\perp}$, the measurement noise $\sigma^2_{\mathbf{w}}$, and the reconstructor error σ^2_R. The errors are computed after propagation through: (*Left*) the MNLS reconstructor (i.e. only 2 truncated eigenmodes). (*Right*) the TLS reconstructor with 10 truncated eigenmodes. The turbulence strength is $D/r_0 = 1$ and SNR = 10.

figure 2.11(a) is still valid for our current study. For the creation of the matrix $\mathbf{H}$, we will consider once again $n^{L_1} = 10$ (i.e. a total of 65 Zernikes for L_1), but we will scale n^{L_2} as a function of the FoV as it was done in section 2.3.2.2. Therefore, the size of the matrices $\mathbf{H}$ and $\mathbf{H}_\perp$ will vary with the considered FoV. Recall that, as explained in section 2.2.3, we proceed in this way in order to keep constant the maximum spatial frequency taken into account in the model of the approximate direct problem for all considered FoVs.

Figure 2.14 shows the evolution of $\sigma^2_{\mathbf{w}}$, σ^2_R, and $\sigma^2_{\varphi_\perp}$ with respect to the considered FoV. Two reconstruction matrices have been considered. Figure 2.14(left) shows the error variances after the propagation through the MNLS reconstructor (i.e. only 2 eigenmodes filtered out corresponding to tip-tilt combinations), and figure 2.14(right) shows the errors after propagation through the TLS reconstructor with 10 eigenmodes filtered out in Σ^{-1}_{fil}. From these plots we can make the following remarks:

- The terms $\sigma^2_{\mathbf{w}}$, σ^2_R, and $\sigma^2_{\varphi_\perp}$ tend to increase as the FoV increases. Note that σ^2_R increases only slightly with the FoV, whereas $\sigma^2_{\mathbf{w}}$ and $\sigma^2_{\varphi_\perp}$ increase substantially (by several orders of magnitude) with the FoV, in particular beyond the 1' FoV.

- Increasing the number of truncated modes (in this case from 2 to 10) helps reduce the absolute values of $\sigma^2_{\mathbf{w}}$ and $\sigma^2_{\varphi_\perp}$, and an optimal number of truncated

modes could be determined for each FoV. Note that when the curves of $\sigma^2_{\mathbf{w}}$ and $\sigma^2_{\varphi_\perp}$ are above the σ^2_R curve means that the performance will be limited by the propagated errors, whereas when the σ^2_R curve is above the other two means that the performance will be limited by the uncompensated turbulence. For instance, note that when only 10 eigenmodes are filtered out (figure 2.14(right)), and when FoV=2', the performance is limited by the propagated errors. More eigenmodes would need to be filtered out and, as we determined in the previous section (see figure 2.13), the optimal number of truncated modes for a FoV=2' turned out to be 50.

2.4.6 Propagation of remaining error: numerical validation

In this section we will validate our analytical model of the propagation of the remaining error —i.e. the diagonal of $\mathbf{C}^{MP}_{\varphi_\perp}$ (equation 2.66)— with numerical simulations in which a much larger range of higher spatial frequencies will be effectively taken into account.

Recall that the analytical computation of $\mathbf{C}^{MP}_{\varphi_\perp}$ involves an approximation of the matrix $\mathbf{H}_\perp$, which in theory should be infinitely large in order to take into account the effect of all the (high-order) turbulent modes that generate the subspace $\mathcal{M}^\perp_V$. The numerical validation will be based on the comparison of the statistics of the turbulence vector estimate, $\hat{\boldsymbol{\varphi}}_{tur}$, obtained from both analytical and simulation results, as we will describe below.

Expected analytical result. Let us compute an analytical expression for the covariance matrix of the turbulence vector estimate in the eigenspace. Let us denote the turbulence vector estimate in the eigenspace as $\hat{\boldsymbol{\varphi}}^{MP}_{tur}$. Then, from equations 2.45 and 2.43, it is straightforward to show that $\hat{\boldsymbol{\varphi}}^{MP}_{tur}$ can be expressed as:

$$\hat{\boldsymbol{\varphi}}^{MP}_{tur} = \left[\Sigma^{-1}_{fil}\mathbf{U}^T\right]\left(\mathbf{H}\boldsymbol{\varphi}_{tur_\parallel} + \mathbf{H}_\perp\boldsymbol{\varphi}_{tur_\perp} + \mathbf{w}\right) \quad . \tag{2.72}$$

Similarly to the procedure followed in section 2.4.3 to compute the covariance matrix of the reconstruction error in the eigenspace, $\mathbf{C}^{MP}_{\boldsymbol{\epsilon}}$, it can be shown that the covariance matrix of the turbulence vector estimate in the eigenspace —denoted as $\mathbf{C}^{MP}_{\hat{\boldsymbol{\varphi}}}$— is given by:

$$\mathbf{C}^{MP}_{\hat{\boldsymbol{\varphi}}} = \mathbf{C}^{MP}_{\mathbf{w}} + \left[\Sigma\Sigma^{-1}_{fil}\right]\mathbf{C}^{MP}_{\varphi_\parallel}\left[\Sigma\Sigma^{-1}_{fil}\right] + \mathbf{C}^{MP}_{\varphi_\perp} \quad , \tag{2.73}$$

where $\mathbf{C}^{MP}_{\varphi_\parallel}$ is given by equation 2.53, $\mathbf{C}^{MP}_{\mathbf{w}}$ by equation 2.64, and $\mathbf{C}^{MP}_{\varphi_\perp}$ by equation 2.66. Since we are interested in this study in the propagated remaining error, we will not consider the covariance matrix of the measurement noise $\mathbf{C}^{MP}_{\mathbf{w}}$. Also, we will not filter

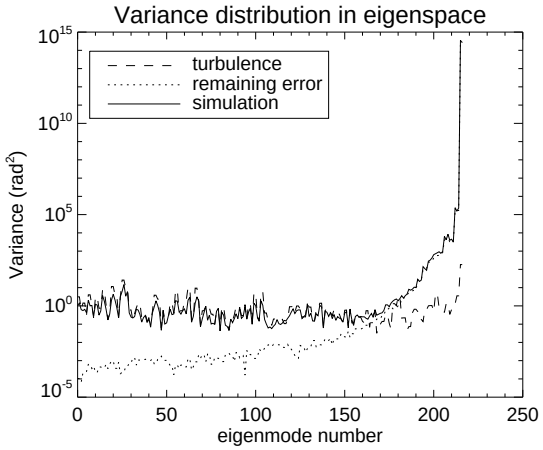

Figure 2.15: Numerical validation of the propagation of the remaining error through the TLS reconstructor. Analytical curves: (- - -) diag$\{\mathbf{C}_{\varphi_\parallel}^{MP}\}$, $(\cdots)$ diag$\{\mathbf{C}_{\varphi_\perp}^{MP}\}$. Simulation curve: (—) diag$\{\mathbf{C}_{\hat{\varphi}}^{MP}\}$.

out any eigenmodes (i.e. $\Sigma_{fil}^{-1} = \Sigma^{-1}$) in order to be able to study the statistics of all of them. Then, the diagonal of $\mathbf{C}_{\hat{\varphi}}^{MP}$ can be simply expressed as:

$$\text{diag}\{\mathbf{C}_{\hat{\varphi}}^{MP}\} = \text{diag}\{\mathbf{C}_{\varphi_\parallel}^{MP}\} + \text{diag}\{\mathbf{C}_{\varphi_\perp}^{MP}\} \ . \tag{2.74}$$

We will consider in this study once again the MCAO configuration and the 2-layer turbulence model of the example case presented in section 2.4.4. The diagonals of $\mathbf{C}_{\varphi_\parallel}^{MP}$ and $\mathbf{C}_{\varphi_\perp}^{MP}$ for this configuration were actually shown in figure 2.12 for a normalized turbulence strength of $D/r_0 = 1$. We will consider in this study a turbulence strength of $D/r_0 = 38$ @ 700 nm and the corresponding diagonals of $\mathbf{C}_{\varphi_\parallel}^{MP}$ and $\mathbf{C}_{\varphi_\perp}^{MP}$ are shown in figure 2.15.

Simulation results. The goal of the simulation is to compute the covariance matrix of $\hat{\boldsymbol{\varphi}}_{tur}^{MP}$ and verify that simulation results follow the analytical result of equation 2.74.

The simulation follows the block diagram presented in figure 2.1. The turbulence is simulated with two phase screens equally weighted and positioned at 0 and 8.5 km giving a turbulence strength of $D/r_0 = 38$ @ 700 nm in the telescope pupil. It is important to emphasize that the simulation of the atmospheric turbulence using phase screens (section 1.1.7) effectively takes into account a considerably larger range of spatial frequencies than the ones considered in the analytical formulation.

At each iteration, the resultant turbulent phase in the telescope pupil for the three GS directions $\{\boldsymbol{\alpha}_k\}$ is measured by *idealized* WFSs each one projecting the phase onto the first 153 Zernikes. No measurement noise is added to these vectors ($\mathbf{w} = \vec{0}$). The concatenation of these vectors forms the 456-element measurement vector $\mathbf{s}$. Finally, the turbulence vector estimate $\hat{\boldsymbol{\varphi}}_{tur}^{MP}$ is computed as:

$$\hat{\boldsymbol{\varphi}}_{tur}^{MP} = \left[\Sigma^{-1}\mathbf{U}^T\right]\mathbf{s} \ . \tag{2.75}$$

A total of 1024 iterations were performed and the covariance matrix of $\hat{\boldsymbol{\varphi}}_{tur}^{MP}$ was computed as:

$$\mathbf{C}_{\hat{\varphi}}^{MP} = \left\langle \hat{\boldsymbol{\varphi}}_{tur}^{MP} \left(\hat{\boldsymbol{\varphi}}_{tur}^{MP}\right)^T \right\rangle \ . \tag{2.76}$$

The diagonal of $\mathbf{C}_{\hat{\varphi}}^{MP}$ is shown in figure 2.15. As can be seen from this plot, the diagonal of $\mathbf{C}_{\hat{\varphi}}^{MP}$ effectively follows the expected analytical result of equation 2.74. That is, for the first eigenmodes (associated with high sensitivities) the diagonal of $\mathbf{C}_{\hat{\varphi}}^{MP}$ follows the diagonal of $\mathbf{C}_{\varphi_\parallel}^{MP}$, which is the dominant term in equation 2.74 for the first eigenmodes. On the other hand, for the last eigenmodes (the badly- and unseen-modes) the diagonal of $\mathbf{C}_{\hat{\varphi}}^{MP}$ follows the diagonal of $\mathbf{C}_{\varphi_\perp}^{MP}$, which is the dominant term in equation 2.74 for the last eigenmodes. These results validate our approximate analytical model of the propagation of the remaining error.

2.5 Statistical estimation method

In the previous sections we have limited our discussion of wavefront reconstruction to the methods based on the least-squares approach. The least-squares estimation method minimizes a deterministic criterion (equation 2.30). The quantity to be estimated, $\hat{\boldsymbol{\varphi}}_{tur}$, is considered to be *fixed* for a given measurement vector $\mathbf{s}$. However, we know that the turbulent phase —and the WFS measurement noise $\mathbf{w}$— are actually random variables with known statistics (Chapter 1). Statistical estimation methods can then be used to take advantage of this prior knowledge to *regularize* the inverse problem and improve the solution [10, Ch.13].

In the least-squares approach, the reconstruction matrix is derived by minimizing a fit-to-data criterion (equation 2.30). In the statistical approach, it is possible to derive a reconstruction matrix that minimizes directly the performance metric of interest. In MCAO, one performance metric of interest was defined in section 2.4.2: the global reconstruction error σ_{rec}^2. Then, from equations 2.59 and 2.28, the minimization criterion

can be expressed as:

$$\begin{aligned} J_{tomo} &\triangleq \left\langle \left\| \hat{\boldsymbol{\varphi}}_{tur} - \boldsymbol{\varphi}_{tur_{\parallel}} \right\|^2 \right\rangle \\ &= \left\langle \left\| \mathbf{R}\mathbf{s} - \boldsymbol{\varphi}_{tur_{\parallel}} \right\|^2 \right\rangle \ . \end{aligned} \tag{2.77}$$

This criterion in MCAO is known as the *tomographic* criterion because the minimization of J_{tomo} is equivalent to the minimization of the mean-square error —or residual variance— on *each* turbulence layer. Finally, minimizing J_{tomo} with respect to $\mathbf{R}$ leads to the general expression for the *minimum-mean-square error* (MMSE) reconstruction matrix:

$$\mathbf{R}_{MMSE} = \langle \boldsymbol{\varphi}_{tur_{\parallel}} \mathbf{s}^T \rangle \langle \mathbf{s}\mathbf{s}^T \rangle \ , \tag{2.78}$$

where $\langle \boldsymbol{\varphi}_{tur_{\parallel}} \mathbf{s}^T \rangle$ stands for the covariance matrix between the turbulence phase and the WFSs measurements, and $\langle \mathbf{s}\mathbf{s}^T \rangle$ denotes the covariance matrix of the WFSs measurements. In order to find an explicit expression for $\mathbf{R}_{MMSE}$ we need to introduce in equation 2.78 the model of the direct problem which, in our case, is given by equation 2.25, namely: $\mathbf{s} = \mathbf{H}\boldsymbol{\varphi}_{tur_{\parallel}} + \mathbf{H}_{\perp}\boldsymbol{\varphi}_{tur_{\perp}} + \mathbf{w}$. However, the well-known expression for $\mathbf{R}_{MMSE}$ found in the literature is actually derived by considering that the direct problem model is approximated by:

$$\mathbf{s} \approx \mathbf{H}\boldsymbol{\varphi}_{tur_{\parallel}} + \mathbf{w} \ . \tag{2.79}$$

That is, the term $\mathbf{H}_{\perp}\boldsymbol{\varphi}_{tur_{\perp}}$ has not been taken into account. Substituting equation 2.79 into 2.78, and assuming that the turbulence phase vector $\boldsymbol{\varphi}_{tur_{\parallel}}$ and the WFSs measurement noise vector $\mathbf{w}$ are uncorrelated, leads to the well-known expressions for the MMSE reconstructor:

$$\mathbf{R}_{MMSE} = \left[\mathbf{H}^T \mathbf{C}_{\mathbf{w}}^{-1} \mathbf{H} + \mathbf{C}_{\varphi_{\parallel}}^{-1} \right]^{-1} \mathbf{H}^T \mathbf{C}_{\mathbf{w}}^{-1} \tag{2.80}$$

$$= \mathbf{C}_{\varphi_{\parallel}} \mathbf{H}^T \left[\mathbf{H}\mathbf{C}_{\varphi_{\parallel}} \mathbf{H}^T + \mathbf{C}_{\mathbf{w}} \right]^{-1} \ , \tag{2.81}$$

where $\mathbf{C}_{\mathbf{w}}$ is the measurement noise covariance matrix (equation 2.49), and $\mathbf{C}_{\varphi_{\parallel}}$ is the covariance matrix of the turbulence vector $\boldsymbol{\varphi}_{tur_{\parallel}}$ (equation 2.50).

The MMSE reconstructor is also known as the *maximum a-posteriori* (MAP) reconstructor because —assuming Gaussian statistics for both the turbulent phase and the measurement noise— it is also possible to derive the same expression following a Bayesian approach that maximizes $p\left(\boldsymbol{\varphi}_{tur_{\parallel}} \mid \mathbf{s}\right)$, that is, the a-posteriori probability on

$\boldsymbol{\varphi}_{tur_{\parallel}}$ given the set of measurements $\mathbf{s}$ [43].

The MMSE reconstructor has been widely studied for the general problem of phase estimation from WFS measurements [128]. Johnston and Welsh [69] introduced the MMSE reconstructor for the case of MCAO. Fusco *et. al.* [42, 45] widely studied the advantages of the MMSE reconstructor in MCAO and demonstrated with numerical simulations the gain in performance brought by this reconstructor with respect to the TLS reconstructor. In the following sections we will complement these previous studies by studying the propagation of the remaining error through the MMSE reconstructor.

2.5.1 Evaluation of the improvement in conditioning

Let us first of all evaluate the improvement in conditioning brought by the MMSE reconstructor. The condition number of $\mathbf{H}$ was defined in equation 2.40 as the product of the spectral norms of $\mathbf{H}$ and $\mathbf{R}_{MNLS}$. In order to evaluate the improvement in conditioning brought by other reconstructors, we can propose a generalization of the definition of the condition number for *any* reconstruction matrix as:

$$\text{cond}\,(\mathbf{H},\mathbf{R}) \triangleq \|\mathbf{H}\|\|\mathbf{R}\| \ , \tag{2.82}$$

where the norms $\|\mathbf{H}\|$ and $\|\mathbf{R}\|$ are simply computed as the maximum singular values of $\mathbf{H}$ and $\mathbf{R}$ respectively. Then, for the case of the MMSE reconstructor, the condition number becomes:

$$\text{cond}\,(\mathbf{H},\mathbf{R}_{MMSE}) = \|\mathbf{H}\|\|\mathbf{R}_{MMSE}\| \ . \tag{2.83}$$

In section 2.3.2.2 we studied the evolution of the condition number of $\mathbf{H}$ as a function of the FoV for the case of the TLS reconstructor, and the results for a 3-GS configuration were presented in figure 2.8. Figure 2.16 shows how $\text{cond}\,(\mathbf{H},\mathbf{R}_{MMSE})$ for the same 3-GS configuration evolves with the FoV when using the MMSE reconstructor. We have used the same system parameters and made the same considerations in order to compare directly figures 2.8 and 2.16. Note that $\text{cond}\,(\mathbf{H},\mathbf{R}_{MMSE})$ increases slightly with the FoV and with the number of estimated modes, but in any case it remains of the same order of magnitude. Let us compare, for instance, the extreme case where $\{n^{L_1}, \text{FoV}\} = \{16, 120''\}$. Note from figure 2.8 that the condition number of $\mathbf{H}$ is $\text{cond}(\mathbf{H}) \approx 10^8$. Using the MMSE reconstructor brings the conditioning down to $\text{cond}\,(\mathbf{H},\mathbf{R}_{MMSE}) \approx 10^1$. Clearly, the improvement in conditioning brought by the regularized approach is very important and, in consequence, there is no longer need to restrict the number of estimated modes in order to improve the stability of the solution, as it was required in the least-squares approach (section 2.3.2.2). Of course, in practice it is always required

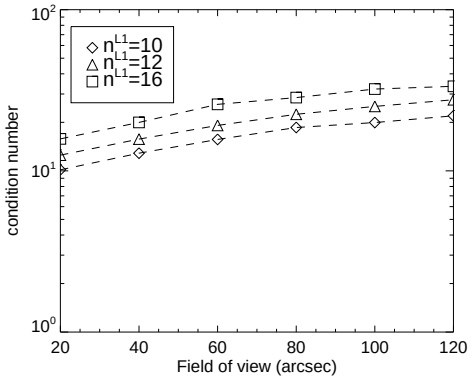

Figure 2.16: Evolution of cond $(\mathbf{H}, \mathbf{R}_{MMSE})$ as a function of the considered FoV and the selected number of Zernike coefficients (expressed in terms of n^{L_1}). The MCAO reconstruction problem in question is to estimate 2 turbulent layers at 0 and 8.5 km using 3 wavefront sensing directions in an equilateral triangle configuration (figure 2.4).

to consider a finite number of estimated modes, but with the statistical approach the number of estimated modes can be very large and can even exceed the number of available measurements. Note that considering a larger number of estimated modes has the advantage of effectively reducing the number of higher-order spatial modes that contribute to the remaining error.

2.5.2 Reconstruction error for the MMSE reconstructor

In section 2.4.3 we derived the covariance matrices in the eigenspace of the contributions to the reconstruction error for the TLS reconstructor. In this section we will derive similar expressions for the case of the MMSE reconstructor. Let us denote as $\mathcal{C}_{\mathbf{w}}^{MP}$, $\mathcal{C}_{R}^{MP}$, and $\mathcal{C}_{\varphi_\perp}^{MP}$ the covariance matrices of the measurement noise, the error related to the reconstruction matrix, and the remaining error in the eigenspace after propagation through the MMSE reconstructor. Then, from equations 2.56, 2.57, and 2.58:

$$\mathcal{C}_{\mathbf{w}}^{MP} = \mathbf{V}^T \mathbf{R}_{MMSE} \mathbf{C}_{\mathbf{w}} \mathbf{R}_{MMSE}^T \mathbf{V} \tag{2.84}$$

$$\mathcal{C}_{R}^{MP} = \mathbf{V}^T \left[\mathbf{R}_{MMSE}\mathbf{H} - \mathbf{I}\right] \mathbf{C}_{\varphi_\parallel} \left[\mathbf{R}_{MMSE}\mathbf{H} - \mathbf{I}\right]^T \mathbf{V} \tag{2.85}$$

$$\mathcal{C}_{\varphi_\perp}^{MP} = \mathbf{V}^T \mathbf{R}_{MMSE} \left[\mathbf{H}_\perp\right] \mathbf{C}_{\varphi_\perp} \left[\mathbf{H}_\perp\right]^T \mathbf{R}_{MMSE}^T \mathbf{V} \ . \tag{2.86}$$

Let us now study the *variance distribution in the eigenspace* after propagation through the MMSE reconstructor. Recall that the variance distribution in the eigenspace after

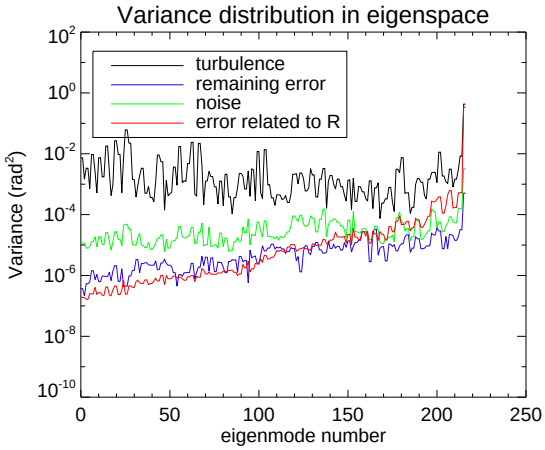

Figure 2.17: Example of the variance distribution in the eigenspace after propagation through the MMSE reconstructor. The turbulence (diagonal of $\mathbf{C}_{\varphi_\parallel}^{MP}$), the remaining error (diagonal of $\mathcal{C}_{\varphi_\perp}^{MP}$), the error related to $\mathbf{R}$ (diagonal of $\mathcal{C}_{R}^{MP}$), and the noise (diagonal of $\mathcal{C}_{\mathbf{w}}^{MP}$) are shown. Summary of relevant parameters: FoV=2', number of estimated modes: $n^{L_1} = 10$ and $n^{L_2} = 16$; turbulence strength: $D/r_0 = 1$, SNR=10.

propagation through the TLS reconstructor was given by the diagonals of the covariance matrices $\mathbf{C}_{\varphi_\parallel}^{MP}$ (eq. 2.53), $\mathbf{C}_{\mathbf{w}}^{MP}$ (eq. 2.64), $\mathbf{C}_{R}^{MP}$ (eq. 2.65), and $\mathbf{C}_{\varphi_\perp}^{MP}$ (eq. 2.66).

For comparison purposes, let us consider once again the example case presented in section 2.4.4. The diagonals of $\mathbf{C}_{\varphi_\parallel}^{MP}$ (eq. 2.53), $\mathcal{C}_{\mathbf{w}}^{MP}$ (eq. 2.84), $\mathcal{C}_{R}^{MP}$ (eq. 2.85), and $\mathcal{C}_{\varphi_\perp}^{MP}$ (eq. 2.86) are shown in figure 2.17 for a turbulence strength of $D/r_0 = 1$, and a SNR=10. The matrices $\mathbf{C}_{\mathbf{w}}$ and $\mathbf{C}_{\varphi_\parallel}$ required to generate $\mathbf{R}_{MMSE}$ (eq. 2.80) have been computed for the same turbulence strength and SNR.

By comparing figures 2.12 and 2.17 we can evidence the substantial reduction in the propagation of both the measurement noise and the remaining error when using the MMSE reconstructor, in particular for the badly- and the unseen-modes for which the variances are always lower than the turbulence level. On the other hand, note that the error related to the reconstruction matrix (diagonal of $\mathcal{C}_{R}^{MP}$) is not equal to zero for any of the eigenmodes. This contrasts with the case of the TLS reconstructor, for which the diagonal of $\mathbf{C}_{R}^{MP}$ (eq. 2.65) was equal to zero for all eigenmodes except for the truncated ones.

In conclusion, the MMSE reconstructor manages to keep down the propagation of the measurement noise and the remaining error thanks to the statistical priors used to regularize the reconstruction process. On the other hand, the MMSE reconstructor introduces an error (i.e. the error related to the reconstruction matrix) due to the

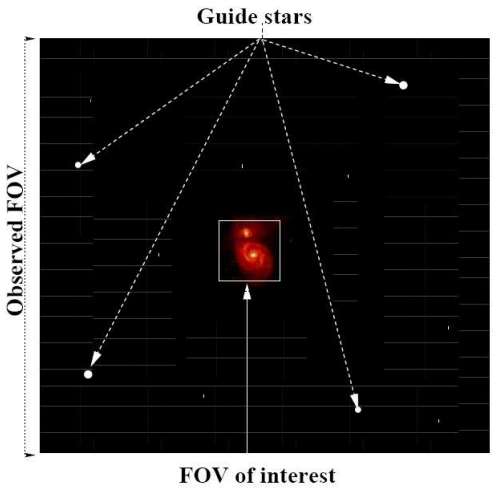

Figure 2.18: Illustration of the FoV of interest $\{\boldsymbol{\beta}_m\}$ where the MCAO correction should be optimized. In this case $\{\boldsymbol{\beta}_m\}$ corresponds to the center of the FoV where the object of interest is located (Courtesy: Jean-Marc Conan).

fact that $\mathbf{R}_{MMSE}\mathbf{H} \neq \mathbf{I}$ in equation 2.85. However, the global reconstruction error $\sigma^2_{rec} = \sigma^2_{\mathbf{w}} + \sigma^2_R + \sigma^2_{\varphi_\perp}$ for the MMSE reconstructor is always smaller than the σ^2_{rec} for the TLS reconstructor. Indeed, for this example, the σ^2_{rec} for the MMSE reconstructor is $\sigma^2_{rec} = 0.71\,\text{rad}^2$ and —as determined in section 2.4.4— the minimum σ^2_{rec} for the TLS reconstructor (i.e. when using the optimal threshold Λ_{opt}) is equal to $\sigma^2_{rec} = 0.98\,\text{rad}^2$.

2.6 Minimum-variance reconstructor

In the previous sections we have studied the problem of wavefront reconstruction in MCAO. That is, the problem of estimating the phase perturbations introduced by N_L turbulence layers. Once the turbulence volume $\boldsymbol{\varphi}_{tur_\parallel}$ has been estimated, the next step is to compensate for it by means of N_{DM} deformable mirrors ($l = \{1 \dots N_{DM}\}$) conjugated at different altitudes, as depicted in figure 2.2. Note that in the general case: $N_L > N_{DM}$. Also, the directions where we would like to optimize the performance — denoted as $\{\boldsymbol{\beta}_m\}$— may not coincide with the directions of the guide stars $\{\boldsymbol{\alpha}_k\}$, as shown in figure 2.18.

T. Fusco *et. al.* [47] derived a reconstruction matrix —known as the *minimum-variance* (MV) reconstructor— that optimizes the performance in the FoV of interest taking into account the finite number of DMs in an MCAO system. The minimization

criterion from which the MV reconstructor is derived, is defined as the residual variance in the telescope pupil for the FoV of interest $\{\boldsymbol{\beta}_m\}$, and it can be expressed as:

$$\sigma_{\beta}^2 = \left\langle \int_{\{\boldsymbol{\beta}_m\}} \int_A \left[\hat{\phi}(\mathbf{r},\boldsymbol{\beta}) - \phi(\mathbf{r},\boldsymbol{\beta})\right]^2 d\mathbf{r}\, d\boldsymbol{\beta} \right\rangle \tag{2.87}$$

where $\phi(\mathbf{r},\boldsymbol{\beta})$ is the resultant phase in the telescope pupil for direction $\boldsymbol{\beta}$, $\int_A$ is an integral over the telescope pupil, $\int_{\{\boldsymbol{\beta}_m\}}$ is an integral over the FoV of interest, and $\langle\cdot\rangle$ denotes an ensemble average. Equation 2.87 can be also expressed in matrix form as [47]:

$$\sigma_{\beta}^2 = \left\langle \int_{\{\boldsymbol{\beta}_m\}} \left\| \mathbf{M}_{\beta}^{DM}\boldsymbol{\varphi}_{cor} - \mathbf{M}_{\beta}^{L}\boldsymbol{\varphi}_{tur_{\parallel}} \right\|^2 d\boldsymbol{\beta} \right\rangle \tag{2.88}$$

where the matrices $\mathbf{M}_{\beta}^{L}$ and $\mathbf{M}_{\beta}^{DM}$ can be easily interpreted from equation 2.7. They perform the sum of the footprints in the N_{L} turbulence layers and the N_{DM} DMs metapupils, respectively, for all the directions $\{\boldsymbol{\beta}_m\}$. The vector $\boldsymbol{\varphi}_{tur}$ was defined in equation 2.4, and $\boldsymbol{\varphi}_{cor}$ is defined as a column vector containing the Zernike coefficients of *all* the N_{DM} correction phases:

$$\boldsymbol{\varphi}_{cor} = [\boldsymbol{\varphi}_{cor,1}; \cdots; \boldsymbol{\varphi}_{cor,l}; \cdots; \boldsymbol{\varphi}_{cor,N_{DM}}] \ . \tag{2.89}$$

The correction phase vector $\boldsymbol{\varphi}_{cor}$ is generated by applying to the DMs a command vector $\mathbf{u}$, defined as:

$$\mathbf{u} = [\mathbf{u}_1; \cdots; \mathbf{u}_l; \cdots; \mathbf{u}_{N_{DM}}] \ . \tag{2.90}$$

According to the DM linear model presented in section 1.2.1.1, the relationship between $\boldsymbol{\varphi}_{cor}$ and $\mathbf{u}$ can be expressed as:

$$\boldsymbol{\varphi}_{cor} = \mathbf{N}\mathbf{u} \ , \tag{2.91}$$

where $\mathbf{N}$ is a block-diagonal matrix containing all the N_{DM} influence matrices of the DMs. Note that in this context the columns of the influence matrix $\mathbf{N}_l$ contain the influence functions expressed in terms of their expansion in Zernike coefficients. The command vector $\mathbf{u}$ that drives the DMs must be generated from the WFSs measurements $\mathbf{s}$ by means of a reconstruction matrix $\mathbf{R}_{MV}$:

$$\mathbf{u} = \mathbf{R}_{MV}\mathbf{s} \ , \tag{2.92}$$

and it is the expression for this reconstruction matrix that we seek. Substituting

equations 2.91, 2.92, and 2.11 into 2.88 leads to:

$$\sigma_{\beta}^{2} = \left\langle \int_{\{\boldsymbol{\beta}_m\}} \left\| \mathbf{M}_{\beta}^{DM} \mathbf{N} \mathbf{R}_{MV} [\mathbf{H}\boldsymbol{\varphi}_{tur_{\parallel}} + \mathbf{w}] - \mathbf{M}_{\beta}^{L} \boldsymbol{\varphi}_{tur_{\parallel}} \right\|^{2} d\boldsymbol{\beta} \right\rangle \quad . \tag{2.93}$$

Finally, minimizing σ_{β}^{2} with respect to $\mathbf{R}_{MV}$ leads to the expression for the MV reconstruction matrix [47]:

$$\mathbf{R}_{MV} \quad = \quad \mathbf{P}_{DM}^{L} \mathbf{C}_{\varphi_{\parallel}} \mathbf{H}^{T} \left[\mathbf{H} \mathbf{C}_{\varphi_{\parallel}} \mathbf{H}^{T} + \mathbf{C}_{\mathbf{w}} \right]^{-1} \quad , \tag{2.94}$$

where the matrix $\mathbf{P}_{DM}^{L}$ is given by:

$$\mathbf{P}_{DM}^{L} = \left[\int_{\{\boldsymbol{\beta}_m\}} \left(\mathbf{M}_{\beta}^{DM} \mathbf{N} \right)^{T} \mathbf{M}_{\beta}^{DM} \mathbf{N} \; d\boldsymbol{\beta} \right]^{\dagger} \left[\int_{\{\boldsymbol{\beta}_m\}} \left(\mathbf{M}_{\beta}^{DM} \mathbf{N} \right)^{T} \mathbf{M}_{\beta}^{L} \; d\boldsymbol{\beta} \right] \quad . \tag{2.95}$$

The matrix $\mathbf{P}_{DM}^{L}$ is a projection matrix that weights and projects the whole turbulent volume (N_{L} layers) onto the N_{DM} deformable mirrors optimizing the correction in the FoV of interest. Finally, note from equation 2.94 that the MV reconstructor is equal to the MMSE reconstructor (eq. 2.80) followed by the projection matrix $\mathbf{P}_{DM}^{L}$. The MV reconstructor is the most general reconstruction matrix that has been derived in the framework of static and open-loop MCAO systems.

2.7 Conclusions

In this chapter we have studied the problem of wavefront reconstruction in MCAO using the formalism of inverse problems theory. The severe *ill-posedness* of the problem of wavefront reconstruction in MCAO —as opposed to the SCAO case— comes from the fact that in MCAO we seek to do a tomographic reconstruction of the atmospheric volume.

We have compared two estimation methods for solving the problem of wavefront reconstruction in MCAO —the truncated least-squares (TLS) and the minimum mean-square error (MMSE) estimation methods—, and we have put in evidence the improvement in the stability of the solution brought by the MMSE reconstructor. In particular, we have shown that it is possible to consider much larger FoVs and a much larger number of estimated modes when using the MMSE reconstructor without putting at risk the stability of the solution, as it happens when using the TLS reconstructor.

We have also evaluated the reconstruction error in MCAO when using both estimation methods, and we have put in evidence the strong propagation of the remaining error —or generalized aliasing— when using the least-squares approach. In particular, we have shown that the propagation of the remaining error is stronger on the badly-seen modes of the MCAO system. On the other hand, we have also shown that the MMSE reconstructor is able to keep the propagation of the remaining error low for all eigenmodes, including the badly-seen ones, thanks to the statistical priors on the atmospheric turbulence taken into account in the regularization of the inverse problem.

Chapter 3

Modal gain optimization for MCAO

3.1 Introduction

In chapter 2 we studied the problem of wavefront reconstruction in MCAO. The atmospheric turbulence was regarded as being static –i.e. not evolving in time– and the dynamics of the components of an MCAO system were not taken into account. In this chapter we will study the problem of temporal control of an MCAO system. In particular, we will focus on the study of *modal control optimization* for MCAO. Modal control optimization for SCAO systems was introduced by Gendron *et. al.* [55] and by B. Ellerbroek *et. al.* [31] in 1994, and it has been successfully implemented in real systems such as NAOS (Nasmyth Adaptive Optics System [130]).

The first step in modal control is to choose a suitable modal basis. As we discussed in section 1.1.5, phase perturbations can be expressed in terms of their modal decompositions in a given basis. For instance, in chapter 2 we widely used the Zernike basis to address the problem of wavefront reconstruction. In this chapter we will continue to use Zernike modes to decompose the perturbed wavefronts. However, the *controlled modes* chosen for modal control will be the *MCAO system modes*. We will justify our choice of basis in section 3.3.

As discussed by E. Gendron [55], each controlled mode will have a characteristic signal-to-noise ratio and correlation time that will depend on the current atmospheric turbulence conditions and guide-star magnitude, among other factors. The goal of modal control optimization is then to use this information (when available) to perform a mode-by-mode optimization of the *system transfer functions* (section 3.3.2) that will

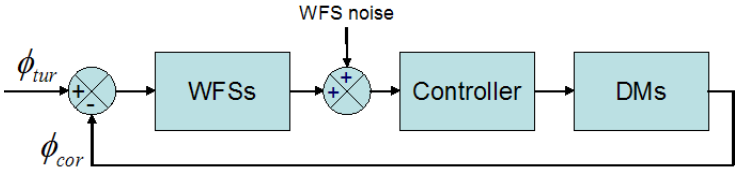

Figure 3.1: Block diagram of a closed-loop AO control system showing the turbulence signal, ϕ_{tur}, as the input to the system.

lead to an improvement of the quality of the AO-corrected images. In general, the optimization of the system transfer functions is achieved by fine-tuning the parameters of the temporal controller of the MCAO system. When the temporal controller is a modal integrator (section 3.2.3) the system transfer functions for each mode can be tuned by adjusting the integrator's modal gains. This is why, in SCAO, this control law is also known as the *Optimized Modal Gain Integrator* (OMGI).

Le Roux *et. al.* [131] studied for the first time the extension of the OMGI control law to MCAO, and called it the *Multi-conjugate Optimized Modal Gain Integrator* (MOMGI). In this work, we will study the MOMGI control law further. In particular, we will study the implications of a phenomenon that we have identified in chapter 2, namely the *propagation of the remaining error*, and that has not been studied before in the framework of MCAO.

3.2 Spatio-temporal MCAO control system model

In this section we will introduce the spatio-temporal models of the components of an MCAO system. Figure 1.8 showed the block diagram of a closed-loop adaptive optics system in which the turbulence is shown as a disturbance signal to the AO system. This is the kind of diagrams that the control theorists are used to work with. However, the AO community is more familiar with block diagrams in which the turbulence signal is shown as the *input* to the AO system, as in figure 3.1. It is straightforward to show that the block diagram of figure 1.8 can be rearranged as shown in figure 3.1. Without loss of generality, we will consider in this chapter that the reference slope vector in figure 1.8 is equal to zero ($\mathbf{s}_{ref} = 0$).

There are in general two approaches to modelling a control system: either using the *frequency domain* formalism, or the *state-space* formalism [35]. The frequency domain formalism has been widely used to analyze and design adaptive optics control systems [90]. This approach is particulary suited for the study of *modal control* because

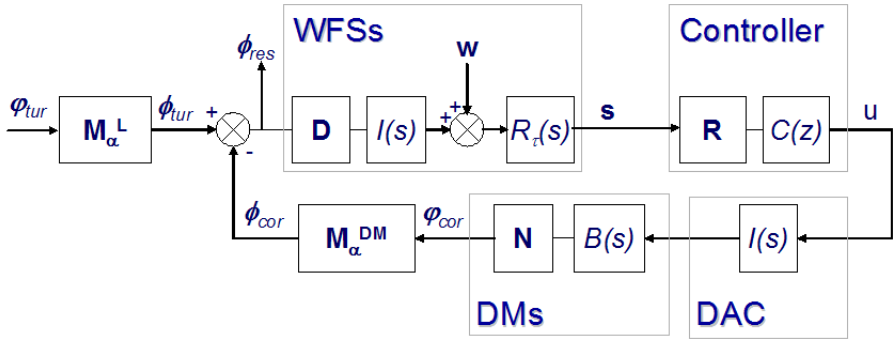

Figure 3.2: Block diagram of a closed-loop MCAO system showing the spatio-temporal model of each component.

each controlled mode is assumed to be independent of the others (i.e. not coupled). Therefore, for n controlled modes there will be n single-input-single-output (SISO) control loops. On the other hand, the state-space formalism is better suited for the analysis of multi-input-multi-output (MIMO) control systems and for the design of optimal controllers. Several authors have studied *optimal control* based on the Kalman filter for adaptive optics systems [103, 82, 132, 158, 108].

In this chapter we will study the problem of modal control optimization for MCAO systems based on the frequency domain formalism. We will generalize to MCAO the spatio-temporal modelling developed by E. Gendron [53] and C. Desssenne [22] for SCAO systems. Following their approach, the linear model of each AO component will be described with two matrices, one for the spatial response and one for the temporal response. Figure 3.2 shows the block diagram of an MCAO system detailing the components' models. The spatio-temporal model of each MCAO component will be described further below.

3.2.1 Deformable mirrors

Let us consider an MCAO system with N_{DM} deformable mirrors ($l = \{1 \dots N_{DM}\}$). The spatio-temporal model of the deformable mirrors is defined by a matrix $\mathbf{N}$, and a transfer matrix denoted by $\mathbf{B}(s)$. The matrix $\mathbf{N}$ is the *influence matrix* defined in equation 2.91. Recall that it is a block-diagonal matrix that contains all the N_{DM} influence matrices. Similarly, the transfer matrix $\mathbf{B}(s)$ is a block-diagonal matrix containing all the N_{DM} transfer matrices. The transfer matrix of the lth DM, denoted as $\mathbf{B}_l(s)$, is required to model the temporal response of its actuators. If there is no mechanical coupling among the actuators of the lth DM, the matrix $\mathbf{B}_l(s)$ will become

diagonal. Furthermore, if all actuators have the same response, the transfer matrix $\mathbf{B}_l(s)$ will be reduced to a single transfer function $B_l(s)$. For the case of piezo-stacked DMs it can be assumed that the DM reacts instantaneously to the commands, hence $B(s) = 1$. In other words, the DM dynamics are negligible. For bimorph DMs and large deformable mirrors this may not be true so $\mathbf{B}_l(s)$ might have to be taken into account when studying the temporal response of the corresponding AO system.

Finally, the spatio-temporal linear model of the DMs can be written as[1]:

$$\tilde{\boldsymbol{\varphi}}_{cor}(s) = \mathbf{NB}(s)\tilde{\mathbf{u}}(s) \tag{3.1}$$

where $\mathbf{u}$ is the command vector that drives the DMs (equation 2.90), and $\boldsymbol{\varphi}_{cor}$ is the correction phase vector produced by the DMs (equation 2.89).

An important simplification that we will do in this chapter is to consider that there are as many turbulent layers as deformable mirrors ($N_{_L} = N_{_{DM}}$) and that the turbulent layers and the DMs are conjugated to the same heights. This is basically the so-called *model approximation* proposed by T. Fusco [43]. Then, —as it was done in section 2.2.1— we will define the *turbulence volume phase space* $\mathcal{E}_V$, but this time it will be formed by *only* $N_{_L} = N_{_{DM}}$ infinite-dimensional phase spaces $\mathcal{E}_j$ each one of them defined in its corresponding DM metapupil. Following the linear algebra formalism related to the DM spaces introduced in section 1.2.1.2 and generalized to several layers in section 2.2.2, we will also redefine in this chapter as $\mathcal{M}_V$ the subspace of $\mathcal{E}_V$ that can be generated by the $N_{_L} = N_{_{DM}}$ DMs. Then, by construction, the vector $\boldsymbol{\varphi}_{cor}$ is a coordinates vector of $\mathcal{M}_V$. Finally, we will also denote as $\mathcal{M}_V^{\perp}$ the orthogonal complement of $\mathcal{M}_V$, so that $\mathcal{E}_V$ can be expressed as $\mathcal{E}_V = \mathcal{M}_V \oplus \mathcal{M}_V^{\perp}$.

3.2.2 Wavefront sensors

Let us consider an MCAO system with $N_{_{GS}}$ Shack-Hartmann wavefront sensors. The spatio-temporal model of the WFSs is defined by a matrix $\mathbf{D}$ and a transfer function denoted by $I(s)$. The matrix $\mathbf{D}$ was defined in equation 2.11. However, since in this chapter we are considering an MCAO system operating in closed loop then the WFSs will measure the *residual* phase in the telescope pupil $\boldsymbol{\phi}_{res}$. Therefore, the measurement vector can be expressed as:

[1] We will use the symbol ˜ to denote a given vector in the (temporal) frequency domain (i.e. Laplace, z-transform or Fourier transform depending on the context).

$$\begin{aligned} \mathbf{s} &= \mathbf{D}\boldsymbol{\phi}_{res} + \mathbf{w} \\ &= \mathbf{D}\left(\boldsymbol{\phi}_{tur} - \boldsymbol{\phi}_{cor}\right) + \mathbf{w} \\ &= \mathbf{D}\left(\mathbf{M}_{\alpha}^{L}\boldsymbol{\varphi}_{tur} - \mathbf{M}_{\alpha}^{DM}\boldsymbol{\varphi}_{cor}\right) + \mathbf{w} \ . \end{aligned} \tag{3.2}$$

Since we will assume that $N_{L} = N_{DM}$, then $\mathbf{M}_{\alpha}^{L} = \mathbf{M}_{\alpha}^{DM}$, so we will simply denote these matrices as $\mathbf{M}_{\alpha}$:

$$\mathbf{M}_{\alpha} \stackrel{\triangle}{=} \mathbf{M}_{\alpha}^{L} = \mathbf{M}_{\alpha}^{DM} \ . \tag{3.3}$$

Let us now split the turbulent phase vector $\boldsymbol{\varphi}_{tur}$ in two components: $\boldsymbol{\varphi}_{tur_{\parallel}}$ and $\boldsymbol{\varphi}_{tur_{\perp}}$, as it was done in the formulation of the approximate direct problem in section 2.2.2. Note that, similarly to the vector $\boldsymbol{\varphi}_{cor}$ (section 3.2.1), the vector $\boldsymbol{\varphi}_{tur_{\parallel}}$ is also a coordinates vector of the DMs subspace $\mathcal{M}_{V}$ whereas $\boldsymbol{\varphi}_{tur_{\perp}}$ is a coordinates vector of the subspace $\mathcal{M}_{V}^{\perp}$.

The matrix $\mathbf{M}_{\alpha}$ will be split in two meta-matrices too, namely $\mathbf{M}_{\alpha_{\parallel}}$ and $\mathbf{M}_{\alpha_{\perp}}$, as it was done in equations 2.18 and 2.19. Finally, equation 3.2 can be rewritten as:

$$\mathbf{s} = \mathbf{D}\mathbf{M}_{\alpha_{\parallel}}(\boldsymbol{\varphi}_{tur_{\parallel}} - \boldsymbol{\varphi}_{cor}) + \mathbf{D}\mathbf{M}_{\alpha_{\perp}}\boldsymbol{\varphi}_{tur_{\perp}} + \mathbf{w} \ . \tag{3.4}$$

The matrix $\mathbf{D}\mathbf{M}_{\alpha_{\perp}}$ characterizes the response of the WFSs to those high-order modes $\{\boldsymbol{\varphi}_{tur_{\perp}}\}$ that cannot be produced by the deformable mirrors.

Regarding the temporal response of the WFSs, there are two transfer matrices involved: $\mathbf{I}(s)$ and $\mathbf{R}_{\tau}(s)$. We will consider that the temporal response of all WFSs channels is the same and that there is no coupling between them. Hence, the temporal response is simply described by two transfer functions: $I(s)$ and $R_{\tau}(s)$. $I(s)$ accounts for the integration time of the WFSs' detectors, denoted as T, and is given by [90]:

$$I(s) = \frac{1 - e^{-Ts}}{Ts} \ . \tag{3.5}$$

The sampling frequency of the MCAO system is given by $f_{s} = 1/T$. The transfer function $R_{\tau}(s)$ accounts for a pure time delay τ introduced by the read-out of the WFSs' detector, the digitalization of the signals, and the computation of the measurement vector $\mathbf{s}$. It is simply given by:

$$R_{\tau}(s) = e^{-\tau s} \ . \tag{3.6}$$

The complete spatio-temporal linear model for the wavefront sensors becomes:

$$\tilde{\mathbf{s}}(s) = R_\tau(s)\left[I(s)\mathbf{D}\tilde{\boldsymbol{\phi}}_{res}(s) + \tilde{\mathbf{w}}(s)\right] \quad . \tag{3.7}$$

3.2.3 Controller

The controller generates the command vector $\mathbf{u}$ that drives the DMs from the measurement vector $\mathbf{s}$ and ensures the temporal stability of the MCAO system. Note that the controller is the only discrete-time component of the AO system. The spatio-temporal model of the controller is defined with two matrices: the reconstruction matrix $\mathbf{R}$ and the controller discrete-time transfer matrix $\mathbf{C}(z)$.

Modal gain optimization is based on a simple integrator controller. The discrete-time transfer function of an integrator is [35]:

$$C(z) = \frac{g}{1 - z^{-1}} \tag{3.8}$$

where g is the integrator gain. As we will discuss in section 3.4, there will be a different integrator gain for each controlled mode. If there is no coupling between the controlled modes the matrix $\mathbf{C}(z)$ will be diagonal, and each element of the diagonal will be given by equation 3.8. The complete spatio-temporal model of the controller is given by:

$$\tilde{\mathbf{u}}(s) = \mathbf{C}(s)\mathbf{R}\tilde{\mathbf{s}}(s) \quad , \tag{3.9}$$

where the continuous-time transfer matrix $\mathbf{C}(s)$ can be computed from $\mathbf{C}(z)$ by substituting $z = e^{Ts}$ [36]. Then, the equivalent transfer function of a simple integrator in the Laplace domain is:

$$C(s) = \frac{g}{1 - e^{-Ts}} \quad . \tag{3.10}$$

3.2.4 DAC and HVA

The digital-to-analog (DAC) converter and the high-voltage amplifier (HVA) interface the digital controller with the deformable mirrors. We will consider that all the channels have the same temporal response, so these components can be characterized with simple transfer functions. The transfer function of the DAC is given by [90]:

$$I(s) = \frac{1 - e^{-Ts}}{Ts} \quad , \tag{3.11}$$

where T is the sampling period of the system. The DAC must be synchronized with the WFSs detectors. Note that the transfer functions of the WFSs and the DAC have the same expression. The HVA produces the high voltages required to drive the deformable mirrors. The settling time is in general much faster than the sampling period so its dynamics can be neglected. Hence, its transfer function is equal to an amplification constant and it won't be considered explicitly in our formulation.

3.2.5 Feedback equation and coupling

From diagram 3.2, and introducing the spatio-temporal models presented in the subsections above, it can be shown that:

$$\begin{aligned}\tilde{\boldsymbol{\phi}}_{cor}(s) &= [I^2(s)R_\tau(s)B(s)]\mathbf{M}_\alpha^{DM}\mathbf{NC}(s)\mathbf{RD}[\tilde{\boldsymbol{\phi}}_{tur}(s)-\tilde{\boldsymbol{\phi}}_{cor}(s)] \\ &+ [I(s)R_\tau(s)B(s)]\mathbf{M}_\alpha^{DM}\mathbf{NC}(s)\mathbf{R}\tilde{\mathbf{w}}(s)\,. \end{aligned} \tag{3.12}$$

This is the multi-variable feedback equation expressed in the Laplace domain that totally describes the closed-loop MCAO system. Now, we would like to decouple the MCAO control system so that each controlled mode can be controlled independently of the others. However, *decoupling* has two different connotations; one spatial and one temporal. From the spatial point of view, the *coupling matrix* $\mathbf{A}$ is defined as [22]:

$$\mathbf{A} = \mathbf{R}\mathbf{M}_{int} \tag{3.13}$$

where $\mathbf{M}_{int}$ denotes the MCAO interaction matrix:

$$\mathbf{M}_{int} = \mathbf{D}\mathbf{M}_\alpha^{DM}\mathbf{N}\ . \tag{3.14}$$

A system is said to be spatially decoupled if $\mathbf{A}$ is a diagonal matrix. For example, a control system based on the MMSE reconstructor (eq. 2.80) computed as:

$$\mathbf{R}_{MMSE} = \left[\mathbf{M}_{int}^T\mathbf{C}_\mathbf{w}^{-1}\mathbf{M}_{int} + \mathbf{C}_\varphi^{-1}\right]^{-1}\mathbf{M}_{int}^T\mathbf{C}_\mathbf{w}^{-1} \tag{3.15}$$

would not be decoupled because clearly $\mathbf{R}_{MMSE}\mathbf{M}_{int}$ is not diagonal. On the other hand, a control system based on the least-squares reconstructor (eq. 2.32) would be decoupled because:

$$\begin{aligned}\mathbf{A}_{LS} &= \mathbf{R}_{LS}\mathbf{M}_{int} \\ &= (\mathbf{M}_{int}^T\mathbf{M}_{int})^{-1}\mathbf{M}_{int}^T\mathbf{M}_{int} = \mathbf{I}_d\ .\end{aligned}$$

Note that this is not the case for the truncated least-squares reconstructor (eq. 2.43) because the truncation of badly-seen modes actually introduces a coupling. Using the same notation presented in section 2.3.2.3 to represent the SVD of $\mathbf{M}_{int}$:

$$\mathbf{M}_{int} = \mathbf{U}\Sigma\mathbf{V}^T \tag{3.16}$$

it is straightforward to show that the coupling matrix is equal to:

$$\mathbf{A}_{TLS} = \mathbf{V}\Sigma_{fil}^{-1}\Sigma\mathbf{V}^T \ . \tag{3.17}$$

Nevertheless, the coupling introduced by the TLS reconstructor is not strong, so it is usually assumed that systems using this reconstruction matrix are spatially decoupled.

From the temporal point of view, decoupling implies that the transfer functions of the controlled modes are independent of each other. Formally, a system is temporally decoupled if the closed-loop transfer matrix is a diagonal matrix. In the following sections we will show how we can decouple an MCAO system, both spatially and temporally, in order to control each controlled modes independently of the others.

3.3 Modal Control for MCAO

In order to do modal gain optimization in MCAO we first need to define which are going to be the modes to be controlled, and then define a method to optimize the gains associated with each of these modes. In this section we will discuss the first issue. Gain optimization methods will be presented in section 3.4.

Choosing the modes to be controlled is equivalent to selecting a suitable modal basis for $\mathcal{M}_V$. The controlled modes are the vectors of the chosen basis of $\mathcal{M}_V$. As discussed by E. Gendron [53], there are two basic properties that this modal basis should have. The first one is that the controlled modes should be orthogonal.

The second one is that the chosen basis should span the widest range of sensitivities. The simplest modal basis that has these two properties is the one formed by the eigenmodes of $\mathbf{M}_{int}^T\mathbf{M}_{int}$. The eigenmodes of $\mathbf{M}_{int}^T\mathbf{M}_{int}$ are also known as the *MCAO system modes*.

The MCAO interaction matrix $\mathbf{M}_{int}$ establishes the link between the space of the WFSs measurements and the DMs space $\mathcal{M}_V$, so the MCAO system modes contain all the information about which modes the system can or cannot compensate for. These are the modes that we will choose to study modal gain optimization for MCAO.

We will show below how an MCAO system can be decoupled in the system space, and define an independent control loop for each system mode. In order to do that we will first need a reconstruction matrix that we can use to estimate the system modes from the WFSs measurements. Expressing the least-squares (LS) reconstructor $\mathbf{R}_{LS}$ as:

$$\mathbf{R}_{LS} = \mathbf{V}\Sigma^{-1}\mathbf{U}^T \tag{3.18}$$

it becomes clear that the reconstruction matrix that we are looking for is simply given by:

$$\mathbf{R}_{LS}^{MP} = \Sigma^{-1}\mathbf{U}^T \ . \tag{3.19}$$

3.3.1 Decoupling in the MCAO system space

Modal control techniques assume that there is no coupling between controlled modes. Hence, the control loop for each mode can be optimized independently of the others. We will show below by manipulating the feedback equation (eq. 3.12) that the control loop for each system mode can be decoupled from the others. Multiplying both sides of equation 3.12 by $\mathbf{D}$ and recalling the expression for the MCAO interaction matrix (eq. 3.14) we obtain:

$$\begin{aligned} \mathbf{D}\tilde{\boldsymbol{\phi}}_{cor} &= [I^2 R_\tau B]\mathbf{M}_{int}\mathbf{C}\mathbf{R}_{LS}\mathbf{D}(\tilde{\boldsymbol{\phi}}_{tur} - \tilde{\boldsymbol{\phi}}_{cor}) \\ &+ [I R_\tau B]\mathbf{M}_{int}\mathbf{C}\mathbf{R}_{LS}\tilde{\mathbf{w}}\,. \end{aligned} \tag{3.20}$$

To improve legibility we have omitted the dependency on the complex variable (s). Substituting the SVD expressions of $\mathbf{M}_{int}$ and $\mathbf{R}_{LS}$ (eq. 3.16 and 3.18):

$$\begin{aligned} \mathbf{D}\tilde{\boldsymbol{\phi}}_{cor} &= [I^2 R_\tau B]\mathbf{U}\Sigma\mathbf{V}^T\mathbf{C}\mathbf{V}\Sigma^{-1}\mathbf{U}^T\mathbf{D}(\tilde{\boldsymbol{\phi}}_{tur} - \tilde{\boldsymbol{\phi}}_{cor}) \\ &+ [I R_\tau B]\mathbf{U}\Sigma\mathbf{V}^T\mathbf{C}\mathbf{V}\Sigma^{-1}\mathbf{U}^T\tilde{\mathbf{w}}\,. \end{aligned} \tag{3.21}$$

In order to show explicitly the effect of the orthogonal components of $\boldsymbol{\varphi}_{tur}$ we introduce equations 3.2, 3.3, and 3.4 and we obtain:

$$\begin{aligned} \mathbf{D}\mathbf{M}_{\alpha_\parallel}\tilde{\boldsymbol{\varphi}}_{cor} &= [I^2 R_\tau B]\mathbf{U}\Sigma\mathbf{V}^T\mathbf{C}\mathbf{V}\Sigma^{-1}\mathbf{U}^T\mathbf{D}\mathbf{M}_{\alpha_\parallel}\left(\tilde{\boldsymbol{\varphi}}_{tur_\parallel} - \tilde{\boldsymbol{\varphi}}_{cor}\right) \\ &+ [I^2 R_\tau B]\mathbf{U}\Sigma\mathbf{V}^T\mathbf{C}\mathbf{V}\Sigma^{-1}\mathbf{U}^T\mathbf{D}\mathbf{M}_{\alpha_\perp}\tilde{\boldsymbol{\varphi}}_{tur_\perp} \\ &+ [I R_\tau B]\mathbf{U}\Sigma\mathbf{V}^T\mathbf{C}\mathbf{V}\Sigma^{-1}\mathbf{U}^T\tilde{\mathbf{w}}\,. \end{aligned} \tag{3.22}$$

Note that the previous steps have simply reformulated the feedback equation in the WFSs space. We can now reformulate it in the system space by multiplying both sides of eq. 3.22 by the reconstruction matrix $\mathbf{R}_{LS}^{MP} = \Sigma^{-1}\mathbf{U}^T$ (eq. 3.19):

$$\begin{aligned}\Sigma^{-1}\mathbf{U}^T\mathbf{DM}_{\alpha_\parallel}\tilde{\boldsymbol{\varphi}}_{cor} &= [I^2R_\tau B]\mathbf{V}^T\mathbf{CV}\Sigma^{-1}\mathbf{U}^T\mathbf{DM}_{\alpha_\parallel}\left(\tilde{\boldsymbol{\varphi}}_{tur_\parallel} - \tilde{\boldsymbol{\varphi}}_{cor}\right)\\ &+ [I^2R_\tau B]\mathbf{V}^T\mathbf{CV}\Sigma^{-1}\mathbf{U}^T\mathbf{DM}_{\alpha_\perp}\tilde{\boldsymbol{\varphi}}_{tur_\perp}\\ &+ [IR_\tau B]\mathbf{V}^T\mathbf{CV}\Sigma^{-1}\mathbf{U}^T\tilde{\mathbf{w}} \end{aligned} \quad (3.23)$$

where we have used the fact that $\mathbf{U}^T = \mathbf{U}^{-1}$. Let us now define all the variables of interest in the system space:

$$\boldsymbol{\varphi}_{cor}^{MP} \triangleq \Sigma^{-1}\mathbf{U}^T\mathbf{DM}_{\alpha_\parallel}\boldsymbol{\varphi}_{cor} \quad (3.24)$$

$$\boldsymbol{\varphi}_{tur_\parallel}^{MP} \triangleq \Sigma^{-1}\mathbf{U}^T\mathbf{DM}_{\alpha_\parallel}\boldsymbol{\varphi}_{tur_\parallel} \quad (3.25)$$

$$\boldsymbol{\varphi}_{tur_\perp}^{MP} \triangleq \Sigma^{-1}\mathbf{U}^T\mathbf{DM}_{\alpha_\perp}\boldsymbol{\varphi}_{tur_\perp} \quad (3.26)$$

$$\mathbf{w}^{MP} \triangleq \Sigma^{-1}\mathbf{U}^T\mathbf{w}\ . \quad (3.27)$$

We will call $\boldsymbol{\varphi}_{tur_\parallel}^{MP}$ the *turbulent eigenmode*, $\boldsymbol{\varphi}_{cor}^{MP}$ the *correction eigenmode*, $\boldsymbol{\varphi}_{tur_\perp}^{MP}$ the *propagated remaining error in system space*, and $\mathbf{w}^{MP}$ the *propagated measurement noise in system space*. Equation 3.23 can be rewritten as:

$$\begin{aligned}\tilde{\boldsymbol{\varphi}}_{cor}^{MP} &= [I^2R_\tau B]\mathbf{V}^T\mathbf{CV}\left(\tilde{\boldsymbol{\varphi}}_{tur_\parallel}^{MP} - \tilde{\boldsymbol{\varphi}}_{cor}^{MP}\right)\\ &+ [I^2R_\tau B]\mathbf{V}^T\mathbf{CV}\tilde{\boldsymbol{\varphi}}_{tur_\perp}^{MP}\\ &+ [IR_\tau B]\mathbf{V}^T\mathbf{CV}\mathbf{w}^{MP}\ . \end{aligned} \quad (3.28)$$

The matrix $\mathbf{V}^T\mathbf{CV}$ in equation 3.28 is the controller's transfer matrix in system space, and will be denoted as $\mathbf{C}^{MP}$:

$$\mathbf{C}^{MP} = \mathbf{V}^T\mathbf{CV}\,. \quad (3.29)$$

In order to decouple the control system in the system space we just need to define a diagonal transfer matrix $\mathbf{C}^{MP}$. As mentioned in section 3.2.3, the ith element of the diagonal of $\mathbf{C}^{MP}$ will contain the transfer function of a simple integrator controller whose gain is denoted as g_i. Finally, we can write an independent feedback equation for the ith system mode as:

$$\begin{aligned}\tilde{\varphi}_{cor,i}^{MP} &= [I^2R_\tau B]C_i^{MP}(\tilde{\varphi}_{tur_\parallel,i}^{MP} - \tilde{\varphi}_{cor,i}^{MP})\\ &+ [I^2R_\tau B]C_i^{MP}\tilde{\varphi}_{tur_\perp,i}^{MP}\end{aligned}$$

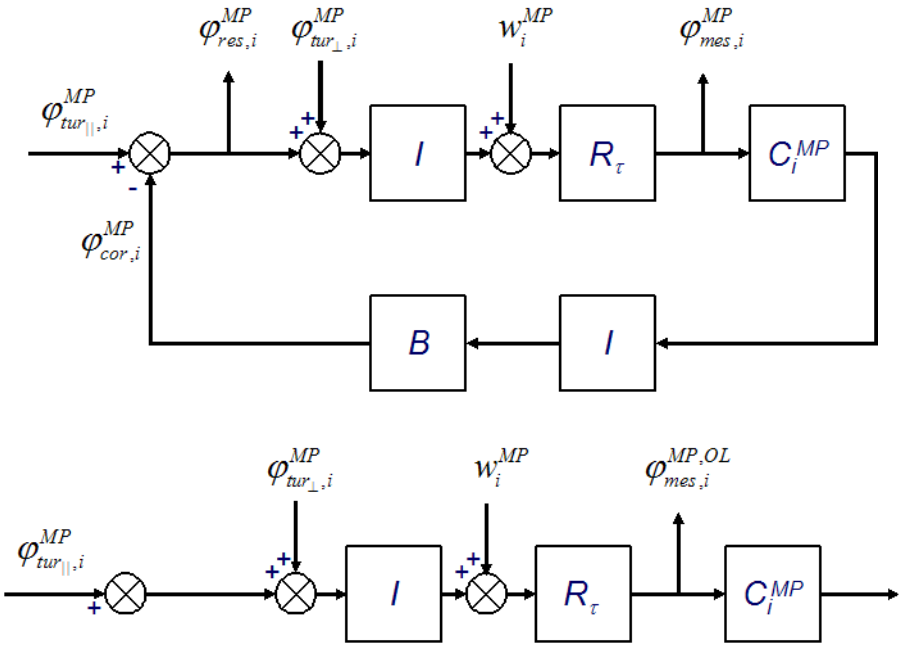

Figure 3.3: Block diagram of the independent control loop for each system mode of an MCAO system. (*Top*) Closed-loop operation. (*Bottom*) Open-loop operation.

$$+ \quad [IR_\tau B]C_i^{MP}\tilde{w}_i^{MP} \tag{3.30}$$

where C_i^{MP} denotes the ith element of the diagonal of $\mathbf{C}^{MP}$. Figure 3.3(top) shows the equivalent independent control loop for each system mode.

Open-loop operation In the following sections we will also talk about the *open-loop operation* of an MCAO system. Figure 3.3(bottom) shows the equivalent control loop for each system mode in open-loop. It is important to realize that *open-loop operation* simply means that there is no correction applied to the DMs. Therefore, the WFSs are measuring directly the turbulence phase and not the residual phase.

3.3.2 System Transfer Functions

We can now compute the transfer functions for each independent control loop. From figure 3.3, it can be seen that the *open-loop transfer function* is given by:

$$G_i = I^2 R_\tau B C_i^{MP} \quad . \tag{3.31}$$

Substituting the expressions for all transfer functions in equation 3.31, and considering that $B(s) = 1$, leads to the well-known open-loop transfer function of an AO system [90]:

$$G_i(s) = \left[\frac{1 - e^{-Ts}}{Ts}\right]^2 e^{-\tau s} C_i^{MP}(s) \tag{3.32}$$

The equivalent discrete-time open-loop transfer function $G_i(z)$ can be obtained by following a standard procedure described in reference [36]. It consists in computing the inverse Laplace transform of $G_i(s)$ to obtain a function in the continuous-time domain $G_i(t)$. Then, this function is sampled every T seconds to obtain the function $G_i(kT)$. Finally, the z-transform of this function is computed to obtain $G_i(z)$. The pure time delay τ must be expressed as $\tau = lT - mT$ where l is an integer and $0 \leq m < 1$. It can be shown that applying this method to equation 3.32 leads to [24]:

$$G_i(z) = z^{-l}\left(m(1 - z^{-1}) + z^{-1}\right) C_i^{MP}(z) \ . \tag{3.33}$$

Other system transfer functions of interest are the *rejection transfer function* E_i and the *closed-loop transfer function* H_i. They are defined as:

$$E_i = \frac{1}{1 + G_i} \ , \tag{3.34}$$

$$H_i = \frac{G_i}{1 + G_i} \ . \tag{3.35}$$

The last transfer function we will be interested in is the *noise transfer function* $H_{n,i}$. From figure 3.3 it can be shown that:

$$H_{n,i} = \frac{IR_\tau B C_i^{MP}}{1 + G_i} \ . \tag{3.36}$$

Figure 3.4 shows the modulus of all the transfer functions for $f_s = 400$Hz, and $\tau = T$, and for three different values of g_i. Note that $|H_i|$ and $|H_{n,i}|$ only differ at high frequencies.

Correction bandwidth We will define the *correction bandwidth* of the MCAO system as the 0dB cross-over frequency of the rejection transfer function.

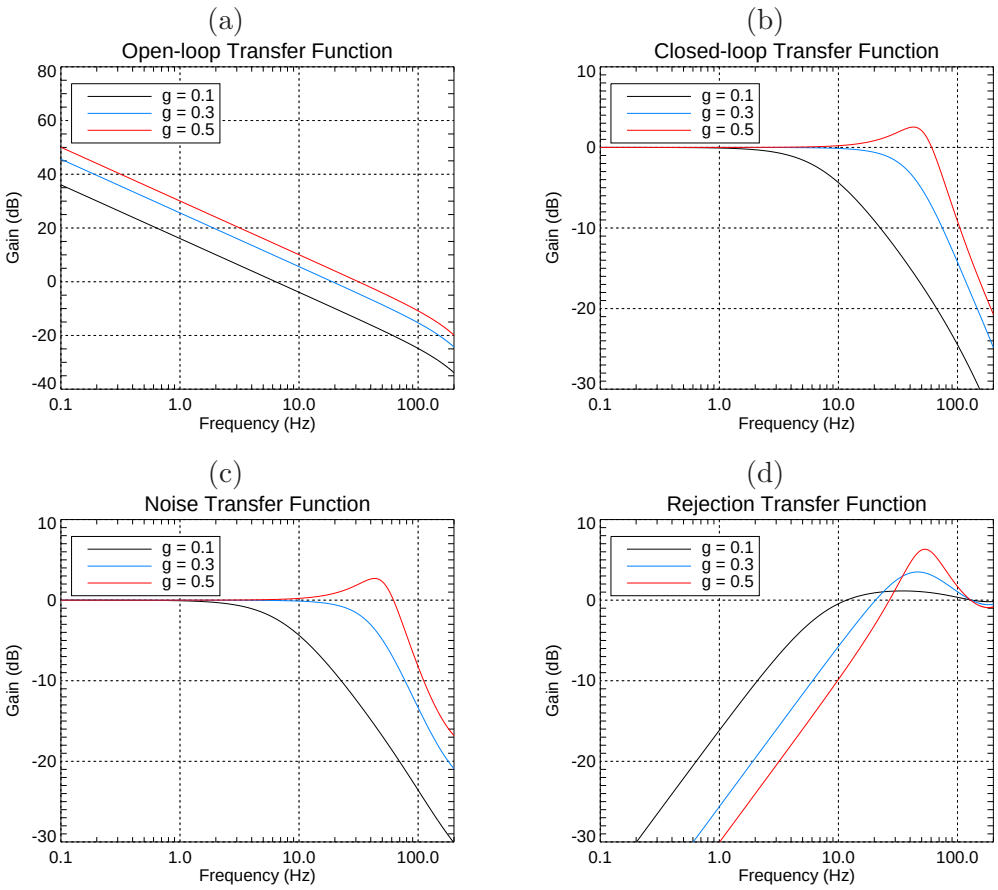

Figure 3.4: Examples of the modulus of the system transfer functions for different gains g_i, and for $f_s = 400$Hz, and $\tau = T$. *(a)* Open-loop transfer function, *(b)* Closed-loop transfer functions, *(c)* Noise transfer functions, *(d)* Rejection transfer functions.

3.4 Optimized modal control for MCAO

In this section we will study different methods to compute the optimized modal gains for each MCAO system mode. We will attempt to generalize to the MCAO case the original methods created for SCAO systems and that have been successfully implemented for instance in NAOS, the SCAO system of the Very Large Telescope (VLT) [50].

The goal of optimized modal control is to minimize the variance of the residual phase $\boldsymbol{\varphi}_{res}$ by minimizing the residual variance of each controlled mode. From figure 3.3, the residual of the ith eigenmode is given by:

$$\tilde{\varphi}^{MP}_{res,i} = \tilde{\varphi}^{MP}_{tur_{\parallel},i} - \tilde{\varphi}^{MP}_{cor,i} \quad . \tag{3.37}$$

Solving eq. 3.30 for $\tilde{\varphi}^{MP}_{cor,i}$ and substituting it in eq. 3.37 leads to:

$$\begin{aligned}\tilde{\varphi}^{MP}_{res,i} &= \frac{1}{1+I^2R_\tau BC_i^{MP}}\tilde{\varphi}^{MP}_{tur_\parallel,i} - \frac{I^2R_\tau BC_i^{MP}}{1+I^2R_\tau BC_i^{MP}}\tilde{\varphi}^{MP}_{tur_\perp,i} \\ &- \frac{IR_\tau BC_i^{MP}}{1+I^2R_\tau BC_i^{MP}}\tilde{w}_i^{MP} \ . \end{aligned} \tag{3.38}$$

Recalling the definitions of the system transfer functions presented in section 3.3.2 equation 3.38 can be simply rewritten as:

$$\tilde{\varphi}^{MP}_{res,i} = E_i\tilde{\varphi}^{MP}_{tur_\parallel,i} - H_i\tilde{\varphi}^{MP}_{tur_\perp,i} - H_{n,i}\tilde{w}_i^{MP} \ . \tag{3.39}$$

This expression is totally equivalent to the one derived by E. Gendron *et. al.* [55]. The residual phase is the sum of three terms. The first term is the contribution to the residual phase coming from the uncompensated portion of $\varphi^{MP}_{tur_\parallel,i}$. The second term characterizes the propagation of the remaining error, and the third one characterizes the propagation of the measurement noise. As shown in figure 3.4, increasing g_i leads to a higher correction bandwidth, i.e. a better rejection of $\varphi^{MP}_{tur_\parallel,i}$. However, increasing g_i also leads to higher propagation of both the remaining error and the measurement noise. A compromise is required, and in fact the goal of modal gain optimization methods is to find the gain g_i that minimizes the variance of $\varphi^{MP}_{res,i}$, for each eigenmode. The variance of $\varphi^{MP}_{res,i}$, denoted as σ_i^2, can be computed as:

$$\sigma_i^2 = \int_{-\infty}^{\infty} \langle |\tilde{\boldsymbol{\varphi}}^{MP}_{res,i}(j\omega)|^2 \rangle d\omega \tag{3.40}$$

where we have made the substitution $s = j\omega$. The operator $\langle|\dot{\cdot}|^2\rangle$ denotes the power spectral density (PSD). Assuming that the propagated measurement noise w_i^{MP} is not correlated with neither the turbulence $\varphi^{MP}_{tur_\parallel,i}$ nor the propagated remaining error $\varphi^{MP}_{tur_\perp,i}$, and assuming also that the correlation between $\varphi^{MP}_{tur_\parallel,i}$ and $\varphi^{MP}_{tur_\perp,i}$ is negligible, the variance of $\varphi^{MP}_{res,i}$ can be expressed as:

$$\begin{aligned}\sigma_i^2 &= \int_{-\infty}^{\infty} |E_i(j\omega)|^2 \langle |\tilde{\varphi}^{MP}_{tur_\parallel,i}(j\omega)|^2 \rangle \, d\omega \\ &+ \int_{-\infty}^{\infty} |H_i(j\omega)|^2 \langle |\tilde{\varphi}^{MP}_{tur_\perp,i}(j\omega)|^2 \rangle \, d\omega \\ &+ \int_{-\infty}^{\infty} |H_{n,i}(j\omega)|^2 \langle |\tilde{w}_i^{MP}(j\omega)|^2 \rangle \, d\omega \ . \end{aligned} \tag{3.41}$$

It is important to note that for SCAO systems the contribution of the second term is in general negligible with respect to the others two. Modal gain optimization methods developed for SCAO actually do not take it into account [55]. As we discussed in chapter 2, the propagation of the remaining error in MCAO is not negligible, so we will have to take it into account. We should note that B. Le Roux *et. al.* [132] did not consider the propagation of the remaining error in their study of the MOMGI control law. Therefore, in this work we have extended their approach by taking into account this additional phenomenon in the computation of the optimized modal gains.

There are two methods for computing the optimized modal gains originally proposed for SCAO systems. These methods are the *Gendron method* [55] and the *Dessenne method* [24]. Both methods are equivalent in the sense that both are intended to minimize the variance of the residual phase. We will review each of these methods in the following sections, and discuss the possibility of extending them for the MCAO case.

3.4.1 Case study: simulation parameters

In this section we will illustrate with numerical simulations the problems encountered in modal gain optimization for MCAO. We will consider an MCAO system configuration already presented in chapter 2, comprising 2 deformable mirrors ($N_{DM} = 2$) conjugated at 0 and 8.5 km, and three wavefront sensors ($N_{GS} = 3$) coupled to natural guide stars located on the vertices of an equilateral triangle inscribed in a 2' FoV (figure 2.4). The telescope diameter is $D = 8$m.

For the chosen FoV=2', the diameters of the DMs metapupils are 8m and 12.95m. We will consider that the influence functions of the DMs are directly Zernike polynomials. The lower DM can correct up to 10 radial orders (65 Zernikes) whereas the higher DM up to 16 radial orders (152 Zernikes). Hence, there will be a total of 217 system modes.

We will also consider that the three WFSs are *idealized* WFSs measuring directly Zernike coefficients. Each WFS can measure directly the first 16 radial orders (152 Zernike coefficients). The measurement noise on each Zernike coefficient will be simulated as described in section 2.4.4 in order to mimic the characteristic noise propagation of a Shack-Hartmann WFS. We will study the case for two different signal-to-noise ratios, namely SNR=10, and SNR=100. For the current system configuration and a NAOS-like zeropoint ($Z_0 = 6.4\text{x}10^{11}$ photons/s) these SNRs are roughly equivalent to star magnitudes M_V=12 and M_V=9.5 respectively.

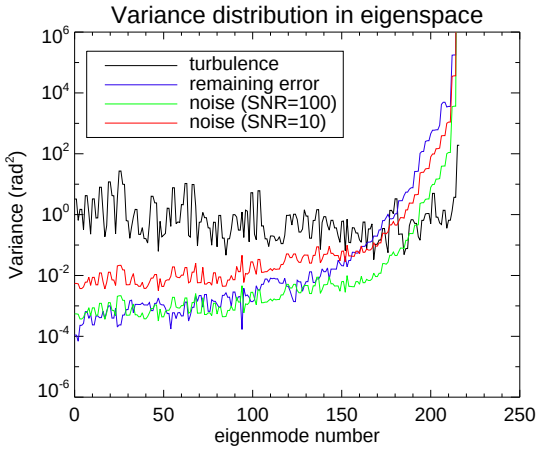

Figure 3.5: Variance distribution in the system space (or eigenspace) for $\frac{D}{r_0} = 38$ @ 700nm and for a SNR equal to 10 and 100.

We have also considered a simplified Kolmogorov turbulence model comprising two layers of equal strength conjugated at the DMs altitudes: 0km and 8.5km respectively. The equivalent wind speed at each turbulent layer will be set to $V = 10\,\mathrm{m}\cdot\mathrm{s}^{-1}$.

The wavefront sensing wavelength is $0.7\mu m$ and the imaging wavelength is $2.2\mu m$. We have simulated a seeing value of 0.73 arcsec. Then, $r_0 = 0.21$m at $0.7\mu m$ and $r_0 = 0.83$m at $2.2\mu m$. The global $\frac{D}{r_0}$ ratio is equal to 38 at $0.7\mu m$ and to 9.6 at $2.2\mu m$.

Figure 3.5 shows the variance distribution in eigenspace for the present simulation parameters and for a SNR equal to 10 and 100. The gain associated with each eigenmode needs to be optimized for each SNR.

The sampling frequency is set to 400 Hz ($T = 2.5$ms). We will set the pure time delay to one sampling period: $\tau = T$. DMs dynamics will not be simulated: $|B(s)| = 1$. From equation 3.33, the discrete-time open-loop transfer function becomes:

$$G_i(z) = z^{-2}\frac{g_i}{1 - z^{-1}} \quad . \tag{3.42}$$

Note that the MCAO system is simply characterized by a two-frames delay. The equivalent block diagrams for both closed-loop and open-loop operations are shown in figure 3.6. The reconstruction and control equations at iteration n can be written as:

$$\boldsymbol{\varphi}_{mes}^{MP}(n) \quad = \quad \mathbf{R}_{LS}^{MP}\mathbf{s}(n) \tag{3.43}$$

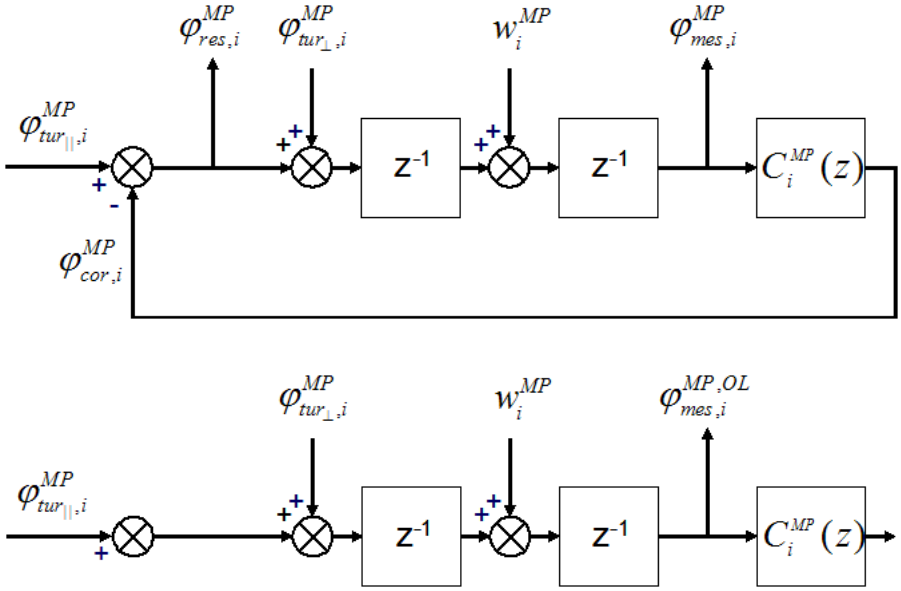

Figure 3.6: Discrete-time block diagrams for the ith MCAO eigenmode control loop: *(Top)* closed-loop operation, *(Bottom)* open-loop operation.

$$\varphi^{MP}_{cor}(n) = \varphi^{MP}_{cor}(n-1) + \mathbf{C}_{\mathbf{OMGI}}\varphi^{MP}_{mes}(n-2) \quad (3.44)$$

$$\mathbf{u}(n) = \mathbf{V}\varphi^{MP}_{cor}(n) \quad (3.45)$$

where the matrix $\mathbf{C}_{\mathbf{OMGI}}$ is a diagonal matrix containing the optimized modal gains g_i.

3.5 Gendron method

E. Gendron originally proposed to compute the optimized modal gains g_i by minimizing directly the criterion $J_i^G = \sigma_i^2$ (eq. 3.41). Note that the Gendron method requires an estimate of the temporal power spectra of $\varphi^{MP}_{tur_\parallel,i}$, $\varphi^{MP}_{tur_\perp,i}$ and w_i^{MP}. Also the system transfer functions need to be well characterized. We will first consider the case where the required PSDs can be computed analytically based on some *a-priori* knowledge on the turbulence.

3.5.1 Temporal power spectra

For computing the optimized modal gains with the Gendron method it is required to estimate the power spectra of the turbulent eigenmode $\varphi^{MP}_{tur_\parallel}$, the propagated remaining error $\varphi^{MP}_{tur_\perp}$, and the propagated measurement noise $\mathbf{w}^{MP}$.

Let us consider first the theoretical PSDs of $\boldsymbol{\varphi}_{tur_\parallel}^{MP}$ and $\boldsymbol{\varphi}_{tur_\perp}^{MP}$. These vectors were defined in equations 3.25 and 3.26. Using these definitions we could compute the theoretical PSD of the ith turbulent eigenmode simply as:

$$\langle|\tilde{\varphi}_{tur_\parallel,i}^{MP}(j\omega)|^2\rangle \approx \sum_j (\Sigma^{-1}\mathbf{U}^T\mathbf{D}\mathbf{M}_{\alpha_\parallel})_{i,j}^2 \langle|\tilde{\varphi}_{tur_\parallel,j}(j\omega)|^2\rangle \ , \tag{3.46}$$

where all the cross-spectra between the coefficients of $\boldsymbol{\varphi}_{tur_\parallel}$ have been neglected. Similarly, we could compute the theoretical PSD of the ith coefficient of $\boldsymbol{\varphi}_{tur_\perp}^{MP}$ as:

$$\langle|\tilde{\varphi}_{tur_\perp,i}^{MP}(j\omega)|^2\rangle \approx \sum_j (\Sigma^{-1}\mathbf{U}^T\mathbf{D}\mathbf{M}_{\alpha_\perp})_{i,j}^2 \langle|\tilde{\varphi}_{tur_\perp,j}(j\omega)|^2\rangle \ , \tag{3.47}$$

where all the cross-spectra between the coefficients of $\boldsymbol{\varphi}_{tur_\perp}$ have been neglected too. In order to use these expressions we are now required to know the PSDs of $\boldsymbol{\varphi}_{tur_\parallel}$ and $\boldsymbol{\varphi}_{tur_\perp}$. In our present case study $\boldsymbol{\varphi}_{tur_\parallel}$ and $\boldsymbol{\varphi}_{tur_\perp}$ are vectors of Zernike coefficients and their temporal PSDs for Kolmogorov turbulence are well-known (section 1.1.6.1). The only parameters that are required to compute these spectra are D/r_0 and the wind speed V for each considered layer (section 3.4.1). As an example, figure 3.7 shows the theoretical PSDs of eigenmodes 50 and 200. Note that the former is a well-seen mode whereas the latter is a badly-seen mode.

Let us now consider the theoretical PSD of the propagated measurement noise $\mathbf{w}^{MP}$. We will assume that $\mathbf{w}^{MP}$ can be modelled as a white noise with zero-mean Gaussian statistics and covariance matrix $\mathbf{C}_{\mathbf{w}}^{MP}$. Hence, the PSD of w_i^{MP} is constant and equal to:

$$\langle|\tilde{w}_i^{MP}(j\omega)|^2\rangle = T\,[\mathbf{C}_{\mathbf{w}}^{MP}]_{i,i} \ . \tag{3.48}$$

The diagonal of $\mathbf{C}_{\mathbf{w}}^{MP}$ was shown in figure 3.5 for SNR=10 and SNR=100. Also, figure 3.7 shows the corresponding theoretical PSDs for the eigenmodes 50 and 200.

3.5.2 System transfer functions

For computing the optimized modal gains with the Gendron method it is also required to have an analytical model of the control loop in order to compute the modulus of the system transfer functions, namely $|E_i|$, $|H_{n,i}|$, and $|H_i|$. It is clear that the control loop model has to be validated experimentally for a real MCAO system in order to be sure that the theoretical expressions match the experimental ones. The system transfer functions for our case study and for different gain values were plotted in figure 3.4.

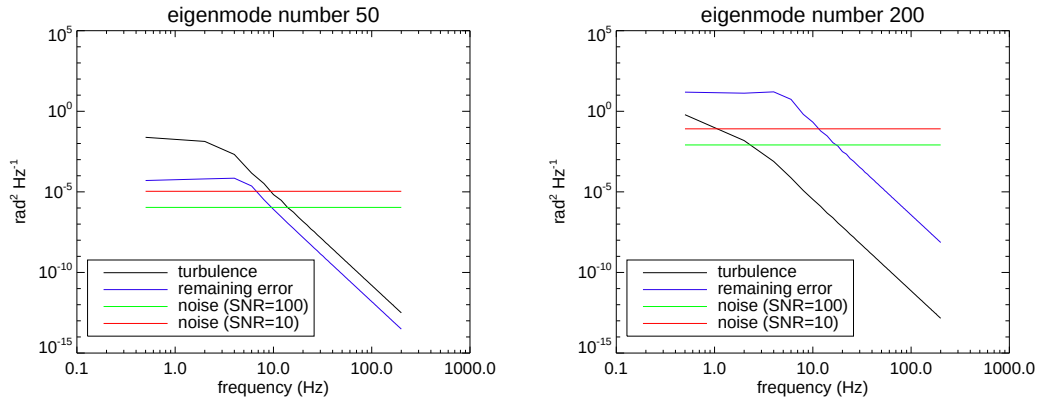

Figure 3.7: Examples of theoretical power spectra required for Gendron method ($\frac{D}{r_0} = 38$ @ 700nm). (*Left*) PSDs associated with eigenmode number 50. (*Right*) PSDs associated with eigenmode number 200.

3.5.3 Optimized modal gains

The optimized modal gain g_i is obtained by minimizing the criterion $J_i^G = \sigma_i^2$ (eq. 3.41). We have now for our case study all required ingredients to proceed to the minimization problem, namely the PSDs of $\boldsymbol{\varphi}_{tur_\parallel}^{MP}$, $\boldsymbol{\varphi}_{tur_\perp}^{MP}$, and $\mathbf{w}^{MP}$, and the modulus of the system transfer functions $|E_i|$, $|H_{n,i}|$, and $|H_i|$.

Figure 3.8 shows the criterion $J_i^G = \sigma_i^2$ as a function of the gain g_i for eigenmodes number 50 and 200. The contributions to J_i^G coming from each of the three terms in equation 3.41 are also shown. The SNR was set to 10. For well-seen modes, such as eigenmode 50, there is a value of g_i for which the residual variance σ_i^2 reaches a minimum. For eigenmode 50 the residual variance σ_{50}^2 reaches a minimum when $g_{50} = 0.33$, as shown in figure 3.8. For badly-seen modes, such as eigenmode number 200, the contributions of both the propagated remaining error and propagated measurement noise always dominate, and the minimum of the residual variance is simply obtained when $g_i = 0$. That is, any attempt to compensate for these eigenmodes will be futile. In particular, note that for eigenmode 200 it is the propagated remaining error that dominates.

It is also interesting to see from figure 3.8 how each of the three contributions evolve as g_i increases. In particular, note that the remaining error term increases rather smoothly with the gain. This is due to the fact that even if the cut-off frequency of $|H_i|$ does increase with g_i, the PSD of $\varphi_{tur_\perp,i}^{MP}$ at higher frequencies rolls off steeply. Hence, the value of the integral $\int |H_i(j\omega)|^2 \langle |\tilde{\varphi}_{tur_\perp,i}^{MP}(j\omega)|^2 \rangle \, d\omega$ does not in-

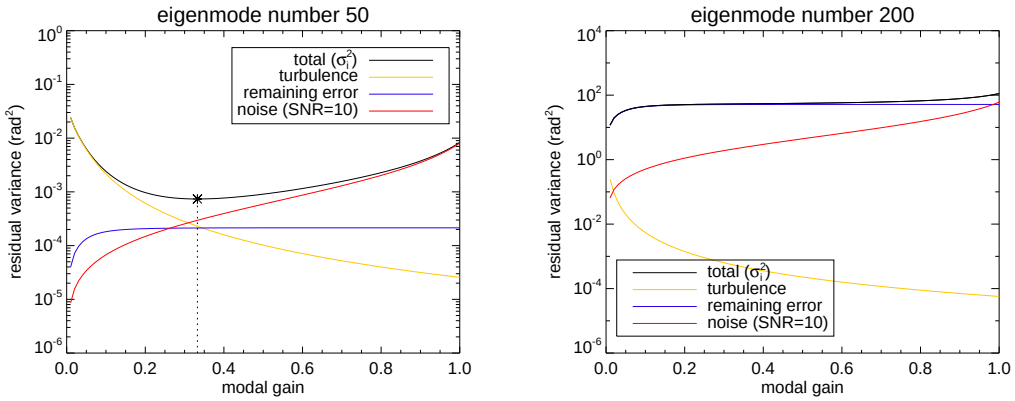

Figure 3.8: Residual variance σ_i^2 as a function of the gain g_i. The individual contributions to σ_i^2 are also shown: turbulence $\int |E_i(j\omega)|^2 \langle |\tilde{\varphi}^{MP}_{tur_\parallel,i}(j\omega)|^2 \rangle \, d\omega$, propagated remaining error $\int |H_i(j\omega)|^2 \langle |\tilde{\varphi}^{MP}_{tur_\perp,i}(j\omega)|^2 \rangle \, d\omega$, and propagated measurement noise $\int |H_{n,i}(j\omega)|^2 \langle |\tilde{w}_i^{MP}(j\omega)|^2 \rangle \, d\omega$. The simulation conditions are $\frac{D}{r_0} = 38$ @ 700nm, and SNR=10. (*Left*) eigenmode number 50. (*Right*) eigenmode number 200.

creases dramatically with the gain. On the other hand, the contribution of the noise term does increase steadily with the gain due to the fact that its PSD is a constant and as the cut-off frequency of $|H_{n,i}|$ increases with the gain the value of the integral $\int |H_{n,i}(j\omega)|^2 \langle |\tilde{w}_i^{MP}(j\omega)|^2 \rangle \, d\omega$ increases substantially too.

Analytically, the optimized modal gains can be determined by solving the set of equations $\partial J_i^G / \partial g_i = 0$. The differentiation of J_i^G can be expressed as:

$$\begin{aligned} \frac{\partial J_i^G}{\partial g_i} &= \int_{-\infty}^{\infty} \frac{\partial |E_i(j\omega)|^2}{\partial g_i} \langle |\tilde{\varphi}^{MP}_{tur_\parallel,i}(j\omega)|^2 \rangle \, d\omega \\ &+ \int_{-\infty}^{\infty} \frac{\partial |H_i(j\omega)|^2}{\partial g_i} \langle |\tilde{\varphi}^{MP}_{tur_\perp,i}(j\omega)|^2 \rangle \, d\omega \\ &+ \int_{-\infty}^{\infty} \frac{\partial |H_{n,i}(j\omega)|^2}{\partial g_i} \langle |\tilde{w}_i^{MP}(j\omega)|^2 \rangle \, d\omega \ . \end{aligned} \tag{3.49}$$

The partial derivatives of the system transfer functions can be easily computed analytically from their theoretical expressions [18]. Figure 3.9 shows a plot of $\partial J_i^G / \partial g_i$ as a function of g_i for different eigenmodes. Note that for well-seen modes the optimized modal gain g_i is the one for which the curve of $\partial J_i^G / \partial g_i$ crosses zero. Numerically, a dichotomy algorithm can be used to find the zero-crossing value of g_i. On the other hand, note that for badly-seen modes there is actually no local minimum and so the curve of $\partial J_i^G / \partial g_i$ never crosses zero. Nevertheless, a dichotomy algorithm with an initial value

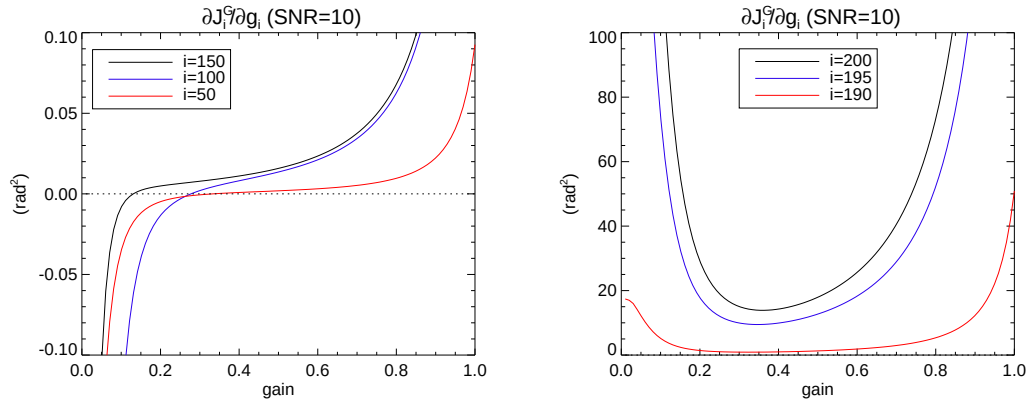

Figure 3.9: $\partial J_i^G / \partial g_i$ as a function of g_i for different eigenmodes (SNR=10). (*Left*) Well-seen modes: 50, 100 and 150. (*Right*) Badly-seen modes: 190, 195, and 200.

of $g_i = g_{\max}$ and programmed to decrease the gain within the interval $0 \leq g_i \leq g_{\max}$ until a change in sign is found will lead to the right optimized modal gain, i.e. $g_i = 0$.

The value of $g_{\max}$ is fixed from stability constraints. It can be shown that in order to ensure the relative stability of an AO system with a total delay of 2 frames the maximum gain of an integrator should be set to $g_{\max} = 0.5$ [90].

We would like to evaluate with numerical simulations what is the improvement in performance brought by taking into account the propagated remaining error term in equation 3.49. Therefore, we have computed two sets of optimized modal gains. The first set is computed by taking into account the three terms in equation 3.49 whereas for the second set the propagated remaining error term has been neglected (like in SCAO systems). The two sets of optimized modal gains for all eigenmodes and for SNR=10 and SNR=100 are shown in figure 3.10. As expected, higher gains are assigned to well-seen modes whereas lower gains (including zero gain) are assigned to badly-seen modes. Note also that taking into account the remaining error term will produce even lower gains for badly-seen modes. This result was expected from figures 3.5 and 3.8(right) from which we saw that the propagated remaining error is in general stronger than the propagated measurement noise for badly-seen modes. Clearly, as the SNR increases the propagated measurement noise decreases and the propagated remaining error becomes more important. This is why the difference between the two sets of optimized modal gains assigned to badly-seen modes is bigger for SNR=100 than for SNR=10.

The performance in the FoV in terms of Strehl Ratio (SR) at 2.2μm obtained from numerical simulations is shown in figure 3.11. Note that for SNR=10 there is a little

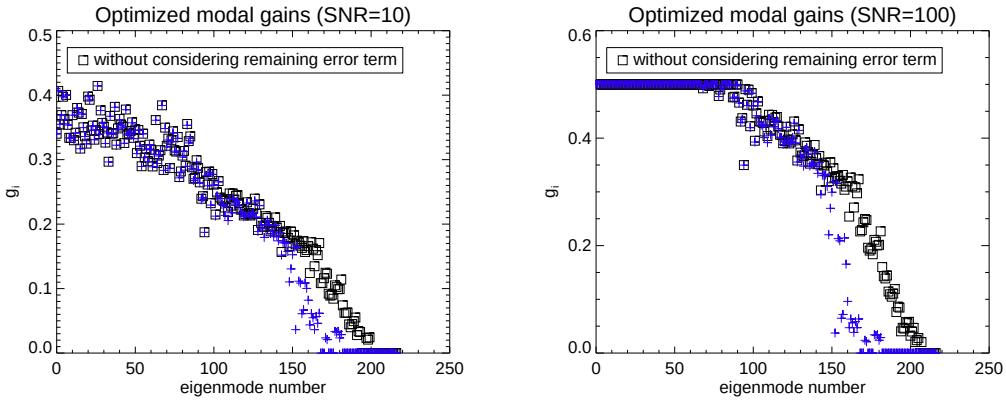

Figure 3.10: Optimized modal gains for all eigenmodes obtained with the Gendron method. (+) Taking into account the three terms of equation 3.49. (□) Neglecting the propagated remaining error term. (*Left*) SNR=10 (*Right*) SNR=100.

difference in performance obtained with the two sets of optimized modal gains. On the other hand, neglecting the propagated remaining error in the computation of optimized modal gains for the case of SNR=100 will lead to a substantial drop in SR in the FoV due to the fact that badly-seen modes have not been controlled correctly.

We should remark that Le Roux *et. al.* [131, 132] did not find this behavior of the MOMGI control law in their numerical simulations because of the method they used to simulate the atmospheric turbulence. Indeed, they used an auto-regressive (AR) model of the turbulence that does not simulate high-order spatial frequencies. In consequence, the propagation of the remaining error is effectively not present, and the optimized modal gains computed using the conventional Gendron method gave them good results.

In conclusion, it is possible in principle to extend the Gendron method to MCAO by taking into account the propagated remaining error term. However, it is required to know a-priori the theoretical PSDs of $\boldsymbol{\varphi}^{MP}_{tur_{\parallel}}$, $\boldsymbol{\varphi}^{MP}_{tur_{\perp}}$ and $\mathbf{w}^{MP}$. The possibility of estimating these PSDs from real-time data will be discussed in section 3.7.

3.5.4 TLS reconstructor versus MOMGI

It is important to note the similarities between a control law based on the TLS reconstructor plus a simple integrator and the MOMGI control law. In fact, the former control law can also be expressed as a LS reconstructor (i.e. no truncated modes) plus

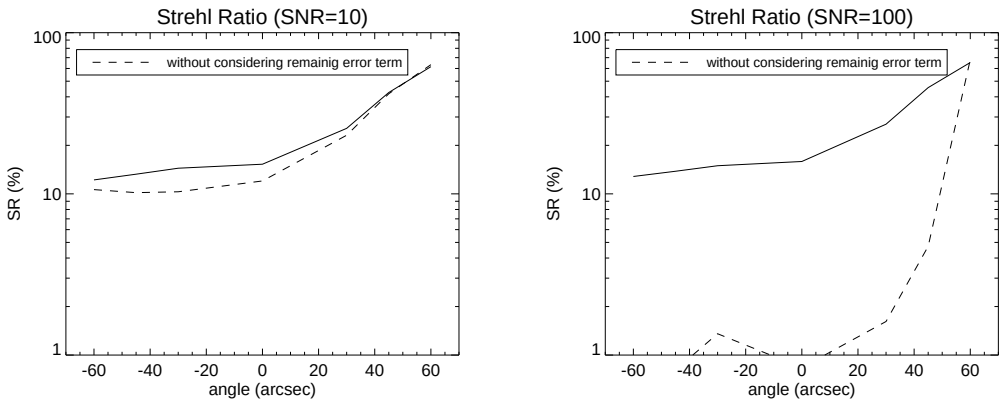

Figure 3.11: Performance in the FoV (SR at 2.2μm) for the Multi-conjugate Optimized Modal Gain Integrator (MOMGI). The gains were computed using the Gendron method, with and without taking into account the propagated remaining error term. (*Left*) SNR=10 (*Right*) SNR=100.

a modal integrator with a transfer matrix given by:

$$C_i^{MP} = \begin{cases} 0 & \text{for truncated eigenmodes} \\ \frac{g_{\max}}{1-z^{-1}} & \text{for others.} \end{cases} \tag{3.50}$$

where the gain $g_i = g_{\max}$ is the same value for all non-truncated system modes. The border between corrected ($g_i = g_{\max}$) and not-corrected ($g_i = 0$) modes is sharp. The main advantage of the MOMGI control law with respect to the TLS reconstructor plus a simple integrator control law is the fact that the modal gains evolve smoothly according to the SNR of each eigenmode. The performance of the MOMGI control law will be better in particular for high-order AO systems, as they will exhibit the full range of optimized modal gains $0 \leq g_i \leq g_{\max}$. A comparison in performance between these two control laws based on numerical simulations can be found in reference [112].

3.6 Dessenne method

Caroline Dessenne [22] proposed an alternative criterion to the one introduced by E. Gendron for SCAO systems. We will study in this section its applicability to MCAO. Before studying the MCAO case, let us review the hypotheses behind the Dessenne method as it was proposed for SCAO systems.

3.6.1 The SCAO case

As opposed to the Gendron method, the Dessenne method has the important advantage of not requiring to know a-priori any theoretical PSDs. Instead, all required information is deduced from the vector $\boldsymbol{\varphi}_{mes}^{MP}$ (see figures 3.3 and 3.6), which can be obtained directly from the WFS slopes as stated in equation 3.43. From figure 3.6 we can see that:

$$\tilde{\varphi}_{mes,i}^{MP} = IR_\tau \tilde{\varphi}_{res,i}^{MP} + IR_\tau \tilde{\varphi}_{tur_\perp,i}^{MP} + R_\tau \tilde{w}_i^{MP} \ . \tag{3.51}$$

Neglecting the remaining error term —as it is done in SCAO— the variance of $\varphi_{mes,i}^{MP}$ can be expressed as:

$$\begin{aligned} \mathrm{var}\{\varphi_{mes,i}^{MP}\} &= \int |I(j\omega)R_\tau(j\omega)|^2 \langle |\tilde{\varphi}_{res,i}^{MP}(j\omega)|^2 \rangle \, d\omega \\ &+ \int |R_\tau(j\omega)|^2 \langle |\tilde{w}_i^{MP}(j\omega)|^2 \rangle \, d\omega \ , \end{aligned} \tag{3.52}$$

where we have also assumed that there is no correlation between $\varphi_{res,i}^{MP}$ and w_i^{MP} although, from equation 3.39, we can see that $\varphi_{res,i}^{MP}$ does depends on w_i^{MP}. This assumption relies totally on the white nature of w_i^{MP} and the fact that the noise is propagated *after* a given time delay τ, so its correlation is equal to zero.

Now, from equation 3.6 it can be seen that $|R_\tau| = 1$ and from equation 3.5 it can be shown that [90]:

$$I(j\omega) = \mathrm{sinc}^2\left(\frac{\omega T}{2}\right) e^{-\omega T/2} \ . \tag{3.53}$$

Therefore, $|I| \approx 1$ since the sinc^2 function has only an impact on the modulus of I at high frequencies. Then, equation 3.52 can be rewritten as:

$$\begin{aligned} \mathrm{var}\{\varphi_{mes,i}^{MP}\} &= \int \langle |\tilde{\varphi}_{res,i}^{MP}(j\omega)|^2 \rangle \, d\omega + \int \langle |\tilde{w}_i^{MP}(j\omega)|^2 \rangle \, d\omega \\ &= \mathrm{var}\{\varphi_{res,i}^{MP}\} + \mathrm{var}\{w_i^{MP}\} \end{aligned} \tag{3.54}$$

From this equation Dessenne realized that the minimization of $\mathrm{var}\{\varphi_{mes,i}^{MP}\}$ was equivalent to the minimization of $\sigma_i^2 = \mathrm{var}\{\varphi_{res,i}^{MP}\}$. Therefore, she proposed to calculate the ith optimized modal gain by minimizing directly the variance of $\varphi_{mes,i}^{MP}$. Hence, the Dessenne criterion can be written as:

$$J_i^D \triangleq \int_{-\infty}^{\infty} \langle |\tilde{\varphi}_{mes,i}^{MP}(j\omega)|^2 \rangle \, d\omega \ . \tag{3.55}$$

Note that the dependence of J_i^D on the system transfer functions is not explicit in

equation 3.55. In order to introduce this dependence Dessenne used a fundamental relationship between the closed-loop measurement $\varphi^{MP}_{mes,i}$ and the open-loop measurement $\varphi^{MP,OL}_{mes,i}$. Indeed, from the two block diagrams in figure 3.3 it can be shown that:

$$\tilde{\varphi}^{MP}_{mes,i} = \frac{1}{1+I^2R_\tau BC^{MP}_i}\left[R_\tau I\tilde{\varphi}^{MP}_{tur_\perp,i} + R_\tau I\tilde{\varphi}^{MP}_{tur_\parallel,i} + R_\tau\tilde{w}^{MP}_i\right] \quad (3.56)$$

$$\tilde{\varphi}^{MP,OL}_{mes,i} = R_\tau I\tilde{\varphi}^{MP}_{tur_\perp,i} + R_\tau I\tilde{\varphi}^{MP}_{tur_\parallel,i} + R_\tau\tilde{w}^{MP}_i \ . \quad (3.57)$$

Dividing eq. 3.56 by eq. 3.57, and recalling the definition of the rejection transfer function (eq. 3.34), leads to:

$$\tilde{\varphi}^{MP}_{mes,i}(j\omega) = E_i(j\omega)\ \tilde{\varphi}^{MP,OL}_{mes,i}(j\omega)\,. \quad (3.58)$$

It is important to note that this fundamental relationship is only valid if the propagated measurement noise and the propagated remaining error are the same in closed-loop and in open-loop. Finally, substituting eq. 3.58 in eq. 3.55 J^D_i becomes:

$$J^D_i = \int_{-\infty}^{\infty} |E_i(j\omega)|^2\langle|\tilde{\varphi}^{MP,OL}_{mes,i}(j\omega)|^2\rangle\, d\omega\,. \quad (3.59)$$

Finally, note that for the Dessenne method it is required to know the PSD of $\varphi^{MP,OL}_{mes,i}$, and the rejection transfer function of the system needs to be well characterized. The spectra of $\boldsymbol{\varphi}^{MP,OL}_{mes}$ can be obtained *experimentally* by running the AO system in open-loop.

3.6.2 The MCAO case

Let us now study the MCAO case starting from equation 3.51. We will derive an expression for the variance of $\varphi^{MP}_{mes,i}$ but this time without neglecting the remaining error term. Considering once again that $|R_\tau| = 1$ and $|I| \approx 1$, and that the noise w^{MP}_i is not correlated with $\varphi^{MP}_{res,i}$ nor $\varphi^{MP}_{tur_\perp,i}$, the variance of $\varphi^{MP}_{mes,i}$ can be expressed as:

$$\begin{aligned}\mathrm{var}\{\varphi^{MP}_{mes,i}\} &= \mathrm{var}\{\varphi^{MP}_{res,i}\} + \mathrm{var}\{\varphi^{MP}_{tur_\perp,i}\} + \mathrm{var}\{w^{MP}_i\} \\ &+ 2\,\mathrm{covar}\{\varphi^{MP}_{res,i}, \varphi^{MP}_{tur_\perp,i}\}\ .\end{aligned} \quad (3.60)$$

Note that we cannot assume that $\varphi^{MP}_{res,i}$ and $\varphi^{MP}_{tur_\perp,i}$ are uncorrelated. We will derive now the covariance term from equation 3.39. We will assume nevertheless that the correlation between $\varphi^{MP}_{tur_\parallel,i}$ and $\varphi^{MP}_{tur_\perp,i}$ is negligible. Then, the covariance term can be

expressed as:

$$\text{covar}\{\varphi^{MP}_{res,i}, \varphi^{MP}_{tur_\perp,i}\} \approx -\int H_i(j\omega)\langle|\tilde{\varphi}^{MP}_{tur_\perp,i}(j\omega)|^2\rangle\, d\omega \ . \tag{3.61}$$

Finally, substituting equation 3.61 into 3.60 leads to:

$$\begin{aligned}\text{var}\{\varphi^{MP}_{mes,i}\} &= \text{var}\{\varphi^{MP}_{res,i}\} + \text{var}\{\varphi^{MP}_{tur_\perp,i}\} + \text{var}\{w^{MP}_i\} \\ &- 2\int H_i(j\omega)\langle|\tilde{\varphi}^{MP}_{tur_\perp,i}(j\omega)|^2\rangle\, d\omega \ .\end{aligned} \tag{3.62}$$

From this equation we can see that the minimization of $\text{var}\{\varphi^{MP}_{mes,i}\}$ *is not equivalent* to the minimization of $\sigma_i^2 = \text{var}\{\varphi^{MP}_{res,i}\}$. Indeed, the covariance term introduces a dependence on the closed-loop transfer function $H_i(j\omega)$ which in turn depends on the gain g_i. Therefore, finding a gain g_i that minimizes $\text{var}\{\varphi^{MP}_{mes,i}\}$ does not mean that it will minimize $\sigma_i^2 = \text{var}\{\varphi^{MP}_{res,i}\}$ too. In the following sections we will verify this argument with the help of numerical simulations. We will apply the Dessenne method to an MCAO case and put in evidence the problems associated with this method.

3.6.3 Temporal power spectra

In order to apply the Dessenne method it is required to estimate the PSD of $\varphi^{MP,OL}_{mes,i}$. Analyzing the block diagrams shown in figure 3.6 it can be shown that:

$$\langle|\tilde{\varphi}^{MP,OL}_{mes,i}(j\omega)|^2\rangle \approx \langle|\tilde{\varphi}^{MP}_{tur_\parallel,i}(j\omega)|^2\rangle + \langle|\tilde{\varphi}^{MP}_{tur_\perp,i}(j\omega)|^2\rangle + \langle|\tilde{w}^{MP}_i(j\omega)|^2\rangle \tag{3.63}$$

where we have neglected all cross-spectra. First, let us study what happens in the absence of measurement noise. In this case we can predict that:

$$\langle|\tilde{\varphi}^{MP,OL}_{mes,i}(j\omega)|^2\rangle \approx \langle|\tilde{\varphi}^{MP}_{tur_\parallel,i}(j\omega)|^2\rangle + \langle|\tilde{\varphi}^{MP}_{tur_\perp,i}(j\omega)|^2\rangle \ . \tag{3.64}$$

We can verify this phenomenon by numerical simulations, just as we did in section 2.4.6 to verify the variance distribution in the eigenspace. Figure 3.12(left) shows the variance distribution in the eigenspace for the present simulation conditions ($\frac{D}{r_0} = 38$ @ 700nm) and computed following the same procedure outlined in section 2.4.6 (including the same approximation for the matrix $\mathbf{M}_{\alpha_\perp}$). Note that the *simulated* variance distribution shown in figure 3.12(left) actually corresponds to the variance distribution of $\boldsymbol{\varphi}^{MP,OL}_{mes}$ when no measurement noise is simulated. Figure 3.12(right) shows an example of the theoretical and simulated PSDs. We chose to show the PSDs associated

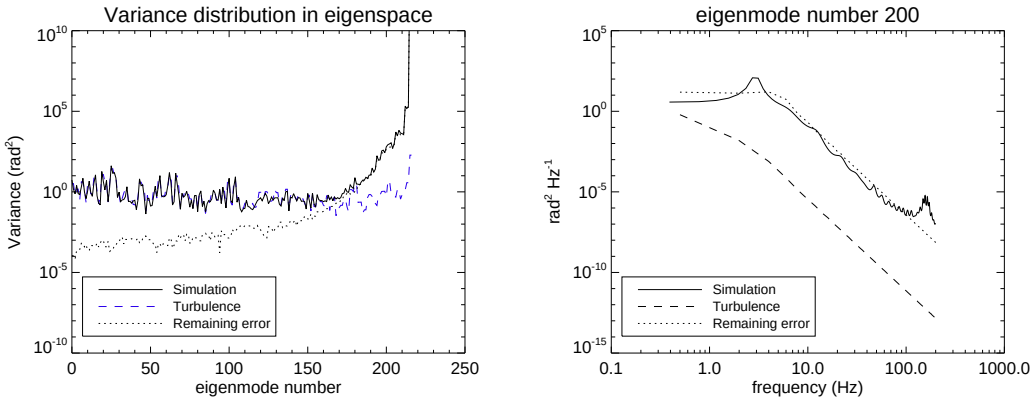

Figure 3.12: (*Left*) Variance distribution in eigenspace ($\frac{D}{r_0} = 38$ @ 700nm). (*Right*) Power spectral density (PSD) associated with eigenmode number 200.

with eigenmode number 200 because this mode is affected by a strong propagation of the remaining error. As predicted from the variance distribution (figure 3.12(left)) and from equation 3.64, the PSD of $\varphi^{MP,OL}_{mes,200}$ is dominated by the PSD of $\varphi^{MP}_{tur_\perp,200}$.

Let us now reconsider the PSD of $\boldsymbol{\varphi}^{MP,OL}_{mes}$ but this time taking into account the effect of the propagated measurement noise. The expected PSD is given by equation 3.63. Figure 3.13 shows the PSD of $\varphi^{MP,OL}_{mes,i}$ obtained from simulations for two eigenmodes: a well-seen one (number 50) and a badly-seen one (number 200). Note that for the eigenmode number 200 the simulated PSD is dominated at low frequencies by the propagated remaining error and at high frequencies by the propagated measurement noise.

3.6.4 Optimized modal gains

The optimized modal gain g_i is obtained by minimizing the criterion J^D_i (eq. 3.59). The required ingredients are in this case the PSD of $\varphi^{MP,OL}_{mes,i}$, and the modulus of the rejection transfer function $|E_i|$. Analytically, the optimized modal gains are determined by solving the set of equations $\partial J^D_i / \partial g_i = 0$. The differentiation of J^D_i can be expressed as:

$$\frac{\partial J^D_i}{\partial g_i} = \int_{-\infty}^{\infty} \frac{\partial |E^{MP}_i(j\omega)|^2}{\partial g_i} \langle |\tilde{\varphi}^{MP,OL}_{mes,i}(j\omega)|^2 \rangle \, d\omega \,. \tag{3.65}$$

We have computed the optimized modal gains using the PSDs of $\boldsymbol{\varphi}^{MP,OL}_{mes}$ generated from simulations and presented in the previous subsection (Figure 3.13). Figure 3.14 shows the optimized modal gains computed with both Dessenne method and Gendron

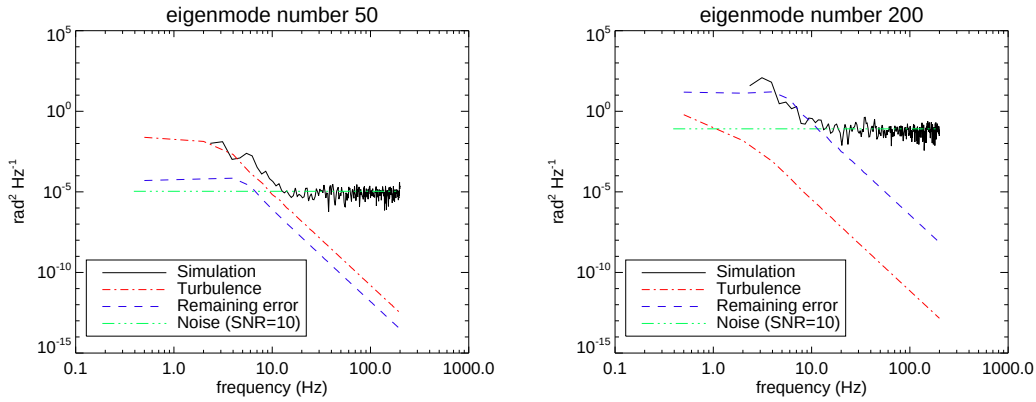

Figure 3.13: PSD of $\varphi^{MP,OL}_{mes,i}$ obtained from simulations. (*Left*) eigenmode number 50. (*Right*) eigenmode number 200. The theoretical PSDs of the turbulence, the propagated remaining error, and the propagated measurement noise (SNR=10) are also shown.

method (all three terms included) under the same simulation conditions (SNR=10). Recall that Dessenne's gains minimize $\text{var}\{\varphi^{MP}_{mes,i}\}$ whereas Gendron's gains minimize $\sigma_i^2 = \text{var}\{\varphi^{MP}_{res,i}\}$. We can see that in general Dessenne's gains are higher, and that the difference between both sets of gains becomes quite important for badly-seen modes. We can explain this trend as follows. Recall that $\text{var}\{\varphi^{MP}_{mes,i}\}$ depends on the integral of the PSD of $\varphi^{MP}_{tur_\perp,i}$ multiplied by $H_i(j\omega)$ (i.e. the last term of eq. 3.62). Then, since the propagation of the remaining error $\varphi^{MP}_{tur_\perp,i}$ is very strong for badly-seen modes, the influence of this term will be important in the minimization of $\text{var}\{\varphi^{MP}_{mes,i}\}$ driving the assigned gains to higher values. If we applied this set of gains to an MCAO system, it is clear that the high gains assigned to the badly-seen modes would lead to a considerable loss in performance and eventually an unstable operation of the MCAO system. In conclusion, the Dessenne method is not applicable to MCAO. The simulation results that put this problem in evidence were the topic of a conference paper [112].

3.7 Discussion: practical implementation

The main advantage of the Dessenne method with respect to the Gendron method is the fact that, for SCAO systems, it is easier to estimate the PSD of $\varphi^{MP,OL}_{mes,i}$ from experimental data —as required by the Dessenne method— than estimating separately the PSDs of $\varphi^{MP}_{tur_\parallel,i}$ and w_i^{MP} from experimental data —as required by the Gendron method [56].

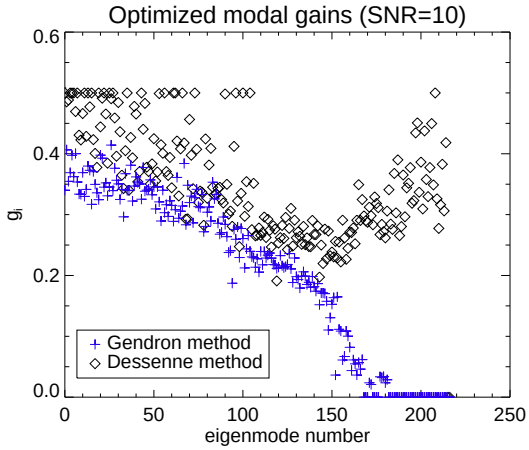

Figure 3.14: Optimized modal gains computed with the Dessenne method. The optimized modal gains computed with the Gendron method –figure 3.10(left)– are also plotted for comparison.

The impossibility of applying the Dessenne method in MCAO is a serious shortcoming of modal gain optimization in MCAO. Furthermore, the practical implementation of the Gendron method is not evident either. As opposed to the SCAO case, the Gendron method in MCAO requires the separate estimation of three PSDs: the PSDs of $\varphi^{MP}_{tur_{\parallel},i}$, $\varphi^{MP}_{tur_{\perp},i}$, and w_i^{MP}. The main difficulty lies in the estimation from experimental data of the first two PSDs related to the atmospheric turbulence because it is not possible to measure separately the contributions of these two terms. In particular, the only possible method to characterize the propagation of the remaining error and estimate the corresponding PSDs of $\varphi^{MP}_{tur_{\perp},i}$ for a given system is by numerical simulations using a calibrated model. In fact, this is the approach that other authors had to follow to characterize the propagation of the remaining error, but in the framework of other different applications. For instance, J.P Veran *et. al.* [153] used a calibrated model of the PUEO[2] system to characterize the propagation of the remaining error in order to estimate the PSFs of SCAO-corrected images which are in turn required for image deconvolution. Even if the characterization of the propagated remaining error using a calibrated model is totally valid for post-processing applications, it is clear that it is not well adapted for real-time applications, such as the MOMGI control law, in which it should be possible to recalculate the modal gains *in situ* to cope with changes in the atmospheric turbulence conditions.

[2]The SCAO system of the Canada-France-Hawaii Telescope (CFHT).

We should recall that it is nevertheless possible to neglect the propagated remaining error term in the computation of the optimized modal gains using the Gendron method when working at low SNRs (SNR$<$ 10 equivalent to $M_V \geq 12$) —as was illustrated in figure 3.11— at the expense of a slight loss in performance. In this case, it would only be required to estimate two PSDs: the PSDs of $\varphi^{MP}_{tur_{\parallel},i}$ and w_i^{MP}. However, once again, the estimation of the PSDs of $\varphi^{MP}_{tur_{\parallel},i}$ from experimental data is not straightforward in the MCAO case. It would be most probably required to combine the use of theoretical PSDs (as the ones used in section 3.5.1) with experimental information (e.g. r_0, mean wind speed, etc.) in order to synthesize the required PSDs of $\varphi^{MP}_{tur_{\parallel},i}$.

In conclusion, the difficulties in estimating all the PSDs required to compute the optimized modal gains in MCAO cast serious doubts on the practical implementation of the MOMGI control law.

Chapter 4

Validation of MCAO with the MAD system

4.1 Introduction

The European Southern Observatory (ESO) in collaboration with external research institutes conceived an instrument prototype, the *Multi-conjugate Adaptive Optics Demonstrator* (MAD), to prove the concepts of both star-oriented and layer-oriented MCAO, and to compare them on the sky [95, 92]. The assembly, integration and testing (AIT) and system characterization of the MAD star-oriented configuration took place at ESO headquarters in Germany during 2004-2006. As part of my PhD training, I had the opportunity to participate in the MAD project during this period.

As a first task, I developed a *MAD simulation tool* matching most of the MAD system specificities. The MAD system characterization and the customization of the simulation tool will be described in section 4.2. We then utilized our simulator to estimate the performance of the star-oriented module of MAD in SCAO, GLAO, and MCAO modes under high flux conditions. These simulation results will be presented in section 4.3. We then carried out SCAO, GLAO, and MCAO experiments in the laboratory and compared the performance with simulations matching all possible experimental conditions. These comparisons will be presented in section 4.5. The results obtained in the laboratory are, to our knowledge, the first experimental results to validate under realistic conditions the concepts of GLAO and MCAO.

The reconstruction and control laws implemented in the real system were limited to the truncated least squares (TLS) reconstructor (section 2.3.2.3) and a two-parameter temporal controller described in section 4.2.3.1.

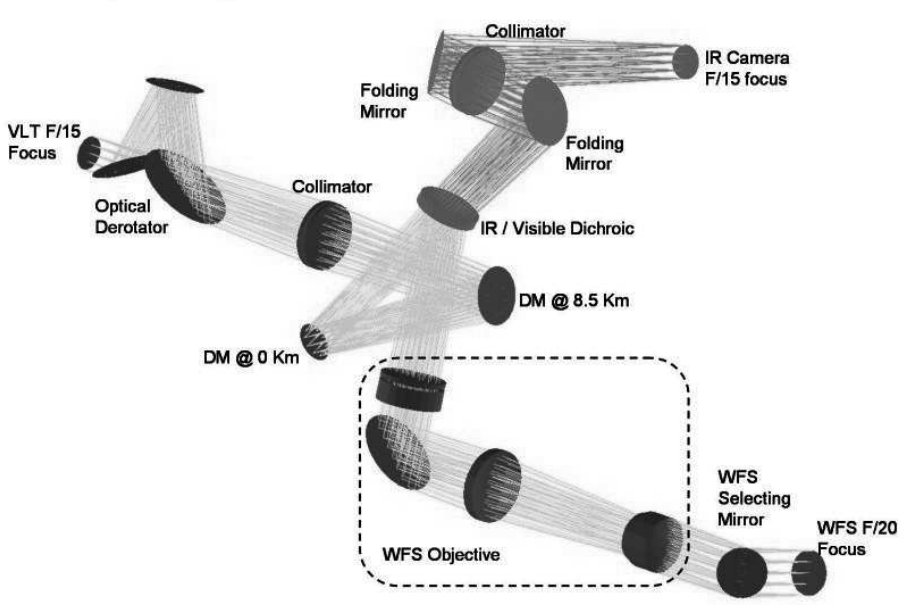

Figure 4.1: MAD optical design.

Understanding the discrepancies between simulation and experiments lead us to produce a very accurate model of the MAD system. The possibility to build reconstruction matrices based on *synthetic* interaction matrices produced with our MAD simulation tool was also studied, and tested in the laboratory. The results of these experiments are presented in section 4.6.

MAD will be installed in one of the VLT telescopes ($D = 8$m with a central occultation of $oc = 14\%$) located in the Paranal Observatory. On-sky tests are scheduled to take place in the first quarter of 2007.

4.1.1 Overview of the MAD system

MAD was conceived to obtain a uniform Strehl ratio in K band over a 2' FoV using only natural guide stars. The implementation was done using existing technology and reusing as much as possible key components developed in the scope of existing AO systems at ESO. The optical layout of MAD is shown in figure 4.1. A detailed description of the optical design of MAD can be found in [95].

The MAD corrective optics is based on two bimorph deformable mirrors (DMs). One mirror (DM1) is conjugated to the telescope pupil for ground layer turbulence

correction, and the second one (DM2) is conjugated at 8.5 km above the telescope aperture. The ground DM is supported by a tip-tilt mount which allows offloading the tip/tilt component from the ground DM in order to relax its stroke requirements. Nevertheless, all experimental results shown in this chapter were produced without offloading. The characterization of the DMs will be presented in section 4.2.2.

The star-oriented wavefront sensing of MAD is based on three Shack-Hartmann wavefront sensors (WFSs) each one coupled to a NGS located within the 2 arcmin FoV. On the other hand, the layer-oriented wavefront sensing of MAD is based on a multi-pyramid wavefront sensor comprising eight movable pyramids (for a maximum of 8 NGSs within 2 arcmin FoV) and two CCD detectors conjugated to the same altitudes as the deformable mirrors. The two wavefront sensing modules cannot be used on MAD simultaneously. The characterization of star-oriented wavefront sensing module will be presented in section 4.2.1. The layer-oriented module of MAD is described further in reference [155].

In order to calibrate the MAD system, a *calibration unit* (CU1) can be placed in the input focus. The CU1 comprises a set of illuminated fibers mounted on a XY table to scan the full 2-arcmin FoV. Two types of fibers can be used: a *single-mode* fiber and a *multi-mode* fiber. The former is used to emulate a point source whereas the latter is used to emulate an extended source producing SH spots of about 2x2 CCD-pixels large.

For testing the MAD system in the laboratory a turbulence generator called MAPS (*Multi Atmospheric Phase screens and Stars*) can be placed at the MAD input focus. The characterization of MAPS will be presented in section 4.2.4, and it has also been presented in reference [77].

For evaluating the improvement in resolution brought by adaptive optics correction MAD uses an infrared camera called CAMCAO (*CAmera for MCAO*). It is a 1' FoV infrared camera based on a 2048x2048-pixels infrared detector ($\lambda_{im} = 2.2\mu$m). CAMCAO is mounted on an XY table for scanning the full 2' FoV. The pixel scale is 0.028" at 2.2 μm, which corresponds to ≈2x2 pixels on the FWHM of the diffraction-limited PSF.

4.2 MAD system characterization

In this section we will describe the characteristics of each MAD component, namely the Shack-Hartmann WFSs, the deformable mirrors, the turbulence generator MAPS, and the real-time computer. We will also present the models and approximations used in

our MAD simulation tool, and where possible, the cross-validation of simulation results with experimental data.

4.2.1 Shack-Hartmann WFSs

The star-oriented version of MAD comprises three Shack-Hartmann wavefront sensors (SH-WFSs). The lenslet array of each SH-WFS is formed by 8x8 squared subapertures (pitch = 192 μm, focal length = 3.2 mm). Each SH-WFS is mounted on an XY motion unit capable of scanning the whole 2 arcmin FoV in order to pick up the light of the selected natural guide star (NGS).

4.2.1.1 Sampling characteristics

The SH-WFS camera is based on a E^2V CCD39 detector (80x80 CCD pixels, 24 μm/pixel, 2^{16} ADUs). The central wavelength of operation is 700 nm. Each subaperture image (alias SH spot) is sampled with a grid of 8x8 CCD pixels. The pixel scale is equal to $0.3''$/pixel.

The MAD's SH-WFSs highly undersample the diffraction-limited PSF of each subaperture. Indeed, the angular size (FWHM) of the subaperture PSF is $\lambda/d = 0.144''$ at 700nm. According to the Shannon (sampling) theorem, the sampling period should be at least equal to the *half* of the FWHM of the PSF: $0.5(\lambda/d)$. In other words, the FWHM of the PSF should be sampled with at least 2x2 pixels. The *undersampling factor* is defined as the ratio between the actual pixel size and the pixel size required for sampling at Shannon:

$$B \triangleq \frac{\text{pixel scale}}{0.5(\lambda/d)} = \frac{0.3''}{(0.5)(0.144'')} \approx 4 \tag{4.1}$$

We can say then that MAD's SH-WFSs sample at *Shannon over 4*. That is, 4 times less than the minimum required by the sampling theorem.

4.2.1.2 Slopes computation

The SH slopes are computed after dark subtraction using a classical centroid algorithm. Hence, the centroid (x_c, y_c) is simply computed as:

$$x_c = \frac{\sum_i x_i I_i}{\sum_i I_i} \quad ; \quad y_c = \frac{\sum_i y_i I_i}{\sum_i I_i} \tag{4.2}$$

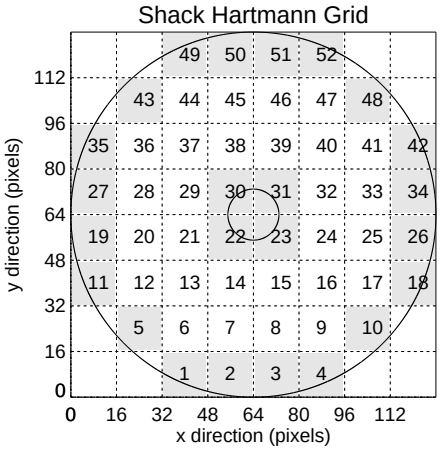

Figure 4.2: Grid of subapertures for the Shack-Hartmann WFSs of MAD. The telescope pupil and the central occultation are also shown. There is a total of 52 valid subapertures (illuminated area $> 50\%$). Partially-illuminated subapertures are shown in grey.

where (x_i, y_i) are the coordinates of the ith pixel, and I_i denotes the intensity on the ith pixel. By default, all 8x8 CCD pixels/subaperture are taken into account in the computation of the centroids. The possibility to apply *windowing*, *thresholding*, and *pixel weighting* has also been implemented in MAD. In this work we will only present a study concerning the advantages of thresholding on MAD in section 4.2.1.5.

4.2.1.3 WFS simulation model

Figure 4.2 shows the Shack-Hartmann grid. A given subaperture is considered to be valid if more than 50% of its area is illuminated. Under these considerations there is a total of 52 valid subapertures.

As discussed in section 1.2.3, we have two possibilities to simulate a SH-WFS; either using a *geometrical* or a *diffractive* model. We have chosen to use the diffractive model in our MAD simulation tool, as it represents more accurately the physical response of a SH-WFS. The telescope pupil will be sampled with 128x128 pixels. Therefore, as seen in figure 4.2, each subaperture will be sampled with 16x16 pixels. Each subaperture image will be computed at Shannon (i.e. 32x32 pixels). Finally, each subaperture image needs to be *binned* into a grid of 8x8 CCD-pixels before centroid computations.

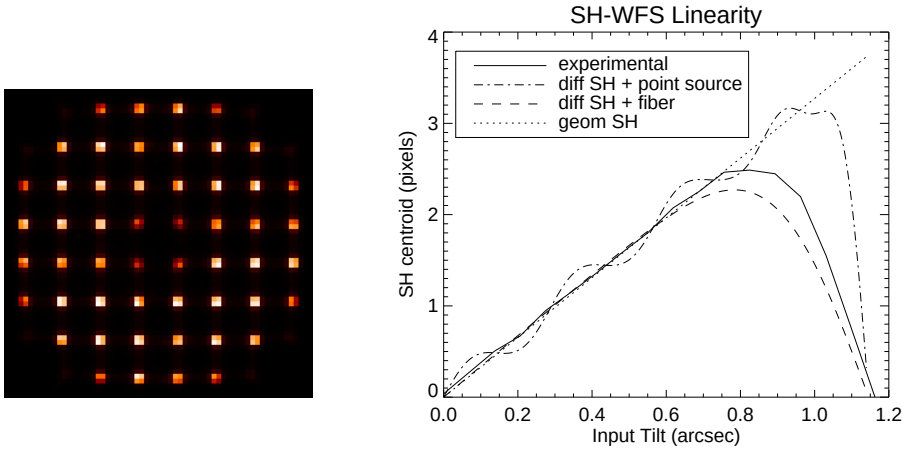

Figure 4.3: (*Left*) Shack-Hartmann spots produced by the multi-mode calibration fiber. (*Right*) Response of one of the MAD's SH-WFSs to a tip Z_2 (x-axis). The experimental curve corresponds to the response obtained with the multi-mode fiber in the laboratory. Simulations were done using both the *geometrical* and the *diffractive* model of a SH-WFS. For the case of the diffractive model, two illumination sources were used: one point source, and one extended source matching the size of MAD's multi-mode calibration fiber.

4.2.1.4 Linearity characterization

The linearity of a SH-WFS is intrinsically related to its sampling characteristics (i.e. the pixel scale). In practice, it is possible to characterize the linearity of a SH-WFS by studying the response of the WFS to a tip (Z_2) or a tilt (Z_3) [133]. We will study below the response obtained with the two types of calibration fibers available in the MAD's calibration unit CU1: a multi-mode fiber (producing SH spots of about 2x2 CCD-pixels), and a single-mode fiber (producing diffraction-limited SH spots which will be undersampled by the CCD camera).

As an example, a real image of the SH spots produced by the multi-mode fiber is shown in figure 4.3(left). For simulation purposes, we have modelled the multi-mode calibration fiber with a Gaussian intensity profile:

$$O(x,y) = \exp\left(-\frac{x^2+y^2}{2\sigma_{fib}^2}\right) , \tag{4.3}$$

where the standard deviation σ_{fib} was obtained by fitting a 2D Gaussian to the SH spots shown in figure 4.3(left), giving a value of $\sigma_{fib} = 0.21''$.

Figure 4.3(right) shows the experimental and the simulated response of the SH-WFS to a tilt (Z_3). The experimental curve corresponds to the response obtained with the multi-mode fiber in the laboratory. Note that the experimental linear range is about ±2.4 CCD-pixels whereas the one from simulations (diff SH+fiber) is about ±2.1 CCD-pixels. The difference is due to the Gaussian approximation used for the calibration fiber. Note that outside the linear range the response of the SH-WFS starts to go back towards zero. This is due to the fact that a SH spot approaching the edge of its subaperture (±4 CCD-pixels for MAD) starts to pollute the neighboring subapertures and biases their centroid estimations. Note that the linear regime of the geometrical model of the SH-WFS is not limited by this effect because the SH slopes are not computed from SH spots (section 1.2.3).

Figure 4.3(right) also shows the (simulated) response of a diffractive SH-WFS when a point source (i.e. the single-mode fiber of MAD) is used for illumination (diff SH + point source). Note that the response is very non-linear. This is due to the fact that the SH spots produced by a point-source are undersampled, i.e. they are smaller than a CCD-pixel (see section 4.2.1.1). Therefore, as seen in figure 4.3(right), the output of the SH-WFS does not change when the (diffraction-limited) SH spots move across the center of a CCD-pixel.

4.2.1.5 Measurement noise

In this section we will present the characterization of the measurement noise σ_w^2 for the MAD's SH-WFSs. We will also discuss the use of thresholding and windowing techniques. As mentioned in section 1.2.2.1, the two main contributions to WFS measurement noise are photon noise σ_{ph}^2 and detector noise σ_{det}^2. From equations 1.55 and 1.56, the theoretical σ_w^2 can be expressed as:

$$\sigma_w^2 = \frac{\pi^2}{2}\frac{1}{n_{ph}}\left(\frac{X_T}{X_D}\right)^2 + \frac{\pi^2}{3}\frac{\sigma_{e^-}^2}{n_{ph}^2}\left(\frac{X_S^2}{X_D}\right)^2 \tag{4.4}$$

where n_{ph} is the number of photons per subaperture and per frame. The meaning of the other parameters and corresponding values for MAD are listed in table 4.1.

The read-out noise $\sigma_{e^-}^2$ for MAD's CCDs was characterized in the laboratory [134]. It is slightly different for each CCD and for each CCD quadrant, but on average it is equal to $\sigma_{e^-} = 7.5\,e^-$ rms per pixel. The CCD gain was also characterized and on average is equal to $1.7\,e^-$/ADU.

Figure 4.4 shows in (– – –) the plot of equation 4.4 as a function of n_{ph}. Note that

Parameter	Description	Value
X_T	FWHM of turbulence-limited SH spots	2 pixels
X_D	FWHM of diffraction-limited SH spots	0.5 pixels
X_S	Size of window to compute centroids	8 pixels
$\sigma^2_{e^-}$	CCD's read-out noise	$7.5\,e^-$

Table 4.1: MAD parameters required to characterize the SH-WFS measurement noise.

this curve is proportional to n^2_{ph} which means that σ^2_w is dominated by the detector noise σ^2_{det}. We have run a simulation to verify that our SH-WFS model follows this trend. The Gaussian calibration fiber (equation 4.3) has been used as illumination source. No atmospheric turbulence is present. Figure 4.4 shows in (−□−) the simulation curve. Note that the simulation curve follows the theoretical one for high and medium flux levels, but it diverges for low fluxes. This is due to the fact that for flux levels below $n_{ph} \approx 10^2$ the SH spots are immersed in noisy CCD pixels that prevent a reliable centroid computation. The WFS measurements are not meaningful anymore and the noise variance σ^2_w explodes.

One technique that can be used to alleviate the effect of measurement noise is thresholding [71]. Thresholding is a non-linear operation applied to the CCD frames prior to the centroids computation. It modifies the intensities $\{I_i\}$ in equation 4.2 according to the following rule:

$$I_{u,i} = \begin{cases} I_i & \text{if } I_i \geq U \\ 0 & \text{if } I_i < U \end{cases} \tag{4.5}$$

where U is called the *threshold value*, and $\{I_{u,i}\}$ denotes the new intensity distribution. There are other alternative ways to apply thresholding —e.g. threshold as a percent of $(I_{max} - I_{min})$ [97]—, but the principle is the same.

Thresholding can effectively reduce the measurement noise variance σ^2_w. However, it may also bias the centroid computation introducing a displacement from the true centroid position [2]. It is important to note that equation 4.4 is not valid anymore when thresholding is applied. J. Ares and J. Arines [2] developed a theoretical expression for σ^2_w when thresholding is applied. This expression is rather complex since it is derived from the analysis of the non-linear effects of thresholding on noise statistics. We will rather study the effect of thresholding with numerical simulations. For example, let us consider a flux level of $n_{ph} \approx 800$ (equivalent to a star magnitude $M_V = 11$ for MAD). Figure 4.5 shows the centroid bias and the effective noise variance σ^2_w as a function

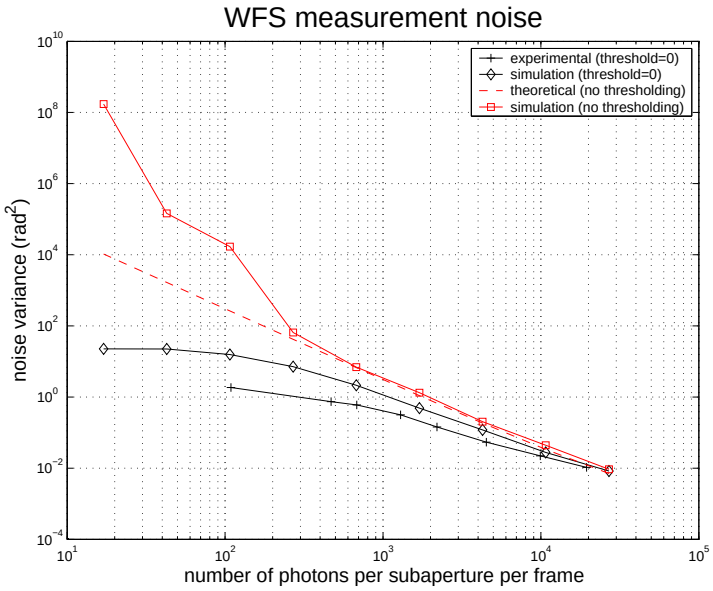

Figure 4.4: WFS measurement noise variance σ_w^2 as a function of the flux per subaperture per frame (n_{ph}).

of the threshold value U (in percent of the maximum intensity I_{max}). We have used once again the Gaussian calibration fiber as illumination source, and no atmospheric turbulence was simulated.

As seen from figure 4.5(left), the centroid bias is not significant under these conditions. However, as stated in reference [2], the centroid bias may become more important for asymmetrical SH spots. Clearly, this would be the case when atmospheric turbulence is present.

The advantage of thresholding, as seen from figure 4.5(right), is that the effective noise variance σ_w^2 can be dramatically reduced. In the case considered here, the best threshold is equal to zero ($U = 0$), which means that only the pixels with *negative* intensity values are set to zero prior to the centroid computation. It is important to note that if a pixel shows a negative intensity is simply due to the presence of additive zero-mean Gaussian noise (in this case the read-out noise). For MAD, a thresholding operation with $U = 0$ has been implemented by default to reduce effectively the variance of measurement noise.

Figure 4.4 shows a curve of the effective measurement noise variance σ_w^2 for MAD as a function of n_{ph} when a threshold $U = 0$ is applied. Both simulation ($- \diamond -$) and experimental ($- + -$) results are displayed. As expected, the threshold $U = 0$

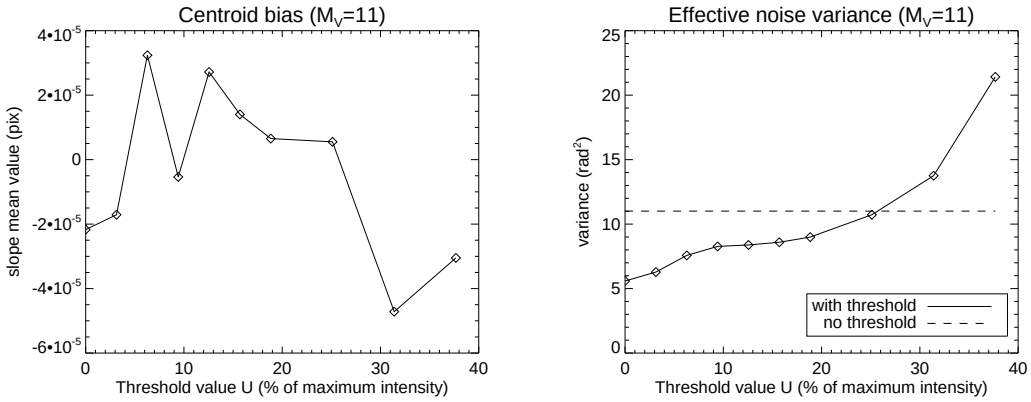

Figure 4.5: Centroid bias (in pixels) and effective noise variance σ_w^2 (in rad^2) as a function of the threshold value (in percent of the maximum intensity I_{max}) for $n_{ph} \approx 800$ (equivalent to a star magnitude $M_V = 11$ for MAD).

effectively reduces the noise variance and its advantage is clearly evidenced at low flux levels. Concerning the simulation results, note that with thresholding ($U = 0$) the effective measurement noise variance σ_w^2 does not diverge anymore at low-flux levels, as it was the case when no thresholding was applied (curve in $-\square-$). Comparing simulation and experimental results (curves in $-\diamond-$ and $-+-$), note that the effective noise variance σ_w^2 computed from experimental data is slightly smaller than the one obtained from simulations.

We will end up our discussion on thresholding by saying that the *optimal* threshold (optimality in the sense of minimum centroid variance) can be different from $U = 0$ when there is an additional background level that contaminates the subaperture images [3]. One common cause of this background level is the illumination cross-talk that may exist between subapertures. The background level for MAD SH-WFSs was also characterized in the laboratory [113]. It is $\approx 1\%$ of n_{ph}. Clearly, the threshold value U would need to be optimized for each flux level n_{ph}. However, we have decided to use the default value $U = 0$ for the experiments presented in this work.

4.2.1.6 Noise covariance matrix

The noise covariance matrix ($\mathbf{C_w}$) of one of the MAD's SH-WFSs was characterized experimentally. Figure 4.6 shows an example of $\mathbf{C_w}$ for a flux level of $n_{ph} = 2 \cdot 10^4$. There is a total of 104 slopes (slopes in x: from 1 to 52, and slopes in y: from 53 to 104). Note that the noise is effectively decorrelated between two different subapertures.

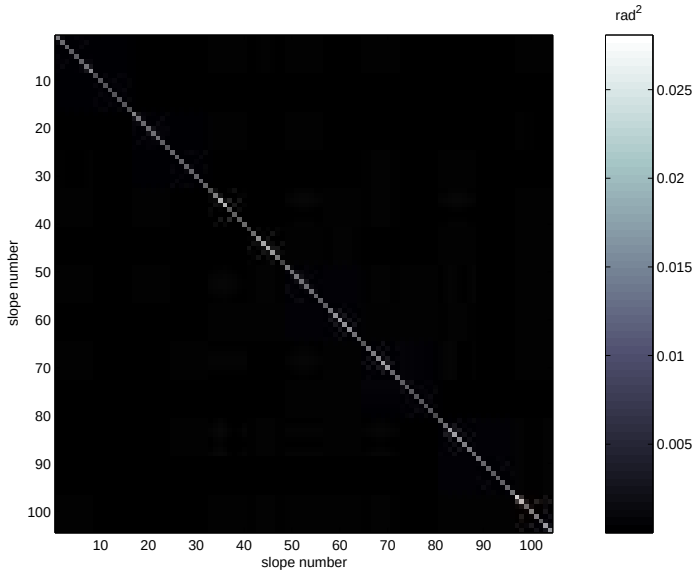

Figure 4.6: Measurement noise covariance matrix for one of the SH-WFSs of MAD. The flux level was $n_{ph} = 2 \cdot 10^4$.

Also, note that partially-illuminated subapertures show a slightly higher noise variance, simply because the flux that falls on these subapertures is less.

4.2.2 Deformable mirrors

The MAD deformable mirrors (DMs) are bimorph-technology DMs [67, 68]. Figure 4.7 shows the DMs geometry. The pupil is defined by the circle D6. Each DM has 60 actuators grouped in 5 rings. Some of the parameters of interest for both DMs are listed in table 4.2. In the following subsections we will describe the characteristics of these DMs.

4.2.2.1 Influence functions

The influence functions (IFs) for both DMs were measured in the laboratory using a *HASO camera*[1] (64x64 pixels) [135]. The influence functions of the inner-ring actuators (ring 1 to 4) are quite different from the ones of the outer ring (ring 5). Examples of IFs for the ground DM are shown in figure 4.8. Note that the IFs of the outer ring are more extended whereas the ones of the inner rings are more localized.

[1] camera from *Imagine Optic*.

	ground DM	upper DM
Conjugated altitude (km)	0	8.5
Number of actuators	60	60
Pupil size (D6) (mm)	60	100
Voltage range (V)	± 400	± 400
Resonant frequencies (Hz)	≈ 300 ≈ 900	≈ 230 ≈ 750

Table 4.2: Parameters of the MAD's bimorph deformable mirrors.

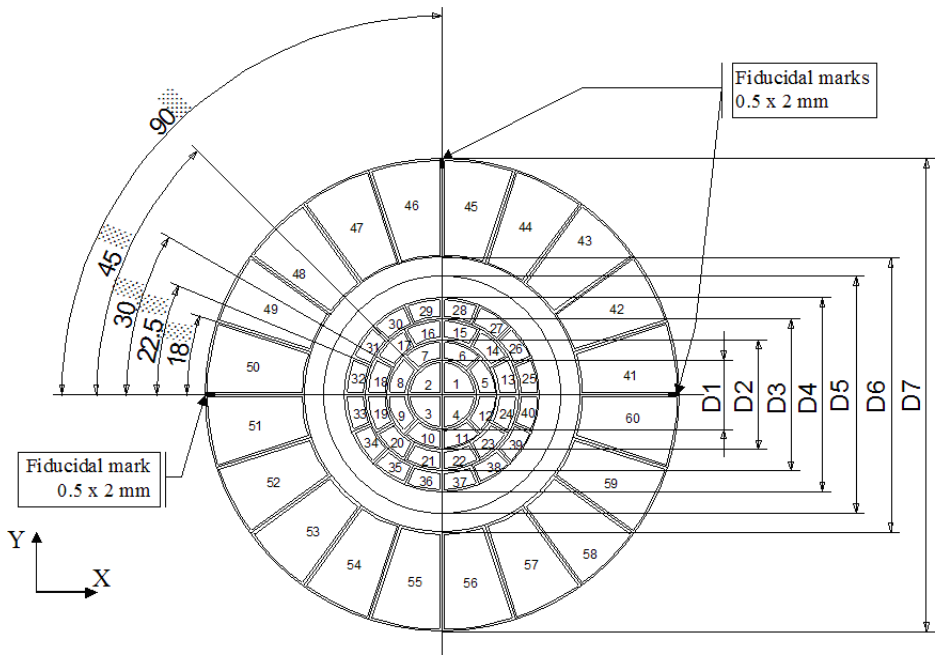

Figure 4.7: Geometry of the bimorph deformable mirrors of MAD. The pupil diameter is D6. There is a total of 60 actuators grouped in 5 rings. (Figure credits: S. Ströbele)

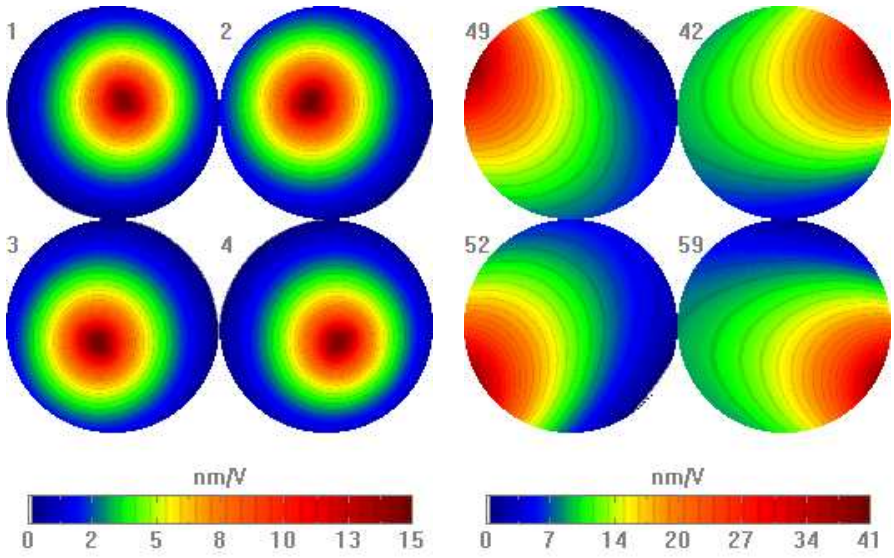

Figure 4.8: (*Left*) Example of influence functions of the inner ring (actuators 1,2,3, and 4). (*Right*) Example of influence functions of the outer ring (actuators 42,49,52, and 59). Deformations are expressed in nm/V.

We have used the actual experimental IFs (64x64 pixels) to simulate the deformable mirrors in the MAD simulation tool. Special care has been taken to interpolate them in order to create IF maps of the required size, i.e. 128x128 pixels for the ground DM, and for the altitude DM the required size can be computed from equation 2.3. Since the altitude DM spans the whole 2 arcmin FoV the required size turns out to be 210x210 pixels.

4.2.2.2 The mirror space

In this section we will study what is the effective number of degrees of freedom of the MAD's DMs. In principle, since MAD's DMs have 60 actuators, then they have 60 degrees of freedom. In other words, the dimension of the mirror space generated by each DM is equal to 60. However, as we discussed in section 1.2.1.2, this is only true when the influence functions of a DM are linearly independent. We will study below if this condition is satisfied by MAD's DMs.

The geometrical covariance matrix (Δ) is defined as the matrix containing the internal products between all influence functions [52]. The matrix Δ can be computed

from the influence function matrix $\mathbf{N}$ of a DM as:

$$\Delta = \mathbf{N}^T\mathbf{N} \ . \tag{4.6}$$

The matrix Δ provides insight on the *coupling* existing between the influence functions of a DM. In principle, if the IFs are strongly coupled it means that the IFs are not *sufficiently* independent and the effective degrees of freedom of the DM will be reduced. In other words, the dimension of the mirror space spanned by the IFs will be less than the number of actuators. Figure 4.9(a) shows the matrix Δ for the ground DM of MAD. Note that there is a strong coupling between the outer-ring actuators. We can expect then the effective number of degrees of freedom to be less than 60. An analysis of the eigenmodes and eigenvalues of Δ can help us to find out the effective number of degrees of freedom. Figure 4.9(c) shows the eigenmodes of Δ and figure 4.9(b) shows the associated eigenvalues. Note that the last five eigenmodes are associated with very low eigenvalues. We can then affirm that the effective number of degrees of freedom for the ground DM of MAD is $\approx$55. A similar conclusion applies to the upper DM of MAD.

As we will discuss in section 4.2.2.3, we will require to compute the matrix Δ^{-1} in order to generate projection matrices of interest. From our discussion above, it should be clear that the matrix Δ is badly-conditioned. Then, the inversion must be computed using the TSVD method and the last 5 eigenmodes should be filtered out.

4.2.2.3 Projection matrices for Zernikes

In this section we will introduce the projection matrices *Zernike to Volts* $\mathbf{P}_{Z2V}$ and *Volts to Zernikes* $\mathbf{P}_{V2Z}$. In principle, any phase function $\varphi(\mathbf{r})$ can be expressed in the DM basis as a linear combination of influence functions $\varphi(\mathbf{r}) \approx \mathbf{Nu}$. Also, $\varphi(\mathbf{r})$ can be approximated by a finite sum of Zernike polynomials $\varphi(\mathbf{r}) \approx \mathbf{Zz}$. The equivalence between the two approximations can only be guaranteed in a least-squares sense by minimizing the criterion:

$$J = \|\mathbf{Zz} - \mathbf{Nu}\|^2 \ . \tag{4.7}$$

The solution to this problem leads to the projection matrices $\mathbf{P}_{Z2V}$ and $\mathbf{P}_{V2Z}$:

$$\mathbf{P}_{Z2V} = \Delta^{\dagger}\mathbf{N^T Z} \tag{4.8}$$

$$\mathbf{P}_{V2Z} = (\mathbf{Z^T Z})^{\dagger}\mathbf{Z^T N} \ , \tag{4.9}$$

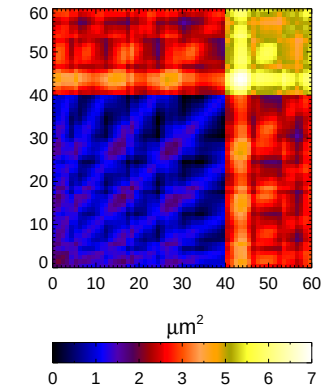

(a)

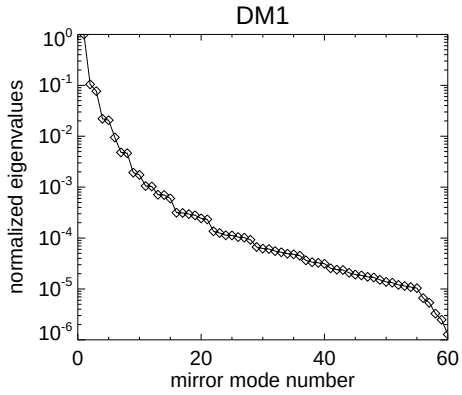

(b)

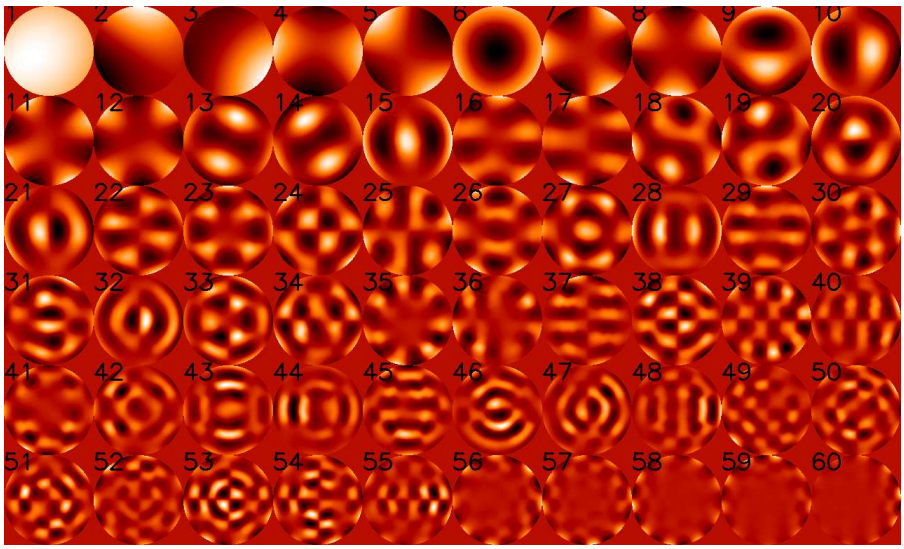

(c)

Figure 4.9: (a) Geometrical covariance matrix Δ for the ground DM of MAD. (b) Eigenvalues associated with the eigenmodes of Δ. (c) Representation of the eigenmodes of Δ.

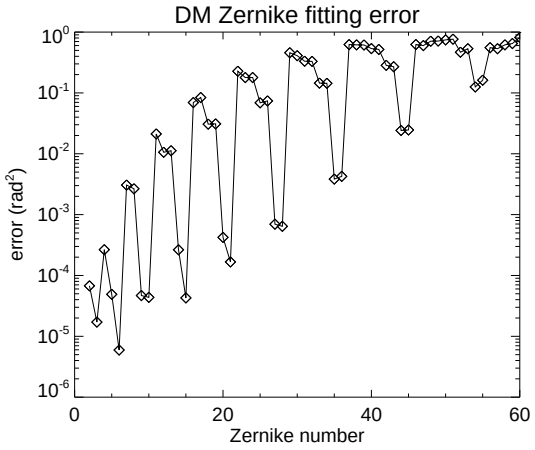

Figure 4.10: Mean-square error in rad^2 ($\lambda = 700$ nm) between pure Zernikes and best-fit Zernikes produced by the ground DM, for the first 60 Zernike polynomials.

where Δ is the geometrical covariance matrix introduced in section 4.2.2.2. Then, if $\mathbf{u}$ or if $\mathbf{z}$ is known for a given phase function, the equivalent representation can be computed as $\mathbf{z} = \mathbf{P}_{V2Z}\mathbf{u}$ or $\mathbf{u} = \mathbf{P}_{Z2V}\mathbf{z}$ respectively.

The matrix $\mathbf{P}_{V2Z}$ is useful, for instance, to estimate turbulence parameters from real-time data (section 4.2.4). On the other hand, the matrix $\mathbf{P}_{Z2V}$ is useful, for instance, to drive the DM to take the shape of a desired Zernike mode, as it was required to calibrate the non-common path aberrations (NCPA) of MAD [75].

Figure 4.10 shows the mean-square error between a pure Zernike and the best-fit Zernike that can be produced by the ground DM of MAD, for the first 60 Zernikes. Note that the error increases with the radial order. However, for a given radial order n the error decreases with azimuthal frequency m. In section 4.3.1.2 we will estimate with numerical simulations how many Zernike modes can be effectively compensated by the MAD system.

4.2.3 Real-time computer

The real-time computer (RTC) of MAD is based on a multi-processor architecture [33]. It is responsible for reading out the CCD frames of the SH-WFSs, computing the SH slopes, and computing the command signals that drive the DMs. The MAD RTC software was developed at ESO by E. Fedrigo, R. Donaldson, and C. Soenke. MAD can operate at two sampling frequencies: $f_s = 207.3$Hz (≈ 200Hz) and $f_s = 393.8$Hz (≈ 400Hz). The corresponding sampling periods are $T = 4.82$ ms and $T = 2.54$ ms. A

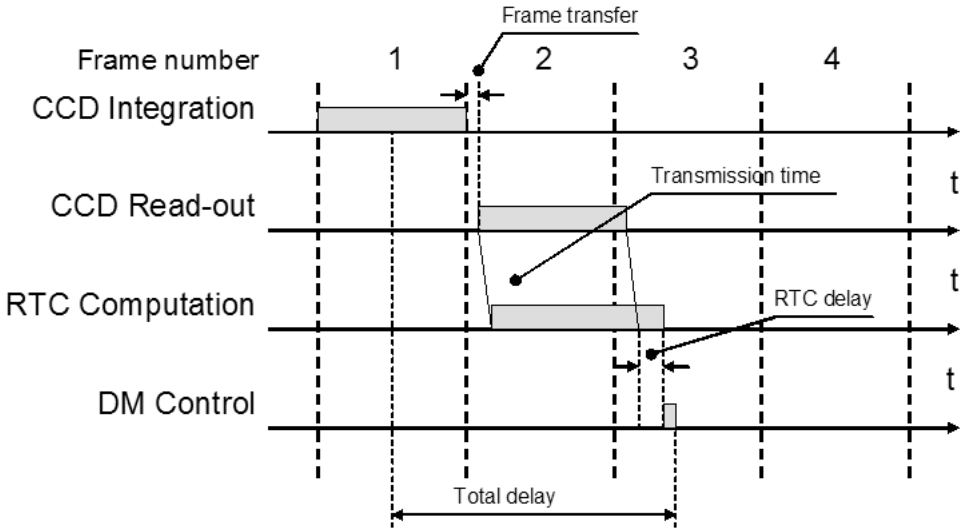

Figure 4.11: Timing diagram for the real-time computer (RTC) of the MAD system.

sketch of the time diagram for MAD is shown in figure 4.11.

The CCDs read-out time (τ_{read}) has been fixed to one frame ($\tau_{read} = T$) regardless of the sampling frequency. CCD frames are processed in pipeline so slope computations start as soon as the first subaperture data is available. This helps reducing the latency of the system. The RTC delay is defined as the time elapsed between the last CCD data is read out and the time the DMs command signals are sent to the HVAs. The command signals are also computed in pipeline. The RTC delay of MAD has been characterized and it is equal to 815 μs. An additional delay is attributed to the DMs control, which is due to the settling time of the HVAs ($\approx 30\mu$s). The voltages applied to the DMs are held constant (i.e zero-order hold) until the next updated command vector is computed. The total delay (τ_{tot}) at each sampling frequency is calculated in table 4.3.

For simulation purposes we will consider that the total delay is equal to exactly 2 frames: $\tau_{tot} = 2T$. Therefore, the equivalent *pure time delay* (eq. 3.6) will be equal to one frame: $\tau = T$. This has the advantage that the open-loop transfer function of the MAD system can be simply approximated by:

$$G(z) = z^{-2}C(z) \ . \tag{4.10}$$

Hence, the temporal sequences of the simulated variables (e.g. slopes and voltages) at time nT only depend on the previous values at times $(n-1)T$, $(n-2)T$, etc. For

	200 Hz	400 Hz
Exact sampling frequency	207.3 Hz	393.8 Hz
Sampling Period (T)	4.82 ms	2.54 ms
Frame transfer	80 μs	80 μs
Read-out time (τ_{read})	T	T
RTC delay	815 μs	815 μs
DM control delay	30 μs	30 μs
Total delay (τ_{tot})	$1.69T$	$1.86T$

Table 4.3: Total delay computation at each sampling frequency for the MAD system.

fractional time delays, as it is actually the case for MAD, it would be necessary to compute the temporal response within two sampling periods, and this would be too time consuming. In any case, as it will be shown in section 4.2.3.3, the approximation $\tau_{tot} = 2T$ is not far from the actual response.

4.2.3.1 Temporal controller

MAD is an AO system that will be operated with bright reference sources. Previous studies have shown that the main limitation on performance in high-flux conditions is the time delay. The time delay introduces a phase lag that reduces the correction bandwidth of the AO system. The proportional-integral (PI) controller and the Smith predictor are two simple controllers that can be used to reduce the effects of the time delay [90].

The temporal controller implemented in MAD is a PI controller. The analog transfer function is $C(s) = g_p + k_I/s$. The digital implementation is based on a bilinear approximation of $C(s)$ [35, Ch.8]. The discrete transfer function, $C(z)$, is computed by replacing s by $\frac{2}{T}\left(\frac{1-z^{-1}}{1+z^{-1}}\right)$ in $C(s)$. Note also that the integral gain of the digital controller, g_I, and the integral gain of the analog controller, k_I, are related by $g_I = k_I T$. Hence, the discrete transfer function becomes:

$$C(z) = \frac{\left(\frac{g_I}{2} + g_p\right) + \left(\frac{g_I}{2} - g_p\right) z^{-1}}{1 - z^{-1}} \ . \tag{4.11}$$

If $C(z) = Y(z)/X(z)$, the difference equation of the PI controller can be written as:

$$y(n) = y(n-1) + \left(\frac{g_I}{2} + g_p\right) x(n) + \left(\frac{g_I}{2} - g_p\right) x(n-1) \ . \tag{4.12}$$

Note that a simple integrator can be implemented simply by setting $g_p = g_I/2$. Figure

4.12 shows examples of the theoretical system transfer functions of MAD at 400Hz and using a PI controller. The integral gain was set to $g_I = 0.5$ and the effect of different g_p/g_I ratios is shown. Note how the overshoot and the correction bandwidth can be fine-tuned by changing the proportional gain g_p, as we will discuss further below.

4.2.3.2 Stability constraints

The stability can be defined in the absolute or the relative sense. The *absolute* stability is determined by the position of the poles of the closed-loop transfer function $H = G/(1 + G)$. In the continuous case, the absolute stability is assured if the poles of $H(s)$ lie on the left-hand side of the complex plane. In the discrete case, the absolute stability is assured if the poles of $H(z)$ lie within the unitary circle. On the other hand, the *relative* stability is defined in terms of the *gain margin* (GM) and the *phase margin* (PM). Both of these margins can be read directly from the Bode plots of the open-loop transfer function (figure 4.12(a)). Larger margins increase the robustness of the control system to unexpected changes of the system parameters. A good reference covering these topics in detail is [36].

It is well known that for an AO system with a total of two frames delay ($\tau_{tot} = 2T$) and with a simple integrator controller, the absolute stability is assured if the integral gain (g_I) lies within the range $0 \leq g_I \leq 1$. The gain range is further reduced when assuring the relative stability. For instance, for PM$> 45^\circ$ and GM$>$ 3 dB, it can be shown that the integral gain must lie within the range $0 \leq g_I \leq 0.53$ [22].

In the case of the PI controller, the gain margin, the phase margin, and the control bandwidth can be fine-tuned with the proportional gain (g_p), as shown in figure 4.13. Note how in general the correction bandwidth and the phase margin increase with g_p. On the other hand, the gain margin curves present a maximum value at $g_p \approx g_I/2$ and then decrease with g_p. Also note that for $g_I > 0.5$ both the PM and the GM curves are below the margins (PM$= 45^\circ$ and GM$=$ 3 dB) regardless of the g_p value. In general, a compromise between performance and stability is required. For MAD, it was found experimentally that at high-flux conditions a good compromise between stability and performance is obtained when $g_p \approx g_I$.

4.2.3.3 Rejection transfer functions

The rejection transfer function of an AO system can be estimated experimentally using the method proposed by C. Dessenne [22], which makes use of the fundamental relationship between open-loop and closed-loop data stated in equation 3.58. Hence, the

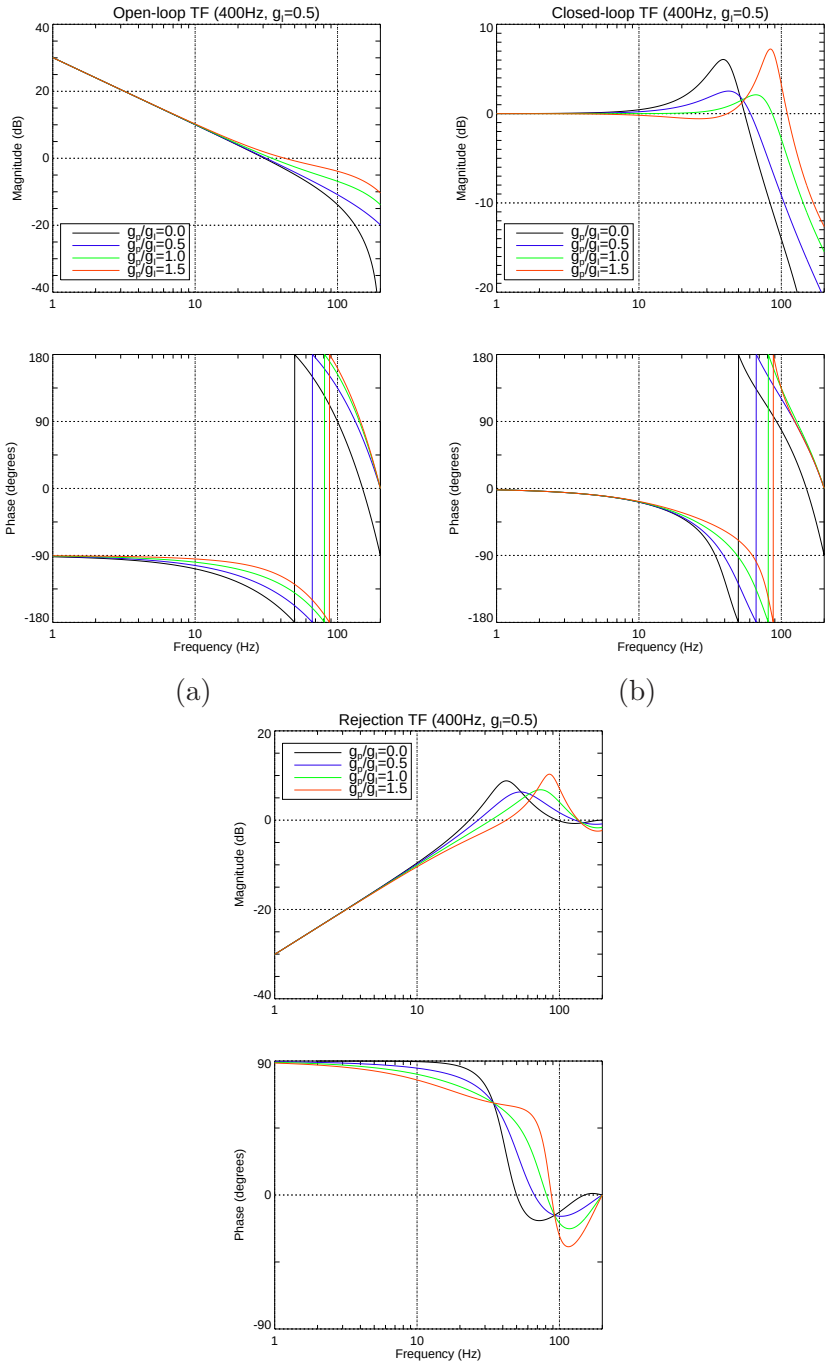

Figure 4.12: Examples of theoretical system transfer functions of MAD using a PI Controller (400Hz, $g_I = 0.5$). (a) Open-loop transfer function. (b) Closed-loop transfer function. (c) Rejection transfer function.

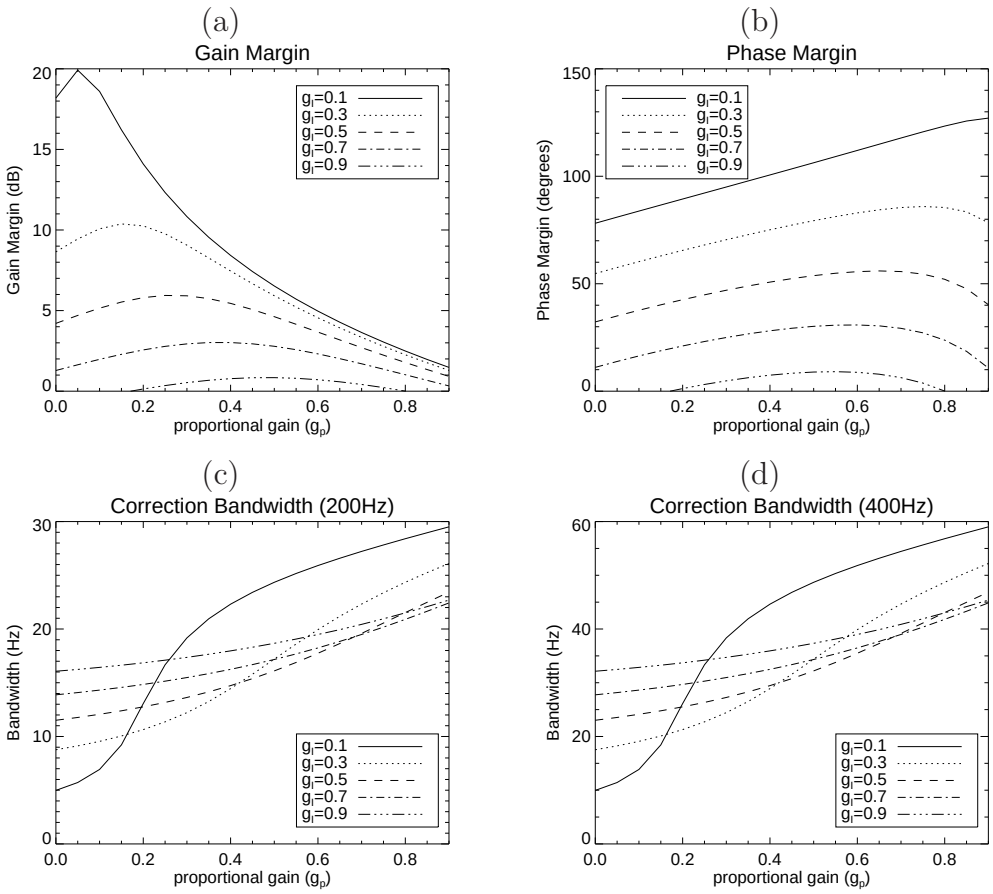

Figure 4.13: (a) Gain margin. (b) Phase margin. (c) Correction bandwidth at 200 Hz. (d) Correction bandwidth at 400 Hz.

RTF can be estimated as:

$$E(j\omega) = \left\langle \frac{\tilde{\varphi}^{MP}_{mes,i}(j\omega)}{\tilde{\varphi}^{MP,OL}_{mes,i}(j\omega)} \right\rangle_i \tag{4.13}$$

where $\langle\cdot\rangle_i$ denotes the average of the RTFs of all eigenmodes[2]. The procedure is as follows. First, temporal sequences of open-loop and closed-loop slopes are recorded. Then, from equation 3.43, the corresponding temporal sequences of open-loop and closed-loop eigenmodes are reconstructed using the reconstruction matrix $\mathbf{R}^{MP}_{LS} = \Sigma^{-1}\mathbf{U}^T$ (equa-

[2]Note that the RTFs are in principle the same for all (non-filtered) eigenmodes when the same control parameters apply to all eigenmodes. This would not be the case, for instance, for the optimized modal gain integrator.

tion 3.19). Note that this method is only applicable if the SH-WFS can operate in the linear regime (figure 4.3) when recording open-loop data. We will assume that this condition is satisfied by MAD. Finally, the Fourier transforms of the open-loop and closed-loop eigenmodes temporal sequences are computed and substituted in equation 4.13.

Figure 4.14 shows a comparison of the experimental, simulated, and theoretical modulus of the RTF at 200Hz, and for different PI parameters. For the simulated and the theoretical curves we have considered that the total delay is equal to exactly 2 frames ($\tau_{tot} = 2T$). Note that all the curves show good agreement between them. The experimental curves show a slightly smaller overshoot due to the fact that the total time delay τ_{tot} is actually smaller than $2T$ (see table 4.3).

4.2.3.4 Reconstruction of open-loop data

The fundamental relationship between open-loop and closed-loop data used above to estimate the RTFs experimentally, can also be used to reconstruct open-loop data from closed-loop data. As we will discuss in section 4.2.4.2, this will be useful to estimate turbulence parameters from closed-loop data.

Let us consider once again equation 3.58, but since we are dealing here with discrete-time systems we will express it in the z-domain:

$$\varphi^{MP}_{mes,i}(z) = E_i(z)\ \varphi^{MP,OL}_{mes,i}(z)\,. \tag{4.14}$$

Recalling that E_i is defined as $E_i = 1/(1+G_i)$ (eq. 3.34), we can then solve equation 4.14 for $\varphi^{MP,OL}_{mes,i}(z)$ rewriting it as:

$$\varphi^{MP,OL}_{mes,i}(z) = [1 + G_i(z)]\,\varphi^{MP}_{mes,i}(z)\ \ . \tag{4.15}$$

Note that this is a general expression to reconstruct open-loop data that can only be applied if the open-loop transfer function, $G_i(z)$, is well characterized. In order to proceed, let us assume once again that $G_i(z)$ is given by equation 4.10, i.e. we are considering once again that the total delay is equal to exactly 2 frames ($\tau_{tot} = 2T$). Then, equation 4.15 can be rewritten as:

$$\varphi^{MP,OL}_{mes,i}(z) = \varphi^{MP}_{mes,i}(z) + z^{-2}C_i(z)\,\varphi^{MP}_{mes,i}(z)\ \ . \tag{4.16}$$

The following step requires to recall the block diagram shown in figure 3.6 in order to realize that the correction eigenmode is given by $\varphi^{MP}_{cor,i}(z) = C_i(z)\,\varphi^{MP}_{mes,i}(z)$. Taking

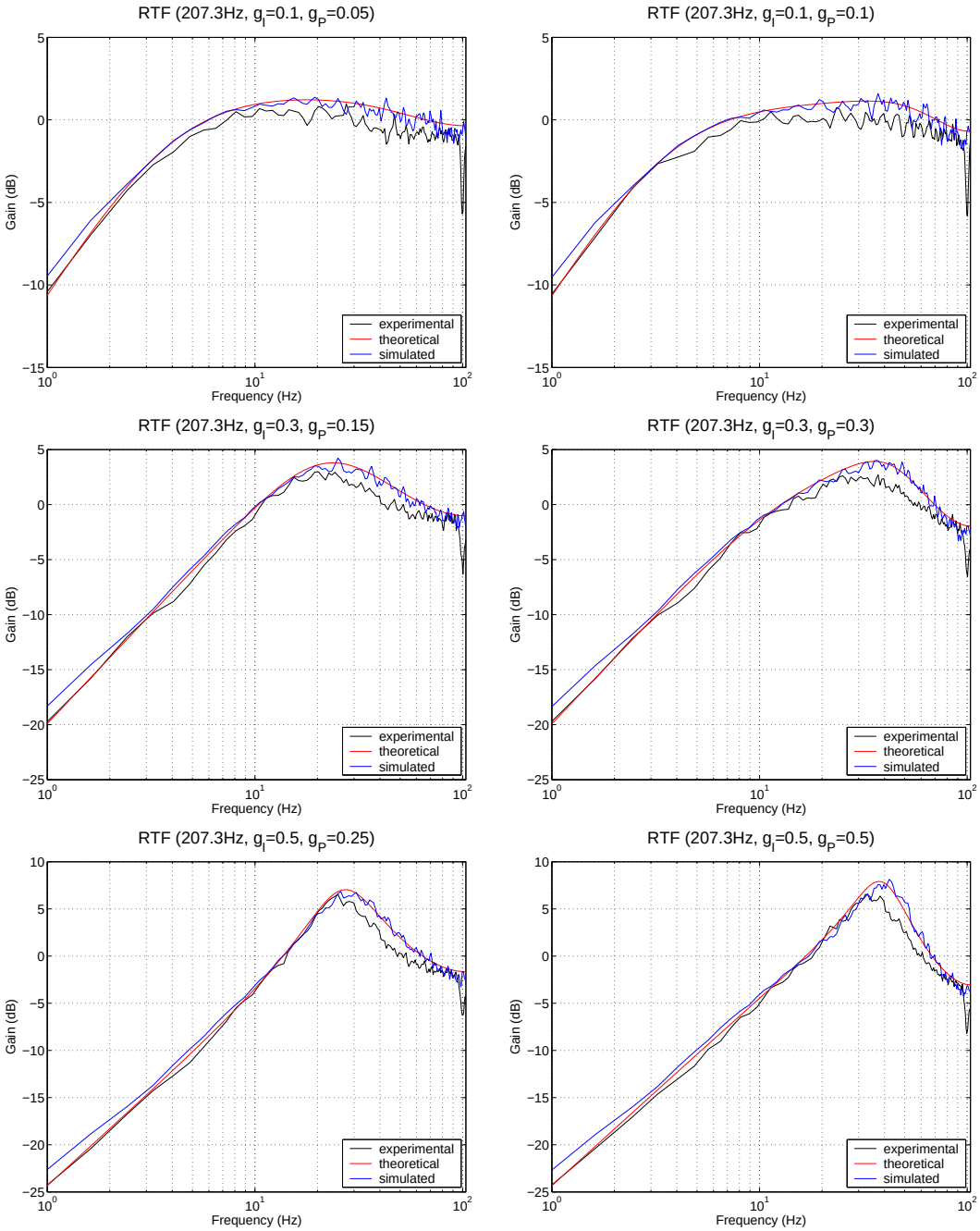

Figure 4.14: Comparison of experimental, simulated, and theoretical modulus of the rejection transfer functions (RTF) of MAD at 200Hz and for different PI parameters: (*Top*) $g_I = 0.1$, (*Middle*) $g_I = 0.3$, (*Bottom*) $g_I = 0.5$.

into account this relationship we can finally express equation 4.16 as:

$$\varphi_{mes,i}^{MP,OL}(z) = \varphi_{mes,i}^{MP}(z) + z^{-2}\varphi_{cor,i}^{MP}(z) \ . \tag{4.17}$$

The corresponding equation in the discrete-time domain is simply given by:

$$\varphi_{mes,i}^{MP,OL}(n) = \varphi_{mes,i}^{MP}(n) + \varphi_{cor,i}^{MP}(n-2) \ . \tag{4.18}$$

Recalling equations 3.43 and 3.45, it is straightforward to show that the temporal sequences of the vectors $\boldsymbol{\varphi}_{mes}^{MP}(n)$ and $\boldsymbol{\varphi}_{cor}^{MP}(n)$ can be estimated from closed-loop slopes $\mathbf{s}(n)$ and DM voltages $\mathbf{u}(n)$. Finally, the whole procedure to reconstruct open-loop data (in the eigenspace) is summarized by the following equations:

$$\begin{aligned} \boldsymbol{\varphi}_{mes}^{MP}(n) &= \mathbf{R}_{LS}^{MP}\mathbf{s}(n) & (4.19)\\ \boldsymbol{\varphi}_{cor}^{MP}(n) &= \mathbf{V}^T\mathbf{u}(n) & (4.20)\\ \boldsymbol{\varphi}_{mes}^{MP,OL}(n) &= \boldsymbol{\varphi}_{mes}^{MP}(n) + \boldsymbol{\varphi}_{cor}^{MP}(n-2) \ . & (4.21) \end{aligned}$$

Although we have shown above how to reconstruct open-loop data in the eigenspace, the same procedure can be applied to reconstruct open-loop data in any other modal basis as long as the required projection matrices are available. As we mentioned already, we will use this procedure in section 4.2.4.2 to reconstruct open-loop data in the Zernike modal basis in order to estimate some turbulence parameters of MAPS.

4.2.4 Atmospheric turbulence generator

Atmospheric turbulence is emulated in the laboratory with the turbulence generator MAPS (Multi Atmospheric Phase screens and Stars). It emulates a three-layered evolving atmosphere using rotating phase screens that were encoded with aberrations that follow von Kármán statistics [74]. There is a total set of four phase screens (PS1, PS2, PS3, and PS4), each one of them characterized by a given r_0 and L_0. The rotating speed of each phase screen can be tuned to emulate different wind profiles between 0 and 35 m/s. The natural guide stars (NGSs) are emulated by visible/IR light transmitting fibers. Figure 4.15 shows the distribution of NGSs emulated by MAPS covering a 2 arcmin FoV.

MAPS was originally conceived to emulate *median* (0.73″) and *good* (0.46″) seeing conditions of Paranal observatory [94]. The original design parameters (r_0 and L_0) per emulated layer are listed in table 4.4. The design parameters were later modified

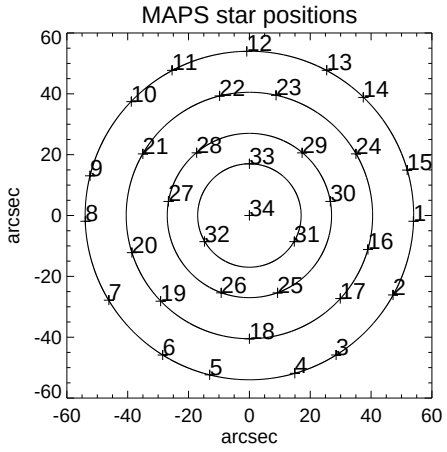

Figure 4.15: Distribution of the natural guide stars (as seen from CAMCAO) emulated by MAPS and covering a 2 arcmin FoV. The diameters of the concentric circles are 34, 54, 81, and 108 arcsec.

		Median seeing			Good seeing		
	Height	PS	r_0 (500 nm)	L_0	PS	r_0 (500 nm)	L_0
Layer 1	0 km	1	20 cm	22 m	2	30 cm	22 m
Layer 2	6 km	2	30 cm	22 m	3	50 cm	22 m
Layer 3	8.5 km	3	50 cm	22 m	4	80 cm	22 m
Global r_0 (500 nm)		14.4 cm			22.4 cm		
Equivalent seeing (500 nm)		$0.73''$			$0.45''$		
FWHM of PSF (500 nm)		$0.58''$			$0.34''$		

Table 4.4: Original design parameters for MAPS conceived to emulate median and good seeing conditions of Paranal Observatory. All values are referred to a pupil diameter of 8 m. The physical size of the pupil on MAPS is 15 mm.

to force the FWHM of the turbulence PSF to be equal to $0.73''$ (at $\lambda = 500$nm) for the PS1+2+3 combination and $0.45''$ (at $\lambda = 500$nm) for the PS2+3+4 combination because it was thought at that point that the FWHM and the seeing were equivalent. In fact, the FWHM of the long-exposure turbulence PSF is always smaller than the seeing value when the outer scale is finite ($L_0 = 22$m in our case). We will discuss further this issue below.

4.2.4.1 FWHM v. L_0

The seeing (s) is defined as the angular size (FHWM) of the long-exposure PSF produced by Kolmogorov turbulence ($L_0 \to \infty$). It can be computed from r_0 as [17]:

$$s = 0.9759 \frac{\lambda}{r_0} \ . \tag{4.22}$$

For von Kármán turbulence, the FWHM does depend on the outer scale L_0. C. Dessenne [22] studied for the first time this dependence with numerical simulations and plotted curves of FWHM versus L_0. R. Conan [17] studied thoroughly the effect of L_0 on different parameters of interest in adaptive optics, including the FWHM. The analytical expressions developed by R. Conan involve integrals that can only be solved numerically. Based on R. Conan expressions, A. Tokovinin [143] developed the following approximation for the FWHM:

$$\text{FWHM} = s \sqrt{1 - 2.183 \left(\frac{r_0}{L_0} \right)^{0.356}} \ . \tag{4.23}$$

Figure 4.16 shows a plot of FWHM at 500nm as a function of r_0 for both Kolmogorov and von Kármán ($L_0 = 22$m) statistics. For instance, note that for the PS1+2+3 combination ($r_0 = 14.4$cm), the FWHM is equal to $0.73''$ when $L_0 \to \infty$ and equal to $0.58''$ when $L_0 = 22$m. We have also validated this through numerical simulations, as shown in figure 4.17.

Since the design of the MAPS phase screens was later modified in order to make the FWHM of the long-exposure turbulence PSF equal to the seeing value, the *true seeing* became actually stronger. We will present below the experimental characterization of the MAPS phase screens delivered to ESO, and show the true seeing value obtained in the laboratory.

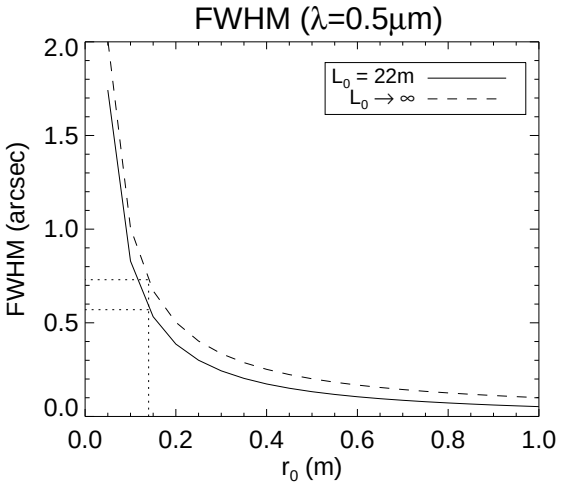

Figure 4.16: FWHM of the long-exposure turbulence PSF at 500nm for both Kolmogorov ($L_0 \to \infty$) and von Kármán ($L_0 = 22$m) statistics. Note that the FHWM for $r_0 = 14.4$cm is equal to $0.73''$ when $L_0 \to \infty$ and equal to $0.58''$ when $L_0 = 22$m.

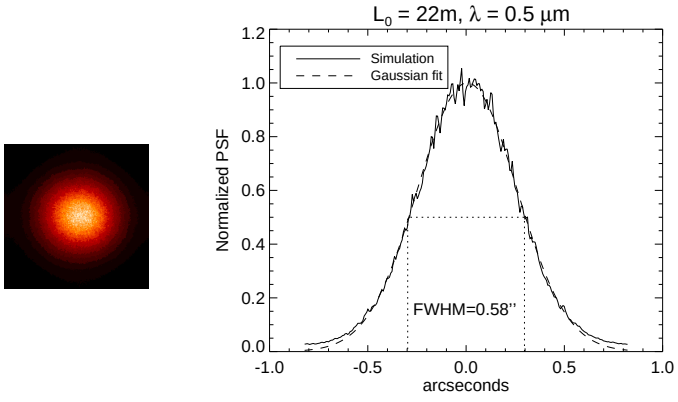

Figure 4.17: (*Left*) Turbulence long-exposure Point Spread Function (PSF) obtained from simulations when using the MAPS original design parameters intended to emulate seeing conditions at Paranal Observatory ($s = 0.73''$). (*Right*) A cut of the PSF along the x-axis and its Gaussian fit. The FWHM is approximately $0.58''$.

4.2.4.2 Phase screens characterization

This section presents the experimental characterization of the MAPS phase screens in terms of their r_0 values. The estimation of the r_0 values was based on a *best-fit* of the variance distribution of Zernike coefficients. This method will be detailed below. Also, two different procedures were followed to get the required experimental data: one *static* and one *dynamic*, as described below.

Static characterization

Each of the four MAPS phase screens (PS1, PS2, PS3, PS4) was characterized following the static procedure. The experimental data for each PS collected by J. Kolb consisted on 20 independent phase map realizations sampled on the telescope pupil ($D = 8m$) using a HASO camera (53x53 subapertures, λ =500nm). The phase maps were projected onto the first 300 Zernikes, and the (experimental) variance distribution of the Zernike coefficients was computed (Figure 4.18). Note that the last radial orders are affected by numerical errors related to the pixelization of the considered phase maps (53x53 pixels size). Therefore, the last radial orders were not considered in the fitting of r_0.

The von Kármán theoretical variance distribution of Zernike coefficients is given by equation 1.35. It depends on both L_0 and r_0, with L_0 mostly affecting the variance of the first radial orders. In order to avoid the effect of L_0, the first radial orders were not considered in the fitting of r_0.

Figure 4.18 shows the best fits for the four MAPS phase screens. We considered a fixed value of $L_0 = 22m$. The fitting was limited to radial orders $9 \leq n \leq 12$ (i.e. Zernikes 46 to 91). The estimated $r_0 s$ corresponding to the best-fits are also shown in figure 4.18. Note that the theoretical and experimental variance distributions also match well for the first radial orders, except for PS3 which is characterized by stronger tip-tilt variances not matching with the theoretical $L_0 = 22$m value.

The static characterization was useful to verify that the phase screens follow the desired turbulence statistics in a wide spatial-frequency range, as shown in figure 4.18. However, the r_0s should be estimated using a higher number of phase maps realizations. This was possible to achieve with the dynamic procedure described below.

Dynamic characterization

We will now present a *dynamic* method that can be used to estimate the variance distribution of Zernike coefficients, from which the estimation of r_0 can follow. This

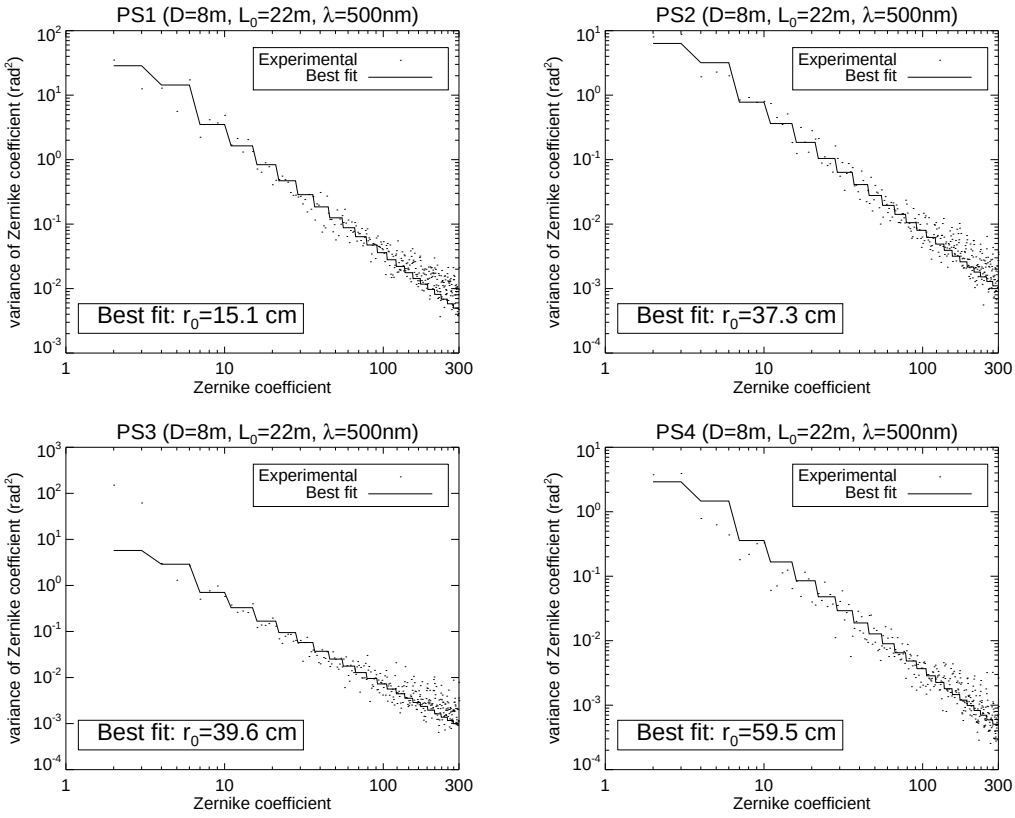

Figure 4.18: Static characterization of phase screens: experimental and best-fit variance distribution of Zernike coefficients for PS1, PS2, PS3, and PS4. The estimated r_0 values are shown as well.

method was originally proposed and validated by C. Dessenne [22]. Also, it has been already implemented in the NAOS system [50]. Let us describe below this method as it was applied in MAD [100].

Each PS was mounted on MAPS, one at a time, at an equivalent altitude of 0 km (i.e. conjugated to the telescope pupil). The PS rotation was enabled and the MAD system was operated in closed-loop in SCAO mode, and temporal sequences of closed-loop data (i.e. slopes and DM voltages) were collected. Then, based on the procedure to reconstruct open-loop data from closed-loop data described in section 4.2.3.4, open-loop data in the Zernike modal basis was reconstructed using the following equations:

$$\boldsymbol{\varphi}_{mes}(n) = P_{V2Z}\,\mathbf{R}_{_{TLS}}\mathbf{s}(n) \tag{4.24}$$

$$\boldsymbol{\varphi}_{cor}(n) = P_{V2Z}\mathbf{u}(n) \tag{4.25}$$

$$\boldsymbol{\varphi}_{mes}^{OL}(n) \;=\; \boldsymbol{\varphi}_{mes}(n) + \boldsymbol{\varphi}_{cor}(n-2) \;, \tag{4.26}$$

where $\mathbf{R}_{_{TLS}}$ is the SCAO TLS reconstruction matrix used to close the loop, and P_{V2Z} is the *volts-to-Zernikes* projection matrix presented in equation 4.9. The vectors $\boldsymbol{\varphi}_{mes}(n)$, $\boldsymbol{\varphi}_{cor}(n)$ and $\boldsymbol{\varphi}_{mes}^{OL}(n)$ are vectors containing Zernike coefficients. Note that since in this method the phase reconstruction is limited to the ground DM space, the number of Zernike coefficients that can be estimated can not be as large as in the static characterization. For the dynamic characterization we chose to limit the reconstruction to the first 60 Zernike coefficients.

One of the advantages of this method is that a large number of samples can be accumulated. As a result, the estimation of the experimental variance distribution of Zernike coefficients becomes more accurate. For MAD, we chose to collect temporal sequences of closed-loop data with 5000 contiguous samples. However, we should note that all these samples are not statistically independent, as it was the case for the static characterization. Indeed, the samples are spatio-temporally correlated, and the degree of correlation depends on the PS rotating speed, the sampling frequency, etc. Nevertheless, this was not a practical problem considering the large number of samples collected.

The experimental and the best-fit variance distribution of the Zernike coefficients for PS1, PS2, and PS3 at λ =500nm are shown in figure 4.19. The fitting of r_0 was limited to radial orders $4 \leq n \leq 6$ (Zernikes 15 to 28). Note that the tip-tilt variances for PS2 and PS3 are higher than expected. This is due to the fact that as the phase screens rotate there is an additional wobble that increases the power on these modes [74]. However, the fitting of r_0 is not affected by this effect because we are not taking into account the lower radial orders in the fitting. Note that the estimated r_0s with this method are slightly different from the values estimated with the static method.

The combination PS1+2+3 was also characterized with the dynamic procedure. This is the combination of PSs that we have used for all the laboratory experiments presented in this work. Figure 4.19 also shows the variance distribution of Zernike coefficients for this combination of phase screens, conjugated at 0, 6 and 8.5 km respectively. Note that the estimated global r_0 is equal to 11.9 cm at 500 nm. This is totally in accordance with the expected value computed from the individual r_0s as [127]:

$$r_0 = \left(\sum_i {r_0}_i^{-5/3} \right)^{-3/5} \;. \tag{4.27}$$

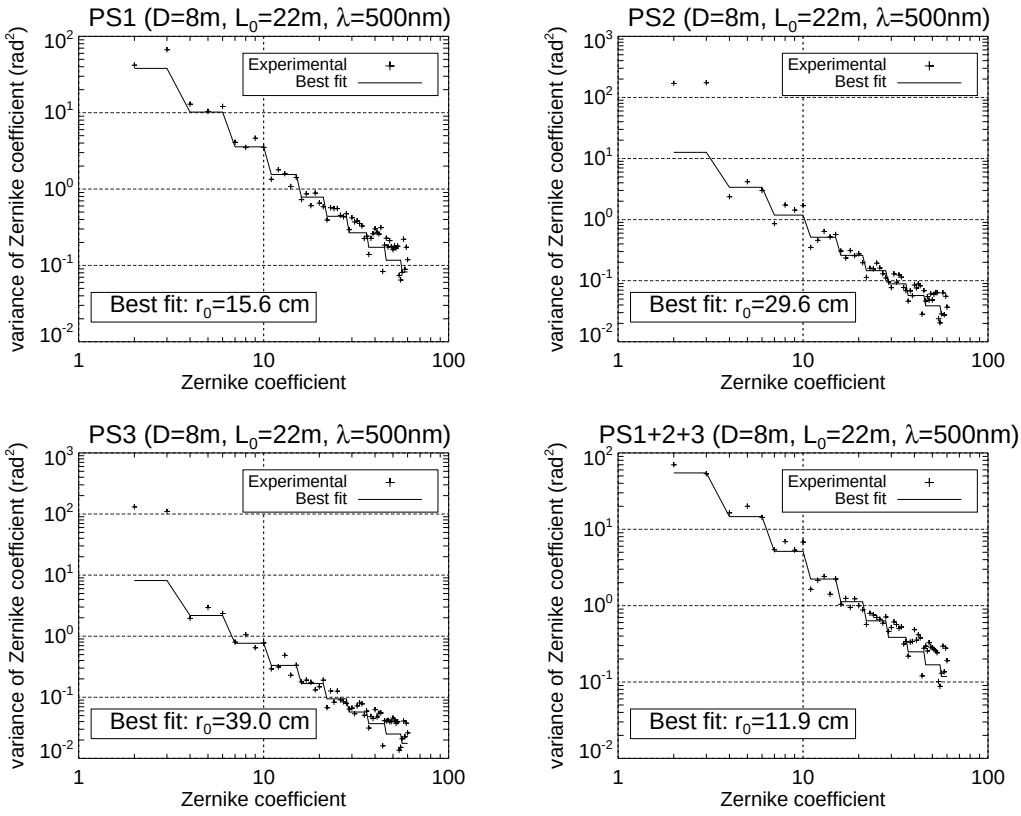

Figure 4.19: Dynamic characterization of phase screens: experimental and best-fit variance distribution of Zernike coefficients for PS1, PS2, PS3, and the combination PS1+2+3. The estimated r_0 values are shown as well.

The corresponding seeing is equal to $0.84''$ and, according to equation 4.23, the FWHM at 500nm is approximately $0.83''$. Finally, table 4.5 summarizes the MAPS turbulence parameters. We will use these values throughout this work and refer to them simply as the PS1+2+3 profile.

4.2.4.3 Simulation of MAPS turbulence profile

The MAD simulation tool was customized to reproduce the turbulence profile generated by the MAPS PS1+2+3 combination. We have simulated three phase screens following the method described in section 1.1.7, and matching the parameters shown in table 4.5. As described in section 1.1.7, the temporal evolution of the turbulence was simulated by shifting the phase screens at each iteration in accordance with the wind speed profile shown in table 4.5.

	PS1	PS2	PS3
height (km)	0	6	8.5
L_0 (m)	22	22	22
r_{0_i} (cm)	15.6	29.6	39.0
Weight	0.64	0.22	0.14
V_{wind} (m/s)	7	13	30
global r_0	11.9 cm @ 500nm		
seeing	$0.84''$ @ 500nm		
mean wind speed $\overline{V}$	13.1 m/s		
τ_0	2.8 ms @ 500nm		

Table 4.5: Parameters of the MAPS turbulence generator for the combination of phase screens PS1+2+3. All values are referred to a pupil diameter of 8 m. The physical size of the pupil on MAPS is 15 mm.

In order to validate that the spatial and temporal statistics produced by our turbulence simulator match the ones of the PS1+2+3 profile (table 4.5), we carried out the following experiment. The turbulence simulator was run for 2048 iterations. The sampling frequency was set to 400 Hz. At each iteration the resultant phase perturbation in the telescope pupil was directly projected onto the first 100 Zernikes. The variance distribution of the Zernike coefficients was computed from the accumulated samples and it is shown in figure 4.20. The experimental variance distribution of the first 60 Zernikes obtained from the dynamic characterization of the MAPS PS1+2+3 combination is also shown in figure 4.20 for comparison. Note that our turbulence simulator follows the desired spatial statistics.

In order to validate the temporal characteristics of the simulated turbulence, we have also computed from the accumulated samples the temporal spectra of each Zernike coefficient, and verify that they follow the theoretical properties described in section 1.1.6.1. As an example, figure 4.21 shows the temporal spectra of Zernike coefficients number 8 and 16. The corresponding cut-off temporal frequencies (ν_c) computed with equation 1.41 are $\nu_c = 1.96$ Hz for Zernike number 8, and $\nu_c = 2.95$ Hz for Zernike number 16. Note how the temporal PSDs follow the theoretical asymptotic behavior presented in equation 1.40. That is, at low temporal frequencies ($\nu \ll \nu_c$) the PSDs follow a ν^0 power law whereas at high temporal frequencies ($\nu \gg \nu_c$) the PSDs follow a $\nu^{-17/3}$ power law.

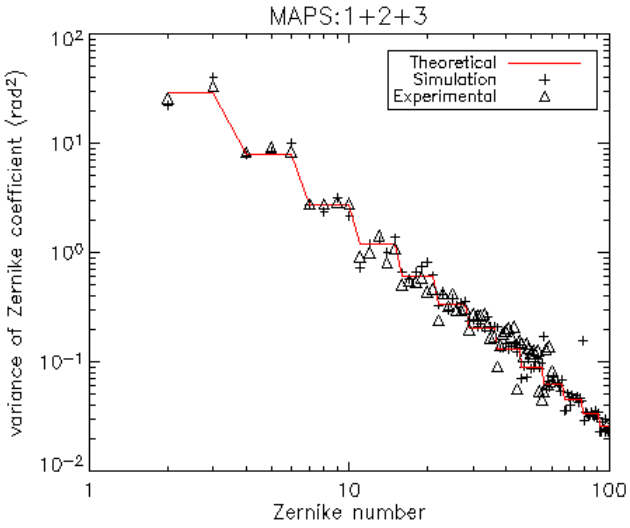

Figure 4.20: Modal expansion of the phase perturbation generated with MAPS 1+2+3 turbulence profile (r_0 = 11.9cm @ 500nm, L_0 = 22m). Simulated and experimental data was expanded in 100 and 60 Zernikes respectively. We see that both sets of data are in agreement with the theoretical curve of von Kármán statistics.

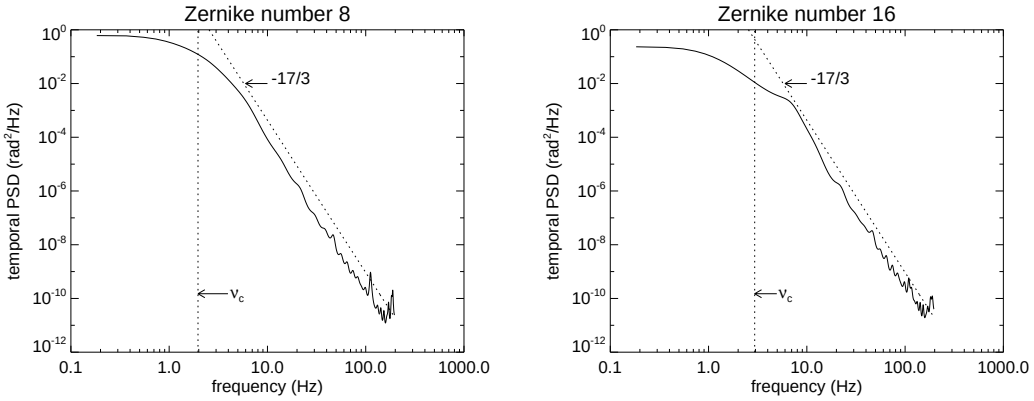

Figure 4.21: Temporal power spectral density (PSD) of (*Left*) Zernike number 8 (ν_c = 1.96 Hz), (*Right*) Zernike number 16 (ν_c = 2.95 Hz).

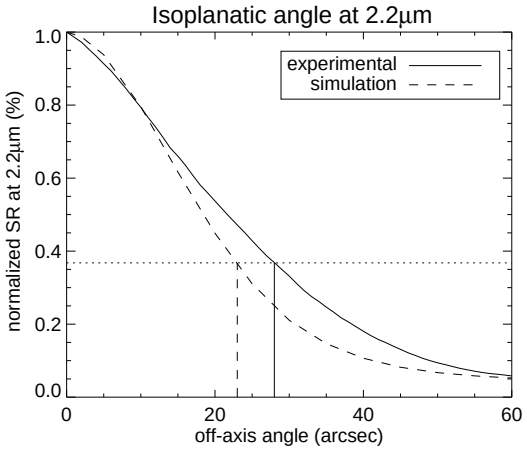

Figure 4.22: Comparison of the isoplanatic angle θ_0 estimated from both experimental and simulation results.

4.2.4.4 Isoplanatic angle

The isoplanatic angle θ_0 was also characterized in MAD using the SR estimations in the FoV. It is important to note that the theoretical θ_0 given by equation 1.75 is only valid for Kolmogorov turbulence. For the MAPS PS1+2+3 profile, the (Kolmogorov) isoplanatic angle is equal to $\theta_0 = 2''$ at 0.5 μm, and $\theta_0 = 12''$ at 2.2 μm. For the case of von Kármán turbulence, the outer scale L_0 will have an impact on the actual isoplanatic angle. The effect of L_0 on θ_0 was studied by R. Conan [17]. As it is well known, the outer scale L_0 affects mostly the properties of low-order turbulent modes, and their angular correlation functions are not an exception. In general, the angular correlation functions of low-order modes decay more smoothly due to L_0 and as a consequence the *effective* isoplanatic angle becomes larger.

The *effective* isoplanatic angle θ_0 can nevertheless be estimated from real data by using its definition (section 1.2.7.2) and the Marechal approximation (eq. 1.70). Indeed, recalling that θ_0 is defined as the angle from the GS at which the mean-square wavefront error σ^2 is equal to 1 rad^2, the equivalent SR loss is $S_R = \exp(-1) \approx 0.37$. Figure 4.22 shows the (normalized) SR as a function of the off-axis angle. Both experimental and simulated curves are shown. The angles at which the normalized SR curves are equal to $S_R = 0.37$ give and estimate of the effective θ_0. The estimated θ_0 from experimental data is $\theta_0 = 28 \pm 3''$, and the one from simulations is $\theta_0 = 23 \pm 1''$. These results are in good agreement.

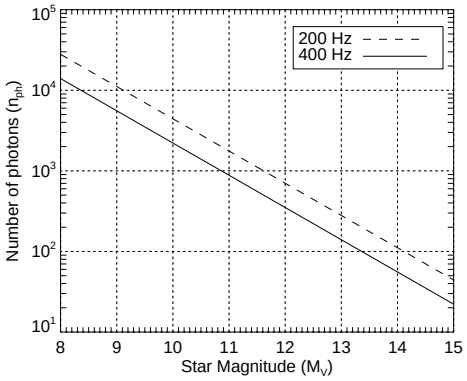

Figure 4.23: Number of photons per SH-WFS subaperture and per frame as a function of star magnitude, and for two sampling frequencies: 200 Hz, and 400 Hz.

4.2.5 Flux level characterization

The star magnitude (M_V) and the number of photons per SH subaperture and per frame (n_{ph}) are related by the following expression:

$$n_{ph} = \frac{Z_0\, 10^{-0.4 M_V}}{f_s} \tag{4.28}$$

where Z_0 is the *zero point*[3] and f_s is the sampling frequency. The zeropoint of MAD was characterized in the laboratory and it is equal to $Z_0 = 8.86 \times 10^9$ photons per subaperture per second. Figure 4.23 shows a plot of n_{ph} versus M_V. Note that it is foreseen that the MAD system will be tested on the sky using only bright GSs ($M_V < 10$).

4.3 Simulation studies

In this section we will present the simulation studies that aim at exploring the parameter space of the MAD system in SCAO, GLAO and MCAO modes. The performance will be evaluated at 2.2 μm in terms of Strehl ratio (SR) and also, for the GLAO and MCAO modes, in terms of the gain in ensquared energy in a square of 0.1"x0.1", denoted as $\text{GEE}_{0.1}$ (section 1.2.6).

[3]The zero point is defined as the number of photons coming from a zero-magnitude ($M_V = 0$) star that are actually detected by the WFS's CCD per unit area and per second. It takes into account the transmission of all the optical components, the detection bandwidth $\Delta\lambda$, and the quantum efficiency of the CCD.

Unless otherwise varied for a particular study, the simulation parameters and system specificities that were fixed for all the simulation studies presented in this section are:

- Operation under high-flux conditions. We have fixed the star magnitude to $M_V = 9.4$, which roughly corresponds to the flux levels we have worked with in the laboratory experiments (section 4.5).

- MAPS PS1+2+3 turbulence profile (Table 4.5).

- Control law: TLS reconstruction matrix $\mathbf{R}_{TLS}$ and PI temporal controller (section 4.2.3.1). The effect of different filtered eigenmodes in the matrix $\mathbf{R}_{TLS}$ and different PI gains will be evaluated.

- SH-WFSs slopes computation: simple centroid algorithm with threshold set to $U = 0$. All CCD pixels (8x8) taken into account in the computation of the centroid.

- All SH-WFSs are considered to be identical. The true relative orientations between the different WFSs will be taken into account in the simulations that will be presented in section 4.5.

4.3.1 SCAO mode

The MAD system operating in SCAO mode consists of only the ground DM and a single SH-WFS. We will consider that the GS is located at the center of the FoV.

The MAD's SCAO interaction matrix has 104 rows (2 measurements —s_x and s_y— for each of the 52 valid subapertures shown in figure 4.2) and 60 columns (60 actuators of the ground DM). Figure 4.24 shows the eigenmodes and the associated normalized singular values of the MAD's SCAO interaction matrix. Note that the first eigenmodes (associated with high sensitivities) are very similar to the first Zernike polynomials. On the other hand, the last eigenmode (associated with the lowest sensitivity) corresponds to the piston mode.

4.3.1.1 SR v. control law parameters

The purpose of this study is to determine what are the best control law parameters that result in the maximum SR at 2.2μm under high-flux conditions ($M_V = 9.4$) and for the MAPS PS1+2+3 turbulence profile ($s = 0.84$", $\tau_0 = 2.8$ ms). The parameters explored are the number of filtered modes of $\mathbf{R}_{TLS}$, and the gains of the PI temporal controller. The proportional and the integral gain were nevertheless set to the same

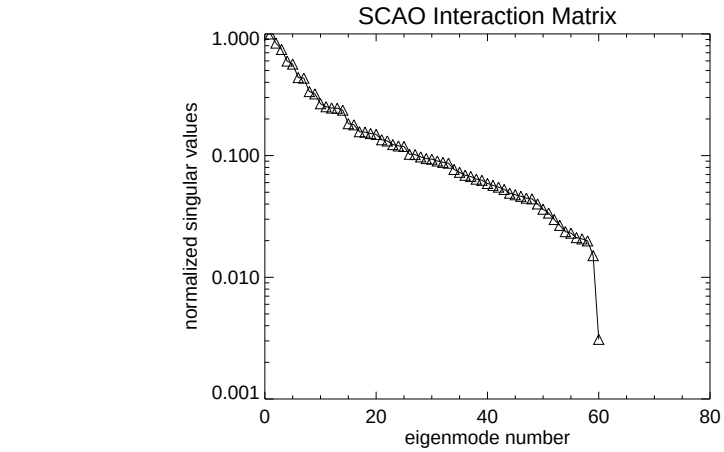

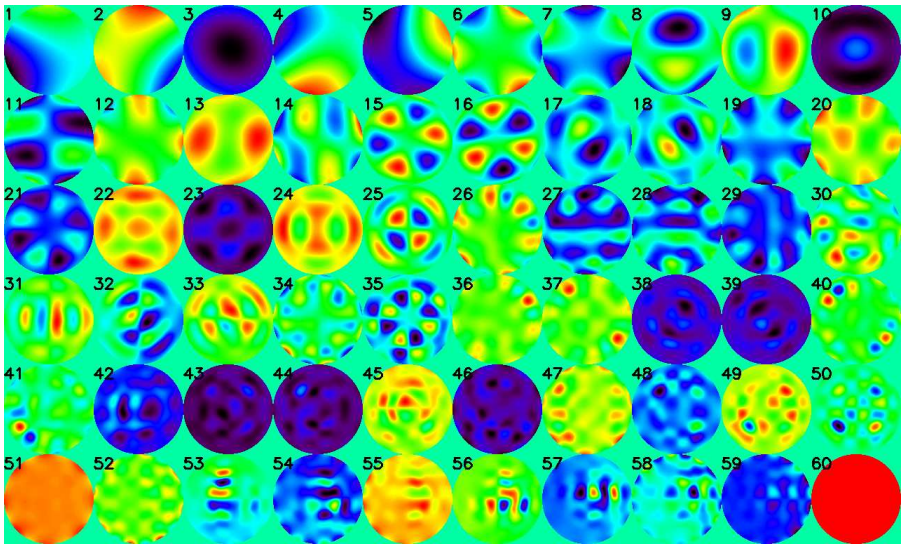

Figure 4.24: (*Top*) Normalized singular values associated with the eigenmodes of the SCAO interaction matrix. (*Bottom*) Eigenmodes of the SCAO interaction matrix.

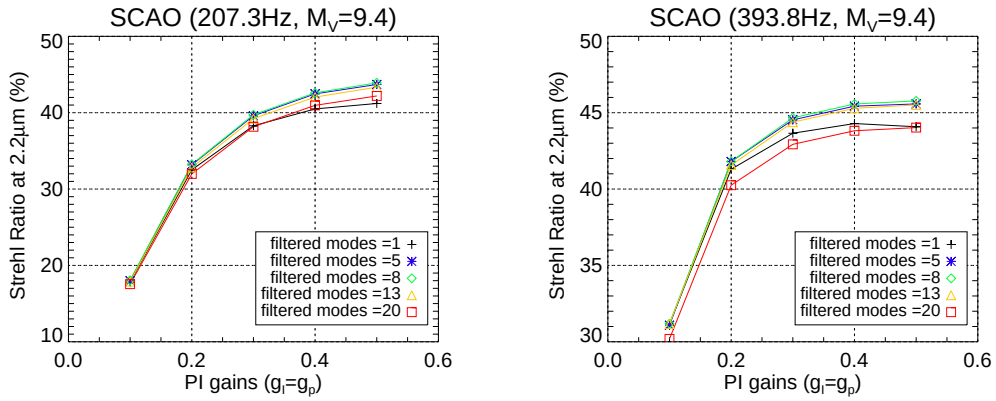

Figure 4.25: Maximum performance attained for different PI gains and number of filtered modes when operating at high-flux conditions ($M_V = 9.4$) and for the MAPS1+2+3 turbulence profile ($s = 0.84''$). (*Left*) Sampling frequency 200 Hz. (*Right*) Sampling frequency 400 Hz.

value ($g_I = g_p$). Figure 4.25 shows the simulation results for both sampling frequencies: 200 Hz and 400 Hz.

The maximum SR values were 43.9% @ 200 Hz and 45.8% @ 400 Hz. Note that both maxima were attained when $g_I = g_p = 0.5$ and when the number of filtered modes was 8.

4.3.1.2 SR v. atmospheric variations

The purpose of this study is to determine what are the expected variations in SR at 2.2 μm due to changes in atmospheric conditions i.e. seeing s and coherence time τ_0. We have studied the case for both sampling frequencies: 200 Hz and 400 Hz, and we have fixed the controller parameters to the ones that provide the best performance at high-flux levels (section 4.3.1.1), namely, the PI gains to $g_I = g_p = 0.5$ and the number of filtered modes to 8.

Figure 4.26(left) shows the variation in SR as a function of the seeing s. The mean wind speed was fixed to $\overline{V} = 13.1$ m/s, which is the median value for Paranal Observatory. Note that no major gain is obtained at 400 Hz with respect to 200 Hz for this value of $\overline{V}$. In this figure it is also indicated in (− − −) the performance that would be obtained after compensating *perfectly* all Zernikes up to radial order $n_{\max}$. These theoretical curves were obtained as explained below. Assuming a Kolmogorov turbulence model, the residual variance after correcting all Zernikes up to radial order

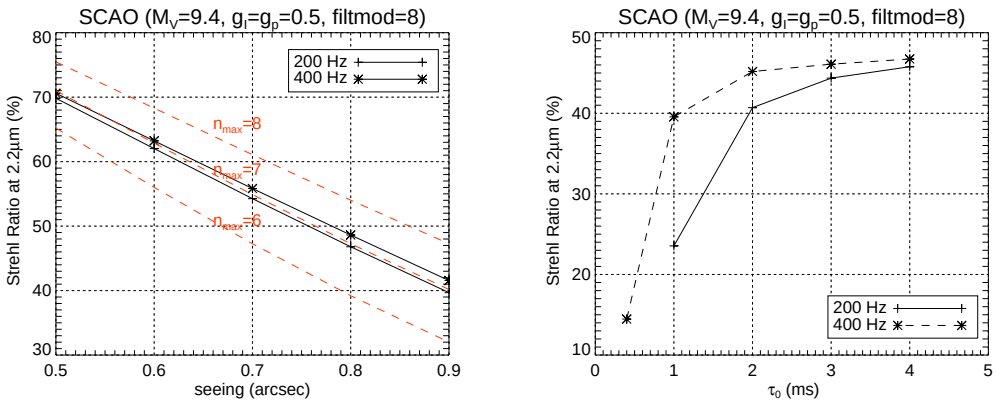

Figure 4.26: (*Left*) Variations in SR as a function of the seeing value (fixed $\overline{V} = 13.1$ m/s). (*Right*) Variations in SR as a function of coherence time τ_0 (fixed $s = 0.84''$).

$n_{\max}$ is given by [15]:

$$\sigma^2_{n_{\max}} = 0.458\,(n_{\max}+1)^{-5/3}\left(\frac{D}{r_0}\right)^{5/3} \quad , \tag{4.29}$$

where r_0 and the seeing s are related by equation 4.22. The SR curves shown in $(---)$ were computed using the approximation $S_R \approx \exp(-\sigma^2_{n_{\max}})$ for the radial orders $n_{\max} = \{6, 7, 8\}$. From these plots we can see that the curves obtained from the simulations follow quite closely the slope predicted by the theoretical expressions. Furthermore, we can see also that the maximum performance obtained with MAD is equivalent to the performance obtained with an ideal SCAO system correcting perfectly all Zernikes up to $n_{\max} = 7$, i.e. a total of 36 Zernikes.

Figure 4.26(right) shows the SR as a function of the coherence time τ_0. The seeing value was fixed to $s = 0.84$". Note how the system suffers an important loss in performance at 200 Hz for $\tau_0 < 2$ ms. The loss in performance at 400 Hz occurs when $\tau_0 < 1$ ms. As expected, higher sampling frequencies are advantageous when the atmospheric turbulence is evolving fast. Recall that the median coherence time in Paranal Observatory is $\tau_0 = 3.4$ ms.

4.3.1.3 SR v. star magnitude

In section 4.3.1.1 we studied the performance optimization under high-flux conditions by fine-tuning the controller parameters (number of filtered modes and PI gains). In this section we will study how the performance varies when the flux level changes.

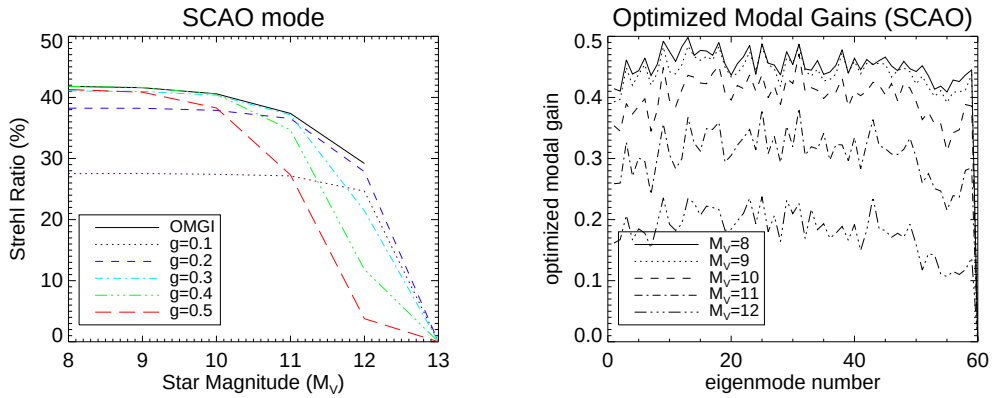

Figure 4.27: (*Left*) Estimated performance of MAD in SCAO mode (400 Hz) as a function of star magnitude, and for different integral gains. Strehl values are given for the GS position. The performance obtained when using the optimized modal gain integrator is also shown. (*Right*) Optimized modal gains for each star magnitude considered.

Clearly, in order to optimize the performance at each flux level we would require to fine-tune the number of filtered modes and PI gains for each case. However, in this study we will not proceed in this way. Instead, we will let the *optimized modal gain integrator* (OMGI) find the best controller parameters to be applied at each considered flux level.

The optimized modal gain integrator (OMGI) was widely studied in chapter 3. For this study, we have selected the controlled modes to be the eigenmodes of the SCAO interaction matrix (figure 4.24). We have applied the Dessenne method (section 3.6) to determine the optimized modal gains for these controlled modes. Figure 4.27(right) shows the optimized modal gains for each of the star magnitudes considered in this study.

Figure 4.27(left) shows the performance obtained with the OMGI control law as a function of the guide star magnitude M_V. The sampling frequency was set to 400 Hz. For comparison, the curves of SR v. star magnitude for some non-optimized cases are also shown in figure 4.27(left). For all these non-optimized cases we have made the following choice of parameters:

- Only one eigenmode (i.e. piston) was filtered out in $\mathbf{R}_{TLS}$.
- The PI controller was set to the *simple integrator* mode (i.e. $g_p = g_I/2$).
- No thresholding was applied in the computation of the SH centroids.

Let us now discuss the results presented in figure 4.27. Note that the OMGI control law always gives a better performance. However, the gain in performance brought by the OMGI control law is not dramatic for the MAD system. In fact, note from figure 4.27(right) that for a given star magnitude, the modal gains are actually quite similar for all the controlled modes. A very similar performance can be easily achieved by setting the single gain of a simple integrator controller to the *mean of the modal gains*. In any case, note that the integral gains that lead to a better performance are higher ($g_I \geq 0.3$) for high flux levels ($M_V < 10$), medium ($0.2 \leq g_I \leq 0.3$) for medium flux levels ($M_V = 11$), and low ($g_I \leq 0.2$) for low flux levels ($M_V = 12$). As was already discussed in chapter 3, this trend is due to the fact that higher integral gains increase the correction bandwidth of the AO system but also lead to stronger noise propagation. At high flux levels the SNR is also high and the integral gain can be as high as possible, i.e. it is only limited by the stability constraints. On the other hand, at low flux levels the SNR is also low and the integral gain needs to be decreased in order to prevent a strong noise propagation.

It is interesting to note from figure 4.27(left) that at even lower flux levels ($M_V = 13$) the performance is $S_R = 0$ regardless of the integral gain used. Let us discuss below why this happens. From figure 4.23, we can see that the number of photons n_{ph} for a star magnitude $M_V = 13$ is $n_{ph} \approx 10^2$. We showed in figure 4.4 (see the curve shown in $-\square-$ corresponding to the *no thresholding* case) that at these flux levels the effective variance of the WFS measurement noise (σ_w^2) became very large. As we explained at that point, the SH spots are totally immersed in noisy CCD pixels and it is not possible anymore to perform a reliable centroid computation. As a consequence, the system cannot operate anymore and the performance is null ($S_R = 0$). However, as we discussed in section 4.2.1.5, it would be possible by optimizing the centroid computation algorithm (e.g. with thresholding, windowing and/or pixel weighting) to operate at lower flux levels. For instance, when using a thresholding value of $U = 0$ (i.e. removal of negative pixel intensities) we managed to obtain with numerical simulations a maximum SR of 8% at $M_V = 13$ (This SR value was obtained with an integral gain of $g_I = 0.1$). In conclusion, the optimization of the performance at low-flux conditions requires to optimize both, the centroid computation algorithm and the controller parameters. A full study concerning the optimization of the MAD system at low-flux levels was beyond the scope of this work.

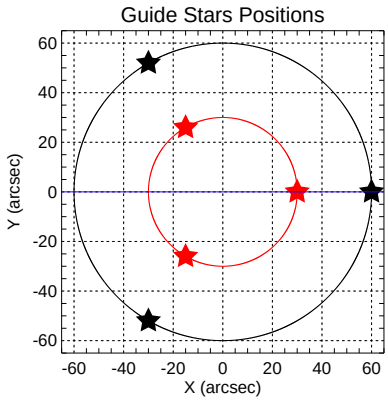

Figure 4.28: Position of the guide stars for the 1' FoV (red) and the 2' FoV (black) configurations. The performance cuts will be evaluated along the line $Y = 0$ (blue).

4.3.2 GLAO mode

The MAD system operating in GLAO mode uses the three SH-WFSs for probing the turbulence, but only the ground DM for wavefront correction. We will consider two FoV configurations: 1' FoV and 2' FoV. The three GSs will be placed in an equilateral triangle inscribed in a circle of 1' and 2' respectively, as shown in figure 4.28. We have considered that all NGSs were of the same magnitude $M_V = 9.4$, which actually corresponds to the experimental conditions we have worked with in the laboratory using the guide stars emulated by MAPS.

The MAD's GLAO interaction matrix ($\mathbf{M}_{int}$) has 312 rows (104 measurements per SH-WFS times three) and 60 columns (60 actuators of the ground DM). The eigenmodes and the associated normalized singular values of the GLAO interaction matrix are shown in figure 4.29. Note that the GLAO and the SCAO eigenmodes and singular values are very similar.

4.3.2.1 Computation of the GLAO reconstruction matrix

There are two main approaches that have been proposed so far to compute a GLAO reconstruction matrix. Both approaches are in any case based on a least-squares approach (section 2.3.1.1). The first approach is straightforward: If we denote as $\mathbf{M}_{int} = \mathbf{U}\Sigma\mathbf{V}^T$ the SVD decomposition of the GLAO interaction matrix, the reconstruction matrix is given by the corresponding truncated least-squares reconstructor $\mathbf{R}_{_{TLS}} = \mathbf{V}\Sigma_{fil}^{-1}\mathbf{U}^T$ (section 2.3.2.3). Note that the $\mathbf{R}_{_{TLS}}$ matrix becomes a 60x312 matrix. The vector-matrix multiply $\mathbf{u} = \mathbf{R}_{_{TLS}}\mathbf{s}$ that generates the ground DM's command vector $\mathbf{u}$ can

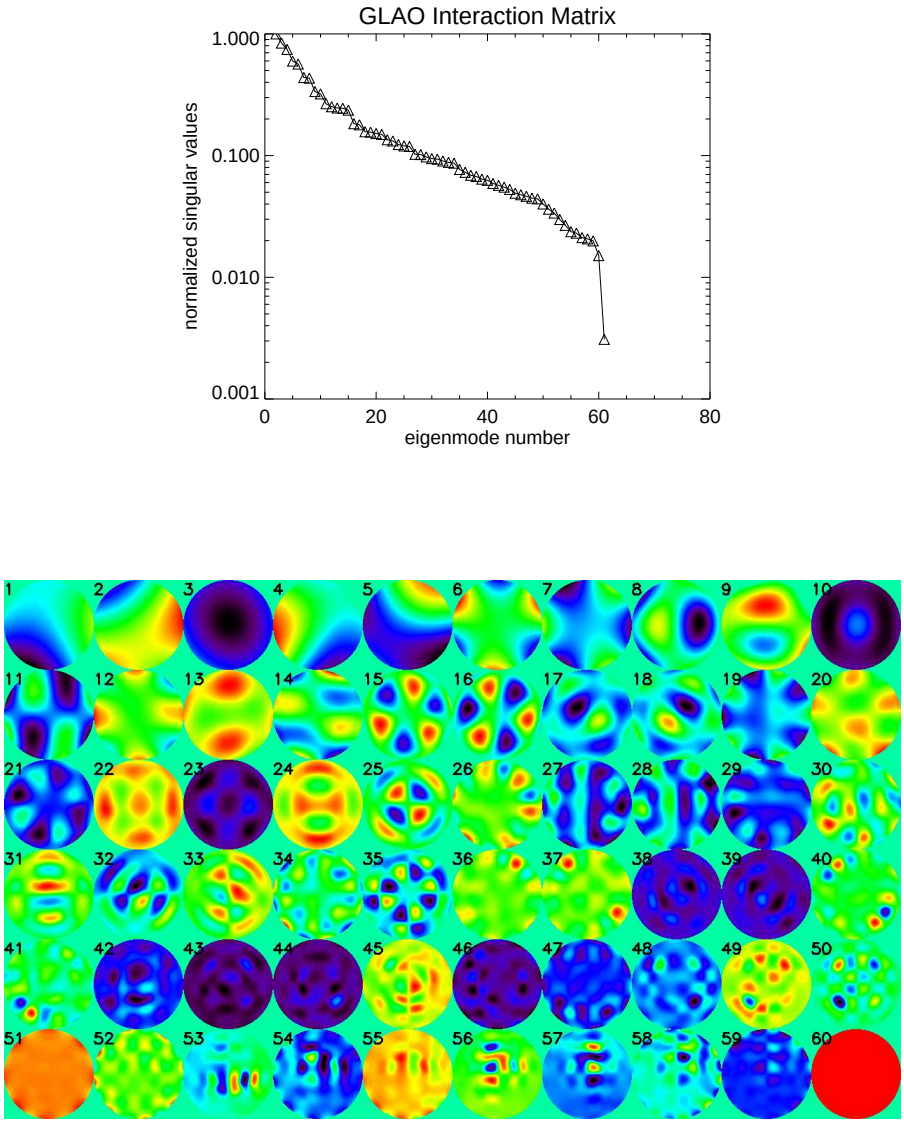

Figure 4.29: (*Top*) Normalized singular values associated with the eigenmodes of the GLAO interaction matrix. (*Bottom*) Eigenmodes of the GLAO interaction matrix.

also be expressed as:

$$\begin{aligned} \mathbf{u} &= \mathbf{R}_{_{TLS}}\mathbf{s} \\ &= [\mathbf{R}_1\mathbf{R}_2\mathbf{R}_3]\,[\mathbf{s}_1\mathbf{s}_2\mathbf{s}_3]^T \\ &= \mathbf{R}_1\mathbf{s}_1 + \mathbf{R}_2\mathbf{s}_2 + \mathbf{R}_3\mathbf{s}_3 \ , \end{aligned} \tag{4.30}$$

where the matrix $\mathbf{R}_k$ is the 60x104 partition of $\mathbf{R}_{_{TLS}}$ associated with the kth WFS. These matrix partitions play a role in the second approach, as we will describe below.

Let us recall from section 1.2.9 that in a GLAO system each WFS measures the contribution of the ground turbulent layer *plus* the contribution of the higher turbulent layers in the direction of the corresponding GS. In principle, an estimate of *just* the ground-layer wavefront perturbation can be obtained by averaging the wavefronts measured by all WFSs. The contributions of the higher-altitude layers would be then *averaged out*. Inspired on this hypothesis, the second approach consists in adding up all WFS measurements $\mathbf{s}_{av} = \mathbf{s}_1 + \mathbf{s}_2 + \mathbf{s}_3$ and then multiplying the vector $\mathbf{s}_{av}$ by an *averaged reconstructor* —denoted as $\mathbf{R}_{av}$— and computed as:

$$\mathbf{R}_{av} = \frac{1}{3}\left(\mathbf{R}_1 + \mathbf{R}_2 + \mathbf{R}_3\right) \ . \tag{4.31}$$

Then, the ground DM's command vector $\mathbf{u}$ would be generated with the vector-matrix multiply:

$$\mathbf{u} = \mathbf{R}_{av}\mathbf{s}_{av} \ . \tag{4.32}$$

Note that the two approaches (equations 4.30 and 4.32) are totally equivalent *if and only if* all matrix partitions are identical, i.e. $\mathbf{R}_1 = \mathbf{R}_2 = \mathbf{R}_3$, and this could only be true if:

1. All SH-WFSs were identical (same orientation, same pixel scale, etc.).
2. The ground DM were perfectly conjugated to the telescope pupil ($h_1 = 0$ km).
3. There were no FoV-dependent aberrations affecting in a different way the pupil imaging of the SH-WFSs positioned at different angles in the FoV.

This is actually the case for the GLAO simulations we will present in this section. However, in reality, each one of the MAD's SH-WFS is oriented in a different way[4] leading to different matrices $\mathbf{R}_k$. In addition, in practice there are always FoV-dependent (static) aberrations. Therefore, the matrix partitions are never in practice the same.

[4]The true orientations of the SH-WFSs of MAD will be determined in section 4.4 and they will be taken into account in the simulations presented in section 4.5.

The second approach has drawn much attention due to the fact that $\mathbf{R}_{av}$ is a SCAO-size (i.e. 60x104) matrix. Therefore, the *computing power* that would be required to perform the vector-matrix multiply $\mathbf{R}_{av}\mathbf{s}_{av}$ would be, for the case of MAD, ≈3 times less than the one required to perform $\mathbf{R}_{TLS}\mathbf{s}$. This is a feature particularly attractive for the high-order GLAO systems envisaged for the future Extremely Large Telescopes [32, 84]. However, the performance obtained with the averaged reconstructor $\mathbf{R}_{av}$ under realistic conditions remains to be investigated.

In this work we have only investigated, both with simulations and with experiments, the first reconstruction approach. In the following sections we will study the high-flux optimization of the GLAO mode based on this reconstruction approach.

4.3.2.2 GLAO performance v. filtered modes

In this section we will study the variations of the GLAO performance with respect to the number of filtered modes in the TLS reconstruction matrix $\mathbf{R}_{_{TLS}} = \mathbf{V}\Sigma_{fil}^{-1}\mathbf{U}^T$. We will consider the following numbers of filtered modes: $\{1, 5, 8, 13, 20\}$. The sampling frequency was set to 400 Hz, and the PI gains were set to $g_I = g_p = 0.3$. We have considered the 1' FoV and the 2' FoV configurations shown in figure 4.28 for positioning the GSs.

Figure 4.30 shows the GLAO performance profiles obtained along the x-axis for the two FoV configurations, and for all the considered number of filtered modes. The plots in (a) and (b) show the profiles of SR and $\text{GEE}_{0.1}$, respectively, for the 1' FoV configuration. Note that there is a very little impact on the performance profiles from the change of the number of filtered modes. Also, note that the maxima occur at $x = 0$. The maximum performance at $x = 0$ ($S_R = 33.5\%$, and $\text{GEE}_{0.1} = 6.4$) is obtained for the case of 13 filtered modes. Note also that filtering just one eigenmode (i.e. piston) gives the lowest performance of the considered cases.

The plots in (c) and (d) of figure 4.30 show the profiles of SR and $\text{GEE}_{0.1}$, respectively, for the 2' FoV configuration. Once again, we put in evidence the little impact of the number of filtered modes on the performance profiles. We can nevertheless remark that the performance profiles are slightly more uniform when filtering only one eigenmode. Filtering more eigenmodes makes the performance slightly higher at the center of the FoV while slightly lower at the borders.

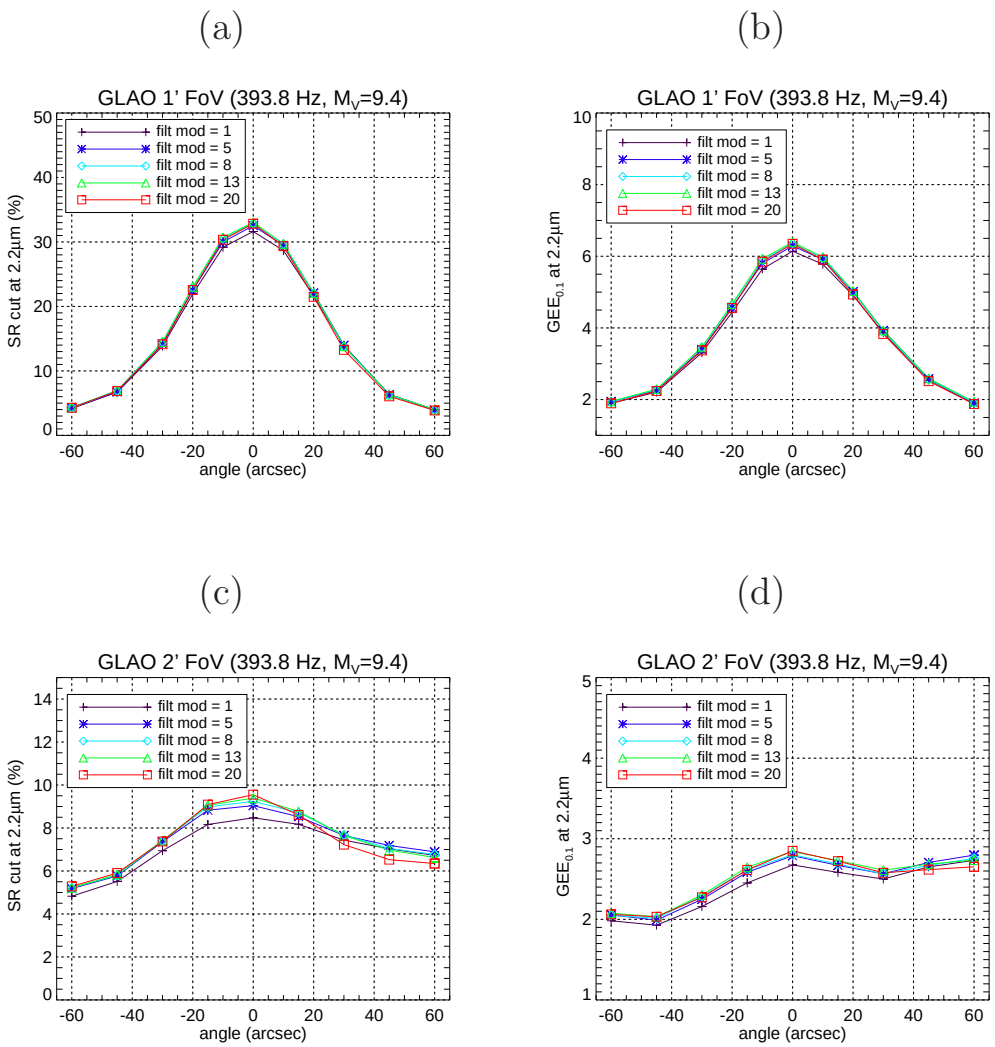

Figure 4.30: GLAO performance at 2.2μm as a function of the number of filtered modes in $\mathbf{R}_{TLS}$ ($M_v = 9.4$, $g = 0.3$, $f_s = 393.8$ Hz, MAPS1+2+3). The performance profiles are evaluated along the x-axis. (a) SR profiles for the 1' FoV configuration. (b) $\text{GEE}_{0.1}$ profiles for the 1' FoV configuration. (c) SR profiles for the 2' FoV configuration. (d) $\text{GEE}_{0.1}$ profiles for the 2' FoV configuration.

4.3.2.3 GLAO performance v. PI gains

In this section we will study the variations of the GLAO performance with respect to the PI gains ($g_I = g_p$) of the temporal controller. We will consider the following PI gains: $g = \{0.1, 0.2, 0.3, 0.4, 0.5\}$. The sampling frequency was set to 400 Hz, and the number of filtered modes in $\mathbf{R}_{_{TLS}}$ was set to 13. We have once again considered the 1' and the 2' FoV configurations presented in figure 4.28.

Figure 4.31 shows the GLAO performance profiles obtained along the x-axis for the two FoV configurations, and for all the considered PI gains. The plots in (a) and (b) show the profiles of SR and $\text{GEE}_{0.1}$, respectively, for the 1' FoV configuration. As we already remarked in section 4.3.2.2, the performance of the 1' FoV configuration reaches its maximum at the center $x = 0$. Note that the minimum performance at $x = 0$ is obtained when $g = 0.1$ whereas the maximum is obtained when $g = 0.5$. Indeed, since the system is operating at high flux levels ($M_V = 9.4$) the noise propagation is not strong. Therefore, increasing the correction bandwidth by increasing the PI gains translates into higher performances at $x = 0$.

Let us now consider the plots in (c) and (d) of figure 4.31. These figures show the profiles of SR and $\text{GEE}_{0.1}$, respectively, for the 2' FoV configuration. Note that, apart from the $g = 0.1$ case which gives a lower SR profile, the performance profiles do not vary much with respect to changes in the PI gains.

4.3.2.4 GLAO contour plots

In this section we will evaluate the GLAO performance at 2.2μm in the whole FoV. Figure 4.32 shows the GLAO contour plots for the 1' and the 2' FoV configurations. The black stars (★) indicate the positions of the GSs. The performance was evaluated at the positions indicated with a small cross (+) and then interpolated to generate the iso-Strehl lines in the whole FoV. The number of filtered modes in $\mathbf{R}_{_{TLS}}$ was fixed to 13, and the PI gains were fixed to $g = 0.5$. Figures (a) and (b) show the SR and $\text{GEE}_{0.1}$ contour plots for the 1' FoV configuration. We can clearly see that the maximum performance (both in SR and $\text{GEE}_{0.1}$) is obtained at the center of the FoV. These results are in accordance with the analytical studies of A. Tokovinin [144] who had predicted already that if the GSs lie too close to each other the performance will be boosted at the center of the FoV.

Figures (c) and (d) show the SR and $\text{GEE}_{0.1}$ contour plots for the 2' FoV configuration. By comparing the contour plots of the 1' and the 2' FoV configurations we can see that placing the GSs further away from each other improves the homogeneity

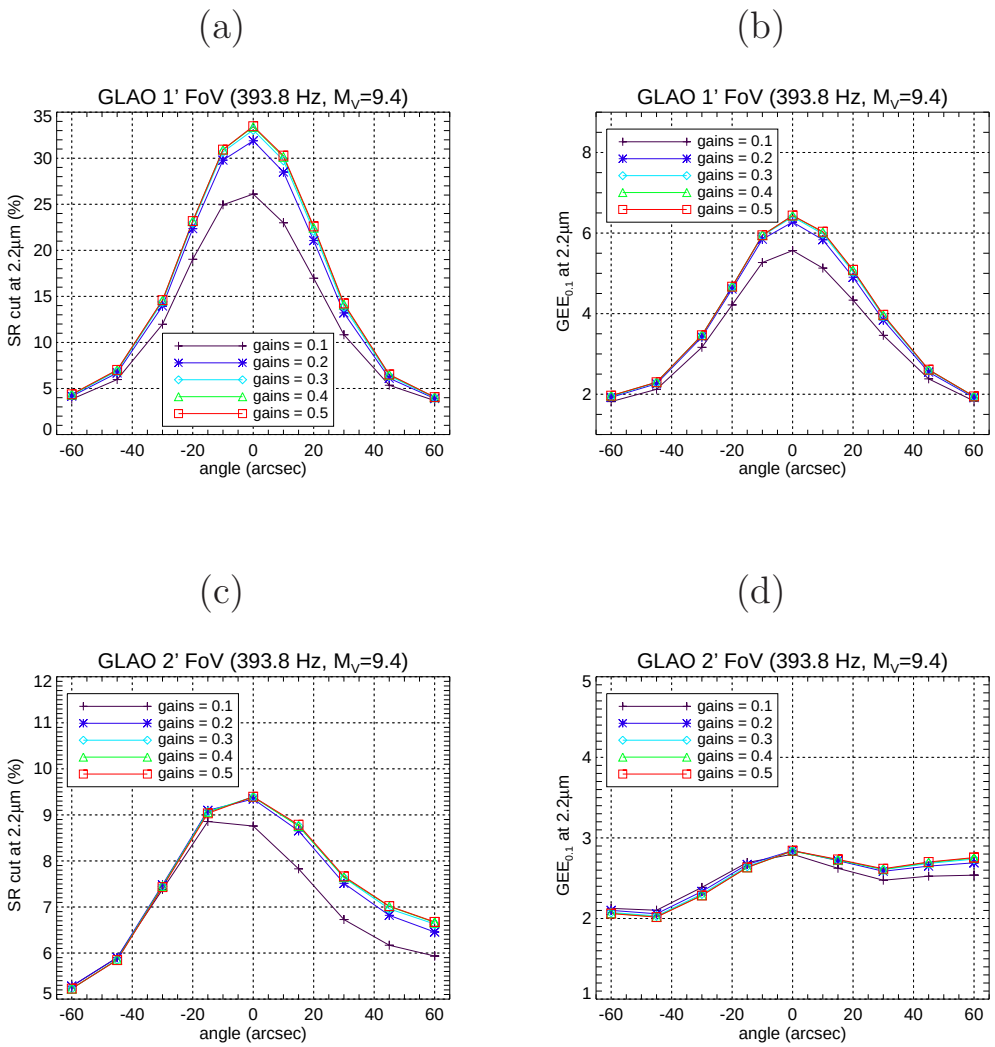

Figure 4.31: GLAO performance at 2.2μm as a function of the PI gains ($M_v = 9.4$, 13 filtered modes, $f_s = 393.8$ Hz, MAPS1+2+3). The performance profiles are evaluated along the x-axis. (a) SR profiles for the 1' FoV configuration. (b) $\text{GEE}_{0.1}$ profiles for the 1' FoV configuration. (c) SR profiles for the 2' FoV configuration. (d) $\text{GEE}_{0.1}$ profiles for the 2' FoV configuration.

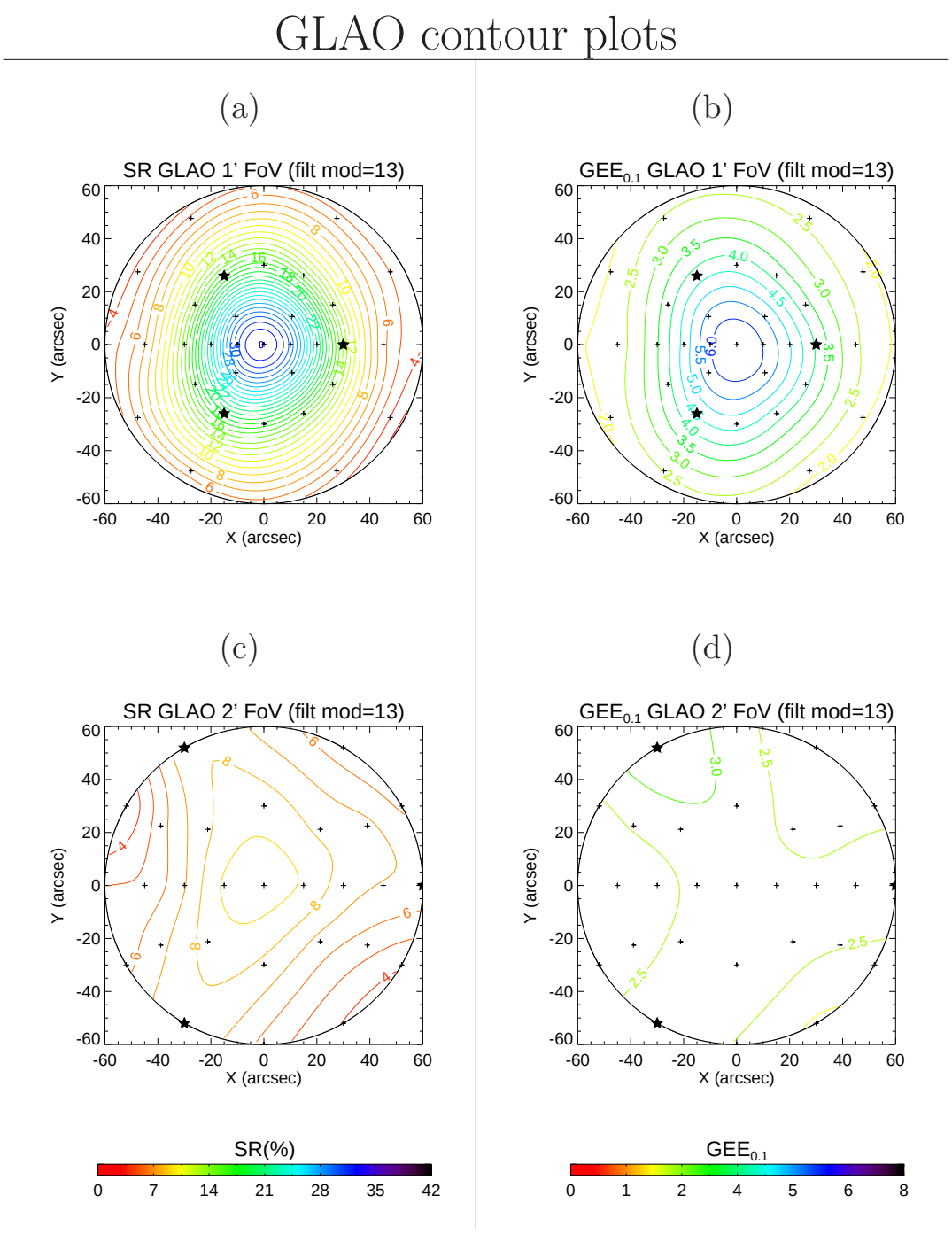

Figure 4.32: GLAO performance at 2.2μm evaluated in the whole FoV. (M_v = 9.4, 13 filtered modes, g = 0.5, f_s = 393.8 Hz, MAPS1+2+3). (a) SR contour plot for the 1' FoV configuration. (b) $GEE_{0.1}$ contour plot for the 1' FoV configuration. (c) SR contour plot for the 2' FoV configuration. (d) $GEE_{0.1}$ contour plot for the 2' FoV configuration.

of the performance at the expense of a lower mean performance in the whole FoV.

4.3.3 MCAO mode

The MAD system operating in MCAO mode uses the three SH-WFSs for probing the turbulence and the two deformable mirrors for wavefront correction. We will consider once again the 1' and 2' FoV configurations described in figure 4.28. We have also considered that all NGSs are of the same magnitude: $M_V = 9.4$.

The MAD's MCAO interaction matrix ($\mathbf{M}_{int}$) has 312 rows (104 measurements per SH-WFS) and 120 columns (60 actuators per DM). The eigenmodes of MAD's MCAO interaction matrix for the 1' FoV and the 2' FoV configurations are shown in figure 4.34 and figure 4.35, respectively. The associated (normalized) singular values are shown in figure 4.33. Mode number 1 corresponds to the best-seen eigenmode. Note that each eigenmode can be represented graphically with two phase maps, one associated with each DM.

The condition number of the MCAO interaction matrix for the 1' FoV configuration is 2770 whereas the one for the 2' FoV configuration is 1150. Recall from section 2.3.2.2 that the condition number normally increases with the considered FoV. The reason why for MAD the condition number for the 1' FoV configuration is larger than the one for the 2' FoV configuration is because the altitude DM spans the whole 2' FoV regardless of the position of the GSs. Hence, when the GSs are located at 1' the periphery of the 2' FoV becomes a non-seen area. The difficulty to reconstruct this portion of the FoV is translated into a larger condition number for the 1' FoV configuration.

It is interesting to note also from figures 4.34 and 4.35 that the last eigenmodes (associated with low sensitivities) are mainly tip-tilt combinations with different orientations (from eigenmode number 91 to 120 for the 1' FoV configuration, and from 111 to 120 for the 2' FoV configuration).

4.3.3.1 MCAO performance v. filtered modes

In this section we will study the variations of the MCAO performance with respect to the number of filtered modes in the TLS reconstruction matrix $\mathbf{R}_{TLS}$. We have considered the following number of filtered modes: $\{12, 16, 30, 45, 60\}$. We will study both the 1' FoV and the 2' FoV configurations. The sampling frequency was set to 400 Hz, and the PI gains were set to $g_I = g_p = 0.3$.

Figure 4.36 shows the MCAO performance profiles obtained along the x-axis for the two FoV configurations, and for all the considered number of filtered modes. The plots

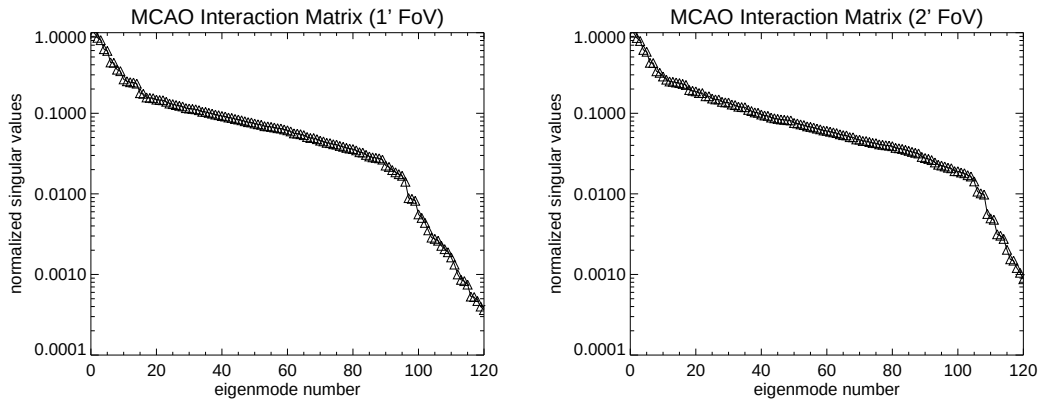

Figure 4.33: Normalized singular values of the MAD's MCAO interaction matrix: (*Left*) for the 1' FoV configuration. (*Right*) for the 2' FoV configuration.

in (a) and (b) show the profiles of SR and $GEE_{0.1}$, respectively, for the 1' FoV configuration. Note the poor performance obtained when only 16 eigenmodes are filtered out. This is due to the fact that many badly-seen modes (i.e. tip-tilt combinations) have not been filtered out. As shown in figure 4.34, there are ≈30 badly-seen modes of this type for the 1' FoV configuration that should always be filtered out. It is also interesting to note from the profiles shown in (a) and (b) that increasing the number of filtered modes improves the homogeneity of the correction in the 1' FoV. An almost-perfect homogeneity ($S_R \approx 37\%$) is achieved inside the 1' FoV after filtering 60 eigenmodes, at the expense of a slightly lower mean performance in the 1' FoV.

The plots in (c) and (d) of figure 4.36 show the profiles of SR and $GEE_{0.1}$, respectively, for the 2' FoV configuration. Note that the maximum SR and $GEE_{0.1}$ values occur at $x = +60''$, which coincides with the location of one of the three GSs (see figure 4.28). It is interesting to note that as the number of filtered modes increases the performance at $x = +60''$ goes down whereas the performance at the other positions goes up. Hence, the uniformity of the correction in the 2' FoV is slightly improved for a larger number of filtered modes.

It is important to note that it is not trivial to decide what is the *best* number of filtered modes. In the end, the decision depends on the FoV of interest in which we want to optimize the performance. As we discussed in section 2.6, there are other reconstruction approaches more suitable to perform a FoV-dependent optimization. As we will discuss in section 4.7, more advanced control laws allowing this kind of optimization will be also validated in MAD in the near future.

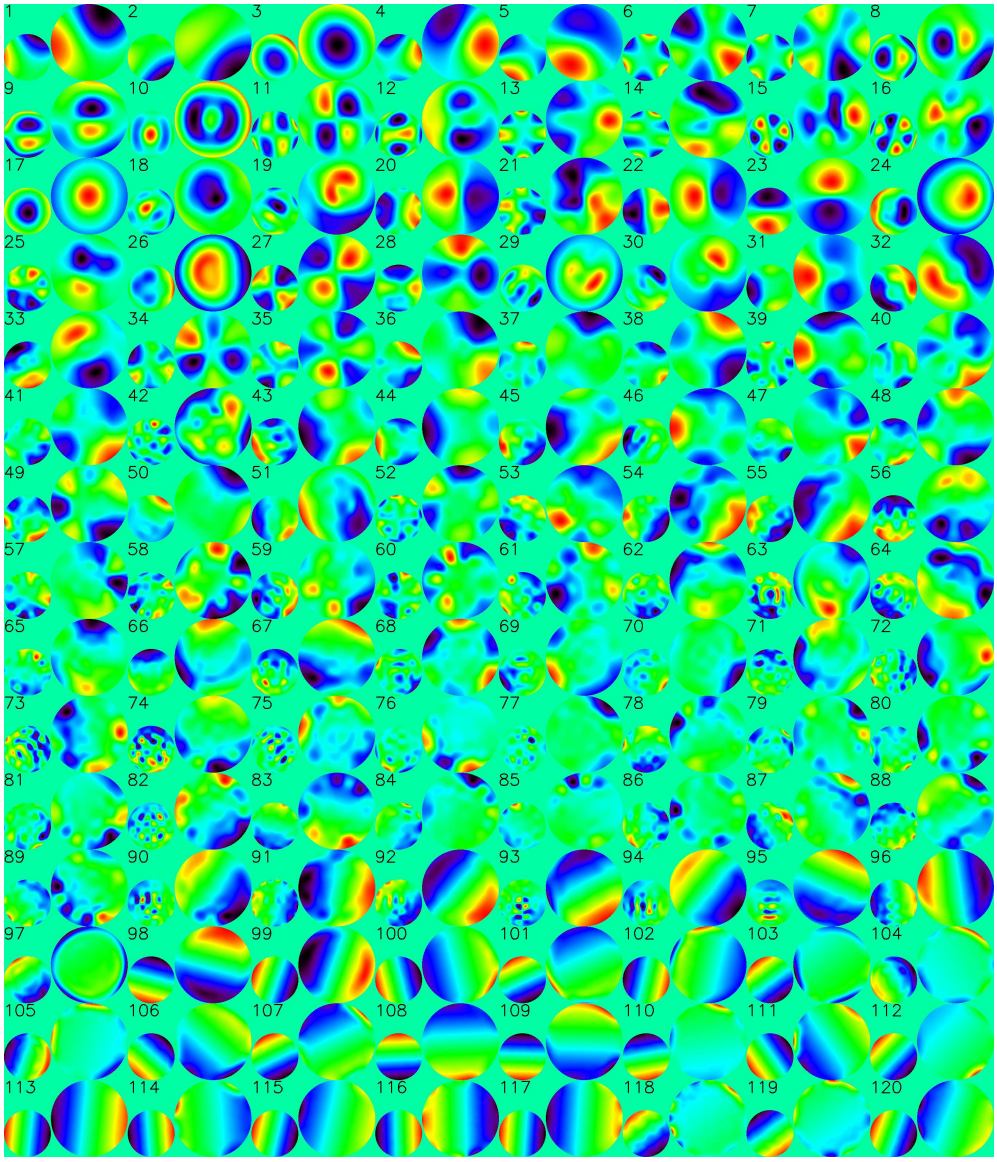

Figure 4.34: Eigenmodes of the MAD's MCAO interaction matrix for the 1' FoV configuration.

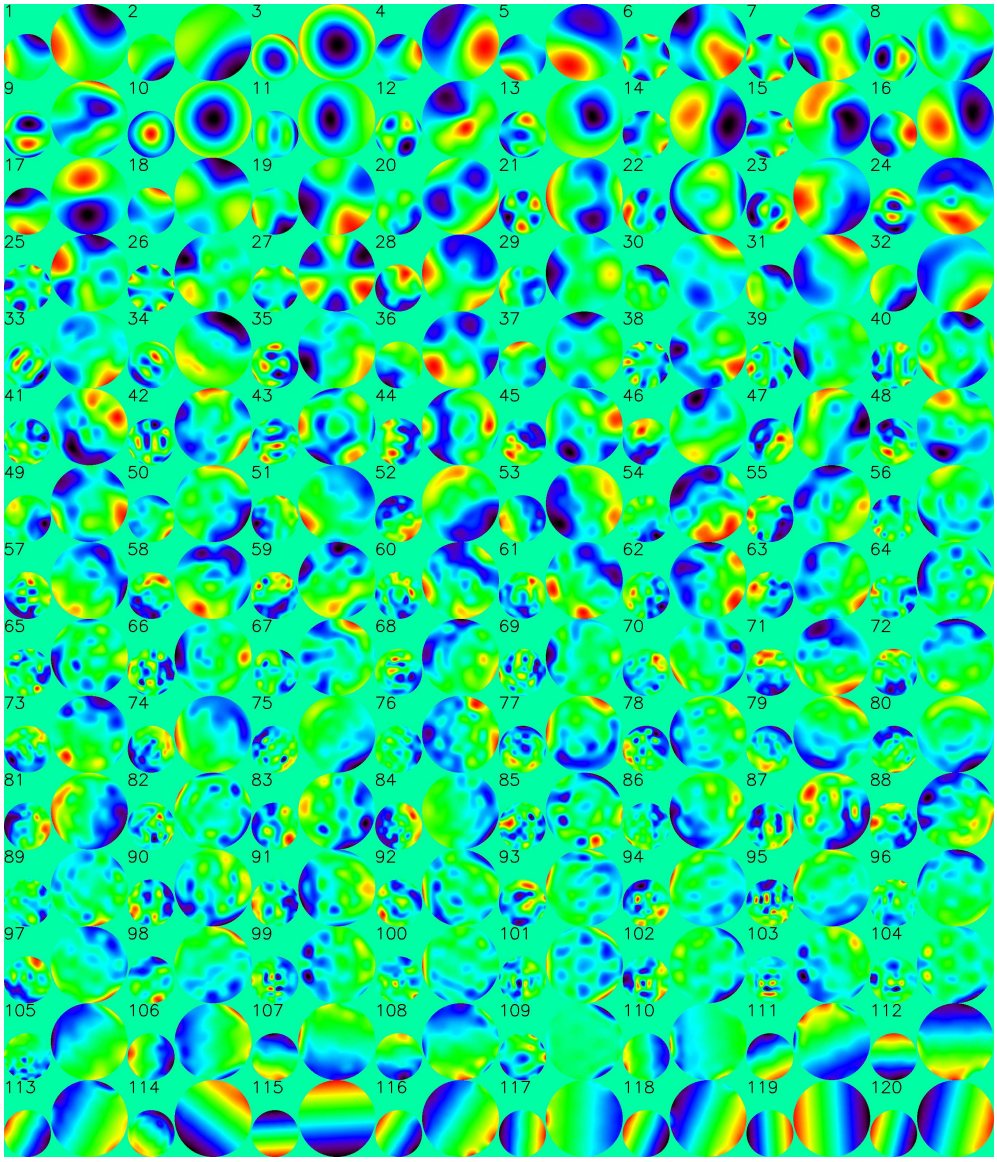

Figure 4.35: Eigenmodes of the MAD's MCAO interaction matrix for the 2' FoV configuration.

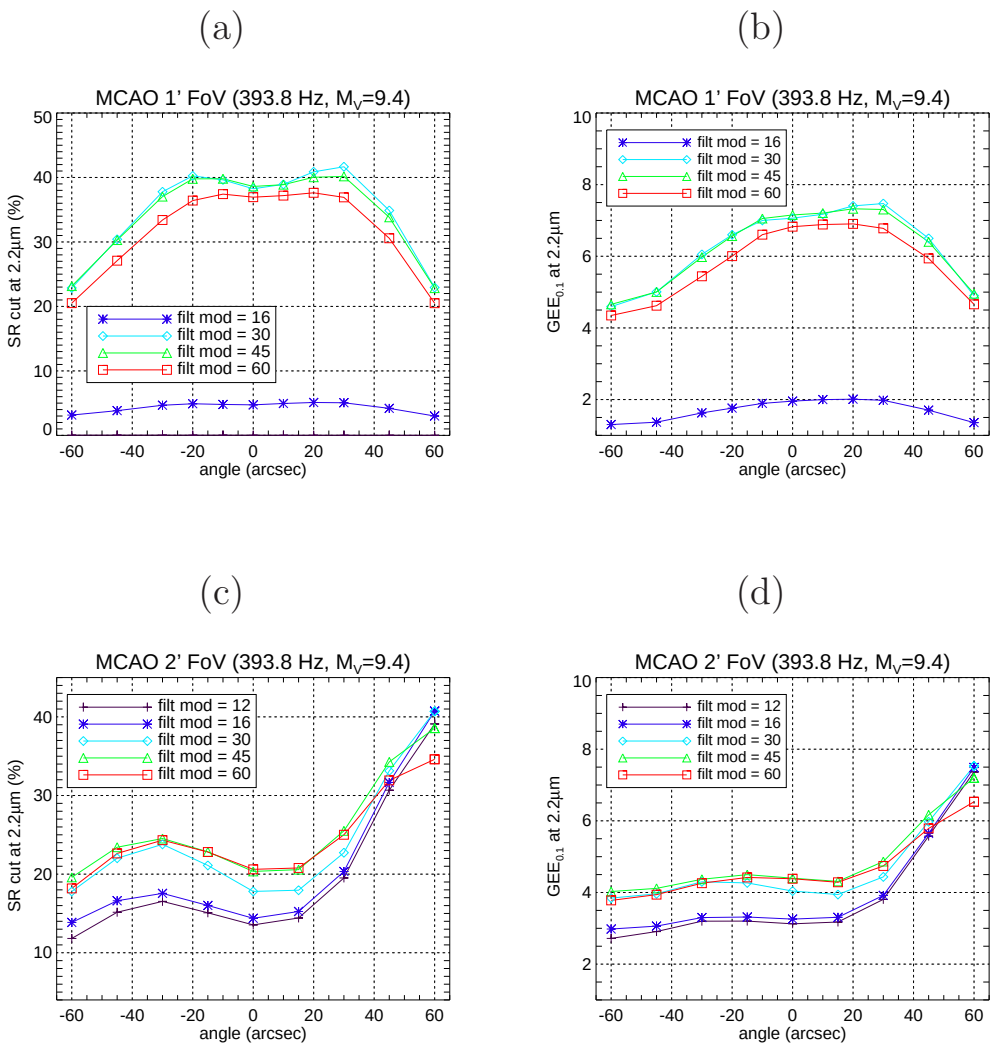

Figure 4.36: MCAO performance at 2.2μm as a function of the number of filtered modes in $\mathbf{R}_{TLS}$ ($M_v = 9.4$, $g = 0.3$, $f_s = 393.8$ Hz, MAPS1+2+3). The performance profiles are evaluated along the x-axis. (a) SR profiles for the 1' FoV configuration. (b) $\text{GEE}_{0.1}$ profiles for the 1' FoV configuration. (c) SR profiles for the 2' FoV configuration. (d) $\text{GEE}_{0.1}$ profiles for the 2' FoV configuration.

4.3.3.2 MCAO performance v. PI gains

In this section we will study the variations of the MCAO performance with respect to the PI gains ($g_I = g_p$) of the temporal controller. We will consider the following PI gains: $g = \{0.1, 0.2, 0.3, 0.4, 0.5\}$. The sampling frequency was set to 400 Hz, and the number of filtered modes in $\mathbf{R}_{_{TLS}}$ was set to 45. We have studied once again both the 1' and the 2' FoV configurations.

Figure 4.37 shows the MCAO performance profiles obtained along the x-axis for the two FoV configurations, and for all the considered PI gains. The plots in (a) and (b) show the profiles of SR and $\text{GEE}_{0.1}$, respectively, for the 1' FoV configuration. Note that since we have filtered out 45 eigenmodes, there is a good uniformity of the correction in the 1' FoV for all considered PI gains. Note also that the performance increases with the PI gains. The best performance is obtained when $g = 0.5$. As mentioned already in section 4.3.2.3, this is due to the fact that we are considering a high flux case.

The plots in (c) and (d) of figure 4.37 show the profiles of SR and $\text{GEE}_{0.1}$, respectively, for the 2' FoV configuration. As mentioned already in section 4.3.2.3, the maximum SR and $\text{GEE}_{0.1}$ values occur at the position of one of the GSs ($x = +60''$). Note that increasing the gains increases the performance of the whole profiles. However, the performance at the GS position ($x = +60''$) is the most susceptible to PI gains variations.

4.3.3.3 MCAO contour plots

In this section we will evaluate the MCAO performance at 2.2μm in the whole FoV. Figure 4.38 shows the MCAO contour plots for the 1' and the 2' FoV configurations. The black stars (★) indicate the positions of the GSs. The performance was evaluated at the positions indicated with a small cross (+) and then interpolated to generate the iso-Strehl lines in the whole FoV. The number of filtered modes in $\mathbf{R}_{_{TLS}}$ was fixed to 45, and the PI gains were fixed to $g = 0.5$. Figures (a) and (b) show the SR and $\text{GEE}_{0.1}$ contour plots for the 1' FoV configuration. Note that a very good homogeneity of the correction is achieved within the 1' FoV, both in terms of SR and in $\text{GEE}_{0.1}$. Outside the 1' FoV the performance drops steadily. Figures (c) and (d) show the SR and $\text{GEE}_{0.1}$ contour plots for the 2' FoV configuration. Note that uniformity of correction is not achieved in the whole 2' FoV. The maximum performance is obtained at the GSs positions and then it decreases steadily towards the center of the FoV. The minimum performance is obtained at the borders of the 2' FoV between the GSs.

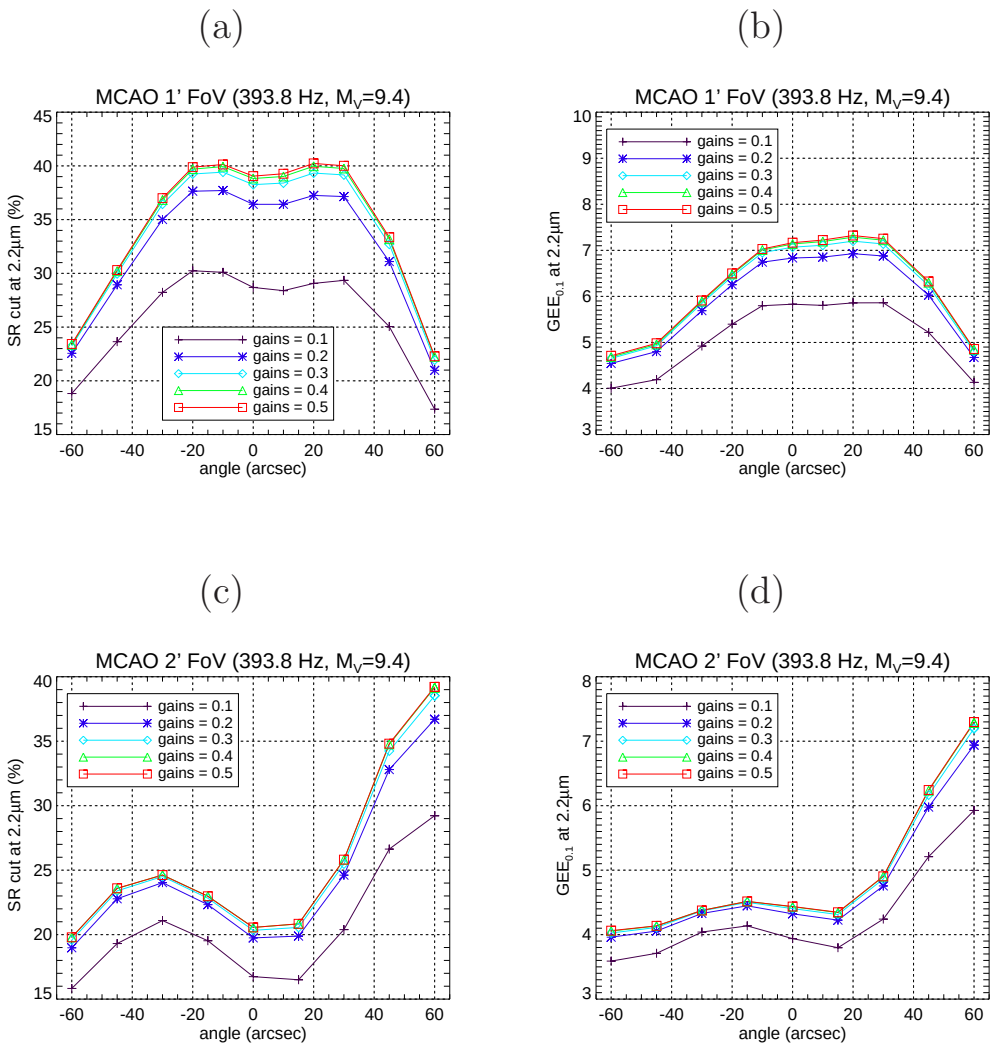

Figure 4.37: MCAO performance at 2.2μm as a function of the PI gains of the temporal controller (M_v = 9.4, 45 filtered modes, f_s = 393.8 Hz, MAPS1+2+3). The performance profiles are evaluated along the x-axis. (a) SR profiles for the 1' FoV configuration. (b) $\mathrm{GEE}_{0.1}$ profiles for the 1' FoV configuration. (c) SR profiles for the 2' FoV configuration. (d) $\mathrm{GEE}_{0.1}$ profiles for the 2' FoV configuration.

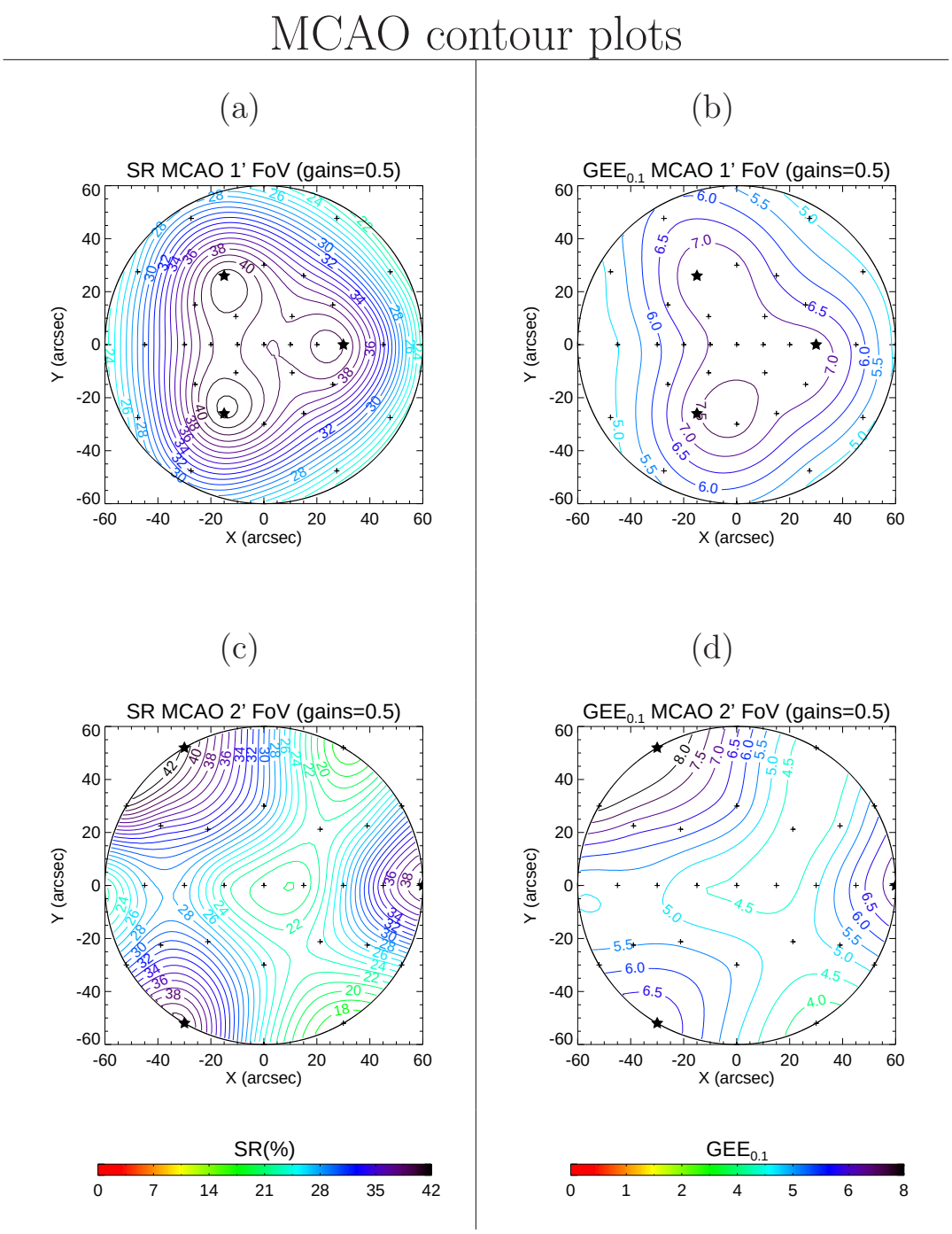

Figure 4.38: MCAO performance at 2.2μm evaluated in the whole FoV. (M_v = 9.4, 45 filtered modes, g = 0.5, f_s = 393.8 Hz, MAPS1+2+3). (a) SR contour plot for the 1' FoV configuration. (b) $GEE_{0.1}$ contour plot for the 1' FoV configuration. (c) SR contour plot for the 2' FoV configuration. (d) $GEE_{0.1}$ contour plot for the 2' FoV configuration.

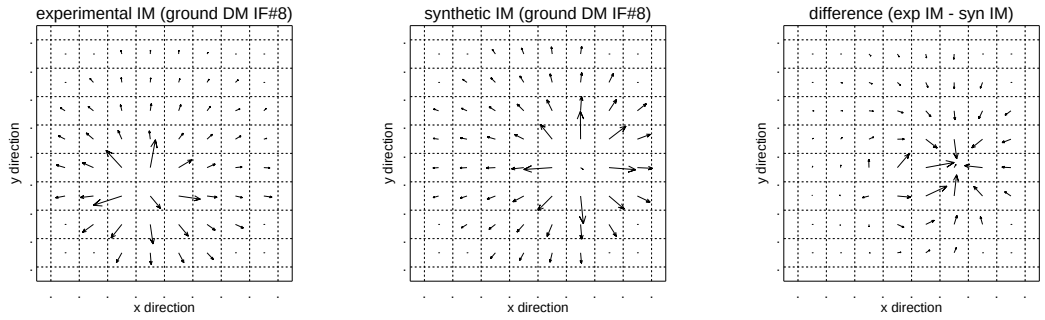

Figure 4.39: Slope map representing the response of MAD's SH#2 to an unit command vector applied to actuator#8 of the ground DM. The information was extracted from the 8th column of: *(a)* experimental IM, *(b)* synthetic IM (1st iteration). *(c)* The difference between the 8th columns of both IMs is a measure of the mismatch between them. The large mismatch is due to a relative rotation between real and simulated SH-WFS of ≈ 90 degrees.

4.4 Opto-geometrical calibration

For all the MAD simulation studies presented in section 4.3 we considered that all SH-WFSs were physically oriented in the same way (as shown in figure 4.2), and that both DMs were also perfectly aligned and oriented as depicted in figure 4.7. In this section we will present the procedure we followed to determine the true opto-geometrical relationships between the MAD components.

The opto-geometrical calibration refers to the determination of the relative positions (i.e. rotation, shift in x, and shift in y) between both DMs and the three SH-WFS of MAD, as well as the determination of the GSs mapping in the FoV.

The procedure we have used to estimate the relative positions is based on an iterative comparison between an *experimental IM* calibrated in the laboratory and a *synthetic IM* generated with our MAD simulation tool. Indeed, as illustrated with an example in figure 4.39, the interaction matrix contains all the information about the relative positions between the wavefront sensors and the deformable mirrors. Therefore, it is possible to retrieve this information by an iterative comparison in which the rotations and shifts of the simulated components are adjusted until a best fit between the two matrices is found.

As illustrated in figure 4.39(c), the difference between an experimental and a synthetic IM is a measure of the misalignments between the real components and the simulated ones. The best fit in the least-squares sense between the two IMs can be ob-

tained by minimizing the mean-square error between *all* the elements of the IMs. This is equivalent to minimizing the *squared distance* between the two matrices, defined as:

$$\begin{aligned} \mathbf{d}^2 &= \|\mathbf{M}_{exp} - \mathbf{M}_{syn}\|^2 \\ &= \text{trace}\left\{(\mathbf{M}_{exp} - \mathbf{M}_{syn})^T(\mathbf{M}_{exp} - \mathbf{M}_{syn})\right\} \end{aligned} \tag{4.33}$$

where $\mathbf{M}_{exp}$ denotes the experimental IM and $\mathbf{M}_{syn}$ the synthetic one. Of course, before attempting to compare the two matrices, it is important to be sure that one follows the same convention in the numbering of actuators and subapertures in both IMs. Figure 4.7 shows the sequential numbering of the actuators for the MAD's DMs, and figure 4.2 shows the sequential numbering of the subapertures for all SH-WFSs. Also, a convention in the ordering of the SH slopes needs to be defined. We will order first the x-slopes followed by the y-slopes for all subapertures.

We will outline below the steps that need to be followed in order to estimate the relative positions between the different DMs and the different WFSs of an MCAO system like MAD [111]:

1. *Alignment of SH-WFSs with respect to ground DM.* An experimental (SCAO) IM between the ground DM and a SH-WFS is calibrated. On the simulation side, the position of the (simulated) ground DM is set to a given reference position (e.g. zero rotation, zero shifts), and the relative position (i.e. rotation, shift in x, shift in y) of the (simulated) SH-WFS is iteratively adjusted until a best fit between $\mathbf{M}_{exp}$ and $\mathbf{M}_{syn}$ is found. This procedure is repeated for all SH-WFS.

2. *Alignment of altitude DM with respect to all SH-WFS.* Recall that in MCAO, the interaction matrix involving a DM conjugated in altitude depends on the position of the GSs in the FoV. In order to avoid the FoV-dependence as a first step, all SH-WFSs should be coupled to a GS located in the optical axis. Then, an experimental IM between the altitude DM and each of the SH-WFS is calibrated. On the simulation side, the absolute position of each (simulated) SH-WFS is set to the values determined in step 1. Then, the relative position of the altitude DM is iteratively adjusted until a best fit between the experimental and the synthetic IM is found. This procedure is repeated for all SH-WFSs, but note that all the results should be the same (i.e. there is only one physical position of the altitude DM). Discrepancies in the results are an indicator of the precision of the method.

SH1 v. DM1	
Rotation	0 degrees
Shift in x	+0.0187 %
Shift in y	-0.0025 %

SH2 v. DM1	
Rotation	90 degrees
Shift in x	-0.001 %
Shift in y	+0.023 %

SH3 v. DM1	
Rotation	0 degrees
Shift in x	+0.022 %
Shift in y	-0.004 %

SH1 v. DM2	
Rotation	-10.81 degrees
Shift in x	+0.563 %
Shift in y	+0.390 %

SH2 v. DM2	
Rotation	-9.00 degrees
Shift in x	+0.071 %
Shift in y	+0.727 %

SH3 v. DM2	
Rotation	-10.3 degrees
Shift in x	-0.708 %
Shift in y	+1.121 %

Table 4.6: Summary of the relative positions between components of the MAD system. The rotations are given in degrees clockwise, and the shifts are given in percent of the telescope pupil size. (*Left*) The three tables on the left show the relative positions of each SH with respect to the ground DM (DM1) determined from the first step of our procedure. (*Right*) The three tables on the right show the relative position of the altitude DM (DM2) with respect to each of the SHs determined from the second step of our procedure. Discrepancies in these numbers indicate the precision of our algorithm.

3. *Mapping of the GSs in the FoV.* The last step is to determine the mapping between the real FoV and the simulated FoV in order to position correctly the GSs in the creation of MCAO interaction matrices. On the experimental side, a full MCAO IM is recorded with the selected GSs. On the simulation side, all the (simulated) DMs and SH-WFSs are set to the positions determined in the previous steps. Then, the positions in the FoV of the (simulated) GSs are adjusted until a best fit between the MCAO IMs is found.

The summary of the relative positions between components of the MAD system is presented in table 4.6. From the discrepancies in the determination of the position of the altitude DM we can conclude that the precision of our algorithm is $\approx \pm 1^\circ$ in rotation and $\approx \pm 1\%$ in the shifts. It is important to note that the precision of our algorithm depends on the interpolation algorithms that were used to simulate the rotations and the shifts of the AO components. We believe that there is room for improvement because the interpolation algorithms that we used are not well adapted for circular geometries, and they introduce non-negligible interpolation errors at the borders of the circular pupil.

Regarding the mapping of the GSs in the FoV (step number 3), we determined the distribution of all the GSs generated by MAPS as seen from the WFSs plane. Note that in figure 4.15 we showed the distribution of the GSs *as seen* from the CAMCAO camera. The difference between the two distribution is just a reflection across the y-axis.

4.5 Experimental v. simulation results

In this section we will present the experimental results obtained in SCAO, GLAO and MCAO configurations and their direct comparison with simulation results. In the case of GLAO and MCAO, two FoV configurations were studied: 1' FoV and 2' FoV. The GSs for the 1' FoV configuration were the MAPS stars number 26, 28 and 30 (Figure 4.15), and for the 2' FoV were the MAPS stars number 5, 10 and 15. Note that the actual FoV covered by the MAPS stars is slightly smaller than 1' and 2', namely 54" and 108" respectively. The equivalent star magnitude of all GSs was set to $M_V = 9.4$. The turbulence conditions are the ones corresponding to the MAPS PS1+2+3 configuration (Table 4.5).

We will present a comparison in performance obtained with a TLS reconstructor $\mathbf{R}_{TLS}$ and a PI controller. The sampling frequency was set to 393.8 Hz. The gains of the PI controller were set to the same value ($g_I = g_p$). For each configuration, the experimental and simulation control law parameters (i.e. the number of truncated modes in $\mathbf{R}_{TLS}$ and the gains $g_I = g_p$ of the PI controller) were tuned independently in order to maximize the performance on each case. The selected control law parameters are summarized in table 4.7.

Note that in general, the number of truncated modes that maximizes the performance in the experiments is larger than the number of truncated modes that maximizes the performance in simulations. Also, the gains that maximize the performance in the experiments are in general much smaller than the ones that maximize the performance in simulations. In general, more truncated modes and lower gains are required when operating at lower flux levels, but we have verified that experiments and simulations were run under similar flux conditions (i.e. $M_V = 9.4$). The reasons behind the difference between these control law parameters remain to be understood.

In addition, we should note that when operating the MAD system at 393.8 Hz and increasing the PI gains beyond 0.25 causes the MAD system to go unstable. According to control theory (see section 4.2.3.2), the relative stability of an AO system with a total of two frames delay ($\tau_{tot} = 2T$) is assured if the integral gain is $0 < g_I \leq 0.5$. The

	SCAO		GLAO				MCAO			
			1' FoV		2' FoV		1' FoV		2' FoV	
	Exp	Sim	Exp	Sim	Exp	Sim	Exp	Sim	Exp	Sim
truncated modes	20	8	15	13	20	13	55	50	45	45
gains	0.25	0.50	0.20	0.40	0.15	0.40	0.25	0.40	0.15	0.40

Table 4.7: Summary of the control law parameters selected for the comparison of experimental and simulation results.

reasons why the MAD system has a lower stability regime at 393.8 Hz also remains to be understood.

The performance obtained with each configuration in the FoV will be evaluated at all MAPS stars positions (Figure 4.15) at $\lambda = 2.2\mu$m in terms of Strehl ratio and gain in ensquared energy in a square of .1"x.1" ($\text{GEE}_{0.1}$). For reference purposes, the ensquared energy in a square of .1"x.1" of the *turbulence* long-exposure PSF is $\text{EE}_{0.1}^{tur} \approx 4\%$ (MAPS PS1+2+3 profile). On the other hand, the ensquared energy in a square of .1"x.1" of the *diffraction-limited* PSF is 70%. Also, the SR without AO correction (i.e. a long exposure on the turbulence) is $\approx 2\%$.

The estimation of the SR and the $\text{GEE}_{0.1}$ from experimental data is not straightforward. Before presenting the comparison of experimental and simulation results, we will discuss in sections 4.5.1 and 4.5.2 how these metrics were computed from an analysis of the images obtained with the CAMCAO infrared camera.

4.5.1 Experimental Strehl ratio computation

In order to estimate meaningful and comparable experimental Strehl ratio values from the infrared-camera images it is required to take into account a handful of practical considerations. The main issues affecting the SR computation that had to be dealt with when working in the laboratory with MAD were:

1. *Non-common path aberrations.* The non-common path aberrations (NCPA) for the MAD system were characterized using the phase diversity technique for several positions in the FoV [75]. The NCPA at the center of the FoV of MAD are in general smaller than the NCPA at other positions in the 2' FoV. On average, the MAD's NCPA in the FoV account for a wavefront error of ≈100 nm rms, which corresponds to a maximum SR of ≈75% at 2.2μm [75].

   In principle, as discussed in section 1.2.4.2, the NCPA can be compensated in real-time by closing the control loop on the reference slope vector $\mathbf{s}_{ref}$. However,

this technique implies that it is possible to accurately transform the DM shape that compensates for the NCPA into a reference slope vector. In the case of MAD operating in SCAO mode with the SH-WFS located at the center of the FoV, the NCPA are not big enough (due to the better optical quality at the center of the FoV) to produce a big response on the SH-WFS. As a result, the reference slopes are always very close to the zero vector ($\mathbf{s}_{ref} \approx \vec{0}$), and the performance obtained with and without the reference slope vector technique is essentially the same. Note that if the MAD's SH-WFSs had better sampling characteristics[5] it would have been possible to record the reference slope vector with a better accuracy. In that case, it might have been possible to compensate in real-time for the NCPA at the center of the FoV with the reference slope vector technique.

For the case of MAD operating in GLAO and MCAO modes, since the SH-WFSs are located away from the FoV center (i.e. in a circle of ≈1' or ≈2' FoV) the NCPA at these positions in the FoV are actually larger, and it is then possible to record reference slope vectors that actually allow to (partially) compensate in real-time for the NCPA in the directions of the GSs.

In any case, for all the experiments presented in this section we have decided to not correct in real-time for the NCPA using the reference slope vector technique. Hence, all reference slope vectors were simply set to $\mathbf{s}_{ref} = \vec{0}$. Nevertheless, the experimental SR values were a-posteriori *normalized* using the procedure described in section 4.5.1.1 in order to take into account the loss in SR introduced by the NCPA in the FoV.

2. *Field-curvature effect.* The curvature of the IR focal plane of MAD was characterized [76]. It is ≈ 1 mm @ F/15 between the center and the border of the 2' FoV. Clearly, when taking 1'x1' images with CAMCAO there will be at most only one star in focus. The images of the other stars in the FoV will be affected by a defocus. The equivalent loss in SR between an in-focus star in the center of the FoV and one in the border is ≈ 13% [76].

   For all the experiments that will be presented below the best focus was set to the center of the FoV (MAPS star #34). Hence, the SR values for all the other stars were affected by the field-curvature effect. Nevertheless, the SR normalization procedure presented in section 4.5.1.1 also helped to take into account the loss in SR induced by the field curvature.

[5] Recall that the MAD's SH-WFSs sample at Shannon over 4 the diffraction-limited spots (section 4.2.1.1).

4.5.1.1 Strehl ratio normalization

As discussed above, the experimental SR values in the 2' FoV were affected by FoV-dependent non-common path aberrations and by the characteristic curvature of the IR focal plane. Nevertheless, it was possible to characterize the SR loss induced by all these effects by measuring the *maximum SR* obtained at each MAPS star position in the absence of atmospheric turbulence (i.e. installing blank phase screens on MAPS). The *maximum SR* values were measured in closed-loop for *each* of the configurations that will be presented below. Then, the SR values obtained with atmospheric turbulence were later normalized by the corresponding *maximum SR* values.

The only source of error that is not taken into account with this normalization procedure is the error caused by the MAPS phase screens chromaticity. Indeed, the atmospheric turbulence emulated by MAPS is not totally achromatic. Hence, the wavefront perturbation seen by the WFSs will be slightly different from the one seen by the infrared camera. This effect will introduce a systematic error during closed-loop operation. The equivalent loss in SR due to this effect was also characterized and it is 4.5% [91]. Therefore, the experimental SR values have to be also normalized by 95.5%, and this was done for all the experimental results that will be presented below.

4.5.1.2 Strehl ratio estimation

The SR of an image can be estimated either by using equation 1.68 or equation 1.69. We have estimated the SR using a method based on equation 1.68. It is important to note that the main issues that have to be taken care of with this algorithm are the correct estimation of the center of the image (i.e. the vector $\vec{0}$ in equation 1.68), and the generation of a diffraction-limited PSF that matches the spatial sampling of the camera (i.e. the denominator of equation 1.68).

E. Marchetti developed a *Strehlometer* routine based on this method that takes into account all CAMCAO specificities (e.g. pixel scale, background level, etc.). All experimental SR values that will be presented below were computed with this routine.

4.5.2 Experimental gain in ensquared energy computation

We are interested in evaluating the gain in ensquared energy in a square of .1"x.1" ($GEE_{0.1}$). This size of square is becoming a standard for evaluating the performance of next-generation GLAO systems operating in the IR (section 1.2.9).

The computation of the GEE in a square of fixed size is not straightforward. Recall that the pixel scale of CAMCAO is equal to 0.028". If the star images were centered

	SR max (%)	$GEE_{0.1}$ max
Experimental	34	11
Simulation	46	7.5
Relative error (%)	26	-46

Table 4.8: SCAO configuration: comparison of the maximum performance (SR and $GEE_{0.1}$) obtained from experiments and simulations.

between 4 pixels, we could compute accurately the EE in a square of size 0.056" or 0.112", and for a square of exactly 0.1"x0.1" we would need to interpolate the EE between these two values. This is actually the way we have proceeded in the computation of the GEE from simulations. However, in experimental data, the image is never centered on four pixels so it is more difficult to define a square of exactly 0.1"x0.1" that is also *centered* on the image. Interpolation methods could have been also used on experimental data, but the presence of the imaging detector noise (not taken into account in the simulation) makes the interpolation less accurate. We have decided then to avoid interpolations and simply integrate the PSFs in 2x2 camera pixels (if the image is relatively centered on four pixels) or 3x3 camera pixels (if the image is relatively centered on a single pixel). Therefore, the GEE will be effectively evaluated in a square of size between 0.056" to 0.084" depending on the actual position of the star image. Unfortunately, the comparison with simulation results is not going to be direct. We will actually expect higher values in GEE for experimental data since in general the size of the square will be smaller.

4.5.3 SCAO mode

In this section we will compare experimental and simulation results obtained in SCAO mode. The GS was located at the center of the FoV (MAPS star # 34). Figures 4.40(a) and (b) show the SR contour plots obtained from experiments and simulations, and (c) and (d) show the corresponding $GEE_{0.1}$ contour plots. The maximum performance values (on the GS position) obtained in SCAO mode are summarized in table 4.8.

Table 4.8 also presents the relative error, which was computed with respect to the simulation results as:

$$\text{Relative error} = \frac{\text{PERF}_{sim} - \text{PERF}_{exp}}{\text{PERF}_{sim}} \times 100 \ . \tag{4.34}$$

Note that the relative error in SR is 26%. This error is an indicator of how much the experimental maximum SR is below the expected maximum SR predicted by the

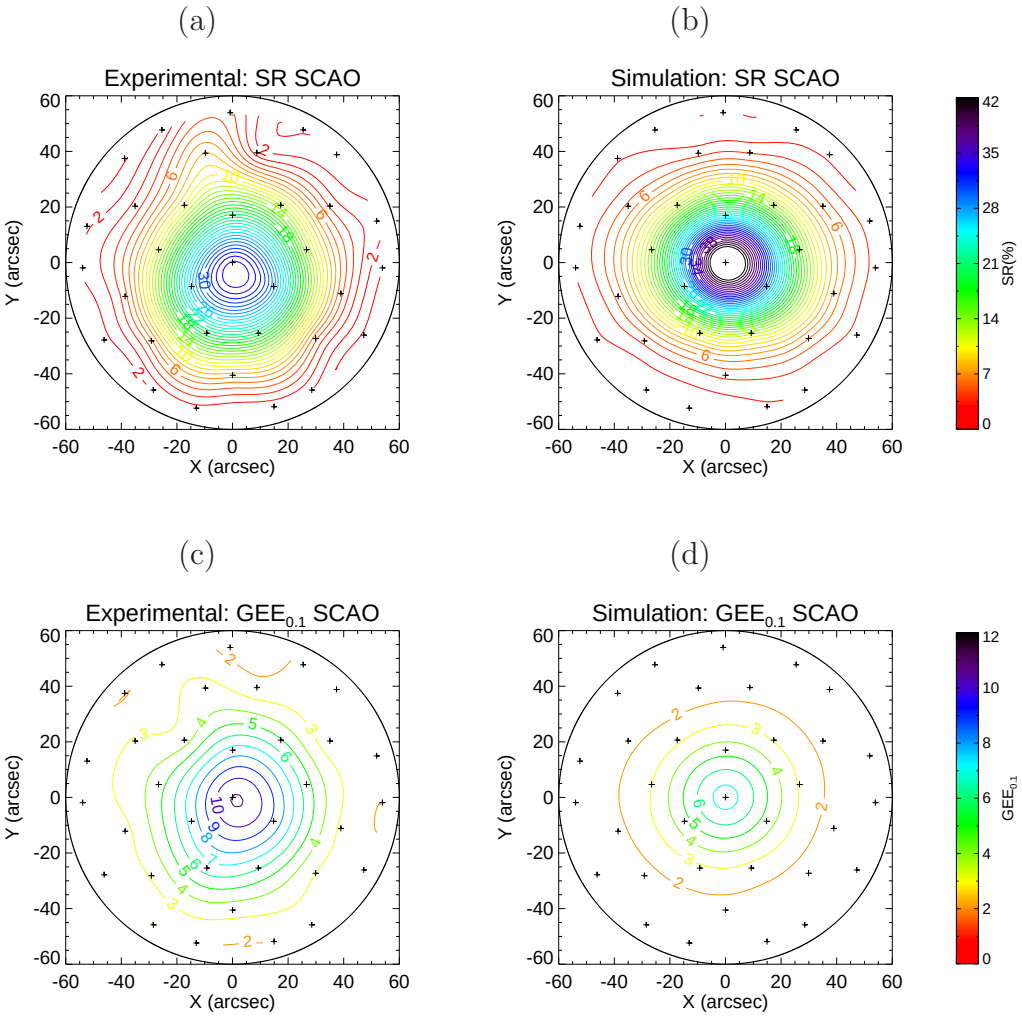

Figure 4.40: SCAO configuration: (a) SR from experiments. (b) SR from simulations. (c) $GEE_{0.1}$ from experiments. (d) $GEE_{0.1}$ from simulations. The GS is located at the center of the FoV. MAPS stars indicated with a (+).

simulations. Note that the mismatch is most probably due to additional error sources not taken into account in neither the simulations nor the normalization of the experimental SR values. So far we have not identified additional error sources that could be responsible for such a mismatch. The reasons behind the mismatch remain to be investigated.

Concerning the $GEE_{0.1}$, note from table 4.8 that the relative error is -46%, the negative sign meaning that the performance obtained from experiments is higher than the one obtained from simulations. As we explained in section 4.5.2, the main reason why the $GEE_{0.1}$ estimated from experiments is higher than the one estimated from simulations is because the square size used in the experimental estimation of $GEE_{0.1}$ is actually smaller than 0.1"x0.1". Therefore, we won't be able to compare directly the absolute values in $GEE_{0.1}$. The experimental estimation method of $GEE_{0.1}$ needs to be improved, and this work remains to be done.

Let us now compare the performance in the whole FoV obtained with the SCAO configuration. Note from figures 4.40(a) and (b) that, as expected, the SCAO correction gets worse as we move away from the GS due to anisoplanatism. A comparison between the SCAO profiles obtained from experiments and simulations was already presented in figure 4.22 from which we estimated the isoplanatic angle θ_0. Note also from figures 4.40(c) and (d) that, similarly to the Strehl, the $GEE_{0.1}$ also gets worse as we move away from the GS due to anisoplanatism.

4.5.4 GLAO mode

In this section we will compare experimental and simulation results obtained in GLAO mode. Figure 4.41 shows the comparison for the 1' FoV configuration, and figure 4.42 shows the comparison for the 2' FoV configuration. The summary of the performance statistics is presented in table 4.9.

Let us first compare the results obtained in the 1' FoV configuration. As seen from figure 4.41, the GLAO performance (both in SR and $GEE_{0.1}$) reaches a maximum at the center of the FoV in both experimental and simulation results. As we mentioned already in section 4.3.2.4, this behavior is also in accordance with the analytical predictions of A. Tokovinin [144]. Note from table 4.9 that the simulations once again predict higher Strehls (min, max, mean) than the ones obtained experimentally.

The difference in SR ($S_{Rsim} - S_{Rexp}$) across the whole FoV is shown in figure 4.41(c). Note that there is a portion of the FoV over which the SR predicted from simulations is actually smaller than the one obtained from experiments. However, we can clearly see from figure 4.41(b) that this result is related to the anisotropic shape (i.e. slightly

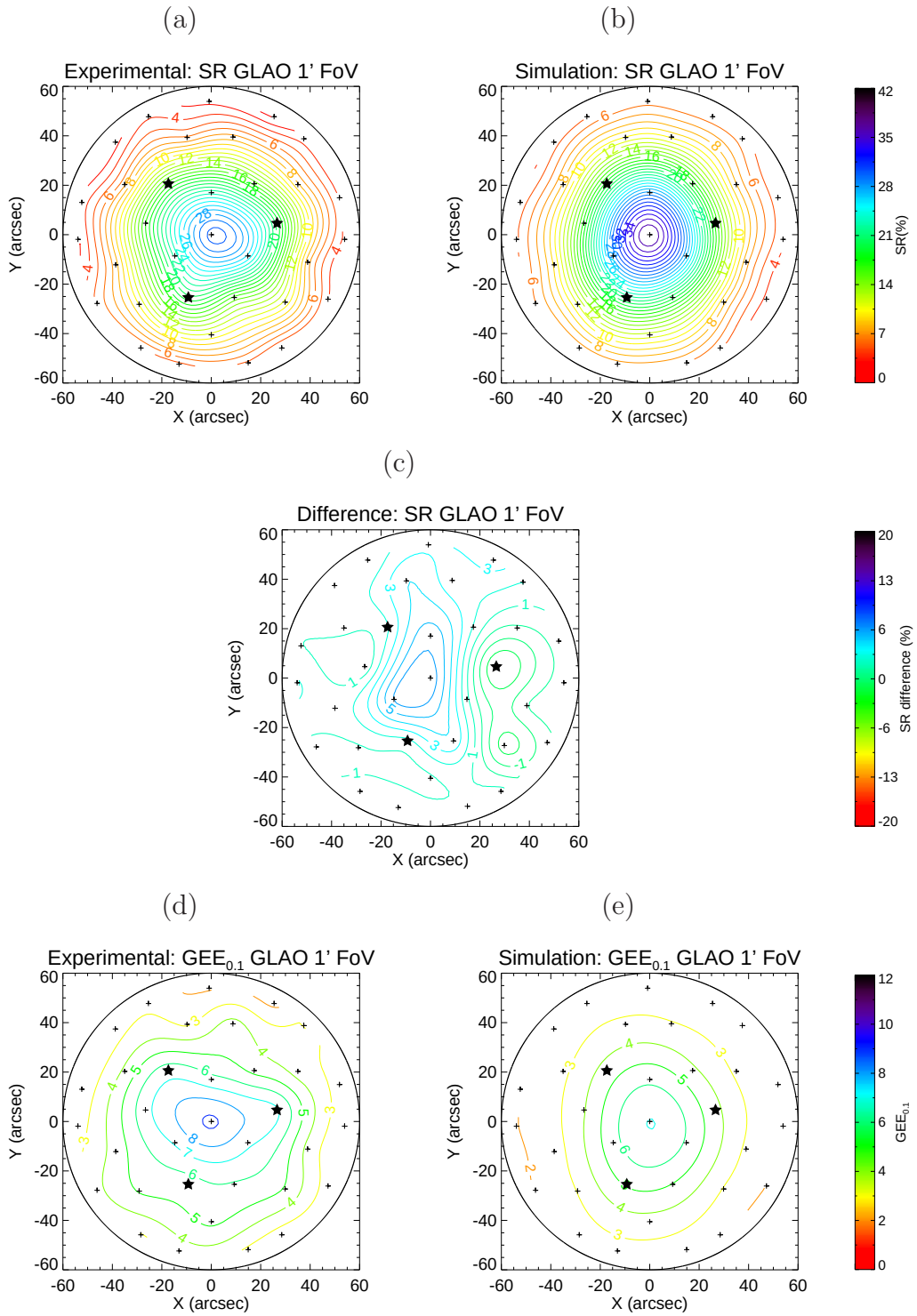

Figure 4.41: GLAO 1' FoV configuration: (a) SR from experiments. (b) SR from simulations. (c) SR difference ($S_{Rsim} - S_{Rexp}$). (d) $\text{GEE}_{0.1}$ from experiments. (e) $\text{GEE}_{0.1}$ from simulations. GSs indicated with a ★. MAPS stars indicated with a +.

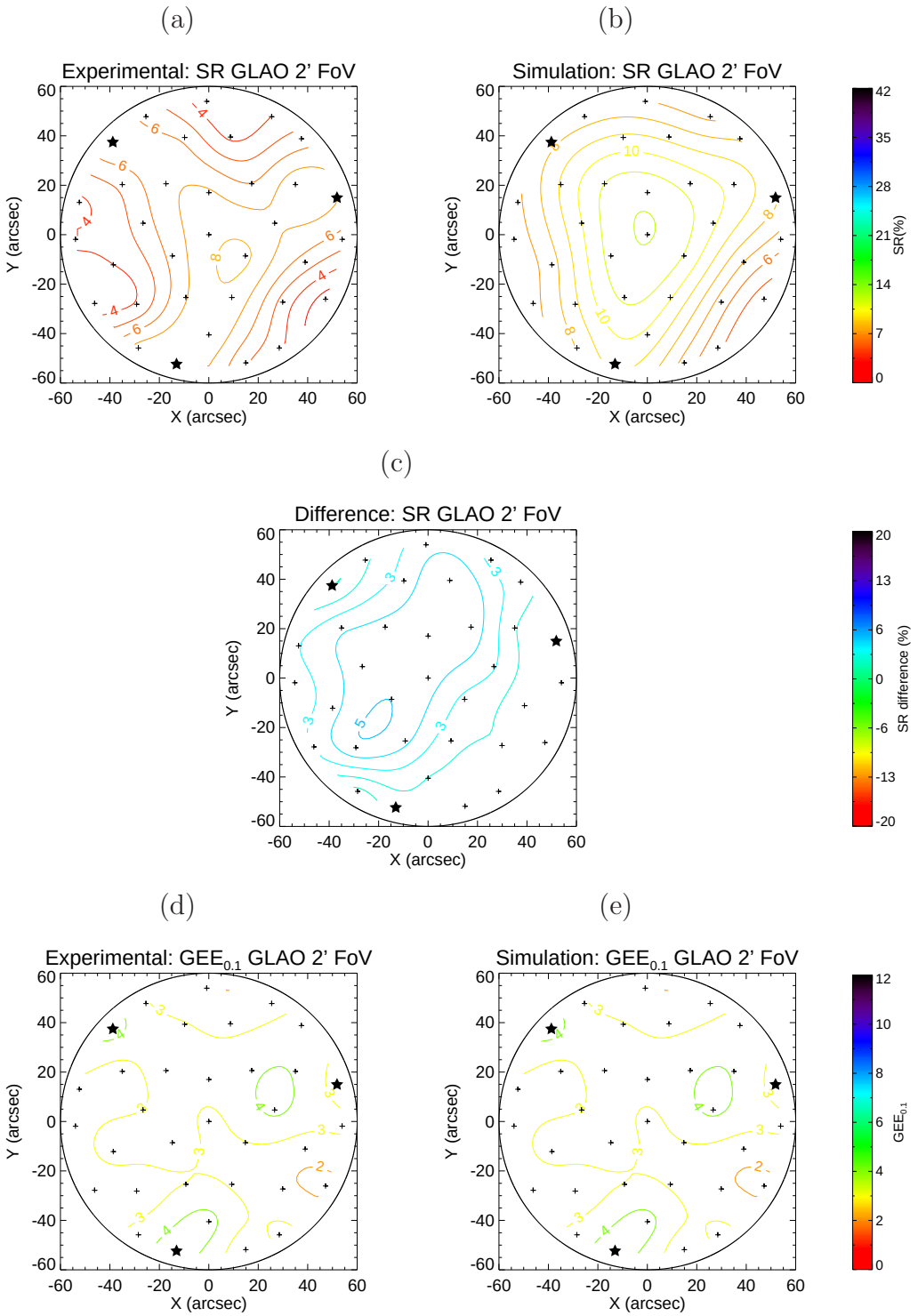

Figure 4.42: GLAO 2' FoV configuration: (a) SR from experiments. (b) SR from simulations. (c) SR difference ($S_{Rsim} - S_{Rexp}$). (d) $GEE_{0.1}$ from experiments. (e) $GEE_{0.1}$ from simulations. GSs indicated with a ★. MAPS stars indicated with a +.

1' FoV								
	Strehl ratio (%)				$GEE_{0.1}$			
	min	max	mean	std	min	max	mean	std
Experimental	15.7	30.4	20.5	4.8	4.8	9.2	6.6	1.2
Simulation	16.6	36.9	23.1	6.7	3.9	7.0	5.1	0.96
Rel. error (%)	5.9	17.8	11.3	–	-20.9	-30.4	-29.5	–

2' FoV								
	Strehl ratio (%)				$GEE_{0.1}$			
	min	max	mean	std	min	max	mean	std
Experimental	2.6	8.2	5.7	1.6	1.86	4.3	3.0	0.68
Simulation	4.4	12.0	8.5	1.9	2.1	3.5	2.8	0.38
Rel. error (%)	40.9	32.1	33.1	–	10.2	-22.4	-7.4	–

Table 4.9: GLAO configuration: statistics of the performance (SR and $GEE_{0.1}$) obtained from experiments and simulations. The statistics for the 1' FoV configuration were computed using only MAPS stars 25 to 34. The relative error for each statistical parameter $Y = \{\min, \max, \text{mean}\}$ was computed as: $(Y_{sim} - Y_{exp})/Y_{sim}$.

elongated along the y-axis) of the SR contour predicted from simulations.

Let us now discuss the results obtained in the 2' FoV configuration. From figure 4.41, it can be seen that GLAO provides a quite uniform performance (both in SR and $GEE_{0.1}$) across the whole FoV, but also it should be noted that the performance is rather low. For a quantitative analysis, take a look at the standard deviation values (characterizing the uniformity of the correction) and the mean performance values reported in table 4.9.

Regarding the comparison between simulation and experimental results, figure 4.42(c) shows the SR difference ($S_{Rsim} - S_{Rexp}$) across the whole FoV. Note that the absolute error is of only ≈3% in SR across the FoV, but the relative errors (reported in table 4.9) are rather large.

4.5.5 MCAO mode

In this section we will compare experimental and simulation results obtained in MCAO mode. Figure 4.43 shows the comparison for the 1' FoV configuration, and figure 4.44 shows the comparison for the 2' FoV configuration. The summary of the performance statistics is presented in table 4.10.

Regarding the 1' FoV configuration, as can be seen from figure 4.43, both simulation and experimental results show that the MCAO performance (SR and $GEE_{0.1}$) is

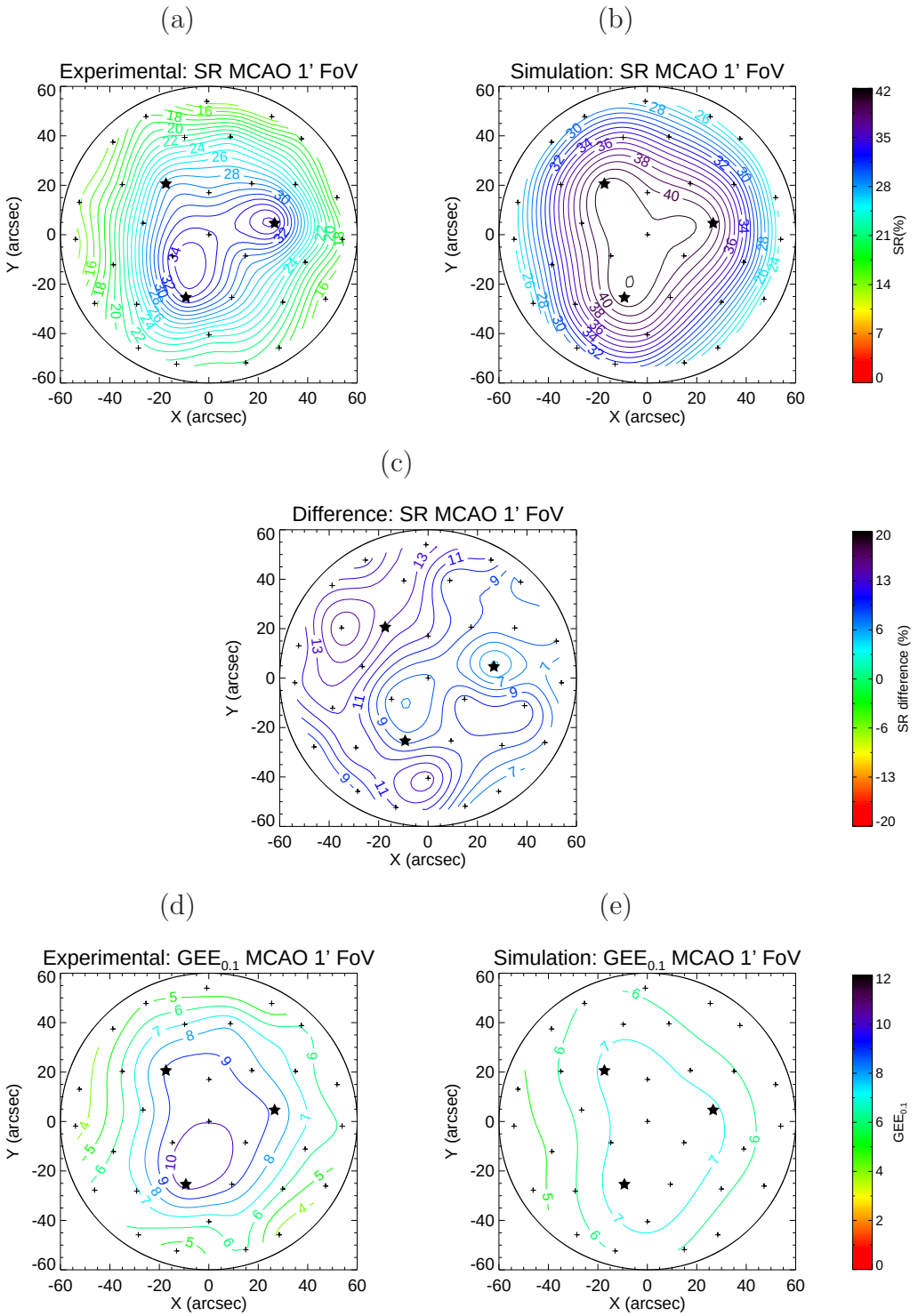

Figure 4.43: MCAO 1' FoV configuration: (a) SR from experiments. (b) SR from simulations. (c) SR difference ($S_{Rsim} - S_{Rexp}$). (d) $\text{GEE}_{0.1}$ from experiments. (e) $\text{GEE}_{0.1}$ from simulations. GSs indicated with a ★. MAPS stars indicated with a +.

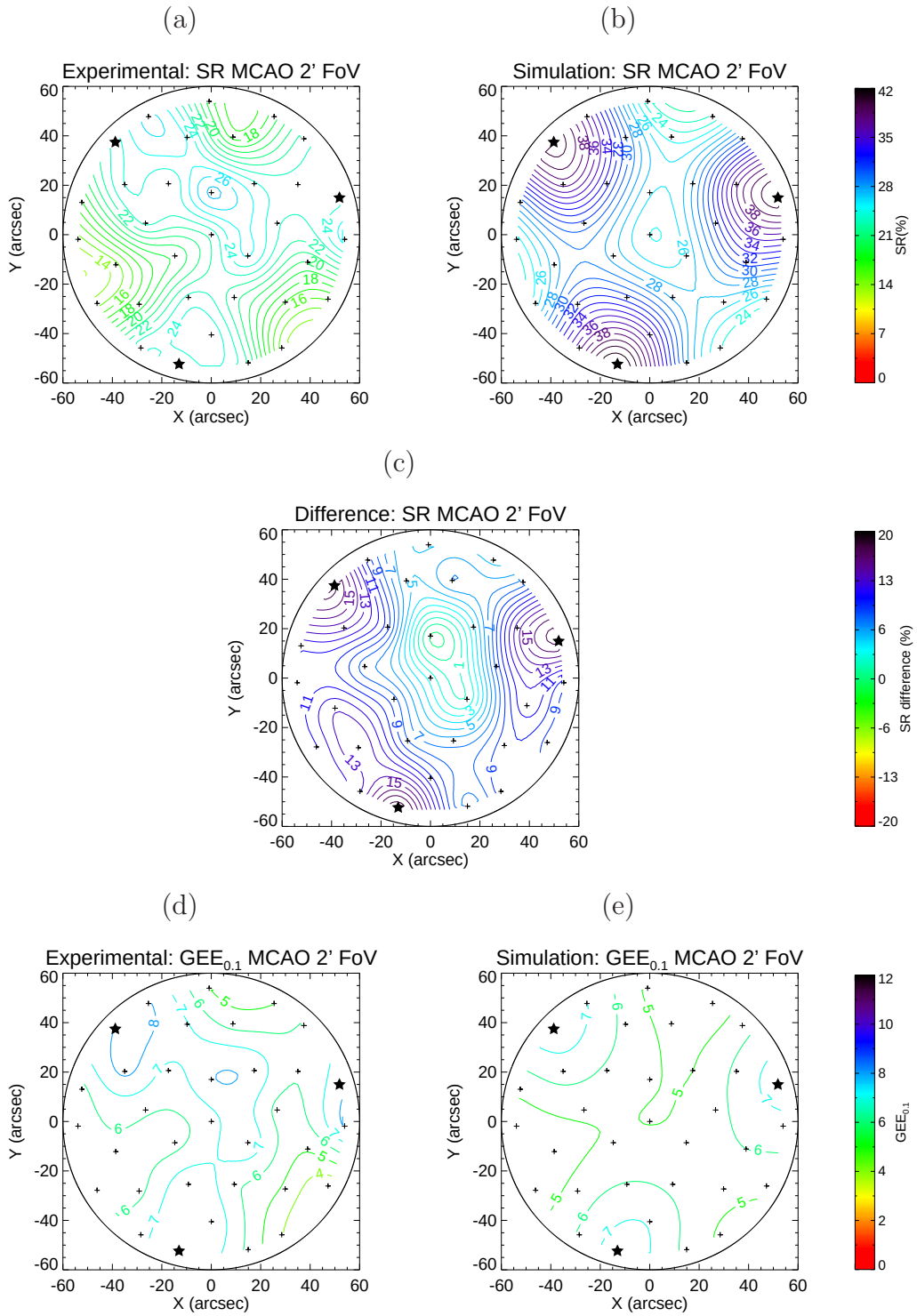

Figure 4.44: MCAO 2' FoV: (a) SR from experiments. (b) SR from simulations. (c) SR difference ($S_{Rsim} - S_{Rexp}$). (d) $\text{GEE}_{0.1}$ from experiments. (e) $\text{GEE}_{0.1}$ from simulations. GSs indicated with a ★. MAPS stars indicated with a +.

1' FoV								
	Strehl ratio (%)				$GEE_{0.1}$			
	min	max	mean	std	min	max	mean	std
Experimental	26.2	35.0	30.7	2.8	7.18	10.4	9.2	0.90
Simulation	38.1	41.7	40.1	1.2	6.3	7.7	7.2	0.46
Rel. error (%)	31.2	15.9	23.5	–	-14.1	-34.6	-26.6	–

2' FoV								
	Strehl ratio (%)				$GEE_{0.1}$			
	min	max	mean	std	min	max	mean	std
Experimental	14.6	27.3	21.2	3.7	3.4	8.2	6.4	1.3
Simulation	23.2	42.2	30.4	5.3	4.4	7.5	5.6	0.88
Rel. error (%)	37.3	35.4	30.1	–	23.3	-9.2	-13.0	–

Table 4.10: MCAO configuration: statistics of the performance (SR and $GEE_{0.1}$) obtained from experiments and simulations. The statistics for the 1' FoV configuration were computed using only MAPS stars 25 to 34. The relative error for each statistical parameter $Y = \{\min, \max, \text{mean}\}$ was computed as: $(Y_{sim} - Y_{exp})/Y_{sim}$.

quite uniform within the whole 1' FoV (see the standard deviation values reported in table 4.10). However, simulations once again predict a much higher performance in the whole 1' FoV (see the mean values in table 4.10). An absolute error of $\approx 9\%$ in SR –see figure 4.43(c)– which translates into a relative error of $\approx 23\%$.

Concerning the 2' FoV configuration, note from figures 4.44(a,b,c) that there is a major difference between experimental and simulation SR results. As was already mentioned in section 4.3.3.3, simulations predict peak Strehl ratios on the GSs dropping off towards the center of the FoV. However, this behavior is not witnessed on the experimental contour plot. In consequence, the uniformity of the correction in the whole 2' FoV obtained from experiments is actually better than the one predicted by simulations (see the standard deviation values in table 4.10).

4.5.6 SCAO, GLAO, MCAO comparison

Let us now compare the performance obtained with the different configurations: SCAO, GLAO, and MCAO. For this purpose let us define a *figure of merit* that will be computed using the performance statistics presented above for each of the configurations. The figure of merit (FoM) we propose is defined as:

$$\text{FoM}(\text{FoV}) \triangleq \frac{\text{mean}(\text{FoV})}{\text{std}(\text{FoV})} \ , \tag{4.35}$$

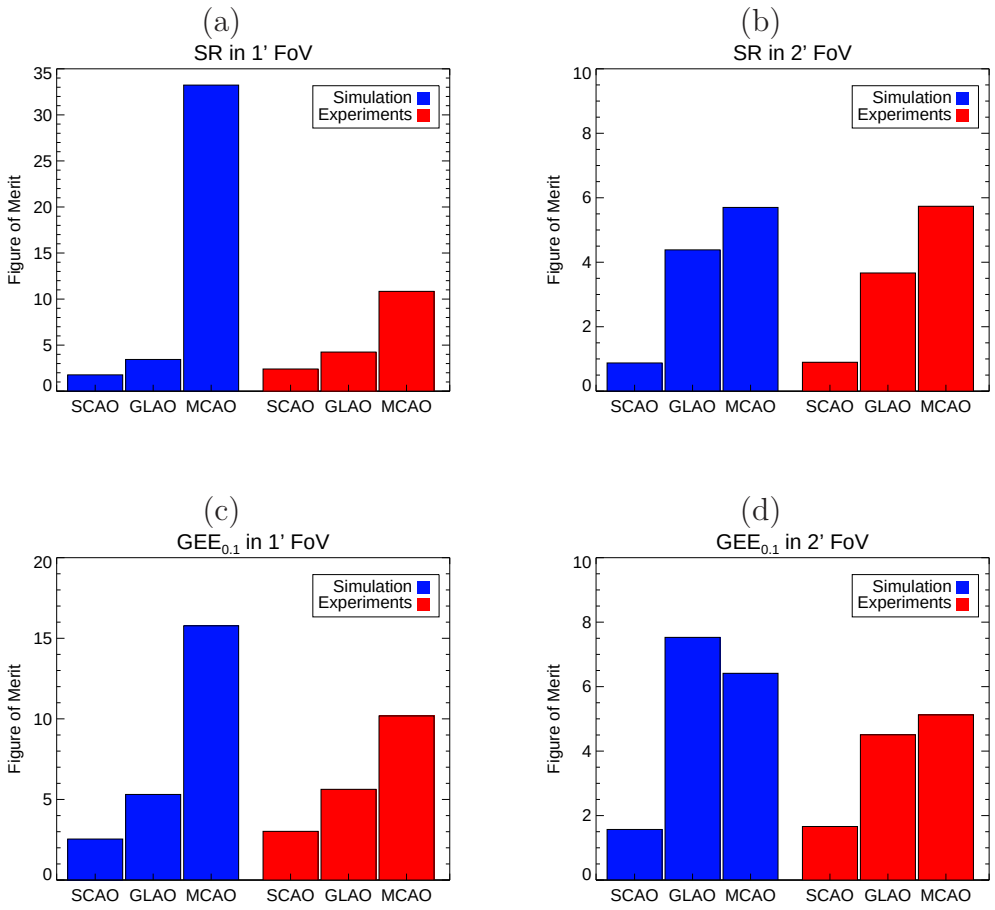

Figure 4.45: Figure of merit (FoM) computed for all configurations (SCAO, GLAO, MCAO) from simulation and experimental results. (a) SR in 1' FoV. (b) SR in 2' FoV. (c) $GEE_{0.1}$ in 1' FoV. (d) $GEE_{0.1}$ in 2' FoV.

where the numerator and the denominator of FoM are, respectively, the mean and the standard deviation of the performance (SR or $GEE_{0.1}$) over the considered FoV (1' or 2'). Note that the FoM is a dimensionless parameter that will be large if the average performance is high *and* the uniformity of the correction is good over the considered FoV. The figures of merit for all the considered configurations computed from simulation and experimental results are illustrated in figure 4.45.

Note that the FoM of the SCAO mode is always the smallest in all cases simply because the uniformity of the correction is very poor due to the anisoplanatism. Regarding the comparison in the 1' FoV configuration —figures 4.45(a) and (c)—, note that the FoM (in SR and $GEE_{0.1}$) of the MCAO mode is greater than the FoM of the

GLAO mode. This is basically due to the fact that MCAO provides a higher mean performance (in SR and $GEE_{0.1}$) and a better uniformity than the GLAO mode (see the contour plots in figures 4.41 and 4.43).

Note also from figures 4.45(a) and (c) that the FoMs computed from simulation and experimental results are comparable except for the MCAO mode, for which the FoM obtained from simulations by far dominates the landscape. This may indicate that the simulation results in this mode of operation are too optimistic. The reasons behind this apparent overestimation of performance in MCAO remain to be investigated in detail. However, it may be related not to the way we *simulate* an MCAO system, but to the way we *calibrate* it in our simulation tool. Indeed, in practice there are always calibration errors (i.e. imperfect centering of the SH-WFSs on the GSs, non-zero measurement noise during the interaction matrix calibration, etc.) that may also affect the ultimate performance. Hence, future work should focus on the accurate modelling of the calibration process in order to evaluate the impact of calibration errors on the ultimate performance of an MCAO system.

Let us now resume our comparison of the FoMs, this time for the case of the 2' FoV configuration. Regarding the Strehl ratio —figure 4.45(b)—, we can see once again that the FoM for the MCAO mode is greater than the FoM for the GLAO mode. However, note that, as opposed to the 1' FoV case, the FoM for the MCAO mode computed from simulation results is not dramatically greater than the one for the GLAO mode. This is basically due to the poorer uniformity of the MCAO correction in the whole 2' FoV (see figure 4.44(b)) which causes its FoM to go down.

Regarding the $GEE_{0.1}$ — figure 4.45(d)—, we can see an interesting swap in the trends obtained from simulation results: GLAO has a larger FoM than MCAO. This is mainly due to the fact that the mean performance evaluated in terms of $GEE_{0.1}$ provided by GLAO and MCAO becomes comparable, but GLAO provides a better uniformity. However, this swap does not occur in the case of experimental results: MCAO still has the largest FoM due to the good uniformity obtained from experimental results. The experimental results presented in this section have been also presented in a conference paper [93].

4.6 Experiment with a synthetic reconstructor

In this section we will present an experiment we conducted with a *synthetic reconstructor*. That is, a reconstruction matrix computed by inverting a *synthetic* interaction matrix generated with our MAD simulation tool. Let us discuss first what is the mo-

tivation behind this kind of test. The results of our experiment will be presented in section 4.6.1.

In general, for current AO systems, the interaction matrix (IM) is calibrated experimentally. The experimental calibration has the advantage that all particularities of the AO system (some of them not easy to model) are taken into account, e.g. optical aberrations, misalignments, etc. For current AO systems, the calibration of the IM is done with the help of a bright artificial source placed at the input focus of the AO system. However, for the next generation of adaptive telescopes comprising large secondary deformable mirrors [4], this procedure won't be possible because the input focus won't be accessible to place an artificial calibrating source. A handful of new techniques based on the on-sky calibration of the IM are currently under study for these kind of telescopes, and described in [101]. Alternatively, the generation of a synthetic IM seems also an interesting approach. The success of this approach relies on the accuracy of the system component models as well as the accurate modelling of the opto-geometrical relationships between them.

As presented throughout this chapter, we have fine-tuned our MAD simulation tool to take into account most of the real system characteristics. In the following section we will present the results of an experiment using an MCAO synthetic reconstructor generated with our MAD simulation tool.

4.6.1 Comparison in performance

We will present a comparison of the performance (SR) obtained when closing the loop in MCAO mode with a TLS reconstructor computed by inverting an experimental and a synthetic IM. The selected GSs were the MAPS stars number 5, 10, and 15 (FoV=108") shown in figure 4.15.

Let us first compare the synthetic and the experimental IMs. Figure 4.46(a) shows the experimental IM and figure 4.46(b) shows the first iteration of the synthetic IM (i.e. all shifts and rotation angles equal to zero). In order to visualize the importance of a correct opto-geometrical calibration (section 4.4), figure 4.46(c) compares a single row (row number 111) of the experimental and the synthetic IMs (first iteration IM and best-fit IM). The row number 111 corresponds to the x-slope of subaperture #7 of SH2. Note that there is an important difference between the 1st iteration IM and the best-fit IM. Also, note that there is a good matching existing between the best-fit synthetic IM and the experimental IM.

We then generated a synthetic TLS reconstructor from the best-fit synthetic IM, and a experimental TLS reconstructor from the experimental IM. A total of 45 eigenmodes

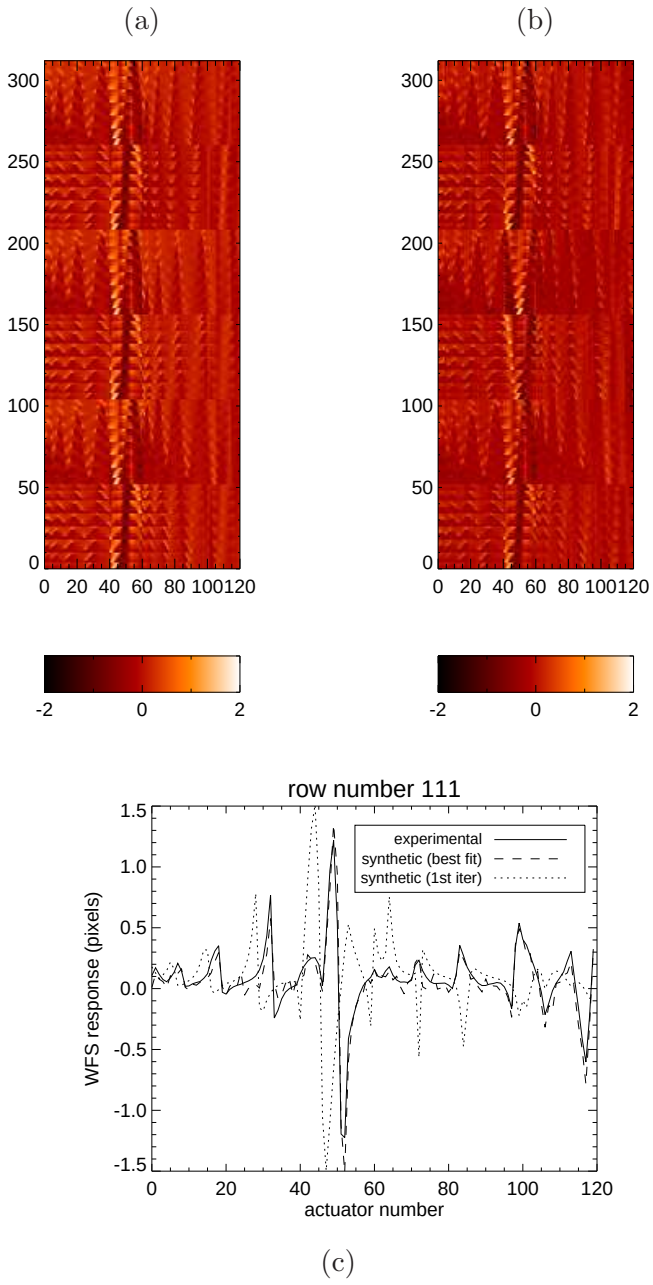

Figure 4.46: Comparison of experimental and synthetic MCAO interaction matrices. *(a)* Experimental MCAO IM. *(b)* Synthetic MCAO IM (1st iteration). *(c)* Comparison of a single row (row number 111 corresponding to the x-slope of subaperture #7 of SH2) of the experimental and the synthetic (1st iteration and best-fit) IMs.

	SR (%)			
	min	max	mean	std
Experimental TLS reconstructor	11.5	24.6	19.8	3.0
Synthetic TLS reconstructor	9.9	22.6	18.0	2.8
Relative error (%)	13.9	8.1	9.1	–

Table 4.11: Summary of the performance statistics obtained with a synthetic and a experimental MCAO reconstructor. The relative error for each statistical parameter $Y = \{\min, \max, \text{mean}\}$ was computed as: $(Y_{sim} - Y_{exp})/Y_{sim}$.

were filtered out in both TLS reconstructors. The MAD system was operated at 400 Hz, and the PI gains of the temporal controller were set to $g_I = g_p = 0.22$. The turbulence conditions used in these experiments are summarized in table 4.5. The comparison in performance in terms of SR at 2.2 μm in the whole 2' FoV obtained with these two reconstructors is presented in figure 4.47. The performance statistics are summarized in table 4.11. From these results we can see that the synthetic TLS reconstructor gives a lower performance in the whole FoV. Note from figure 4.47(c) that the absolute error is $\approx 2\%$ in SR which corresponds to a relative error of $\approx 9\%$ in the mean performance.

We believe that the presence of FoV-dependent static aberrations in the MAD bench —which have not been taken into account in the creation of the synthetic IM— is one of the main issues responsible for the difference in performance. On the other hand, we also believe that it may be possible to improve the performance obtained with the synthetic reconstructor by improving the AO components models. For instance, the models of both the DMs and the SH-WFSs of MAD could be improved as follows:

- *High-resolution influence functions.* As discussed in section 4.2.2.1, the IFs of the DMs were characterized with a HASO camera. The measured IFs have been sampled in a 64x64 pixels grid, but the required sizes for the ground and altitude DM metapupils are 128x128 and 210x210 respectively. There is clearly an interpolation/extrapolation error in the re-sampling process that could be avoided by measuring the IFs with a higher spatial resolution; for instance, with the use of an interferometer.

- *Pixel scale non-uniformity.* As presented in section 4.2.1, we have assumed that the pixel scale for the SH-WFSs of MAD is equal to 0.3". However, variations in the distance between the lenslet array and the CCD leads to a pixel scale non-uniformity across the subapertures. The non-uniformity is mainly caused by a tilt of the lenslet array with respect to the CCD plane, but small pixel scale

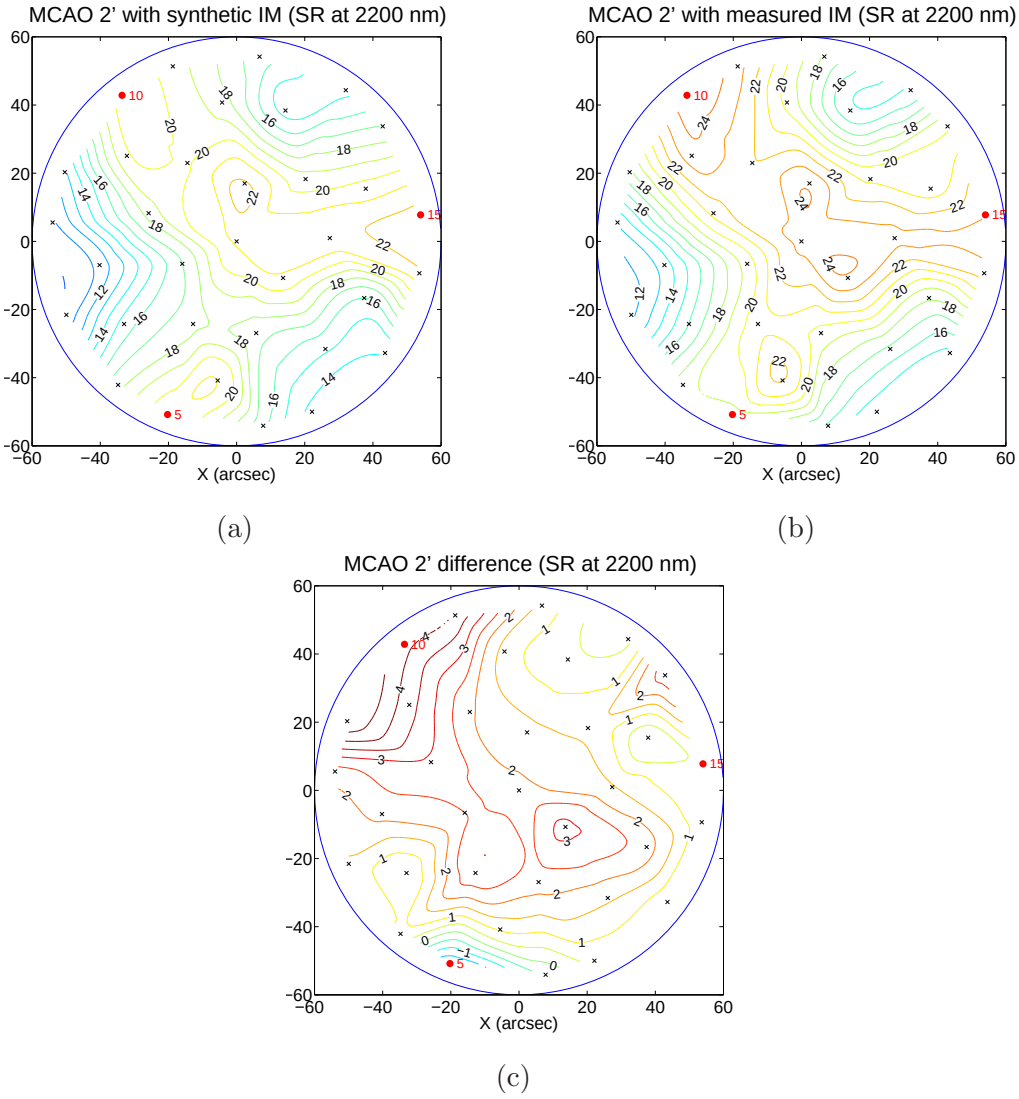

(a) (b)

(c)

Figure 4.47: SR in K band and in the 108" FoV obtained with: *(a)* an MCAO synthetic TLS reconstructor, and *(b)* an MCAO experimental TLS reconstructor. *(c)* SR difference between experimental and synthetic approches.

		0.303	0.306	0.307	0.307		
	0.303	0.306	0.308	0.310	0.312	0.312	
0.303	0.305	0.309	0.312	0.311	0.313	0.315	0.312
0.306	0.304	0.308	0.318	0.311	0.317	0.314	0.314
0.304	0.305	0.309	0.316	0.313	0.316	0.315	0.314
0.304	0.305	0.308	0.311	0.313	0.314	0.316	0.314
	0.306	0.308	0.310	0.313	0.314	0.314	
		0.306	0.309	0.311	0.311		

Figure 4.48: Experimental characterization of the pixel scale non-uniformity for one of the MAD's SH-WFSs. The values are given in arcsec/pixel.

variations can also be due to the optical aberrations of the lenslet array. Figure 4.48 shows the pixel scale non-uniformity for one the MAD's SH-WFSs [133]. The modelling of the SH-WFSs could also be improved by taking into account this effect.

In conclusion, it is not trivial to create synthetic reconstructors that perform as good as the experimental ones. We believe that there is room for improvement in the creation of synthetic IMs and we have identified some possible refinements of the AO components models that may help to reduce the gap in performance between the experimental and the synthetic approaches. Due to time limitations, we could not pursue the refinement of the AO components models within the frame of this work.

4.7 Perspectives on advanced control laws

The control law that was implemented in MAD consisted of a TLS reconstruction matrix, $\mathbf{R}_{TLS}$, coupled with a PI temporal controller. We have validated experimentally the concepts of GLAO and MCAO in closed loop using this control law. Clearly, the next step is to study the advantages of more advanced control laws involving statistical prior knowledge required to improve the performance in a specified field of view. In the time frame of this PhD work, we could not pursue such a study. Nevertheless, we

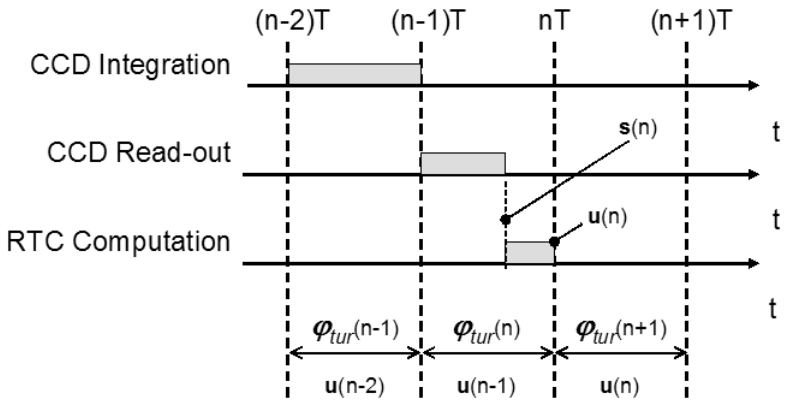

Figure 4.49: Simplified control time diagram for an adaptive optics system with a total of two-frames time delay.

will present in this section an overview of some advanced control laws that could be validated in the MAD system in the near future.

4.7.1 MMSE reconstructor + temporal controller

The statistical estimation methods for the problem of wavefront reconstruction in MCAO were introduced in section 2.5. As we discussed in that section, the *minimum mean-square-error* reconstructor, $\mathbf{R}_{MMSE}$, provides the *optimal* solution to the problem of wavefront reconstruction in MCAO in the sense that it ensures that the mean-square error —or residual variance— on each estimated turbulence layer is minimal. An *ad-hoc* control law can be formed by cascading an MMSE reconstructor with a temporal controller, as shown in figure 4.50(a). For instance, when the temporal controller is a simple integrator with gain g_I, the equations for this ad-hoc control law can be expressed as:

$$\Delta\mathbf{u}(n) = \mathbf{R}_{MMSE}\mathbf{s}(n) \tag{4.36}$$

$$\mathbf{u}(n) = \mathbf{u}(n-1) + g_I\Delta\mathbf{u}(n) \ , \tag{4.37}$$

where $\mathbf{s}(n)$ and $\mathbf{u}(n)$ are the WFSs measurement vector and the command vector at time n respectively (see the time diagram in figure 4.49). The two (equivalent) expressions for the MMSE reconstructor were presented in equation 2.80, in the context of the wavefront reconstruction problem in MCAO. In this context, these expressions can be

rewritten as:

$$\mathbf{R}_{MMSE,1} = \left[\mathbf{M}_{int}^T \mathbf{C}_{\mathbf{w}}^{-1} \mathbf{M}_{int} + \alpha_1 {\mathbf{C}_{\mathbf{u}}}^{-1}\right]^{-1} \mathbf{M}_{int}^T \mathbf{C}_{\mathbf{w}}^{-1} \ , \tag{4.38}$$

$$\mathbf{R}_{MMSE,2} = \mathbf{C}_{\mathbf{u}} \mathbf{M}_{int}^T \left[\mathbf{M}_{int} \mathbf{C}_{\mathbf{u}} \mathbf{M}_{int}^T + \alpha_2 \mathbf{C}_{\mathbf{w}}\right]^{-1} \ , \tag{4.39}$$

where α_1 and α_2 are two additional parameters that will be described further below. Note that the *tomographic* interaction matrix $\mathbf{H}$ in equation 2.80 has been replaced by the AO interaction matrix $\mathbf{M}_{int}$. This implies several things. Firstly, it implies that we are considering that the number of turbulence layers that we seek to estimate equals the number of deformable mirrors ($N_{_L} = N_{_{DM}}$) and that the DMs are conjugated to the same altitudes of the turbulence layers[6]. Secondly, it implies that $\mathcal{M}_V$ (i.e. the subspace of the turbulence volume phase space $\mathcal{E}_V$ that we seek to estimate *and* compensate for) is limited to the subspace that can be generated by the DMs (see also the discussion in section 3.2.1). The matrix $\mathbf{C}_{\mathbf{u}}$ stands for the covariance matrix of the command vector $\mathbf{u}$. It contains the prior knowledge on the turbulence spatial statistics expressed in the DMs space. The matrix $\mathbf{C}_{\mathbf{u}}$ can be computed from the matrix $\mathbf{C}_{\varphi_\parallel}$ (i.e. the turbulence covariance matrix expressed in the Zernike basis) as:

$$\mathbf{C}_{\mathbf{u}} = \mathbf{P}_{Z2V} \mathbf{C}_{\varphi_\parallel} (\mathbf{P}_{Z2V})^T \ , \tag{4.40}$$

where $\mathbf{P}_{Z2V}$ is the *Zernike-to-Volts* projection matrix defined in equation 4.8.

It is important to note that even though the MMSE reconstructor is the optimal solution for the problem of wavefront reconstruction in MCAO (see chapter 2), there is no reason to believe that this ad-hoc control law will guarantee the optimality of the solution in a closed-loop MCAO system. In particular, note that the regularizing term $\mathbf{C}_{\mathbf{u}}$ is not well adapted for closed-loop MCAO systems because it stands for the *open-loop* turbulence statistics which do not correspond to the statistics of the *residual* turbulence after partial correction by the DMs.

Nevertheless, it has been empirically shown that by tweaking the parameters α_1 or α_2 in equations 4.38 or 4.39 it is possible to obtain a better performance than the one obtained with a simpler TLS reconstructor. For instance, M. Le Louarn [83, 85] has widely used this ad-hoc control law in simulation studies of closed-loop SCAO and MCAO systems. Also, M. A. van Dam *et. al.* [151] have implemented this ad-hoc control law in the Keck's SCAO system and they have shown that after tuning the α-parameter this ad-hoc control law can effectively provide a good performance. It

[6]This is the so-called *model approximation* introduced by T. Fusco *et. al.* [43]. Recall that we have also used this approximation in our study of the MOMGI control law in chapter 3.

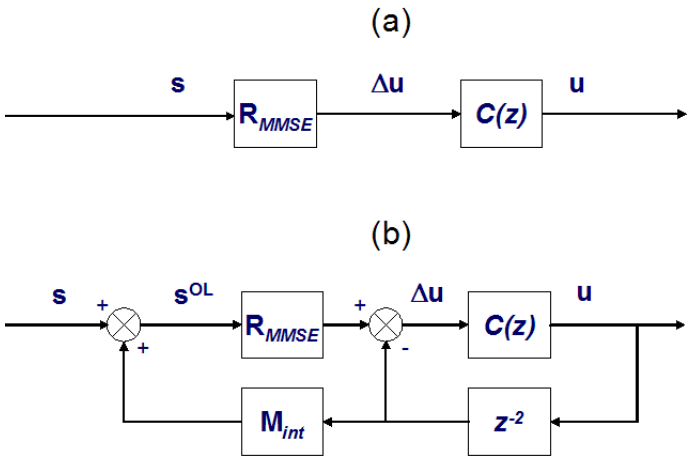

Figure 4.50: *(a)* Ad-hoc control law formed by cascading an MMSE reconstructor with a temporal controller. *(b)* Representation of the pseudo-open loop control (POLC) law.

should be noted that the α-parameter must be tuned for each observing conditions (SNR, flux-level, etc.).

4.7.2 Pseudo-open loop control law

The pseudo-open loop control (POLC) was proposed by B. Ellerbroek *et. al.* [29], and was later thoroughly studied by L. Gilles *et. al.* [57, 110]. The idea behind the POLC law is to apply the MMSE reconstructor (eq. 4.38 or 4.39) to *open-loop* slopes reconstructed from closed-loop data. In this way, the (open-loop) prior knowledge incorporated in $\mathbf{R}_{MMSE}$ is well adapted to regularize the reconstruction process.

Figure 4.50(b) shows a representation of the POLC law. The open-loop slopes vector is denoted as $\mathbf{s}^{OL}$. Following the method of open-loop data reconstruction from closed-loop data presented in section 4.2.3.4, it can be shown that for a system with a total delay of two frames ($\tau_{tot} = 2T$), $\mathbf{s}^{OL}$ is given by:

$$\mathbf{s}^{OL}(n) = \mathbf{s}(n) + \mathbf{M}_{int}\,\mathbf{u}(n-2) \quad . \tag{4.41}$$

where $\mathbf{M}_{int}$ is the interaction matrix of the AO system. Note that the product $\mathbf{R}_{MMSE}\,\mathbf{s}^{OL}$ produces already a command vector that could by applied to the DMs. However, no temporal filtering would be applied to guarantee the stability of the control system. Therefore, the authors of the POLC law proposed to reconstruct a *command incre-*

ment vector $\Delta\mathbf{u}$ as:

$$\Delta\mathbf{u}(n) = \mathbf{R}_{MMSE}\,\mathbf{s}^{OL}(n) - \mathbf{u}(n-2)\ , \tag{4.42}$$

to which a temporal controller can then be applied. For instance, for the case of a simple integrator of gain g_I, the voltage that is actually applied to the DMs is computed as:

$$\mathbf{u}(n) = \mathbf{u}(n-1) + g_I\Delta\mathbf{u}(n)\ . \tag{4.43}$$

In summary, the control equations describing the POLC law (using an integrator controller) are:

$$\mathbf{s}^{OL}(n) = \mathbf{s}(n) + \mathbf{M}_{int}\,\mathbf{u}(n-2) \tag{4.44}$$

$$\Delta\mathbf{u}(n) = \mathbf{R}_{MMSE}\,\mathbf{s}^{OL}(n) - \mathbf{u}(n-2) \tag{4.45}$$

$$\mathbf{u}(n) = \mathbf{u}(n-1) + g_I\Delta\mathbf{u}(n) \tag{4.46}$$

Note that the POLC control law requires two vector-matrix multiplications. L. Gilles [57] has validated with numerical simulations the POLC law in the framework of the future Gemini-south MCAO system (section 1.2.8.3).

4.7.3 Linear Quadratic Gaussian (LQG) control

The Linear Quadratic Gaussian (LQG) control is the most advanced control law presented in this section. The application of this control technique in adaptive optics was first proposed by Paschall *et. al.* [103]. It has been more recently thoroughly studied by B. Le Roux *et. al.* [131, 132] and C. Petit *et. al.* [109, 108] for both SCAO and MCAO configurations. It consists of an optimal estimation of the turbulence volume (in the sense of minimum variance) delivered by a *Kalman filter*, followed by an optimal projection onto the DMs space.

The Kalman filter is a (linear) optimal estimator that can embrace both spatial and temporal aspects in a single framework well suited for closed-loop AO systems. In fact, it can be shown that the minimum-variance estimation method presented in section 2.6 for the problem of wavefront reconstruction in MCAO is a particular case of the Kalman filter estimation method when temporal aspects are not taken into account [131].

The formulation of this control law is based on a *state-space* description of an adaptive optics system. The state-space description is a time-domain mathematical model. The details of this formulation can be found in references [132, 108]. For instance, it can be shown that a possible state-space description of an MCAO system

with a total of two-frames delay is given by:

$$\mathbf{X}(n+1) = \mathcal{A}\mathbf{X}(n) + \boldsymbol{\nu}(n) \quad (4.47)$$

$$\mathbf{s}(n) = \mathcal{C}\mathbf{X}(n) - \mathbf{M}_{int}\,\mathbf{u}(n-2) + \mathbf{w}(n) \quad (4.48)$$

where $\mathbf{X}(n)$ is the *state vector* at instant n, defined as:

$$\mathbf{X}(n) = \begin{pmatrix} \boldsymbol{\varphi}_{tur}(n+1) \\ \boldsymbol{\varphi}_{tur}(n) \\ \boldsymbol{\varphi}_{tur}(n-1) \end{pmatrix} , \quad (4.49)$$

and $\boldsymbol{\varphi}_{tur}(n)$ is the turbulence vector at instant n (see time diagram in figure 4.49). The matrix $\mathcal{A}$ in equation 4.47 represents a mathematical model of the *temporal evolution* of the state vector, and $\boldsymbol{\nu}(n)$ is known as the *state noise* representing the random nature of turbulence. Equation 4.48 describes the measurements delivered by the closed-loop MCAO system. The matrix $\mathcal{C}$ is simply equal to $\mathcal{C} = [0 \quad 0 \quad \mathbf{D}]$, where $\mathbf{D}$ is the WFSs matrix. Note that this equation is totally equivalent to the one presented in equation 3.7. However, in this context it is given in the temporal domain whereas in the context of chapter 3 it was presented in the frequency (Laplace) domain.

For the state-space description considered here, it can be shown that the equations describing the LQG control law are given by [132, 108]:

$$\hat{\mathbf{X}}(n+1) = \mathcal{A}\hat{\mathbf{X}}(n) + \mathcal{A}\mathbf{H}_{\infty}\left[\mathbf{s}(n) + \mathbf{M}_{int}\,\mathbf{u}(n-2)\right] \quad (4.50)$$

$$\mathbf{u}(n) = \mathcal{P}\hat{\mathbf{X}}(n+1) \ , \quad (4.51)$$

in which the first equation represents the optimal estimation of $\mathbf{X}(n+1)$ delivered by the Kalman filter, and the second equation represents the optimal projection onto the DMs. The matrix $\mathbf{H}_{\infty}$ is known as the *asymptotic observer gain*. This matrix involves the temporal and spatial statistical priors on the state vector and the measurement noise. It can be regarded as the generalization to the closed-loop case of the MMSE reconstructor presented in section 2.5. Finally, the matrix $\mathcal{P}$ in equation 4.51 stands for an optimal projection of the state vector onto the DMs space. It is equivalent to the projection matrix stated in equation 2.95 for the MV reconstructor.

It is important to note that this control law not only assures the optimality of the solution (in the sense of minimum residual variance in the FoV of interest), but also guarantees the absolute stability of the control system. On the other hand, this control law also requires more computing power. Indeed, note from equations 4.50 and 4.51

that the implementation of this control law requires four vector-matrix multiplications.

The experimental validation of the advanced control laws described in this section is a required step to demonstrate the gain in performance with respect to simpler control laws such as the TLS reconstructor + integrator control law used throughout this work. C. Petit *et. al.* [108] have already performed a preliminary experimental validation of the LQG on the SCAO bench available at ONERA. The experimental validation of advanced control laws in MAD is also foreseen for the near future.

Summary and conclusions

In this work we have studied some aspects of the problems of spatial reconstruction and temporal control in multi-conjugate adaptive optics (MCAO). The problem of wavefront reconstruction in MCAO was studied in chapter 2 following the traditional approach that considers an *static* and *open-loop* MCAO configuration. We proposed a generalization of the matrix formulation of the *approximate direct problem* in MCAO introduced by T. Fusco [42]. In its compact form, the model of the approximate direct problem we proposed was expressed as (eq. 2.25):

$$\mathbf{s} = \mathbf{H}\boldsymbol{\varphi}_{tur_{\parallel}} + \mathbf{H}_{\perp}\boldsymbol{\varphi}_{tur_{\perp}} + \mathbf{w} \ ,$$

where $\mathbf{s}$ is the WFSs measurement vector, and $\mathbf{w}$ is the corresponding measurement noise vector. Also, $\boldsymbol{\varphi}_{tur_{\parallel}}$ is the finite-dimensional vector that contains the turbulence modes we seek to estimate, and $\boldsymbol{\varphi}_{tur_{\perp}}$ is the (in principle infinite-dimensional) vector that contains the turbulence modes that we have left out from $\boldsymbol{\varphi}_{tur_{\parallel}}$. This last vector is at the source of the aliasing on any adaptive optics system (SCAO, MCAO, ...). The matrix $\mathbf{H}$ was named as the *tomographic interaction matrix* and the matrix $\mathbf{H}_{\perp}$ was named as the *aliasing interaction matrix*. Based on this analytical formulation, we then studied the *reconstruction error* —or estimation error— for the cases of the least-squares (LS) and the minimum mean-square error (MMSE) estimation methods. The reconstruction error was characterized by its covariance matrix, which turned out to be (eq. 2.52):

$$\begin{aligned} \mathbf{C}_{\epsilon} &= \mathbf{R}\mathbf{C}_{\mathbf{w}}\mathbf{R}^{T} + [\mathbf{R}\mathbf{H} - \mathbf{I}]\,\mathbf{C}_{\varphi_{\parallel}}\,[\mathbf{R}\mathbf{H} - \mathbf{I}]^{T} \\ &+ [\mathbf{R}\mathbf{H}_{\perp}]\,\mathbf{C}_{\varphi_{\perp}}\,[\mathbf{R}\mathbf{H}_{\perp}]^{T} \ . \end{aligned}$$

We then focused our attention on the first and the third terms, because the first term characterizes the propagation of the measurement noise through the reconstruction matrix $\mathbf{R}$, and the third term characterizes the propagation of the remaining error through

the reconstruction matrix $\mathbf{R}$, that is, the *generalized aliasing* in MCAO. Clearly, the propagation of the different errors depends on the reconstruction matrix in question. For the case of the least-squares reconstructor, we showed that the propagation of the remaining error was as strong as the propagation of the measurement noise. In particular, by expressing the covariance matrix of the reconstruction error in the *eigenspace* of $\mathbf{H}$, we put in evidence that the remaining error was actually being propagated onto the eigenmodes associated with low eigenvalues, i.e. the *badly-seen modes*. The results of our analytical formulation were also validated with numerical simulations for an example case. On the other hand, for the case of the MMSE reconstructor, we showed that the propagation of the remaining error and the measurement noise is kept at a low level for all eigenmodes, including the badly-seen ones, thanks to the statistical priors taken into account in the creation of the MMSE reconstruction matrix.

In chapter 3 we studied the application of modal gain optimization in MCAO. Modal gain optimization is a temporal control technique based on an modal integrator controller in which the modal integral gains are fine-tuned in order to adjust the correction bandwidth of each controlled mode [55, 31]. The *optimized modal gain* associated with the ith controlled mode is the one that minimizes its residual variance, which was expressed as (eq. 3.41):

$$\begin{aligned}\sigma_i^2 &= \int_{-\infty}^{\infty} |E_i(j\omega)|^2 \langle |\tilde{\varphi}^{MP}_{tur_{\parallel},i}(j\omega)|^2 \rangle \, d\omega \\ &+ \int_{-\infty}^{\infty} |H_i(j\omega)|^2 \langle |\tilde{\varphi}^{MP}_{tur_{\perp},i}(j\omega)|^2 \rangle \, d\omega \\ &+ \int_{-\infty}^{\infty} |H_{n,i}(j\omega)|^2 \langle |\tilde{w}_i^{MP}(j\omega)|^2 \rangle \, d\omega \ ,\end{aligned}$$

where the first term characterizes the residual turbulence after correction, the second term characterizes the propagation of the remaining error, and the third term characterizes the propagation of the measurement noise. Since the propagation of the remaining error can be as strong as the propagation of the measurement noise in MCAO, all the three terms had to be taken into account in the minimization of σ_i^2. We then showed that this fact poses serious limitations to the practical implementation of modal gain optimization in MCAO.

In chapter 4 we presented a series of studies related to the experimental validation of MCAO and GLAO with the *Multi-conjugate adaptive optics Demonstrator* (MAD). This is the first time, to our knowledge, that closed-loop MCAO and GLAO results are obtained in the laboratory, confirming the feasibility of adaptive optics correction

in a larger (1' to 2') FoV. We confronted simulation and experimental results, and put in evidence some differences between the performance in the whole FoV predicted by simulations and the one actually obtained in the laboratory. We identified possible causes for such differences which could lead to an improvement in the modelling of GLAO and MCAO systems. The availability of the MAD system opens the door to the experimental validation of more advanced control laws in the near future.

The work presented in this PhD thesis lead to several communications in collaboration with the ONERA and the MAD team [112, 109, 92, 93, 101, 77]. The characterization of the generalized aliasing in MCAO and its implications in modal gain optimization for MCAO will be the topic of a peer-reviewed paper to be submitted.

Bibliography

[1] A. Abahamid, J. Vernin, Z. Benkhaldoun, A. Jabiri, M. Azouit, and A. Agabi. Seeing, outer scale of optical turbulence, and coherence outer scale at different astronomical sites using instruments on meteorological balloons. *Astronomy and Astrophysics*, 422(3):1123–1127, 2004.

[2] J. Ares and J. Arines. Influence of thresholding on centroid statistics: full analytical description. *Applied Optics*, 43(31):5796–5805, 2004.

[3] J. Arines and J. Ares. Minimum variance centroid thresholding. *Optics Letters*, 27(7):497–499, 2002.

[4] R. Arsenault, R. Biasi, D. Gallieni, A. Riccardi, N. Hubin, E. Fedrigo, R. Donaldson, S. Oberti, and S. Stroebele. A deformable secondary mirror for the VLT. *Advances in Adaptive Optics II, Proc. of SPIE*, 6272, [6272-29], 2006.

[5] R. Arsenault, R. Donaldson, C. Dupuy, E. Fedrigo, N. Hubin, L. Ivanescu, M. Kasper, J. Oberti, J. Paufique, S. Rossi, A. Silber, B. Delabre, J. L. Lizon, and P. Gigan. MACAO-VLTI adaptive optics systems performance. *Advancements in Adaptive Optics, Proc. of SPIE*, 5490:47–58, 2004.

[6] R. Avila, J. Vernin, and E. Masciadri. Whole atmospheric-turbulence profiling with generalized SCIDAR. *Applied Optics*, 36(30):7898–7905, 1997.

[7] R. Avila, J. Vernin, and L. J. Sanchez. Atmospheric turbulence and wind profiles monitoring with generalized SCIDAR. *Astronomy and Astrophysics*, 369(1):364–372, 2001.

[8] M. Azouit and J. Vernin. Optical turbulence profiling with balloons relevant to astronomy and atmospheric physics. *Publications of the Astronomical Society of the Pacific*, 117(831):536–543, 2005.

[9] H. W. Babcock. The possibility of compensating astronomical seeing. *Publications of the Astronomical Society of the Pacific*, 65:229, 1953.

[10] H. H. Barret and Kyle J. Myers. *Foundations of image science*. Hoboken, NJ : Wiley Inc., c2004, 2004.

[11] J. M. Beckers. Increasing the size of the isoplanatic patch with multiconjugate adaptive optics. *Very Large Telescopes and their Instrumentation, ESO Conference and Workshop Proceedings*, 30:693–703, 1988.

[12] D. Bello, J. M. Conan, G. Rousset, and R. Ragazzoni. Signal to noise ratio of layer-oriented measurements for multiconjugate adaptive optics. *Astronomy and Astrophysics*, 410(3):1101–1U16, 2003.

[13] J. L. Beuzit, L. Demailly, E. Gendron, P. Gigan, F. Lacombe, D. Rouan, N. Hubin, D. Bonaccini, E. Prieto, F. Chazallet, D. Rabaud, P. Y. Madec, G. Rousset, R. Hofmann, and F. Eisenhuer. Adaptive optics on a 3.6-meter telescope - the ADONIS system. *Experimental Astronomy*, 7(4):285–292, 1997.

[14] A. Blanc, T. Fusco, M. Hartung, L. M. Mugnier, and G. Rousset. Calibration of NAOS and CONICA static aberrations - application of the phase diversity technique. *Astronomy and Astrophysics*, 399(1):373–383, 2003.

[15] J. M. Conan. *Etude de la Correction Partielle en Optique Adaptative*. PhD thesis, Université de Paris XI Orsay, 1994.

[16] J. M. Conan, G. Rousset, and P. Y. Madec. Wave-front temporal spectra in high-resolution imaging through turbulence. *JOSA A*, 12(7):1559–1570, 1995.

[17] R. Conan. *Modélisation des effets de l'échelle externe de cohérence spatiale du front d'onde pour l'observation à Haute Résolution Angulaire en Astronomie*. PhD thesis, Université de Nice-Sophia Antipolis, 2000.

[18] R. Conan. Adaptive optics modal control modeling. Technical Report ONERA-VLT-PF-WP6340, ONERA, 2003.

[19] R. Conan, R. Avila, L. J. Sanchez, A. Ziad, F. Martin, J. Borgnino, O. Harris, S. I. Gonzalez, R. Michel, and D. Hiriart. Wavefront outer scale and seeing measurements at San Pedro Mártir Observatory. *Astronomy and Astrophysics*, 396(2):723–730, 2002.

[20] A. Consortini, Y. Y. Sun, Z. P. Li, and G. Conforti. A mixed method for measuring the inner scale of atmospheric-turbulence. *Journal of Modern Optics*, 37(10):1555–1560, 1990.

[21] G. M. Dai. Modal wave-front reconstruction with Zernike polynomials and Karhunen-Loève functions. *JOSA A*, 13(6):1218–1225, 1996.

[22] C. Dessenne. *Commande modale et predictive en optique adaptative*. PhD thesis, Université Denis Diderot - Paris VII, 1998.

[23] C. Dessenne, P. Y. Madec, and G. Rousset. Modal prediction for closed-loop adaptive optics. *Optics Letters*, 22(20):1535–1537, 1997.

[24] C. Dessenne, P. Y. Madec, and G. Rousset. Optimization of a predictive controller for closed-loop adaptive optics. *Applied Optics*, 37(21):4623–4633, 1998.

[25] C. Dessenne, P. Y. Madec, and G. Rousset. Sky implementation of modal predictive control in adaptive optics. *Optics Letters*, 24(5):339–341, 1999.

[26] R. H. Dicke. Phase-contrast detection of telescope seeing errors and their correction. *Astrophysical Journal*, 198:605–615, 1975.

[27] A. Dubra, J. S. Massa, and C. Paterson. Preisach classical and nonlinear modeling of hysteresis in piezoceramic deformable mirrors. *Optics Express*, 13(22):9062–9070, 2005.

[28] P. Durbin and R. B. Pettersson. *Statistical theory and modelling for turbulent flows*. Wiley, 2001.

[29] B. L. Ellerbroek, L. Gilles, and C. R. Vogel. Numerical simulations of multiconjugate adaptive optics wave- front reconstruction on giant telescopes. *Applied Optics*, 42(24):4811–4818, 2003.

[30] B. L. Ellerbroek, F. Rigaut, B. Bauman, C. Boyer, S. Browne, R. Buchroeder, J. Catone, P. Clark, C. d'Orgeville, D. Gavel, G. Herriot, M. R. Hunten, E. James, E. Kibblewhite, I. McKinnie, J. Murray, D. Rabaut, L. Saddlemyer, J. Sebag, J. Stillburn, J. Telle, and J. P. Véran. MCAO for Gemini-South. *Adaptive Optical System Technologies II, Proc. of SPIE*, 4839:55–66, 2003.

[31] B. L. Ellerbroek, C. Vanloan, N. P. Pitsianis, and R. J. Plemmons. Optimizing closed-loop adaptive-optics performance with use of multiple control bandwidths. *JOSA A*, 11(11):2871–2886, 1994.

[32] E. Fedrigo. SPARTA for OWL. Standard platform for adaptive optics real time applications. Staw-man design. Technical Report OWL-CSR-ESO-00000-0178, European Southern Observatory, 2005.

[33] E. Fedrigo and R. Donaldson. MAD real time computer final design. Technical Report OWL-TRE-ESO-60000-0087, European Southern Observatory, 2-5-2003.

[34] R. Foy and A. Labeyrie. Feasibility of adaptive telescope with laser probe. *Astronomy and Astrophysics*, 152(2):L29–L31, 1985.

[35] Gene F. Franklin, J. D. Powell, and Abbas Emami-Naeini. *Feedback control of dynamic systems*. Upper Saddle River, N.J., London : Prentice Hall PTR, c2002, 4th ed edition, 2002.

[36] Gene F. Franklin, J. D. Powell, and Michael L. Workman. *Digital control of dynamic systems*. Menlo Park, Calif ; Harlow, England : Addison-Wesley, 3rd ed edition, 1998.

[37] D. L. Fried. Optical resolution through a randomly inhomogeneous medium for very long and very short exposures. *JOSA*, 56:1372–1379, 1966.

[38] D. L. Fried. Least-square fitting a wave-front distortion estimate to an array of phase-difference measurements. *JOSA*, 67:370–375, 1977.

[39] D. L. Fried. Anisoplanatism in adaptive optics. *JOSA*, 72(1):52–61, 1982.

[40] D. L. Fried. Time-delay-induced mean-square error in adaptive optics. *JOSA A*, 7:1224–1227, 1990.

[41] A. Fuchs, M. Tallon, and J. Vernin. Focusing on a turbulent layer: Principle of the "generalized SCIDAR". *Publications of the Astronomical Society of the Pacific*, 110(743):86–91, 1998.

[42] T. Fusco. *Correction Partielle et Anisoplanétisme en Optique Adaptative: Traitements a Posteriori et Optique Adaptative Multiconjuguée*. PhD thesis, Université de Nice Sophia-Antipolis, 2000.

[43] T. Fusco, J. M. Conan, V. Michau, L. M. Mugnier, and G. Rousset. Efficient phase estimation for large-field-of-view adaptive optics. *Optics Letters*, 24(21):1472–1474, 1999.

[44] T. Fusco, J. M. Conan, V. Michau, and G. Rousset. Noise propagation for multiconjugate adaptive optics systems. *Optics in Atmospheric Propagation and Adaptive Systems IV, Proc. of SPIE*, 4538:144–155, 2002.

[45] T. Fusco, J. M. Conan, V. Michau, G. Rousset, and F. Assemat. Multi-conjugate adaptive optics: Comparison of phase reconstruction approaches for large field of view. *Atmospheric Propagation, Proc. of SPIE*, 4167:168–179, 2000.

[46] T. Fusco, J. M. Conan, V. Michau, G. Rousset, and L. M. Mugnier. Isoplanatic angle and optimal guide star separation for multiconjugate adaptive optics. *Adaptive Optical Systems Technology, Proc. of SPIE*, 4007:1044–1055, 2000.

[47] T. Fusco, J. M. Conan, G. Rousset, L. M. Mugnier, and V. Michau. Optimal wave-front reconstruction strategies for multiconjugate adaptive optics. *JOSA A*, 18(10):2527–2538, 2001.

[48] T. Fusco, M. Nicolle, G. Rousset, V. Michau, A. Blanc, J. L. Beuzit, and J. M. Conan. Wavefront sensing issues in MCAO. *Comptes Rendus Physique*, 6(10):1049–1058, 2005.

[49] T. Fusco, C. Petit, G. Rousset, K. Dohlen, J. Chatron, P. Rabou, P. Feautrier, P. Baudoz, J. Beuzit, D. Mouillet, P. Puget, M. E. Kasper, M. D. Downing, E. Fedrigo, N. Hubin, and F. P. Wildi. Design of the extreme AO system for the Planet Finder instrument on the VLT. *Advances in Adaptive Optics II, Proc. of SPIE*, 6272, [6272-19], 2006.

[50] T. Fusco, G. Rousset, D. Rabaud, E. Gendron, D. Mouillet, F. Lacombe, G. Zins, P. Y. Madec, A. M. Lagrange, J. Charton, D. Rouan, N. Hubin, and N. Ageorges. NAOS on-line characterization of turbulence parameters and adaptive optics performance. *Journal of Optics A-Pure and Applied Optics*, 6(6):585–596, 2004.

[51] W. Gaessler, C. Arcidiacono, S. Egner, T. M. Herbst, D. Andersen, H. Baumeister, P. Bizenberger, H. Boehnhardt, F. Briegel, M. Kuerster, W. Laun, L. Mohr, B. Grimm, H. W. Rix, R. R. Rohloff, R. Soci, C. Storz, W. Xu, R. Ragazzoni, P. Salinari, E. Diolaiti, J. Farinato, M. Carbillet, L. Schreiber, A. Eckart, T. Bertram, C. Straubmeier, Y. Wang, L. Zealouk, G. Weigelt, U. Beckmann, J. Behrend, T. Driebe, M. Heininger, K. H. Hofmann, E. Nussbaum, D. Schertel, and E. Masciadri. LINC-NIRVANA: MCAO toward extremely large telescopes. *Comptes Rendus Physique*, 6(10):1129–1138, 2005.

[52] J. P. Gaffard and C. Boyer. Adaptive optics for optimization of image-resolution. *Applied Optics*, 26(18):3772–3777, 1987.

[53] E. Gendron. *Optimisation de la commande modale en optique adaptative: applications a l'astronomie*. PhD thesis, Université Denis Diderot - Paris VII, 1995.

[54] E. Gendron, F. Assemat, F. Hammer, P. Jagourel, F. Chemla, P. Laporte, M. Puech, M. Marteaud, F. Zamkotsian, A. Liotard, J. M. Conan, T. Fusco, and N. Hubin. FALCON: multi-object AO. *Comptes Rendus Physique*, 6(10):1110–1117, 2005.

[55] E. Gendron and P. Lena. Astronomical adaptive optics. 1. Modal control optimization. *Astronomy and Astrophysics*, 291(1):337–347, 1994.

[56] E. Gendron and P. Lena. Astronomical adaptive optics. 2. Experimental results of an optimized modal control. *Astronomy and Astrophysics Supplement Series*, 111(1):153–167, 1995.

[57] L. Gilles. Closed-loop stability and performance analysis of least-squares and minimum-variance control algorithms for multiconjugate adaptive optics. *Applied Optics*, 44(6):993–1002, 2005.

[58] A. V. Goncharov, J. C. Dainty, S. Esposito, and A. Puglisi. Laboratory MCAO test-bed for developing wavefront sensing concepts. *Optics Express*, 13(14):5580–5590, 2005.

[59] R. A. Gonsalves. Phase retrieval and diversity in adaptive optics. *Optical Engineering*, 21(5):829–832, 1982.

[60] J. W. Goodman. *Statistical optics*. Wiley, New York, 1985.

[61] J. E. Graves, M. J. Northcott, F. Roddier, C. Roddier, and L. Close. First light for HOKUPA'A: the 36 element curvature AO system at UH. *Adaptive Optical Systems Technologies, Proc. of SPIE*, 3353:34–43, 1998.

[62] C. W. Groetsch. *Inverse Problems in the Mathematical Science*. Vieweg, Braunschweig/Wiesbaden, 1993.

[63] A. Habib, J. Vernin, Z. Benkhaldoun. Atmospheric-turbulence characterization by single-star scintillation analysis. *Comptes Rendus Physique*, 6(3):385–392, 2005.

[64] J. W. Hardy. *Adaptive optics for astronomical telescopes.* Oxford University Press, New York, 1998.

[65] A. Hartung, A. Blanc, T. Fusco, F. Lacombe, L. M. Mugnier, G. Rousset, and R. Lenzen. Calibration of NAOS and CONICA static aberrations - experimental results. *Astronomy and Astrophysics*, 399(1):385–394, 2003.

[66] N. Hubin, R. Arsenault, R. Conzelmann, B. Delabre, M. Le Louarn, S. Stroebele, and R. Stuik. Ground layer adaptive optics. *Comptes Rendus Physique*, 6(10):1099–1109, 2005.

[67] P. Jagourel. Design report. MACAO-SINFONI and MACAO-CRIRES deformable mirrors. Technical Report VLT-TRE-CIL-11640-0001, CILAS, 11-9-2001.

[68] P. Jagourel. Design report. MACAO-VLTI deformable mirror. Technical Report VLT-TRE-CIL-15600-0001, CILAS, 2-7-2001.

[69] D. C. Johnston and B. M. Welsh. Analysis of multiconjugate adaptive optics. *JOSA A*, 11(1):394–408, 1994.

[70] M. Kasper, D. P. Looze, S. Hippler, T. Herbst, A. Glindemann, T. Ott, and A. Wirth. ALFA: Adaptive optics for the Calar Alto Observatory optics, control systems, and performance. *Experimental Astronomy*, 10(1):49–73, 2000.

[71] J. Kittler, J. Illingworth, and J. Foglein. Threshold selection based on a simple image statistic. *Computer Vision Graphics and Image Processing*, 30(2):125–147, 1985.

[72] V. A. Kluckers, N. J. Wooder, T. W. Nicholls, M. J. Adcock, I. Munro, and J. C. Dainty. Profiling of atmospheric turbulence strength and velocity using a generalised SCIDAR technique. *Astronomy and Astrophysics Supplement Series*, 130(1):141–155, 1998.

[73] P. A. Knutsson and M. Owner-Petersen. Emulation of dual-conjugate adaptive optics on an 8-m class telescope. *Optics Express*, 11(18):2231–2237, 2003.

[74] J. Kolb. *Calibration and test tools for MCAO systems: Application to the ESO Demonstrator MAD.* PhD thesis, Université Paris VI, 2005.

[75] J. Kolb. Eliminating the static aberrations in an MCAO system. *Advances in Adaptive Optics II, Proc. of SPIE*, 6272, [6272-122], 2006.

[76] J. Kolb. Characterization of the anamorphism and curvature of the IR focal plane. Technical Report MAD-TRE-0021, European Southern Observatory, 28-11-2005.

[77] J. Kolb, S. Oberti, E. Marchetti, and F. Quirós-Pacheco. Full characterization of the turbulence generator MAPS for MCAO. *Advances in Adaptive Optics II, Proc. of SPIE*, 6272, [6272-184], 2006.

[78] A. N. Kolmogorov. The local structure of turbulence in incompressible viscous fluid for very large Reynolds numbers (translation). *Proceedings of the Royal Society of London. Series A*, 434(1890):9–13, 1991.

[79] A. Labeyrie. Attainment of diffraction limited resolution in large telescopes by Fourier analysing speckle patterns in star images. *Astronomy and Astrophysics*, 6:85, 1970.

[80] M. Lloyd-Hart, C. Baranec, N. M. Milton, T. Stalcup, M. Snyder, N. Putnam, and J. R. P. Angel. First tests of wavefront sensing with a constellation of laser guide beacons. *Astrophysical Journal*, 634(1):679–686, 2005.

[81] M. Lloyd-Hart and N. M. Milton. Fundamental limits on isoplanatic correction with multiconjugate adaptive optics. *JOSA A*, 20(10):1949–1957, 2003.

[82] D. P. Looze, M. Kasper, S. Hippler, O. Beker, and R. Weiss. Optimal compensation and implementation for adaptive optics systems. *Experimental Astronomy*, 15(2):67–88, 2003.

[83] M. Le Louarn. Multi-conjugate adaptive optics with laser guide stars: performance in the infrared and visible. *MNRAS*, 334(4):865–874, 2002.

[84] M. Le Louarn. OWL AO analysis report. Technical Report OWL-CSR-ESO-00000-0169, European Southern Observatory, 2005.

[85] M. Le Louarn and N. Hubin. Wide-field adaptive optics for deep-field spectroscopy in the visible. *MNRAS*, 349(3):1009–1018, 2004.

[86] M. Le Louarn and N. Hubin. Improving the seeing with wide-field adaptive optics in the near-infrared. *MNRAS*, 365(4):1324–1332, 2006.

[87] M. Le Louarn, N. Hubin, M. Sarazin, and A. Tokovinin. New challenges for adaptive optics: extremely large telescopes. *MNRAS*, 317(3):535–544, 2000.

[88] M. Le Louarn and M. Tallon. Analysis of modes and behavior of a multiconjugate adaptive optics system. *JOSA A*, 19(5):912–925, 2002.

[89] B. A. Macintosh, J. R. Graham, D. W. Palmer, R. Doyon, D. T. Gavel, J. E. Larkin, B. R. Oppenheimer, L. Poyneer, L. K. Saddlemeyer, A. Sivaramakrishnan, J. K. Wallace, and J. Véran. The Gemini Planet Imager. *Advances in Adaptive Optics II, Proc. of SPIE*, 6272, [6272-20], 2006.

[90] P. Y. Madec. Control techniques. In F. Roddier, editor, *Adaptive optics in astronomy*, book chapter 6, pages 131–154. Cambridge University Press, 1999.

[91] E. Marchetti. MAD experimental error budget. Technical Report MAD-TRE-0025, European Southern Observatory, 19-1-2006.

[92] E. Marchetti, R. Brast, B. Delabre, R. Donaldson, E. Fedrigo, C. Frank, N. Hubin, J. Kolb, M. Le Louarn, J. L. Lizon, S. Oberti, F. Quirós-Pacheco, R. Reiss, J. Santos, S. Tordo, E. Vemet, R. Ragazzoni, C. Arcidiacono, P. Bagnara, A. Baruffolo, E. Diolaiti, J. Farinato, and M. Lombini. MAD: practical implementation of MCAO concepts. *Comptes Rendus Physique*, 6(10):1118–1128, 2005.

[93] E. Marchetti, R. Brast, B. Delabre, R. Donaldson, E. Fedrigo, C. Frank, N. Hubin, J. Kolb, M. Le Louarn, J.L. Lizon, S. Oberti, F. Quirós-Pacheco, R. Reiss, J. Santos, S. Tordo, A. Baruffolo, P. Bagnara, A. Amorim, and J. Lima. MAD star-oriented: laboratory results for ground layer multi-conjugate adaptive optics. *Advances in Adaptive Optics II, Proc. of SPIE*, 6272, [6272-62], 2006.

[94] E. Marchetti and N. Hubin. Multi atmospheric phase screens and stars. Technical specifications. Technical Report OWL-SPE-ESO-60000-0038, European Southern Observatory, 19-4-2002.

[95] E. Marchetti, N. Hubin, E. Fedrigo, J. Brynnel, B. Delabre, R. Donaldson, F. Franza, R. Conan, M. Le Louarn, C. Cavadore, A. Balestra, D. Baade, J. L. Lizon, R. Gilmozzi, G. Monnet, R. Ragazzoni, C. Arcidiacono, A. Baruffolo, E. Diolaiti, J. Farinato, E. Viard, D. Butler, S. Hippler, and A. Amorim. MAD the ESO multi-conjugate adaptive optics demonstrator. *Adaptive Optical System Technologies II, Proc. of SPIE*, 4839:317–328, 2003.

[96] B. L. McGlamery. Computer simulation studies of compensation of turbulence degraded images. *Image processing, Proc. of SPIE*, 74:225–233, 1976.

[97] M. Nicolle. Optimisation de mesure du front d'onde pour senseur de Shack-Hartmann. Rapport de stage. DESS outils et systèmes de l'astronomie et de l'espace. Observatoire de Paris Meudon, Office National d'Etudes et de Recherches Aerospatiales (ONERA), 2003.

[98] M. Nicolle, T. Fusco, V. Michau, G. Rousset, A. Blanc, and J. L. Beuzit. Ground layer adaptive optics: Analysis of the wavefront sensing issue. *Advancements in Adaptive Optics, Proc. of SPIE*, 5490:858–869, 2004.

[99] R. J. Noll. Zernike polynomials and atmospheric turbulence. *JOSA*, 66(3):207–211, 1976.

[100] S. Oberti. Characterization of the MAPS bad seeing case. Technical Report MAD-TRE-0019, European Southern Observatory, 17-11-2005.

[101] S. Oberti, F. Quirós-Pacheco, S. Esposito, R. Muradore, R. Arsenault, E. Fedrigo, M. Kasper, J. Kolb, E. Marchetti, A. Riccardi, C. Soenke, and S. Stroebele. Large DM AO systems: synthetic IM or calibration on sky? *Advances in Adaptive Optics II. Proceedings of SPIE*, 6272, [6272-70], 2006.

[102] A. M. Obukhov. Structure of the temperature field in a turbulent current. *Izv. Akad. Nauk SSSR Ser. Geograf. Geofiz.*, 13(1):58–69, 1949.

[103] R. N. Paschall and D. J. Anderson. Linear-quadratic gaussian control of a deformable mirror adaptive optics system with time-delayed measurements. *Applied Optics*, 32(31):6347–6358, 1993.

[104] C. Paterson. Constraints of ground-based observations: The atmosphere. In R. Foy and F. Foy, editors, *Optics in Astrophysics*, NATO Science Series, pages 1–10. Springer, 2005.

[105] D. M. Pennington. Laser technologies for laser guided adaptive optics. In R. Foy and F. Foy, editors, *Optics in Astrophysics*, NATO Science Series, pages 207–248. Springer, 2005.

[106] J. A. Perreault, T. G. Bifano, B. M. Levine, and M. N. Horenstein. Adaptive optic correction using microelectromechanical deformable mirrors. *Optical Engineering*, 41(3):561–566, 2002.

[107] C. Petit. Optique adaptative multiconjuguée: tests en laboratoire. Etude et comparaison des matrices d'interaction et de commande optiques et théoriques. Rap-

port de stage. DEA d'optique et photonique. Université Paris XI, Office National d'Etudes et de Recherches Aerospatiales (ONERA), 2003.

[108] C. Petit, J. M. Conan, C. Kulcsar, H. F. Raynaud, T. Fusco, J. Montri, and D. Rabaud. Optimal control for multi-conjugate adaptive optics. *Comptes Rendus Physique*, 6(10):1059–1069, 2005.

[109] C. Petit, F. Quirós-Pacheco, J. M. Conan, C. Kulcsar, H. F. Raynaud, T. Fusco, and G. Rousset. Kalman filter based control for adaptive optics. *Advancements in Adaptive Optics, Proc. of SPIE*, 5490:1414–1425, 2004.

[110] P. Piatrou and L. Gilles. Robustness study of the pseudo open-loop controller for multiconjugate adaptive optics. *Applied Optics*, 44(6):1003–1010, 2005.

[111] F. Quirós-Pacheco. Opto-geometrical relationships between DMs and SH-WFSs. Technical Report MAD-TRE-0023, European Southern Observatory, 14-12-2005.

[112] F. Quirós-Pacheco, C. Petit, J. M. Conan, T. Fusco, and E. Marchetti. Control laws for a multi-conjugate adaptive optics system. *Advancements in Adaptive Optics, Proc. of SPIE*, 5490:1460–1471, 2004.

[113] F. Quirós-Pacheco and J. Santos. Background characterization of Shack-Hartmann subimages. Technical Report MAD-TRE-0022, European Southern Observatory, 2005.

[114] R. Racine. The Strehl efficiency of adaptive optics systems. *Publications of the Astronomical Society of the Pacific*, 118(845):1066–1075, 2006.

[115] R. Ragazzoni. Pupil plane wavefront sensing with an oscillating prism. *Journal of Modern Optics*, 43(2):289–293, 1996.

[116] R. Ragazzoni, J. Farinato, and E. Marchetti. Adaptive optics for 100m class telescopes: new challenges require new solutions. *Adaptive Optical Systems Technology, Proc. of SPIE*, 4007:1076–1087, 2000.

[117] R. Ragazzoni, E. Marchetti, and F. Rigaut. Modal tomography for adaptive optics. *Astronomy and Astrophysics*, 342(3):L53–L56, 1999.

[118] R. Ragazzoni, E. Marchetti, and G. Valente. Adaptive-optics corrections available for the whole sky. *Nature*, 403(6765):54–56, 2000.

[119] A. Riccardi, G. Brusa, M. Xompero, D. Zannoti, C. Del Vecchio, P. Salinari, P. Ranfagni, D. Gallieni, M. Andrighattoni, S. Miller, and P. Mantegazza. The adaptive secondary mirrors for the Large Binocular Telescope: a progress report. *Advancements in Adaptive Optics, Proc. of SPIE*, 5490:1564–1571, 2004.

[120] F. Rigaut. Ground conjugate wide field adaptive optics for the ELTs. *Beyond Conventional Adaptive Optics, ESO Conference and Workshop Proceedings*, 58:11–16, 2002.

[121] F. Rigaut and E. Gendron. Laser guide star in adaptive optics - the tilt determination problem. *Astronomy and Astrophysics*, 261(2):677–684, 1992.

[122] F. Rigaut, G. Rousset, P. Kern, J. C. Fontanella, J. P. Gaffard, F. Merkle, and P. Lena. Adaptive optics on a 3.6-m telescope - results and performance. *Astronomy and Astrophysics*, 250(1):280–290, 1991.

[123] F. J. Rigaut, B. L. Ellerbroek, and R. Flicker. Principles, limitations and performance of multi-conjugate adaptive optics. *Adaptive Optical Systems Technology, Proc. of SPIE*, 4007:1022–1031, 2000.

[124] F. Roddier. The effects of atmospheric turbulence in optical astronomy. *Progress in Optics*, XIX:283–376, 1981.

[125] F. Roddier. Curvature sensing and compensation - a new concept in adaptive optics. *Applied Optics*, 27(7):1223–1225, 1988.

[126] F. Roddier. *Adaptive optics in astronomy*. Cambridge University Press, Cambridge, U.K, 1999.

[127] M. C. Roggemann and B. Welsh. *Imaging through turbulence*. CRC Press, Boca Raton, 1996.

[128] G. Rousset. Wave-front sensors. In F. Roddier, editor, *Adaptive optics in astronomy*, book chapter 5, pages 91–130. Cambridge University Press, 1999.

[129] G. Rousset, J. C. Fontanella, P. Kern, P. Gigan, F. Rigaut, P. Lena, C. Boyer, P. Jagourel, J. P. Gaffard, and F. Merkle. 1st diffraction-limited astronomical images with adaptive optics. *Astronomy and Astrophysics*, 230(2):L29–L32, 1990.

[130] G. Rousset, F. Lacombe, P. Puget, N. Hubin, E. Gendron, T. Fusco, R. Arsenault, J. Charton, P. Feautrier, P. Gigan, P. Kern, A. M. Lagrange, P. Y. Madec,

D. Mouillet, D. Rabaud, P. Rabou, E. Stadler, and G. Zins. NAOS, the first AO system of the VLT: on-sky performance. *Adaptive Optical System Technologies II, Proc. of SPIE*, 4839:140–149, 2003.

[131] B. Le Roux. *Commande optimale en optique adaptative classique et multiconjuguée*. PhD thesis, Université de Nice Sophia-Antipolis, 2003.

[132] B. Le Roux, J. M. Conan, C. Kulcsar, H. F. Raynaud, L. M. Mugnier, and T. Fusco. Optimal control law for classical and multiconjugate adaptive optics. *JOSA A*, 21(7):1261–1276, 2004.

[133] J. Santos. Linearity and plate scale of the multi-Shack Hartmann WFS. Technical Report MAD-TRE-0010, European Southern Observatory, 1-7-2005.

[134] J. Santos and E. Marchetti. MAD CCDs characterization. Technical Report MAD-TRE-0013, European Southern Observatory, 8-12-2004.

[135] J. Santos, S. Oberti, and L. Ivanescu. Test of MAD altitude DM. Technical Report MAD-TRE-0007, European Southern Observatory, 1-2-2005.

[136] M. Sarazin and F. Roddier. The ESO differential image motion monitor. *Astronomy and Astrophysics*, 227(1):294–300, 1990.

[137] G. Strang. *Linear Algebra and its Applications*. Harcourt, Orlando, 3rd edition, 1988.

[138] H. Takami, N. Takato, Y. Hayano, M. Iye, S. Oya, Y. Kamata, T. Kanzawa, Y. Minowa, M. Otsubo, K. Nakashima, W. Gaessler, and D. Saint-Jacques. Performance of Subaru Cassegrain adaptive optics system. *Publications of the Astronomical Society of Japan*, 56(1):225–234, 2004.

[139] M. Tallon and R. Foy. Adaptive telescope with laser probe - isoplanatism and cone effect. *Astronomy and Astrophysics*, 235(1-2):549–557, 1990.

[140] V. I. Tatarski. *Wave propagation in a turbulent medium*. Dover Publications, New York, 1961.

[141] G. I. Taylor. The spectrum of turbulence. *Proceedings of the Royal Society of London. Series A, Mathematical and Physical Sciences*, 164(919):476–490, 1938.

[142] H Tennekes and J. L. Lumley. *A first course in turbulence*. M.I.T. Press, Cambridge [Mass.] and London, England, 1972.

[143] A. Tokovinin. From differential image motion to seeing. *Publications of the Astronomical Society of the Pacific*, 114(800):1156–1166, 2002.

[144] A. Tokovinin. Seeing improvement with ground-layer adaptive optics. *Publications of the Astronomical Society of the Pacific*, 116(824):941–951, 2004.

[145] A. Tokovinin, V. Kornilov, N. Shatsky, and O. Voziakova. Restoration of turbulence profile from scintillation indices. *MNRAS*, 343(3):891–899, 2003.

[146] A. Tokovinin, M. Le Louarn, and M. Sarazin. Isoplanatism in a multiconjugate adaptive optics system. *JOSA A*, 17(10):1819–1827, 2000.

[147] A. Tokovinin, M. Le Louarn, E. Viard, N. Hubin, and R. Conan. Optimized modal tomography in adaptive optics. *Astronomy and Astrophysics*, 378(2):710–721, 2001.

[148] A. Tokovinin and T. Travouillon. Model of optical turbulence profile at Cerro Pachón. *MNRAS*, 365(4):1235–1242, 2006.

[149] A. Tokovinin, J. Vernin, A. Ziad, and M. Chun. Optical turbulence profiles at Mauna Kea measured by MASS and SCIDAR. *Publications of the Astronomical Society of the Pacific*, 117(830):395–400, 2005.

[150] A. Tokovinin and E. Viard. Limiting precision of tomographic phase estimation. *JOSA A*, 18(4):873–882, 2001.

[151] M. A. van Dam, D. Le Mignant, and B. A. Macintosh. Performance of the Keck Observatory adaptive-optics system. *Applied Optics*, 43(29):5458–5467, 2004.

[152] J. P. Véran. *Estimation de la reponse impulsionnelle et restauration d'image en optique adaptative.* PhD thesis, Ecole Nationale Supérieure des Télécommunications, 1997.

[153] J. P. Véran, F. Rigaut, H. Maitre, and D. Rouan. Estimation of the adaptive optics long-exposure point-spread function using control loop data. *JOSA A*, 14(11):3057–3069, 1997.

[154] C. Verinaud. On the nature of the measurements provided by a pyramid wavefront sensor. *Optics Communications*, 233(1-3):27–38, 2004.

[155] E. Vernet, C. Arcidiacono, A. Baruffolo, E. Diolaiti, J. Farinato, M. Lombini, and R. Ragazzoni. Layer-oriented wavefront sensor for a multiconjugate adaptive optics demonstrator. *Optical Engineering*, 44(9), 2005.

[156] J. Vernin, Raffaele Barletti, Guido Ceppatelli, Lucio Paterno, Alberto Righini, and N. Speroni. Optical remote sensing of atmospheric turbulence: a comparison with simultaneous thermal measurements. *Applied Optics*, 18:243–247, 1979.

[157] E. Weisstein. Modified Bessel function of the second kind. MathWorld–A Wolfram Web Resource. http://mathworld.wolfram.com/ModifiedBesselFunctionoftheSecondKind.html.

[158] D. M. Wiberg, C. E. Max, and D. T. Gavel. Geometric view of adaptive optics control. *JOSA A*, 22(5):870–880, 2005.

[159] R. W. Wilson. SLODAR: measuring optical turbulence altitude with a Shack-Hartmann wavefront sensor. *MNRAS*, 337(1):103–108, 2002.

[160] Q. Yang, C. Ftaclas, M. Chun, and D. Toomey. Hysteresis correction in the curvature adaptive optics system. *JOSA A*, 22(1):142–147, 2005.

[161] F. Zamkotsian, H. Camon, N. Fabre, V. Conedera, and G. Moreaux. Micro-deformable mirror for next generation adaptive optical systems. *Adaptive Optical System Technologies II, Proc. of SPIE*, 4839:711–720, 2003.

[162] A. Ziad, M. Schock, G. A. Chanan, M. Troy, R. Dekany, B. F. Lane, J. Borgnino, and F. Martin. Comparison of measurements of the outer scale of turbulence by three different techniques. *Applied Optics*, 43(11):2316–2324, 2004.